

Dissertation zur Erlangung des Doktorgrades
der Fakultät für Chemie und Pharmazie
der Ludwig-Maximilians-Universität München

**Towards single-site heterogeneous catalysts
for the hydrogen evolution reaction based on
covalent organic frameworks**

Kerstin Gottschling
aus
Trostberg

2020

Erklärung

Diese Dissertation wurde im Sinne von §7 der Promotionsordnung vom 28. November 2011 von Frau Prof. Dr. Bettina V. Lotsch betreut.

Eidesstattliche Versicherung

Diese Dissertation wurde eigenhändig und ohne unerlaubte Hilfe erarbeitet.

München, den 18.05.2020

Kerstin Gottschling

Dissertation eingereicht am: 22.05.2020
Erstgutachterin: Prof. Dr. Bettina V. Lotsch
Zweitgutachter: Prof. Dr. Thomas Bein
Mündliche Prüfung am: 29.06.2020

Was I the same when I got up this morning?

Lewis Carroll



Danksagung

Danke an Bettina Lotsch, die mir die Möglichkeit gegeben hat, meine Doktorarbeit in ihrem Arbeitskreis durchzuführen. Danke für die fachliche Expertise, die du immer wieder eingebracht hast und die Freiheiten, durch die ich wachsen und eigene Ideen entwickeln konnte.

Danke an Prof. Thomas Bein für die Übernahme des Zweitgutachtens und an die gesamte Prüfungskommission – Prof. Lena Daumann, Prof. Achim Hartschuh, Prof. Ivan Huc und Prof. Konstantin Karaghiosoff.

Danke an die Co-Autoren, die entscheidend waren für die tollen Projekte, die wir nur gemeinsam fertigstellen konnten. Danke an die Praktikanten und Bacheloranden, die hoffentlich ein wenig meiner Begeisterung für das Thema mitgenommen haben – Dominic Blätte, Regina Gabler, Lars Grunenberg, Annick Hemmerling, Philipp Mauker und Sandra Schmidt.

Danke nach Stuttgart ans MPI, wo tolle Kollegen viel zu weit weg sind. Besonderen Dank an Claudia Kamella (für bereitwillige Antworten auf unzählige Fragen zum Thema Bestellungen) und Viola Duppel (für das Ausleihen ihres Arbeitsplatzes für Münchner Gäste).

Danke an Sigrid Fuhrmann und Olga Lorenz für die Unterstützung im administrativen Wald am MPI und an der LMU.

Danke an die Teams von NIM und CeNS – für großartige Konferenzen, tolle Erfahrungen im Student Board, die Vergabe des Travel Award. Danke an Chris Hohmann für die Einführung in die Welt des 3D-Grafikdesigns. Danke an Matthias Scheibleger für Illustrator-Nachhilfe und die Erstellung der Icons.

Danke an die Münchner Kollegen, die die letzten Jahre so einzigartig gemacht haben. Wassermelonen-Albi, Yoga-Anna, Auswanderer-Charlie, Glitzer-Gök, Heuschnupfen-Hendrik, Zwillings-Kata, Wein-Leo, Bellini-Sascha, Sorptionshelfer-Stefan. Danke für all die Highlights, die wir gemeinsam erlebt haben – danke für die Bilder, die ich für immer behalte.

Danke an Familie und Freunde, die mich jederzeit und bedingungslos unterstützt haben.

SUMMARY	V
1 INTRODUCTION	1
1.1 Photocatalytic water splitting	1
1.2 Carbon capture and storage	3
1.3 Porous materials	5
1.3.1 Covalent organic frameworks – a new class of polymers	7
1.3.1.1 Boron-based covalent organic frameworks	9
1.3.1.2 C-N-bridged covalent organic frameworks	11
1.3.2 Postsynthetic modification of COFs	20
1.3.3 Covalent organic frameworks as photosensitizers for photocatalytic hydrogen evolution	26
1.3.4 Covalent organic frameworks as gas storage materials	28
1.4 References	30
2 METHODS	39
2.1 Gas adsorption	39
2.1.1 Physisorption isotherms	39
2.1.2 Surface area determination	41
2.1.3 Pore size analysis	42
2.2 Powder x-ray diffraction	43
2.3 Nuclear magnetic resonance spectroscopy	44
2.4 Thin film synthesis	45
2.5 References	47
3 COVALENT ORGANIC FRAMEWORKS AS PHOTOSENSITIZERS FOR PHOTOCATALYTIC HYDROGEN EVOLUTION	49
3.1 Summary	49
3.2 H ₂ evolution with covalent organic framework photocatalysts	51
3.2.1 Abstract	51
3.2.2 Introduction	51
3.2.3 Results and discussion	52

3.2.4	Conclusion.....	65
3.2.5	Acknowledgment	66
3.2.6	Author contributions.....	66
3.2.7	References	66
3.3	Single site photocatalytic H ₂ evolution from covalent organic frameworks with molecular cobaloxime co-catalysts	69
3.3.1	Abstract	69
3.3.2	Introduction.....	69
3.3.3	Results and discussion	70
3.3.4	Conclusion.....	81
3.3.5	Acknowledgments.....	82
3.3.6	Author contributions.....	82
3.3.7	References	82
3.4	Rational design of covalent cobaloxime-COF hybrids for enhanced photocatalytic hydrogen evolution	85
3.4.1	Abstract	85
3.4.2	Introduction.....	86
3.4.3	Results and discussion	87
3.4.4	Conclusion.....	101
3.4.5	Acknowledgements	102
3.4.6	Author contributions.....	102
3.4.7	References	102
4	COVALENT ORGANIC FRAMEWORKS FOR CARBON CAPTURE AND STORAGE	107
4.1	Summary	107
4.2	Molecular insights into carbon dioxide sorption in hydrazone-based covalent organic frameworks with tertiary amine moieties	108
4.2.1	Abstract	109
4.2.2	Introduction.....	109
4.2.3	Results and discussion	111
4.2.4	Conclusion.....	122
4.2.5	Acknowledgments.....	123

4.2.6	Author contributions.....	123
4.2.7	References	123
5	CONCLUSION AND OUTLOOK	127
6	APPENDIX	131
6.1	Supporting information.....	131
6.1.1	Materials and methods for Chapter 3.3	131
6.1.2	Materials and methods for Chapter 3.4	152
6.1.3	Materials and methods for chapter 4.2	185
6.1.4	Supporting References.....	204
6.2	List of figures	206
6.3	List of tables	219
6.4	List of abbreviations	221
6.5	List of publications	223
6.6	Contributions to conferences.....	225

Summary

Covalent organic frameworks (COFs) have emerged as a new class of materials for applications ranging from gas storage and adsorption to optoelectronics and catalysis. They feature crystallinity, high chemical stability and at the same time almost unrestricted diversity due to their molecular tunability.

The growing energy challenges of the 21st century require new solutions from today's scientists. During the last years, photocatalytic hydrogen evolution enabled by COF photosensitizers has emerged as a new field of research. After the seminal discovery of COF photocatalysis in 2014, many different COFs were explored, while only a few proved capable. Skillful organic chemistry allowed the rational design of COF materials to study the mechanism of photocatalytic hydrogen evolution with COFs in more detail.

During this work, variables were defined that need to be adjusted to create an optimized COF photocatalysis system. Those variables range from structural factors (crystallinity, porosity, robustness and stability of the linkages, COF-catalyst interactions) to optoelectronics (light harvesting ability, charge separation and transport, stability of the radical reaction intermediates).

In state-of-the-art COF photocatalysis systems, Pt nanoparticles are used as hydrogen evolution co-catalysts. In this thesis, the utilization of molecular cobaloxime co-catalysts was explored with different azine- and hydrazine-based COFs as photosensitizers. Physisorption of the cobaloximes to the COFs proved the compatibility of the components. The best performing system showed a hydrogen evolution rate of $782 \mu\text{mol g}^{-1} \text{h}^{-1}$ and a turnover number of 54.4 in a water/acetonitrile mixture with triethanolamine as electron donor. In a further step, the cobaloxime catalysts were covalently attached to the COFs. The as-created heterogeneous, but fully single-site photocatalytic system proved double as active than the respective physisorbed system. This could be the foundation for a modular leaf-like architecture leading to a full-water-splitting system.

Additionally, the COFs' molecular tunability was used to create a platform with enhanced CO_2 interactions. Tertiary amines were integrated into different COF systems and their CO_2 and water adsorption properties were investigated. The synergy of amine content, COF polarity and wettability were found crucial for the performance of the COF system leading to very high heats of adsorption at zero coverage (72.4 kJ mol^{-1}) in the best case.



1 Introduction

Living in the so-called anthropocene, mankind is the biggest influence on the earth's wellbeing. Since the start of the industrialization in the beginning of the 19th century, the world's population grew steadily to approximately 7.7 billion people today and is projected to reach 9.8 billion people by 2050.^[1] The heavy increase of population carries a strong need for resources with it. In this context, the concept of renewable and climate friendly green energy is more important than ever. In 2017, the amount of renewable energy grew by 17%, which is the largest increment on record.^[2] Man-made climate change is accepted to be one of the biggest challenges of our century and we need to put our effort into the exploration and the understanding of sustainable power generation.

1.1 Photocatalytic water splitting

The most abundant energy source by far is the sun. The preferably direct use of sunlight provides a great possibility to tackle our energy problems. The energy of the sun is converted to thermal, electrical, or chemical energy in a first step by different technologies as shown in Figure 1-1. Solar water heating uses solar thermal collectors that warm up working fluid which is then distributed or stored for later use. The conversion of sunlight to electricity is achieved by photovoltaics. Conventional solar cells use crystalline or amorphous silicon or other semiconducting materials to absorb and convert the sunlight. In december 2014, the world record for the highest efficiency in a solar cell was set to 46.0 % by the Fraunhofer ISE by using a GaAs-based multi-junction concentrator solar cell.^[3] While traditional photovoltaics prompt more and more questions on electricity storage and fluctuations, new techniques need to be developed. One of the most promising concepts is to convert sunlight to chemical energy by artificial photosynthesis, where the natural photosynthesis is mimicked to convert energy from sunlight, water and carbon dioxide into oxygen and high-energy carbohydrates. Water splitting through artificial photosynthesis is a very complex and demanding four-electron-process. A simplified strategy is photocatalytic hydrogen evolution, where solar fuels like hydrogen are produced from readily available substances like alcohols. Simple high-energy fuels can be used to produce electricity or heat or can be further converted to more chemically demanding structures. These secondary fuels (e. g. gasoline, simple hydrocarbons, hydrogen) can be stored more easily or used as large-scale starting materials in industry. Creation of primary fuels by solar energy conversion is an eco-friendly and nearly inexhaustible process, which makes its understanding and optimization all the way to a possible commercialization highly desirable.

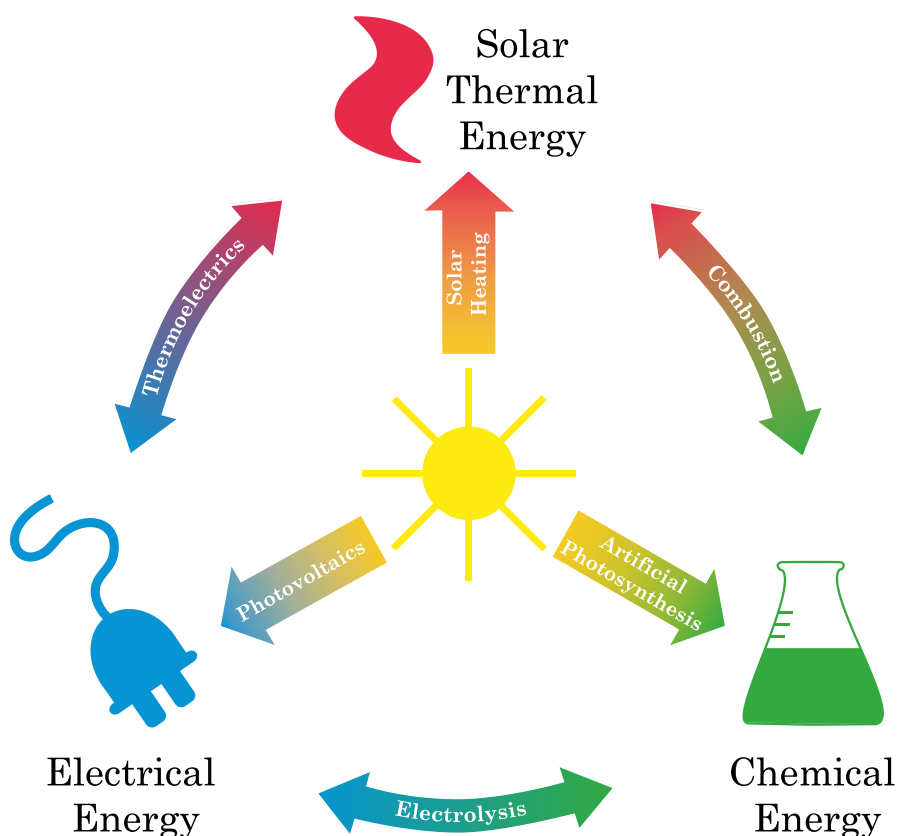


Figure 1-1: Solar energy is transformed into thermal, electrical, or chemical energy by different techniques. Further, these types of energy can be converted into each other.

Since the discovery of titanium dioxide as a solid state water splitting catalyst^[4], the main focus of research in this area has been on inorganic solid semiconductor materials. Other examples for inorganic photocatalysts are TaON^[5-6], NaTaO₃:La^[7], Fe₂O₃^[8] or BiVO₄^[9]. A more detailed description of the water splitting process will be given in Chapter 1.3.3.

Even though the theoretical potential difference of the redox processes involved in overall water splitting is 1.23 eV, the actual minimum energy is significantly higher due to substantial overpotential for both half-reactions. Co-catalysts are used to lower this overpotential. Typically, co-catalyst materials consist of rare and noble metals like platinum or rhodium for the reduction and precious metal oxides like ruthenium(IV) or iridium(IV) oxide for the oxidation reaction.

Many photoabsorbers suffer from intrinsic shortcomings such as fast charge carrier recombination, or extrinsic limitations such as degradation under operation conditions. The long-term catalyst stability is a basic requirement and needs to be assured for any real application. Suppression of recombination can be achieved by a high dielectricity in the semiconductor as well as fast and efficient charge transport.



For the in-depth evaluation of each half-reaction, sacrificial agents are used to quench the respective charge carriers. In this work, the focus will be on the hydrogen evolution reaction. Therefore, readily oxidizable sacrificial electron donors like alcohols and amines are used. Carbon nitrides, a class of crystalline 2D polymeric materials, were shown to perform full water splitting under visible light in 2009 by Wang and coworkers^[10], even though experiments were performed as two separate half-reactions with the respective sacrificial agents. This started intense research on carbon nitride based photocatalysts. Until today, hydrogen evolution rates (HER) up to $331 \mu\text{mol h}^{-1}$ could be achieved.^[11] “Dark photocatalysis” via photoinduced electron trapping^[12] and its use as aqueous solar batteries^[13] have been accomplished with carbon nitride materials. Even though the development of these materials has been very impressive, carbon nitrides are limited in their chemical tunability as they typically consist of triazine or heptazine units.

The structurally related, yet considerably more tunable covalent organic frameworks (COFs, see Chapter 1.3.1) have been found to be very potent for photocatalytic hydrogen evolution by our group in 2014.^[14] The field of COF photocatalysis has undergone vast development since then. A closer look into the progress in this research field will be given in Chapter 3.2.

1.2 Carbon capture and storage

One of the biggest concerns in the context of climate change and global warming is the increased emission of greenhouse gases. Mainly carbon dioxide and methane are emitted by combustion of fossil fuels for energy and transportation as well as large-scale industrial processes like clinker production from limestone. The concentration of CO_2 has increased by 36% since 1750, which is much higher than during the last 800 000 years in total, for which reliable data can be achieved from ice cores. The urgency for the development of key technologies for CO_2 mitigation is high. Besides advancements in industrial processes and energy production, carbon capture and storage (CCS) comes more and more to the fore. In CCS technology, CO_2 is separated from other gases and then stored in geological or submarine sequestration sites.

The first commercial example for a CCS project was the Weyburn-Midale Carbon Dioxide Project that was located in Saskatchewan, Canada from 2000 to 2011. Here, the long-term storage of CO_2 in geological formations with focus on oil reservoirs was tested. After a promising testing phase, leaks were observed in form of bubbling ponds, dead animals near those ponds and sounds of gas explosions. Man-made wellbores are blamed for those leaks that clearly diminish the long-term reliability for such projects. In addition, long-term responsibility for maintenance and safety of the ponds are unclear which increases the demand for new technologies.

An alternative to CCS that is being considered nowadays is carbon capture and utilization (CCU), where the captured CO_2 is further used industrially to be converted into carbonates, carbamates, urea, or polymers.

In both cases, efficient CO_2 separation is crucial. Three different approaches have been proposed as can be seen in Figure 1-2:

- (i) Post-combustion capture. CO_2 is captured from the stream that exits the combustion chamber.
- (ii) Pre-combustion. A fuel gas reformer produces syngas, which is a mixture of H_2 , CO and CO_2 . CO_2 is separated from the syngas before hydrogen is used as a fuel for combustion.
- (iii) Oxy-fuel combustion. Combustion with pure oxygen rather than with air yields high purity CO_2 that can be stored directly.

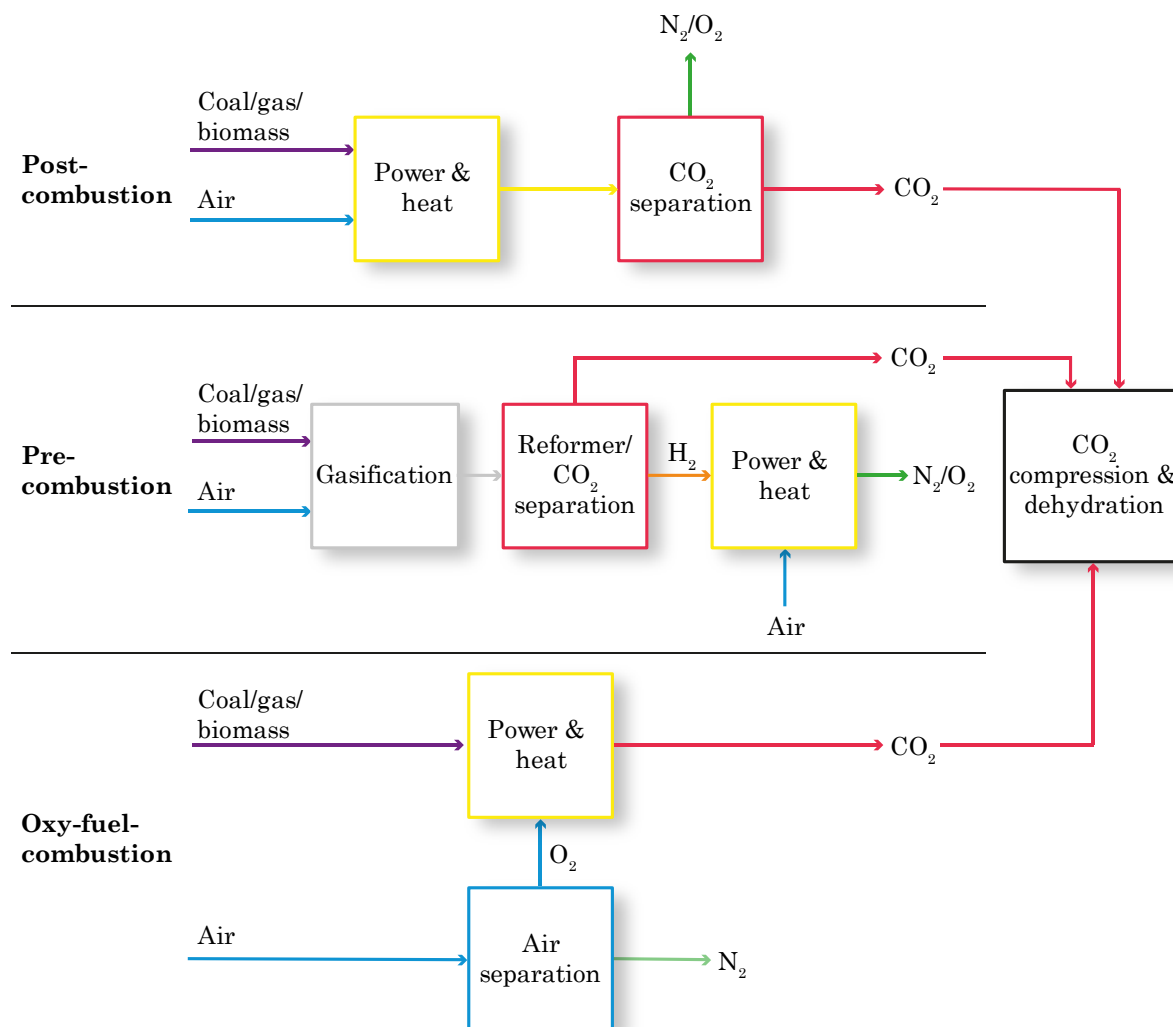


Figure 1-2: Schematic representation of three different approaches for carbon dioxide separation – post-combustion, pre-combustion and oxy-fuel combustion.



The current commercial post-combustion technology is based on the so-called amine scrubbing. In this treatment, solutions of alkylamines in water are used to remove CO₂ from gas mixtures. Commonly used amines are ethanolamine, diethanolamine, methyldiethanolamine and mixtures thereof. The process is well-developed, but still has some drawbacks. The amine solutions continuously degrade which decreases their CO₂ capturing ability significantly and the maintenance costs are fairly high due to the corrosivity and toxicity of the solutions.

Due to the problems with liquid phase processes, solid materials such as activated carbons, metal organic frameworks (MOFs) or COFs acting as heterogeneous adsorbents have gathered great attention during the last years.

Porous polymers often feature high intrinsic adsorption capacities and selectivities as well as suitable heats of adsorption to ensure high reversibility. Nevertheless, one should not forget to think about the future practical applications. Zeolites for example show good adsorption for CO₂ (e. g. 13X: 5.5 mmol g⁻¹ at 30 °C and 20 bar), but are strongly influenced by water vapour in the feed stream due to bicarbonate formation on the surface.

MOFs are more versatile concerning their pore sizes and pore surfaces which makes them good candidates for CCS. For example, Mg-MOF-74 shows an adsorption capacity as high as 8.61 mmol g⁻¹ at 25 °C and 1 bar and high CO₂/N₂ selectivity (195). For comparison, the adsorption capacity of unmodified sandstone is 0.00125 mmol g⁻¹,^[15] while graphene shows an adsorption capacity of 7.95 mmol g⁻¹.^[16] However, MOFs are often unstable against water and lose their crystalline structure as well as their high CO₂ capacity at higher humidity.

1.3 Porous materials

Porous materials feature permanent porosity with different pore sizes ranging from nano- to millimeters in ordered or irregular arrangements. They are classified according to their pore diameter (micropores: < 2 nm, mesopores: 2 – 50 nm, macropores: > 50 nm) corresponding to the classification scheme established by the International Union of Pure and Applied Chemistry (IUPAC).^[17] The pore structure defines the accessibility and shape as shown in Figure 1-3.^[18] Pores can contain fluids or gases depending on the surrounding medium and pore permeability. The structure of the pores has great influence on the chemical and physical properties of the material. They also define important parameters for the characterization of porous materials like the specific surface area or the pore size distribution of the materials. More details can be found in Chapter 2.1.

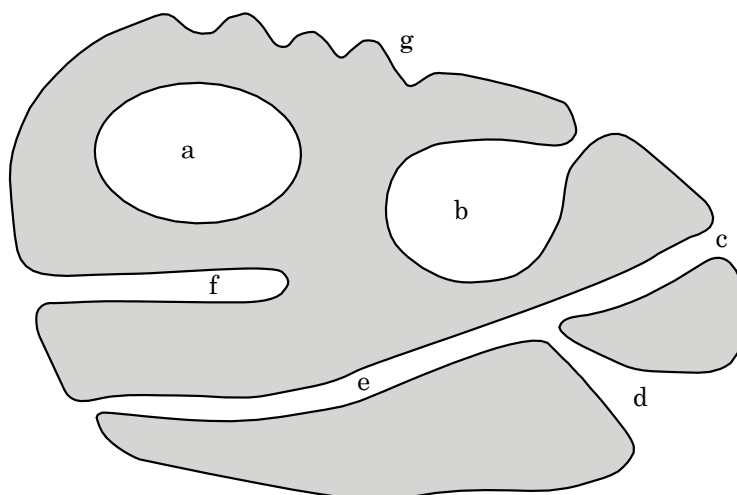


Figure 1-3: Possible pore structures and shapes in porous materials. Accessibility: (a) closed pores, (c) – (f) open pores, (b) and (f) blind pores, (e) through pores; shape: (b) inkbottle shaped, (c) cylindrical open, (d) funnel shape, (f) cylindrical blind, (g) roughness.^[19]

A naturally occurring class of inorganic microporous materials, which is also industrially used, are the aluminosilicate-based zeolites. They are produced on a large scale as sorbents^[20-22], catalysts^[23-25], or in gas separation.^[26-27] Zeolites usually consist of oxygen tetrahedrons linked at the corners and arranged around a cation. The schematic structure of Zeolite A, a sodium aluminate with the chemical formula $\text{Na}_{12}((\text{AlO}_2)_{12}(\text{SiO}_2)_{12}) \cdot 27 \text{H}_2\text{O}$ that is known as Sasil® and is used as molecular sieve,^[28] is depicted in Figure 1-4a.

The combination of inorganic nodes with organic linkers by coordination leads to the material classes of MOFs and, if they have a zeolite-like topology, zeolitic imidazolate frameworks (ZIFs). ZIF-20, which has the same topology as Zeolite A, is shown in Figure 1-4b.^[29] One of the best-known MOF systems is MOF-5, which is shown in Figure 1-4c. The material consists of Zn-based nodes that are linked by 1,4-benzodicycarboxylate ligands. The materials are used in gas storage^[30-32] or in heterogeneous catalysis^[33-35] as well as CCS.^[36-38]

Fully organic porous materials are called porous polymer frameworks (PPFs) or porous organic polymers (POPs).^[39] These amorphous materials are used in gas storage and heterogeneous catalysis due to their particularly high specific surface area.^[34, 40]

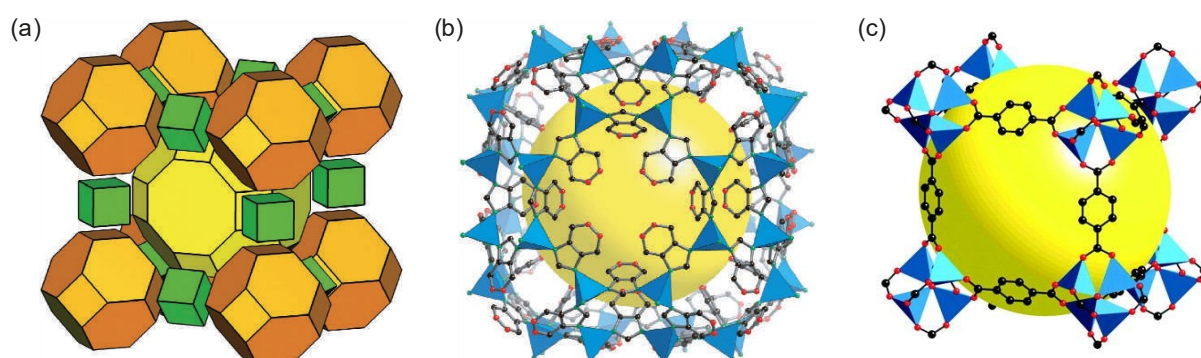


Figure 1-4: (a) Schematic structure of Zeolite A consisting of cubes (green), truncated octahedra (orange) and truncated cuboctahedra (yellow). Reprinted from [29]. (b) X-ray single crystal structure of ZIF-20. ZnN_4 tetrahedra are shown in blue. Both show LTA topology. Reprinted from [29] (c) X-ray single crystal structure of MOF-5 consisting of $[\text{OZn}_4(\text{CO}_2)_6]$ clusters bridged by organic carboxylate linkers. ZnO_4 tetrahedra are shown in blue. Reprinted from [31].

1.3.1 Covalent organic frameworks – a new class of polymers

In 2005, Yaghi and coworkers reported that condensation of phenyl diboronic acids to boroxines or boronate esters yields crystalline porous materials.^[41] This finding initiated a new research field in the porous polymer community. The extended organic polymeric structures featuring permanent porosity as well as crystallinity were named covalent organic frameworks, COFs. Their monomers, the so-called linkers or building blocks, are joined by strong, but reversible covalent bonds to result in two- or three-dimensional structures.^[42-43] The reversibility of the bond forming reaction enables self-healing of defects by formation, breakage and reformation of bonds. This concept is known as dynamic covalent chemistry (DCC).^[44] The chemical reaction is carried out under equilibrium conditions and yields the thermodynamically most stable product by replacing the kinetically favored intermediates. DCC is the key principle for COF synthesis as it enables long-range order and thus crystallinity in this material class.

The molecular composition of the framework not only gives rise to a unique chemical diversity but also opens up the possibility of tuning the systems as required.^[45] COFs feature a low density due to their high porosity, tunable pore sizes^[46-47] and large surface areas.

COFs can be divided into different categories according to their linking units. Boron-based COFs are synthesized by boronic acid condensation,^[42, 48] but suffer from hydrolysis under moist conditions.^[49] C-N-bridged COFs are in general thermally and chemically more stable. Typically, they are synthesized by acid-catalyzed condensation of aldehydes with nitrogen-containing functionalities like amines or hydrazones, but many more are known to date. A chronology of COF linkage types is shown in Figure 1-5.

COF monomers can be classified according to their geometry. The combination of the different linker symmetries (C_2 , C_3 , C_4 , T_d) leads to different framework topologies resulting in e. g. tetragonal or hexagonal 2D or 3D frameworks according to Figure 1-6. In the case of 2D frameworks, the COF sheets are held together by van der Waals forces in the third dimension. The stacking in this direction follows different patterns according to the building blocks. An exact analysis is often difficult as the crystallinity in stacking direction is often limited due to the weak interlayer interactions and hence, missing long-range order. The initially proposed eclipsed stacking is considered as unfavorable nowadays. Dichtel and coworkers predicted an offset of 1.7 Å for hexagonal sheets of boronate ester COFs in 2011^[50] that is often used as an educated guess for the slipping offset in COFs. So far, other slipping distances ranging from 1.4^[51] to 6.5 Å^[52] were observed. In ideal cases, which feature very high crystallinity in all dimensions, in depth characterization of the stacking order is feasible. In 2017, we reported a detailed analysis of the two imine-linked COFs TBI-COF and TTI-COF that show either an averaged eclipsed structure with apparent zero-offset stacking or a unidirectionally slip-stacked structure.^[53]

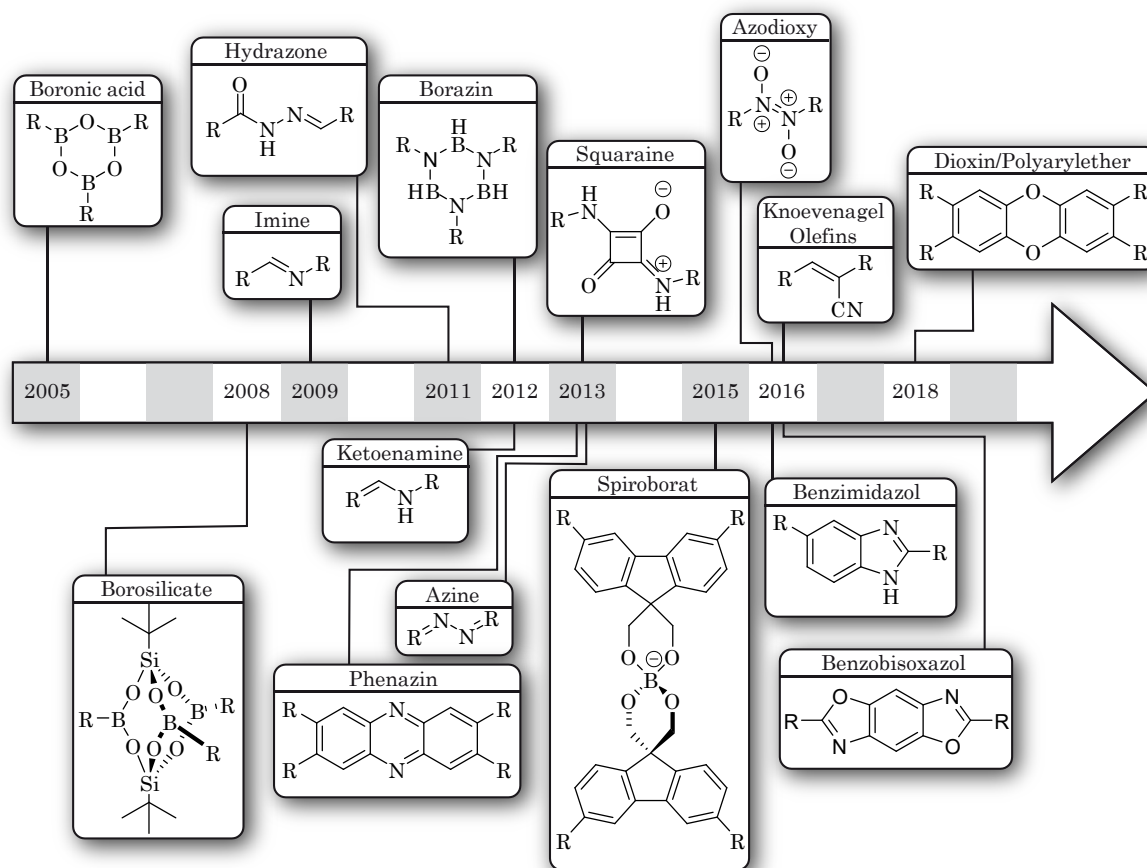


Figure 1-5: Chronology of COF linkage units.

COFs are usually synthesized solvothermally as insoluble powders under heterogeneous conditions. The choice of solvent is crucial for the long-range order of the system. In an appropriate medium, the 2D COF layers can also be exfoliated into multiple layers by ultrasonication.^[14, 54-56] Yaghi and coworkers found that for boron-based COFs, sonication in acetonitrile for several minutes leads to sheets with a height of five layers according to atomic force microscopy (AFM) measurements. Further, nitrile-containing co-solvents were found to form stable colloidal suspensions with boron-based COFs that can be used for formation of freestanding porous thin films by solution casting.^[57]

A more detailed overview of the different COF types will be given in the following.

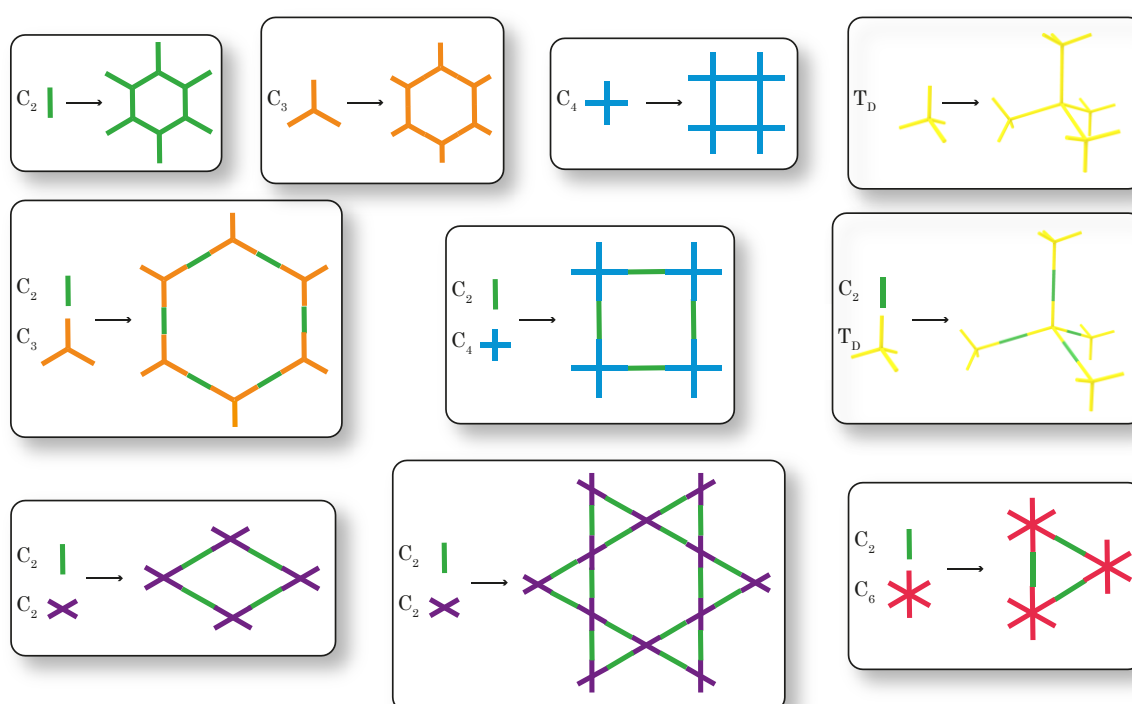


Figure 1-6: Schematic examples of different building blocks used for COF synthesis. Framework morphologies resulting from different building block symmetries.

1.3.1.1 Boron-based covalent organic frameworks

Most of the COFs synthesized so far are boron-containing frameworks that can be further divided into two synthetic strategies.

The first strategy is the self-condensation of boronic acids as shown in Figure 1-7a. The simplest example is the reaction of 1,4-benzenediboronic acid (BDDBA) to form a hexagonal COF structure containing planar B_3O_3 rings. The so-called COF-1 has a pore diameter of 0.7 nm and a BET surface area (see Chapter 2.1.2 for details) of $711 \text{ m}^2 \text{ g}^{-1}$. More complex structures like the 3D COF-103 have also been synthesized by self-condensation.

The second strategy is co-condensation of two or more building blocks (see Figure 1-7b). This method is more versatile; therefore, a larger number of COFs was synthesized so far than with self-condensation. Condensation of alcohols and boronic acids leads to formation of five-membered BO_2C_2 rings as linking unit. Borosilicate units (Figure 1-7c) have also been used by condensation of boronic acids and silanols.^[48] 2D and 3D COFs were reported in all cases. Another linkage strategy that leads to ionic frameworks is the use of spiroborate linkages as depicted in Figure 1-7d. These are created by the reaction of diols and trimethyl borate. The counter ion can be adjusted, $[\text{Me}_2\text{NH}_2]^+$ and Li^+ were used in the case of ICOF-1 and -2.^[58]

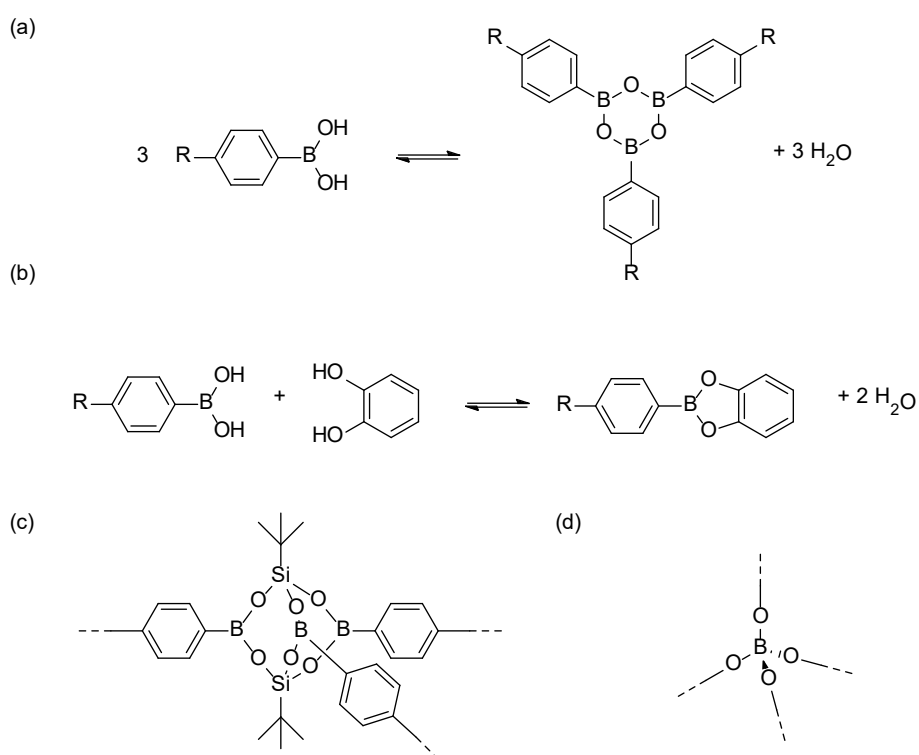


Figure 1-7: Schematic representations of (a) boronic acid self-condensation, (b) boronic acid co-condensation, (c) borosilicate linking unit, and (d) spiroborate linking unit.

Further, an effective film formation has been shown for different boron-based COFs. Solvothermal deposition on graphene was followed by utilization of different substrates like silicon and fluorinated tin oxide (FTO)/glass. Controlling the choice of solvents during synthesis enables the growth of oriented films.

Despite their thermal stability, high surface area and low density, the practical applicability of boron-based COFs is limited so far due to their instability in the presence of water. To date, the borosilicate COF-202 shows the highest longevity in terms of retained crystallinity and porosity when exposed to ambient air for 24 hours.^[48]

Great attention has been given to mechanistic studies on COF formation during the last years. The easy to synthesize boron-based COFs have turned out to be very convenient substrates for those investigations. In 2014, Dichtel and coworkers synthesized the boronate-ester bridged COF-5 as a prototypical hexagonal 2D framework from homogeneous solution and analyzed the COF formation kinetically. Reversible and irreversible stages were observed. The reversible stages were attributed to dynamic bond formation, the irreversible one to precipitation of the COF powder. Further, the crystallite size was controlled by the addition of excess water during synthesis.^[59] High control of the COF formation by seeded growth through slow monomer addition was reported as a general route to single crystal formation on the micrometer scale of boron-based COFs in 2018.^[60] A controlled, universally usable synthesis method for COF single crystals could lead way to a great knowledge gain by investigations on defect-free COF materials.

1.3.1.2 C-N-bridged covalent organic frameworks

Another class of COFs are bridged by nitrogen containing bonds. They often show lower crystallinity than boron-based systems, but are chemically more stable, especially towards hydrolysis. The most widely used linkages are imine, imide, and hydrazone bonds, but also others are known today. An overview of the most common linkage types is given in the following.

Imine COFs

The imine reaction (see Figure 1-8) is the most commonly used synthesis strategy in nitrogen-bridged COFs to date. The imine bond is created by condensation of amines with aldehydes. When using both aromatic amines and aldehydes, a full π -conjugation over the COF framework can be achieved.

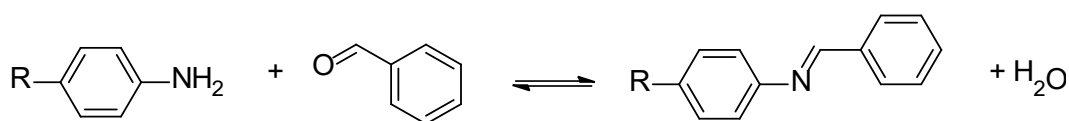


Figure 1-8: Schematic representation of the condensation of an aromatic amine and aromatic aldehyde to form an imine bond.

The vast number of easily accessible amines and aldehydes lead to a high variety of imine COFs with very different topologies. Yaghi and coworkers reported the first imine COF in 2009,^[61] which was COF-300, synthesized from the condensation of tetrakis-(4-anilyl) methane and terephthalaldehyde (see Figure 1-9). That resulted in a 5-fold interpenetrated 3D-COF. The first two-dimensional imine COF was published two years later. Its hexagonal

diamond-shaped pores are framed by 1,3,5-triformylbenzene (TFB) and 1,4-phenylenediamine (PDA).^[62]

Other pore topologies have been achieved with imine COFs as well. The condensation of C_4 -symmetric porphyrin linkers like in the case of CuP-DMNDA-COF, where 5,10,15,20-tetra(*p*-amino-phenyl)porphyrinatocopper(II) (CuTAPP) is reacted with 2,6-dimethoxynaphthalene-1,5-dicarbaldehyde (DMNDA), leads to the formation of tetragonal pores.^[63] Another porphyrin-based example is COF-366 that consists of 5,10,15,20-tetra(*p*-amino-phenyl)porphyrin (TAPP) and terephthalaldehyde. The square geometry of the pores results in the tetragonal $P4/m$ space group.^[64] The possibility for the integration of different metals and the electron-donating properties of the porphyrin unit makes porphyrin COFs highly interesting in optoelectronic applications. When using thieno[3,2-*b*]thiophene-2,5-dicarboxaldehyde as C_2 linker, the formation of extended J-aggregates of the porphyrin units could be observed, which prolongs the excited state lifetime of the COF – a promising feature for application in photovoltaics.^[65]

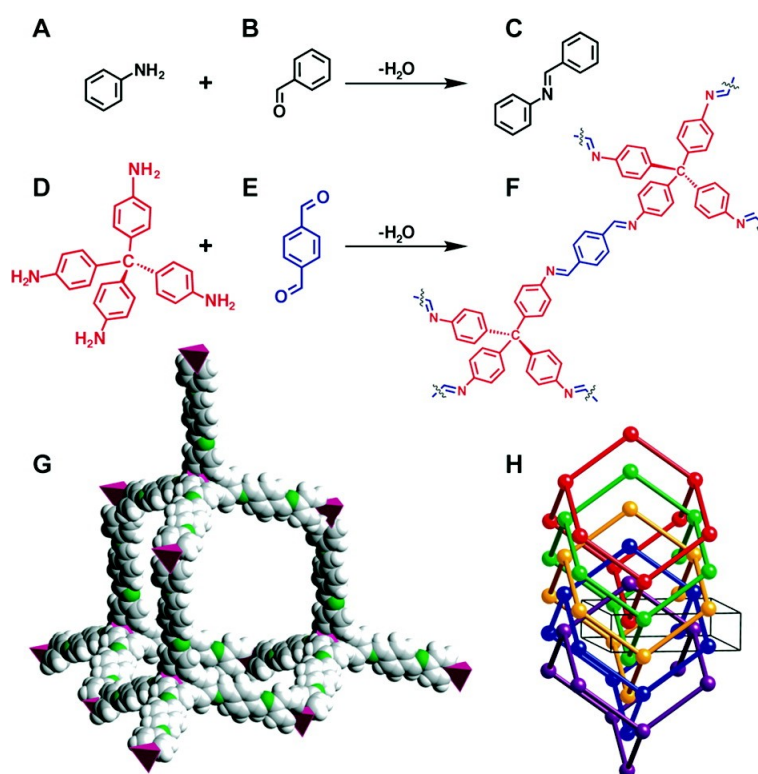


Figure 1-9: Condensation of aniline **A** with benzaldehyde **B** forms the molecular N-benzylidene-aniline **C**. Condensation of divergent **D** with ditopic **E** leads to the rod-like bis-imines **F** which will join together the tetrahedral building blocks to give the diamond structure of COF-300: **G** single framework (space filling, C gray and pink, N green, H white) and **H** representation of the dia-c5 topology. Reprinted from ^[61].

According to the linker geometry, the use of fourfold-functionalized linkers can also lead to rhombic pores as can be seen in Figure 1-10. Such a rhombic pore of 2.4 nm was achieved

by condensation of 1,3,6,8-tetrakis(4-formylphenyl)pyrene (TFPPy) and 2,6-diaminoanthracene (DAAn) which could then be used as a heterogeneous catalyst for Diels-Alder reactions.^[66] The solvatochromic properties of the integrated pyrene unit were used in the rhombic system Py-TT COF. Thin films of the COF were integrated into a humidity sensor with very fast response times.^[67] The pyrene linker was also incorporated into the three-dimensional and twofold penetrated 3DPy-COF which creates cuboid pores.^[68] An extended pyrene linker was used in the ATEXPY-COF series (see Figure 1-10) by our group, to investigate the influence of the linker electronics towards photocatalytic hydrogen evolution.^[52]

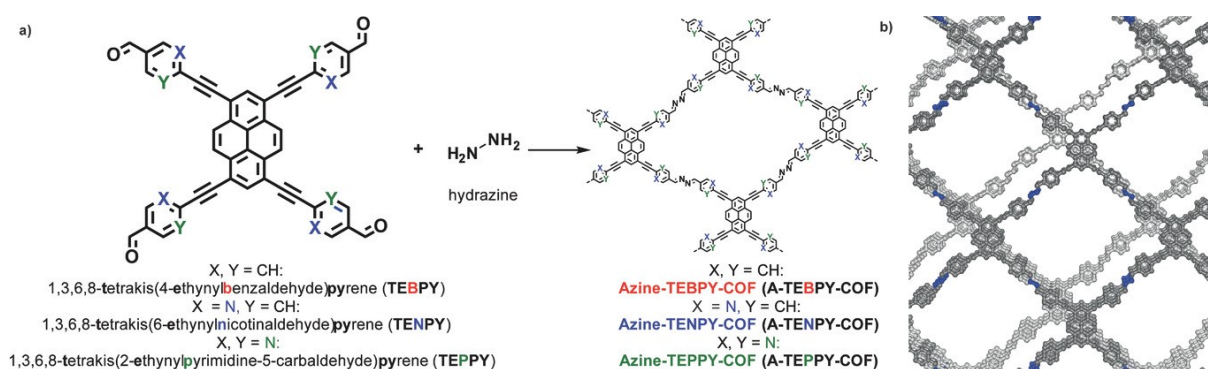


Figure 1-10 (a) Synthesis of azine-linked COFs by the acetic acid catalyzed condensation reaction between the pyrene-based aldehyde linkers and hydrazine. (b) Ball-and-stick model of the shifted AA' arrangement of A-TEBPY-COF. All COFs in this series adopt similar stackings. Reprinted from ^[52].

A very special array of a rectangular pore is the brick-wall topology which was realized by combination of a t-shaped tritopic linker with a linear linker.^[69]

By the incorporation of the C_6 linkers $[\text{H}_2\text{N}]_6\text{HPB}$ and $[\text{H}_2\text{N}]_6\text{HBC}$, which have a propeller-like shape, triangular pores can be created. Polymerization with terephthalaldehyde leads to microporous crystalline materials with pore sizes of 1.2 and 1.8 nm.^[70]

Triangular pores also appear in multi-pore COF systems that are also called heteropore COFs.^[71] The pores can be heterogeneous or hierarchical. Condensation of (4,4',4'',4''')-(ethene-1,1,2,2-tetrayl)tetraaniline (ETTA), which shows D_{2h} symmetry, and terephthalaldehyde leads to star-shaped pores, where a central hexagonal pore is surrounded by smaller triangular ones. Interestingly, substitution of the terephthalaldehyde molecule with ethoxy or butoxy groups changes the topology towards rhombic pores.^[72]

More advanced linker design and mixed linker strategies result in even more complex pore structures. Triple pore systems combining inequilateral hexagonal and trigonal pores of two different sizes as shown in Figure 1-11 have been realized in 2016.^[73] Other hierarchical structures were created by truncation of specific linkers to yield v-shaped molecules.

Condensation with linear linkers results in large hexagonal pores that are surrounded by smaller hexagonal ones joint by very narrow rectangular pores.^[74]

The smart combination of different orthogonal linkage strategies in the same COF broadens the scope of different structures even more. Mixed boronate-imine COFs based on bifunctional linkers with aldehyde and boronic acid functionality were used for the synthesis of double-stage hexagonal and tetragonal COFs with varying pore sizes.^[75-76] The same strategy can be applied for the construction of 3D COFs when using 1-adamantanamine as node molecule.^[77] The sophisticated bifunctionality of the COFs was used in acid-base catalyzed one-pot cascade reactions.

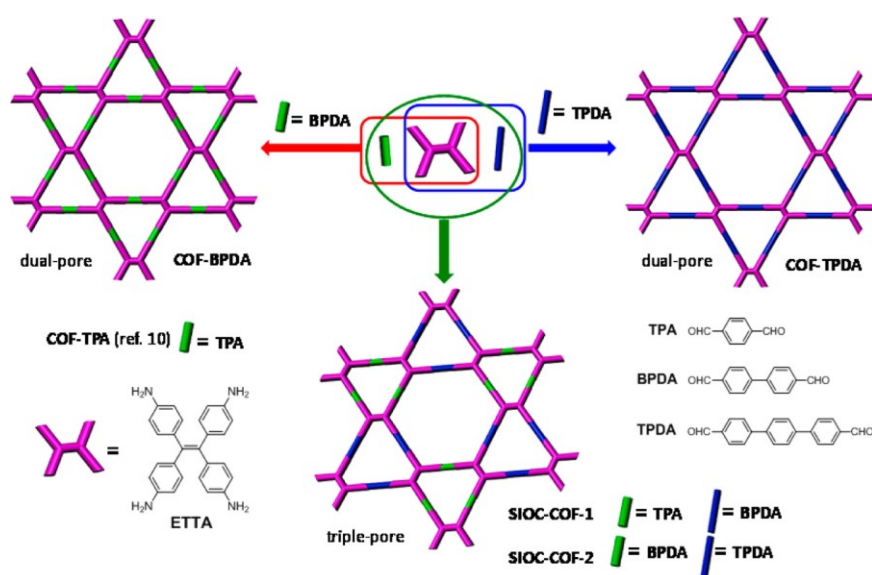


Figure 1-11: Cartoon representation for the synthesis of dual-pore and triple-pore COFs. Reprinted from ^[73].

Ketoenamine COFs

A further advancement especially regarding the stability of imine COFs in strong acids and bases was the discovery of the so-called β -ketoenamine COFs. They are based on triformyl phloroglucinol (TFG) as aldehyde linker. Here, three hydroxyl groups are located next to the three formyl groups of TFB. By reaction with amines, an imine bond forms reversibly as described before. This enol irreversibly tautomerizes to the keto form of the COF as depicted in Figure 1-12.^[78]

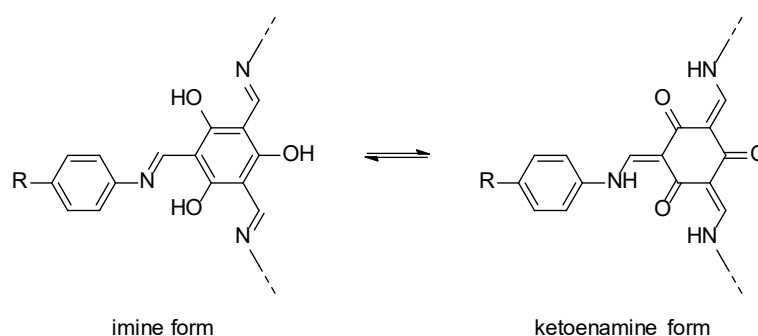


Figure 1-12: Schematic representation of the keto-enol-tautomerism used in COF formation. The imine form (left) reacts to form the more stable ketoenamine form (right).

The β -ketoenamine COFs can also be synthesized by linker exchange of the respective imine COFs (from TFB to TFG).^[79] Due to their high stability, β -ketoenamine COFs were used for more demanding applications such as proton conduction in strong acids^[80] or pH sensing in a very broad pH range.^[81] Combination with redox-active anthraquinone-based amine linkers resulted in COFs with interesting redox properties and very stable capacitances in sulfuric acid electrolyte.^[82] By thin film fabrication on Au working electrodes, an increase in capacitance of 400% could be achieved in oriented films compared to randomly distributed powder.^[83]

Hydrazone COFs

The condensation of aldehydes and hydrazides to form hydrazone linkages was first applied in COF synthesis in 2011 by Yaghi and coworkers.^[84] 2,5-Diethoxyterephthalohydrazide (DETH) was combined with TFB and 1,3,5-tris-(4-formylphenyl)benzene to yield the reticular hexagonal COF-42 (see Figure 1-13a) and COF-43 with high porosity and crystallinity. After that, more hydrazone COFs were synthesized, most of them based on DETH (e. g. TFPT-COF^[14], LZU-21^[85], NUS-3^[86]; chemical structure of DETH is shown in Figure 1-13b) or its modifications. Most examples were synthesized with TFB, or less frequently TFG, as aldehyde linker. As the DETH modification mostly directs the properties of the resulting materials, the following examples are categorized accordingly.

The modified linker without side chains, terephthalic dihydrazide, reacted with TFG in a liquid-assisted mechanochemical synthesis to form TpTh.^[87] The reaction with TFB yielded a COF that was coated on a fiber and applied for the preconcentration of pyrethroids.^[88]

Hydroxyl functionalized terephthalic hydrazide in different substitution patterns were used in NUS-50 (2,5-dihydroxyterephthalohydrazide; 2,5-DHTH) and NUS-51 (2,3-dihydroxyterephthalohydrazide; 2,3-DHTH; see Figure 1-13e). Both COFs show catalytic activity in Lewis-acid catalyzed cyanosilylation of aldehydes when decorated with Co^{II} ions.^[89]

The DETH modification with shorter methoxy sidechains is 2,5-dimethoxy terephthalohydrazide. When reacted with TFB as aldehyde, it yields TFB-COF, which is active in the photocatalytic cross-dehydrogenative coupling of tetrahydroisoquinolines and nucleophiles.^[90] COF-JLU4 is synthesized with TFG as aldehyde linker and used as a fluorescent pH responsive sensor.^[81] Longer carbon side chains have been demonstrated in Pr-COF-42, which is the propoxy-modified version of COF-42.^[91]

Functionality can be added to the framework via allyl modification of the DETH linker. 2,5-Bis(allyloxy)terephthalohydrazide (see Figure 1-13d) was used with TFG in the synthesis of COF-AO, which was then loaded with Pd nanoparticles and cross-linked with PSI-SH oligomer to form a copolymer membrane. The membrane was used in aqueous continuous-flow chlorobenzene dechlorination reactions.^[92]

TTB-COF contains the thioether-bearing 2,5-bis(2-(ethylthio)ethoxy)terephthalohydrazide (BETH, see Figure 1-13f), and selectively captures and displays Au ions at trace-levels in water.^[93] Another thioether-containing COF is COF-LZU8 based on 2,5-bis(3-(ethylthio)propoxy) terephthalohydrazide, which was similarly used for mercury removal from water.^[94]

The introduction of chirality to the COF was achieved with 2,5-bis[(2S)-2-methylbutoxy]terephthalohydrazide (MTh, see Figure 1-13g) as a building block. With TFB as aldehyde linker, BtaMth COF was formed and used as a COF-silica composite material as stationary HPLC phase.^[95] The introduction of tertiary amine functionalities with 2,5-bis(2-(dimethylamino)ethoxy)terephthalohydrazide is demonstrated in chapter 4.2.

A combination of many different hydrazone COFs based on DETH and its modifications was used as a multicomponent solid-state emitter with fine-tuned emission from blue to yellow and white.^[96]

Examples for hydrazone COFs without DETH-based molecular linkers are less frequent. Bth-Dha COF and Bth-Dma COF contain the trifunctional hydrazide benzene-1,3,5-tricarbohydrazide (Bth) and the linear aldehyde 2,5-dihydroxyterephthalaldehyde (Dha) or 2,5-dimethoxyterephthalaldehyde (Dma). The COFs show a selective luminescence response towards aqueous Fe^{3+} ions due to coordination interactions with the hydrazone bond on the pore wall.^[97]

The smallest possible bifunctional hydrazide oxalyldihydrazide (ODH) forms the COFs TpODH with TFG and TFBODH with TFB, which were used for the selective adsorption of Cu(II) and Hg(II).^[98]

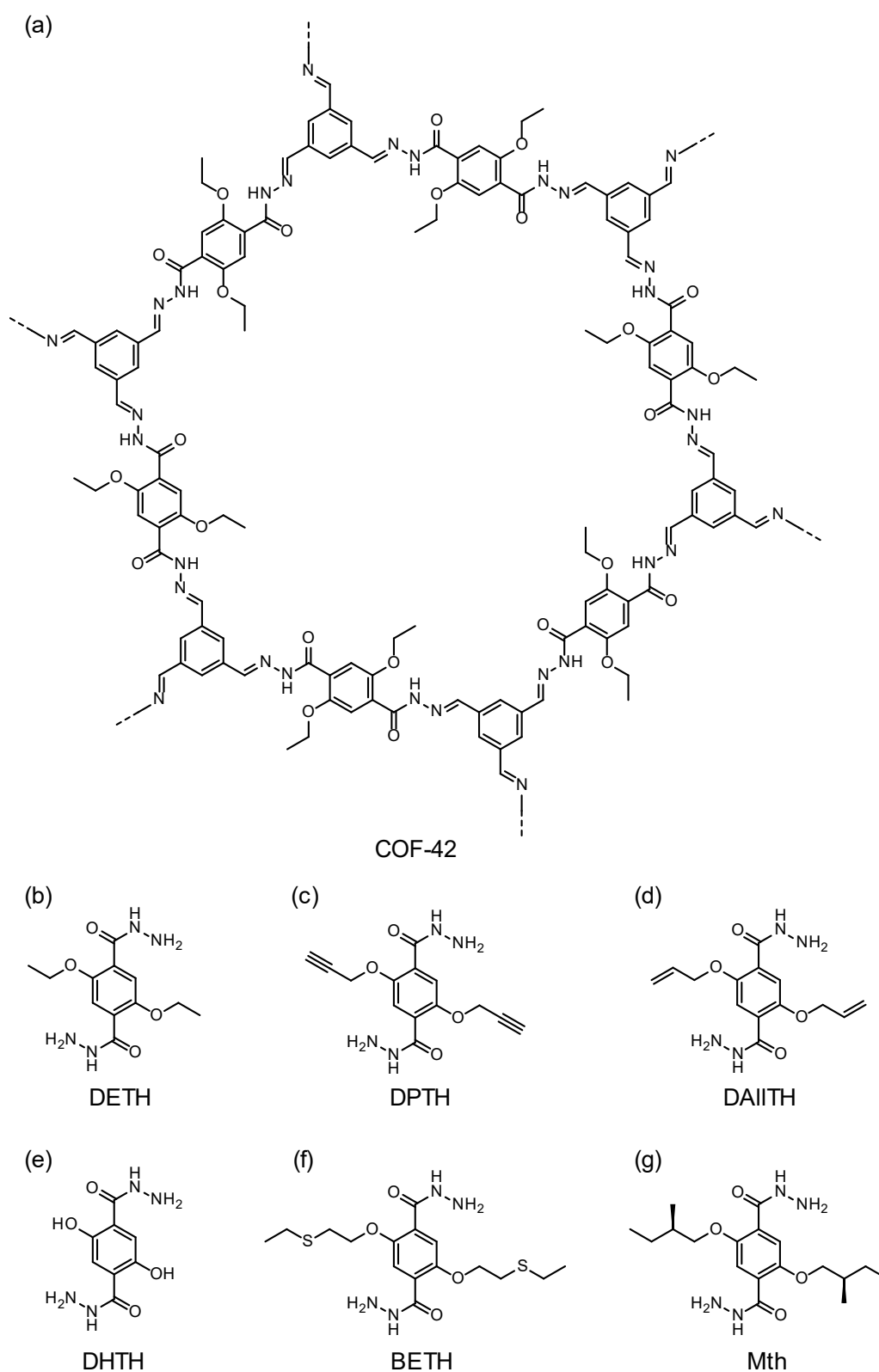


Figure 1-13: (a) Chemical structure of COF-42. Chemical structures of (b) 2,5-diethoxyterephthalohydrazide and (c-g) a selection of its modifications.

Azine COFs

The first COF that was linked via diazabutadiene units was published in 2013.^[99] This azine COF was synthesized by condensation of hydrazine with 1,3,6,8-tetrakis(4-formylphenyl)pyrene and used as a chemosensing device for trinitrophenol type explosives. The application of hydrazine as linear linking unit is what defines azine COFs, but also what restricts their versatility. Nevertheless, several azine COFs with different aldehyde linkers are known today.

The smallest hexagonal azine COF pores with a theoretical diameter of 1.3 nm were synthesized with TFB and TFG and published with a variety of different names, such as ACOF-1^[100]/AB-COF^[101] and COF-JLU2^[102]/NUS-2^[86]/ATFG-COF^[101]/RIO-13^[103]/HCOF-1,^[104] respectively.

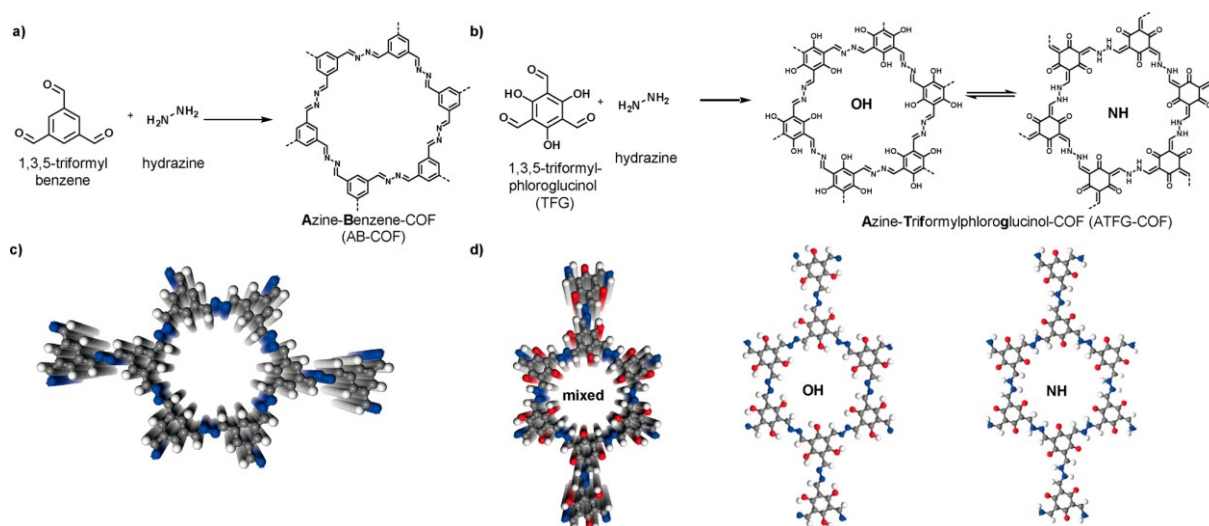


Figure 1-14: Acetic acid-catalyzed azine formation furnishes two microporous honeycomb frameworks. (a) Scheme shows the condensation of hydrazine and 1,3,5-triformylbenzene to AB-COF. (b) The condensation of the two monomers to ATFG-COF results in two different tautomers: OH (left) and NH (right). (c) Structure representation of AB-COF with quasi-eclipsed layer stacking; (d) a mixture of both OH and NH tautomers within ATFG-COF with quasi-eclipsed layer stacking, and structure of the OH and NH tautomers (red, oxygen; blue, nitrogen; black, carbon; white, hydrogen). Reprinted from^[101].

A higher complexity was achieved by condensation of hydrazine with 1,1,2,2-tetrakis(4-formyl-(1,1'-biphenyl))ethane (TFBE). In NUS-30, a dual pore system with hexagonal and trigonal pores was created. In HP-COF-1 and HP-COF-2, a linker desymmetrization approach was used to create dual pore systems with C_{2v} symmetric building blocks.^[105] Linker fluorination was used to improve the crystallinity and porosity of TFX-COF by more favorable stacking energetics due to integration of electron poor fluorinated aromatic rings.^[106]



Applications range from gas separation^[107] and storage^[102], metal ion sensing^[108], and atmospheric water harvesting^[101] to photocatalytic hydrogen evolution^[52, 109-110] and photocatalytic carbon dioxide reduction^[111].

Other linkage types

During the last years, more and more types of linkage chemistry have proven to be suitable for COF synthesis (see Figure 1-5 for an overview).

Condensation of squaraine acid with amines leads to formation of *squaraine*-linked COFs.^[112]

Phenazine-linked COFs are obtained from the condensation of triphenylhexamine and *tert*-butylpyrene tetraone.^[113] The reaction of 3,3'-diaminobenzidine and TFG yields the *benzimidazole*-linked IISERP-COF3 that was used as a support for Ni₃N in oxygen evolution reaction.^[114]

Benzobisoxazole-linking was achieved by cyanide-catalyzed reaction of aldehydes with 2,5-diamino-1,4-benzenediol dihydrochloride (DABD).^[115-117]

COFs based on irreversible nucleophilic aromatic substitution reactions show high chemical stability. *1,4-Dioxin*-linked COFs can be synthesized by nucleophilic aromatic substitution between catechols and fluorinated aromatic carbonitriles.^[118] The same strategy was published as *polyarylether*-based COFs.^[119]

A very interesting condensation reaction to form fully sp²-conjugated *olefin* linkages is the Knoevenagel condensation. It converts aldehydes or ketones into nitrile-substituted *cis*-olefins with base catalysis. It was first demonstrated by Zhuang *et al.* in the formation of 2DPPV from *p*-phenylenediacetonitrile and 1,3,5-tris(4-formylphenyl)benzene.^[120] Later, tetrakis(4-formylphenyl)pyrene was used as aldehyde linker to form a framework with rhombic pores that was found to show paramagnetism after oxidation with iodine^[121] due to confined radicals at the pyrene units. The same pyrene linker was then combined with elongated nitriles to form the reticular COFs sp²c-COF-2 and -3 as highly luminescent photofunctional materials.^[122]

Integration of the starburst-shaped aldehyde building unit 2,3,8,9,14,15-hexa(4-formylphenyl)diquinoxalino[2,3-*a*:2',3'-*c*]phenazine (HATN-6CHO) leads to CCP-HATN, a COF that was hybridized with carbon nanotubes and used as Li storage material.^[123]

Por-sp²-c-COF is synthesized from 5,10,15,20-tetrakis(4-benzaldehyde)porphyrin (*p*-Por-CHO) and 1,4-phenylenediacetonitrile (PDAN) and was used for the photocatalytic aerobic oxidation of amines to imines.^[124] TP-COF that was synthesized from PDAN and TFPT was used as artificial photosystem I and regenerated NADH in 97% yield after 12 minutes which was monitored by the conversion of α -ketoglutarate to L-glutamate.^[125]

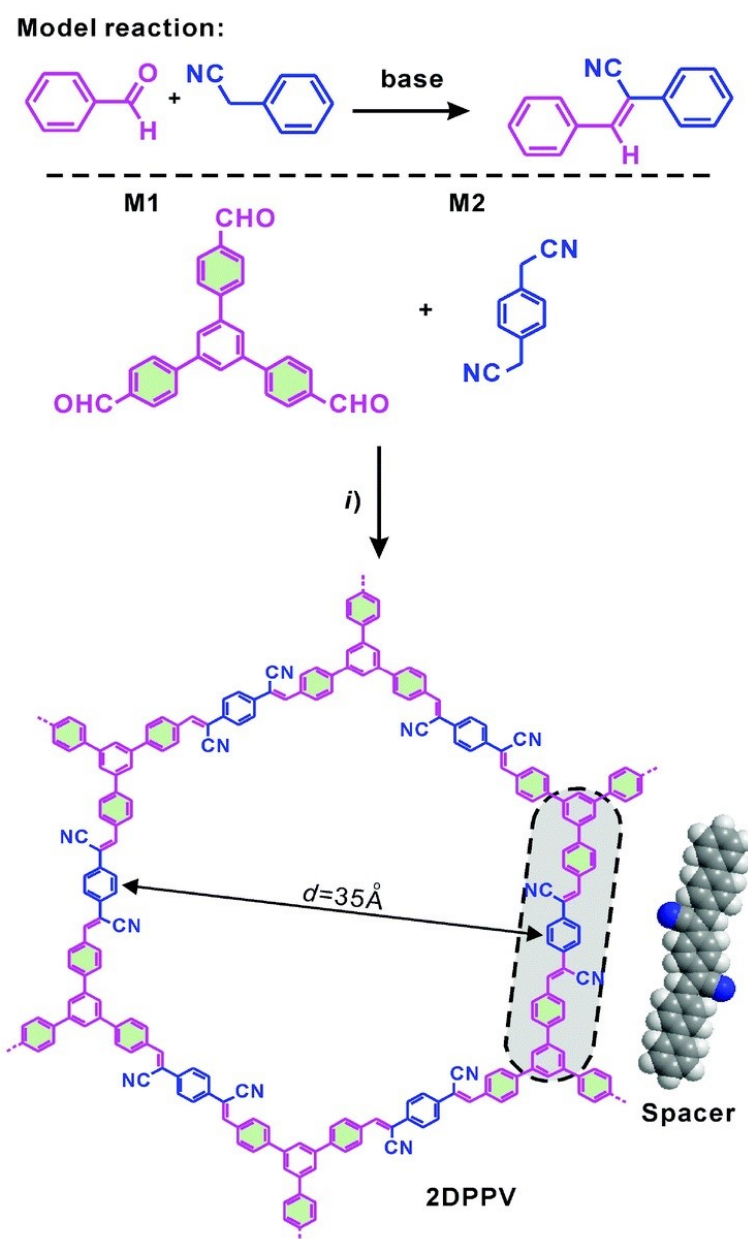


Figure 1-15: Synthesis and structures of the olefin-linked 2D conjugated polymer framework (2DPPV). (i) Argon, cesium carbonate, 1,2-dichlorobenzene, 150 °C, 3 days. Reprinted from ^[120] - Published by The Royal Society of Chemistry.

The diversification of linkage strategies is a growing area of research that will further brighten the scope of COF chemistry and applications in the future.

1.3.2 Postsynthetic modification of COFs

The modification of existing networks is a concept that has been known for a very long time in the MOF field. It was first mentioned by Hoskins and Robson in 1990.^[126] Postsynthetic modification allows for the introduction of chemical functionality to already synthesized materials.^[127] The framework is formed and isolated in a first step and heterogeneously

modified in a second step. That opens the possibility for the adaptation of physical and chemical properties while benefitting from the known characteristics of the underlying material like synthetic conditions, stacking behaviour or the like. For a comprehensive overview the reader is referred to ^[128].

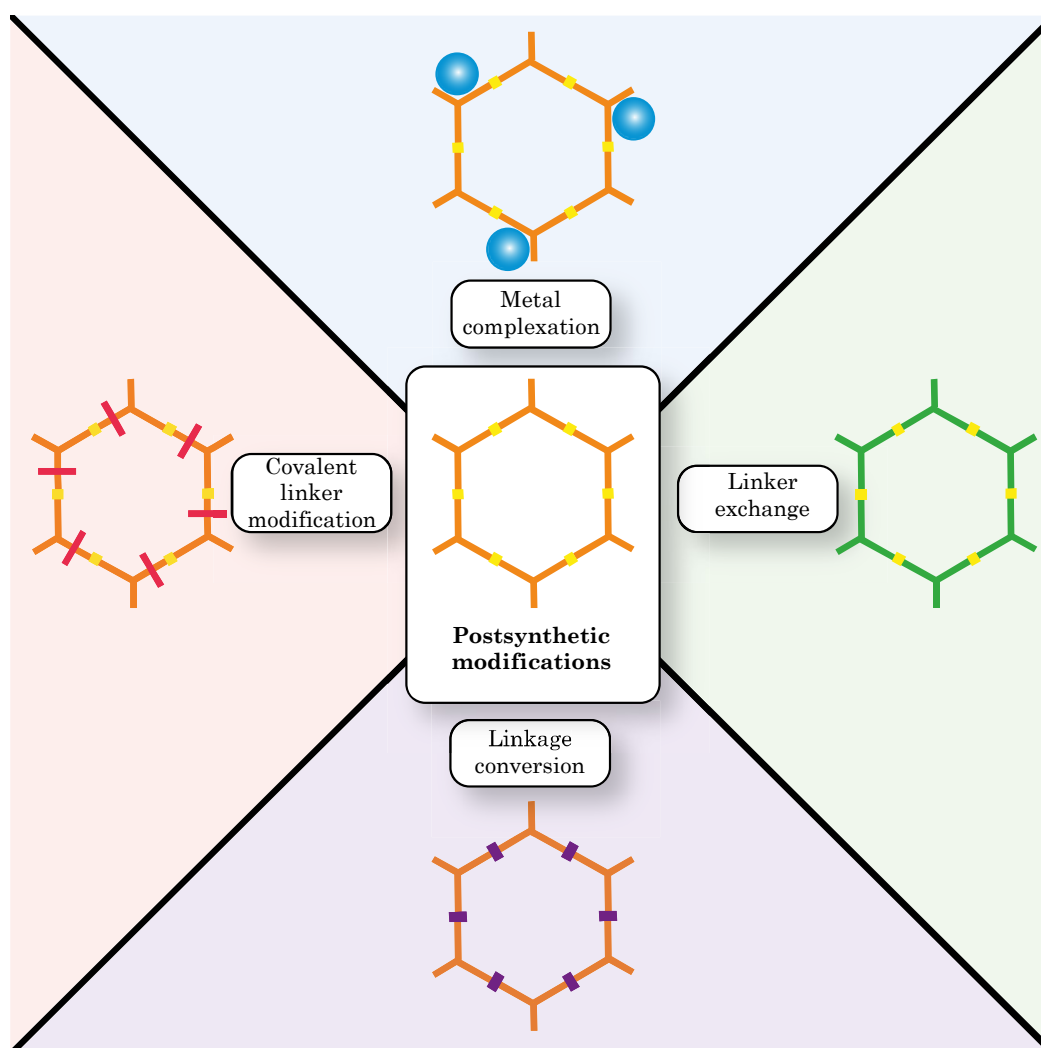


Figure 1-16: Postsynthetic modification of COFs can be realized via metal complexation, covalent linker modification, linker exchange, or linkage conversion.

Due to their high chemical stability, COFs are as suitable for postsynthetic modification as MOFs, if not even more. Different approaches have been transferred from the MOF chemistry to the COF field so far, ranging from coordinative to covalent modifications: metal incorporation by complexation, covalent attachment of molecules, some of which will be discussed in the following.

Complexation of metals

COF linkers often provide coordination sites for molecular building blocks or active metals that are uniformly distributed in the material.^[129] The metals are integrated by solvent-based post-treatment of the isolated COF with a respective metal salt solution. They are either coordinated in the COF sheet layer or intercalated between the COF sheets.

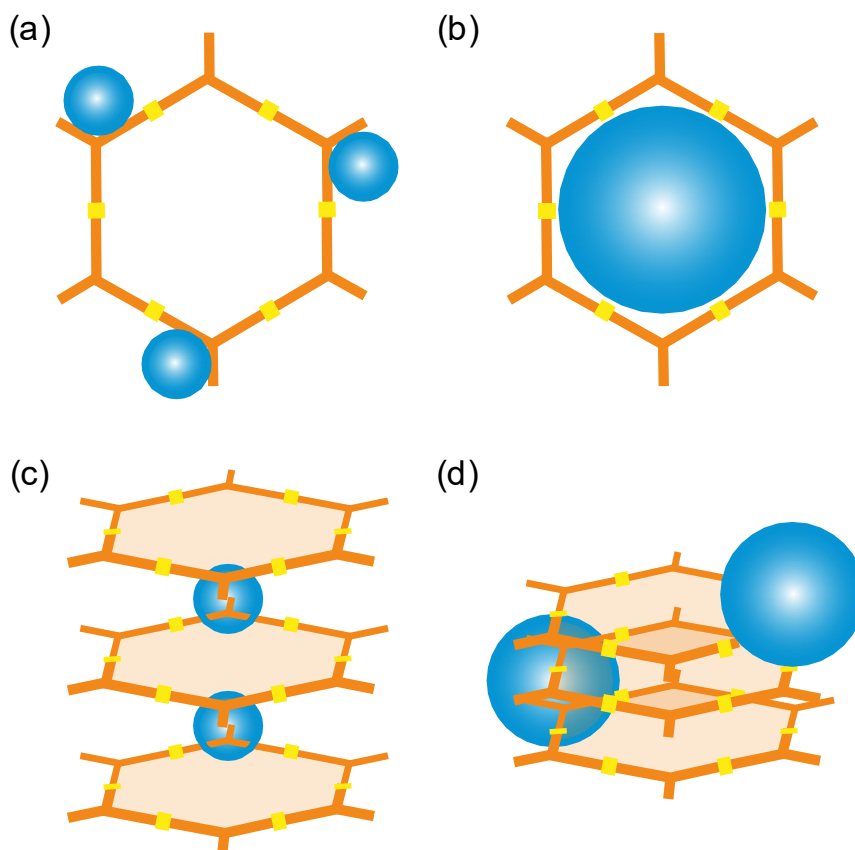


Figure 1-17: Schematic representation of metal complexation strategies. (a) Metal complexation in the COF sheet, (b) confinement of metal nanoparticles in the COF pores, (c) complexation of metal between COF sheets, and (d) metal nanoparticles on the outer COF surface.

A myriad of different metals has been integrated in different COFs ranging from group 2 elements $\text{Ca}^{[130]}$ and $\text{Sr}^{[130]}$ to transition metals of period 4 ($\text{Ti}^{[131]}$, $\text{V}^{[132]}$, $\text{Mn}^{[133-134]}$, $\text{Fe}^{[135]}$, $\text{Co}^{[89, 133, 136]}$, $\text{Ni}^{[133]}$, $\text{Cu}^{[133, 137-138]}$, $\text{Zn}^{[133]}$), period 5 ($\text{Mo}^{[139]}$, $\text{Rh}^{[140]}$, $\text{Pd}^{[62, 141-142]}$), and period 6 ($\text{Re}^{[143-144]}$, $\text{Ir}^{[145]}$). Mostly, metalation is used to create catalytically active sites in the COFs which can then be used for Suzuki-Miyaura coupling^[62], as Lewis acid catalyst for cyanosilylation^[89], the selective oxidation of styrene to benzaldehyde^[137], or sulfide oxidation in the Prins reaction.^[132] Another application is the tuning of the adsorption properties of the systems. For example, the ammonia adsorption capacity is increased by integration of alkaline earth metals.^[130]



The same strategy can be used to graft metal nanoparticles to COFs. The complexation is used as a crystal seed for metals like Au^[146] or Pd^[147] and the resulting materials are again used as heterogeneous catalysts, e. g. in nitrophenol reduction. ^[146] Pachfule *et al.* demonstrate here, that as the nanoparticle size is larger (5 to 7 nm) than the pore size of the TpPa-1 that was used (1.8 nm), it is likely that the nanoparticles are deposited on the COF's outer surface.^[147] By the introduction of strong anchoring groups like thioethers, the controlled confinement of 1.7 nm small Au nanoparticles encapsulated in a COF with 2.4 nm pores is also possible. The composite material is active in Suzuki-Miyaura coupling as well as nitrophenol reduction.^[148]

Linker exchange

The reversible character of the bond formation in COF synthesis allows the postsynthetic exchange of linkers in the framework, even after isolation of the material. In contrast to the MOF field, where the building block exchange based on dynamic covalent chemistry is a widely used concept, only few examples are known for COFs.

In 2017, Zhao and coworkers for the first time achieved a COF-to-COF transformation via linker exchange.^[74] The addition of a high excess of 10 equivalents of a more electron-donating and thus more active linker at the initial synthesis conditions gives rise to a new COF.

The strategy can also be used to synthesize COFs that are unreachable *via* the traditional synthesis method. Amino-modified linkers which did not result in crystalline materials by a simple condensation reaction were introduced to COFs synthesized beforehand from unmodified linkers.^[149]

Further, exchanging TFB with TFG leads to a conversion from imine-linked to β -ketoenamine COFs. The latter then benefit from the high crystallinity of the underlying imine COFs and show superior quality than traditional condensation reactions.^[79]

Recently, linker exchange in the 3D-COFs COF-300 and COF-320 was realized as well as transformation from the 3D COF-301 to the 2D TPB-DHTP-COF.^[150]

Linkage conversion

The reversibility of the bond formation is key to crystallinity in COF synthesis as mentioned in Chapter 1.3.1. At the same time, it is the materials weak spot concerning chemical stability. A solution to this contradiction is the transformation of the linkage unit after successful crystallization of the material by an irreversible chemical reaction. Especially imine bonds have been subject to many different chemical transformations.

In 2016, Yaghi and coworkers transformed the imine linkages of two COFs to amide linkages by oxidation with sodium chlorite, acetic acid, and 2-methyl-2-butene. Both COFs

showed retention of crystallinity and porosity and higher chemical stability, especially in acidic conditions.^[151]

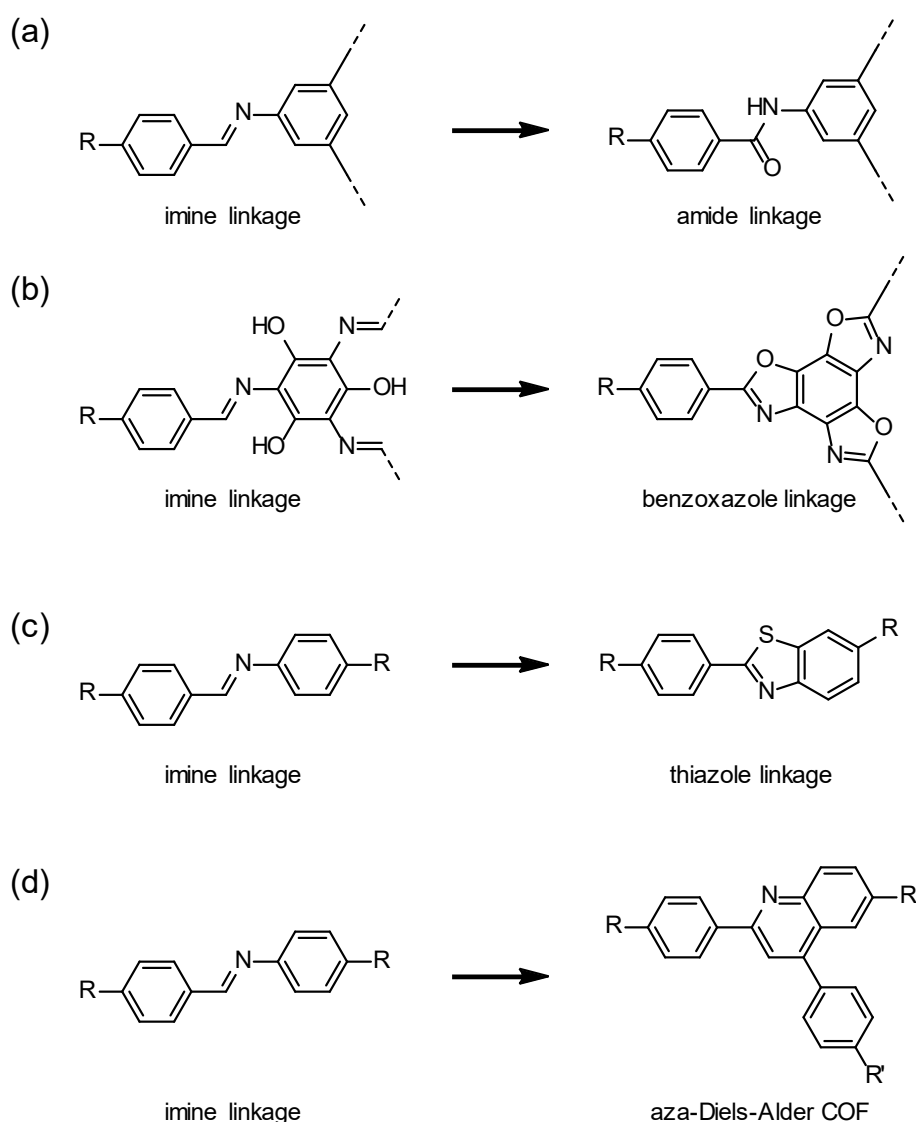


Figure 1-18: Possible linkage conversion strategies for imine-linked COFs. Formation of (a) amide linkage, (b) benzoxazole linkage, (c) thiazole linkage, and (d) an aza-Diels-Alder COF.

Post-oxidative cyclization of imine-COFs to benzoxazole-linked materials has been achieved with 2,3-dichloro-5,6-dicyano-1,4-benzoquinone (DDQ) as the oxidizing agent.^[152] The transformation improved thermal and chemical stability of the system in both acidic and alkaline media.

A combination of a linker exchange reaction of 1,4-phenylenediamine to the bifunctionalized thiol linker 2,5-diaminobenzene-1,4-dithiol and subsequent linkage conversion by oxidation with oxygen leads to formation of thiazole containing COFs.^[153] Also in this case, crystallinity and porosity are retained.



Another possibility to convert imine to thiazole bonds is the reaction with elemental sulfur under elevated temperature.^[154] In this case, the higher stability against reactive conditions particularly in alkaline environment is accompanied by an increase in electron beam stability which then allows in-depth real structure analysis by transmission electron microscopy. Defects like grain boundaries and edge dislocations by integration of 5- and 7-membered rings in the material can be visualized.

A linkage conversion reaction can be used at the same time to add new functionality to the COF. Lui and coworkers use the aza-Diels-Alder reaction between the imine linkage and a variety of arylalkynes with functional moieties like methyl, fluoride, methyl ether, or trifluoromethyl to alter the surface properties of the COFs. Water contact angles of 35° to 155° were measured on the pressed pellets of the COFs.^[155]

Covalent linker modification

Another possibility for the post-synthetic integration of functionality into COFs is the covalent modification of linkers. This method is often referred to as pore wall engineering or channel-wall functionalization. There are almost infinite options regarding the chemistry used for this type of modification based on the available functional groups in the COF material. The modification approaches can be subdivided according to their underlying chemistry. Some selected reactions will be discussed in the following.

In 2011, Jiang and coworkers were the first to demonstrate covalent linker modification in COFs.^[156] They synthesized an azide-functionalized COF which was then modified by copper-catalyzed click-chemistry (see Figure 1-19a) with different alkynes like 1-hexyne, 2-propynyl acetate or (3 α ¹, 3 α ²-dihydropyren-1-yl)methyl propionate as a fluorescent tag. Later, they used the same reaction with inverted functionalities (acetylene moiety on the COF, azide on the clicked molecule) to add pyrrolidine azide to the COF.^[157] The pyrrolidine-functionalized COF showed decent activity in Michael addition reactions. Addition of functional groups like carboxyl or amino groups enables tuning of the adsorption capacity towards carbon dioxide.^[158] Even acetylene-functionalized bucky balls can be integrated into COF lattices by the click-chemistry approach.^[159]

Terminal alkenes have been integrated and used in thiol-ene coupling reactions (see Figure 1-19b).^[160-162] The method was for example used to integrate high hydrophobicity on COFs by the addition of 1*H*,1*H*,2*H*,2*H*-perfluorodecanethiol to an allyl-functionalized imine COF.^[163]

An amine-functionalized COF that was obtained by reduction from nitro groups was modified by the aminolysis of acetic anhydride as shown in Figure 1-19c. The resulting amide-functionalized COF was used in a liquid-phase adsorption study with lactic acid, where strong interactions with the COF pore wall were found.^[164]

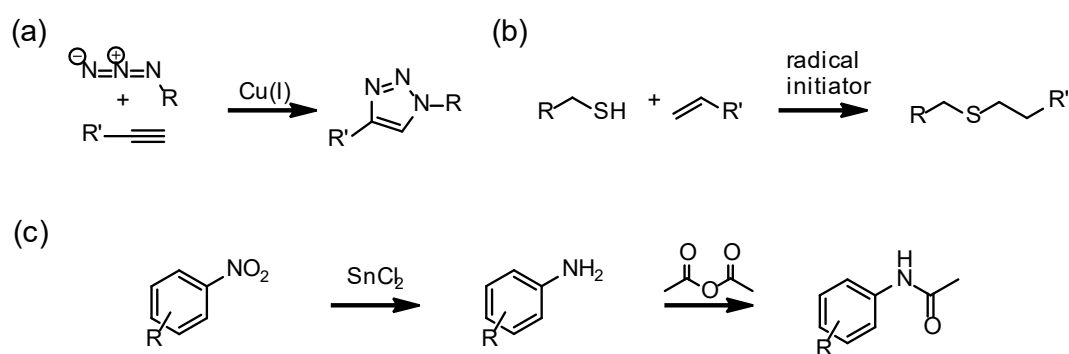
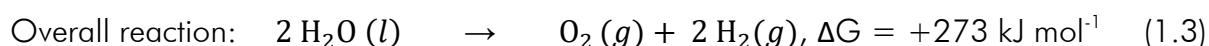
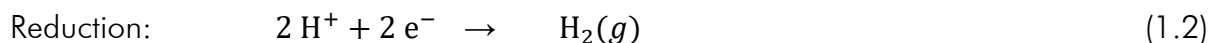
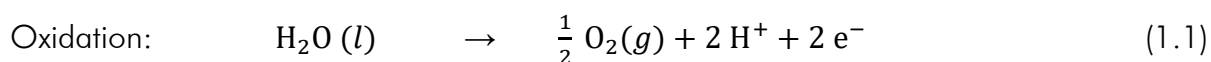


Figure 1-19: Schematic representation of (a) copper-click reaction, (b) thiol-ene click reaction, and (c) aminolysis of acetic anhydride.

The tools of organic chemistry have been widely explored in the COF field to transform the materials heterogeneously with respect to a variety of applications. The tailoring of their physical and chemical behavior opens doors into fields that might not be accessible without post-synthetic modification routes. Selected examples of such fields of application for functional COFs will be discussed in the following.

1.3.3 Covalent organic frameworks as photosensitizers for photocatalytic hydrogen evolution

The splitting of water to hydrogen and oxygen is an endergonic reaction with a Gibbs free energy of $\Delta G = +237.2 \text{ kJ mol}^{-1}$ under standard conditions at $\text{pH} = 0$ (see equation 1). As water is transparent to the entire solar spectrum, sensitizers are used to drive the reaction. Sensitizers act as the semiconducting materials that enable exciton formation. The potential difference of the reaction is 1.23 eV, thus light with a wavelength of $\leq 1008 \text{ nm}$ can in principle induce water splitting.^[165] To allow the conversion of photons to chemical energy by water splitting at visible light, additionally, an overpotential is required to overcome kinetic hindrance of the reaction. Catalysts are used to reduce this overpotential.



Irradiation with energy greater than the band gap E_g of the semiconductor results in generation of excitons and excitation of the electrons to the conduction band of the semiconductor while the holes remain in the valence band. After charge separation, the charges migrate to the semiconductor surface, where they react with water molecules on the surface by evolution of hydrogen and oxygen (see Figure 1-20a).

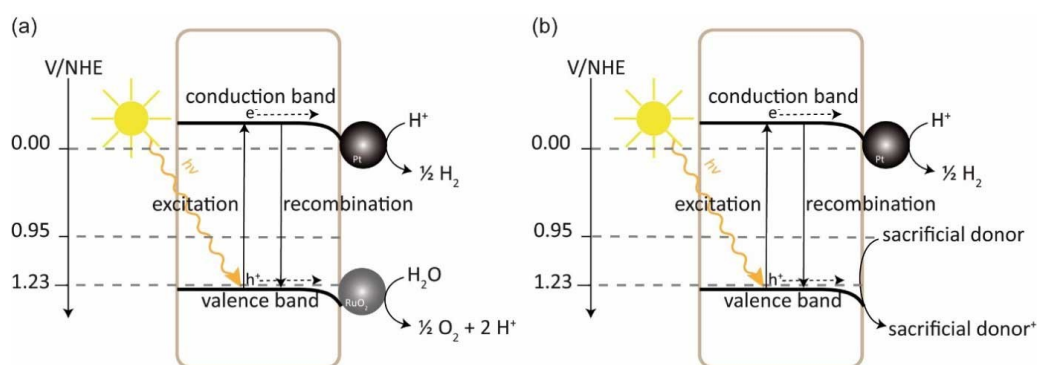


Figure 1-20: (a) Basic principle of overall water splitting. After excitation, charge carriers migrate to the surface to react with surface bound co-catalysts and water. Hydrogen and oxygen are generated. (b) Simplified reaction conditions to evaluate the hydrogen evolution reaction. A sacrificial donor is introduced to trap generated holes by oxidation. NHE is standard hydrogen electrode.

For the in-depth evaluation of each half-reaction, sacrificial agents are typically used to neutralize the respective charge carriers. In this work, the focus will be on the hydrogen evolution half-reaction. Therefore, sacrificial electron donors like alcohols and amines that are readily oxidized are used as can be seen in Figure 1-20b. With transition-metal-modified TiO_2 , hydrogen evolution rates as high as $8500 \mu\text{mol h}^{-1} \text{g}^{-1}$ were achieved.^[166]

In 2015, our group performed a comprehensive study on the chemically related, yet different $\text{N}_x\text{-COFs}$ ^[109]. In the order $\text{N}_0\text{-COF}$, $\text{N}_1\text{-COF}$, $\text{N}_2\text{-COF}$, $\text{N}_3\text{-COF}$, the number of nitrogen atoms in the central aryl ring of the COF linker rises from 0 to 3. All COFs are photocatalytically active, but the hydrogen evolution rates (HER) differ. Addition of each nitrogen atom leads to a four times higher HER. Theoretical calculations suggest that different radical anion stabilization energies are at the heart of this effect, which would be in line with a reductive quenching pathway that the $\text{N}_x\text{-COFs}$ undergo during photocatalysis. Another series of COFs - the ATEPHY-COF series – was synthesized from pyrene-containing linkers with different numbers of peripheral nitrogen atoms. Their hydrogen evolution rates were determined to correlate with the theoretically calculated radical cation stabilization energies of the systems.^[52]

The superior performance of crystalline materials over amorphous or semi-crystalline ones was shown by comparison of the $\text{N}_x\text{-COFs}$ with its amorphous counterpart PTP-COF.^[110]

Later, this finding was confirmed by Cooper and coworkers. In their study, dye-sensitized sulfone-containing COFs were shown to exhibit HERs as high as $16.3 \text{ mmol h}^{-1} \text{g}^{-1}$. Both wettability and crystallinity were determined crucial for the good performance of the system.^[167]

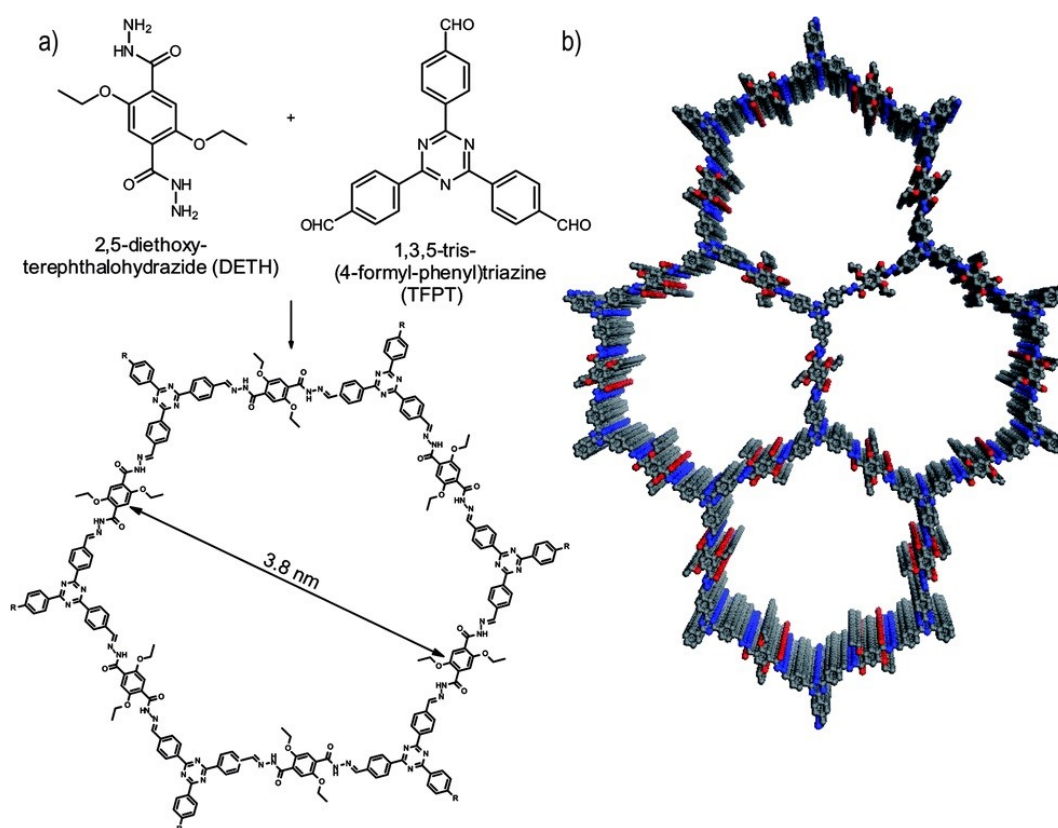


Figure 1-21: Acetic acid catalyzed hydrazone formation furnishes a mesoporous 2D network with a honeycomb-type in-plane structure. (a) Scheme showing the condensation of the two monomers to form the TFPT-COF. (b) TFPT-COF with a cofacial orientation of the aromatic building blocks, constituting a close-to eclipsed primitive hexagonal lattice (grey: carbon, blue: nitrogen, red: oxygen). Reprinted from [14].

In the ATEPHY-COF series, it was also shown, that COF thin films have the potential of serving as photocathodes in water reduction. Later, Bein and coworkers synthesized oriented thin films from a thiophene-based COF on indium tin oxide (ITO) substrates and proved efficient light harvesting as well as suitable band positioning. An increased photocurrent of the system was observed by the addition of Pt co-catalyst.^[168]

In 2017, we performed a study on the utilization of the noble-metal-free molecular cobaloximes as hydrogen evolution co-catalysts with COF-photosensitizers using the aforementioned N_x -COF series as well as COF-42.^[169] A closer look into the progress in this research field will be given in Chapter 3.2.

1.3.4 Covalent organic frameworks as gas storage materials

Technology for gas storage is becoming more and more important, especially in the field of energy and environmental applications. Intrinsically porous materials are widely used for selective gas binding and separation. COFs are especially advantageous due to their precisely adjustable and controllable pore sizes as well as straightforward modification of



their physical and chemical properties as has been discussed before, which facilitates their use for the adsorption of different gases.^[100, 170-171]

Starting in 2008, different computational studies on the hydrogen uptake capacities of COFs predicted their exceptional suitability as ambient temperature hydrogen storage materials.^[172-178] Experimental validation was given for COF-1 with 1.28 wt% at 1 atm and 77 K^[179], and COF-5, which showed an uptake of 3.4 wt% at 50 bar and 77 K.^[172] Other mesoporous 2D-COFs were found to exhibit moderate hydrogen adsorption capacities as for example ILCOF-1, which stores 1.3 wt% hydrogen at 77 K and 1.0 bar.^[180]

3D COFs showed enhanced capacities compared to 2D systems.^[172, 181] The hydrogen uptake of COF-102 was found to be 72 mg g⁻¹ at 77 K and 35 bar.^[182]

The decoration of COFs with metal nanoparticles increases their hydrogen uptake even further.^[183] A hybrid material with Pd nanoparticles in COF-102 enhanced the hydrogen capacity of the COF by a factor of 2 to 3 depending on the Pd content at 298 K and 20 bar^[184] The doping of COF-301 with PdCl₂ leads to a material that can store 4.2 wt% hydrogen at 298 K and 100 bar.^[185] This is due to the hydrogen spillover effect, which is also known in other adsorbents, such as MOFs or activated carbons.^[186-187] Doping with transition metals leads to dissociation of hydrogen on the metal sites and thus atomic diffusion and chemisorption to the sorbent. Hydrogen spillover facilitates hydrogen storage at ambient temperature, which makes it a promising approach for future research.^[188]

COFs were also used as reversible storage materials for the corrosive gas ammonia. Currently, the commercially used active carbon shows an ammonia uptake of 11 mmol g⁻¹.^[189] While most MOFs are unstable upon ammonia exposure, the high chemical stability of COFs offers the possibility to design materials that are optimized towards the Lewis basic guest molecule ammonia.^[190] It strongly interacts with Lewis acidic boron sites in COF-10 which leads to a very high uptake capacity of 15 mmol g⁻¹ at 298 K and 1 bar.^[171] Integration of metal cations (Ca²⁺, Mn²⁺, Sr²⁺) that serve as Lewis centers to coordination sites in a carboxylic acid functionalized COF increased its ammonia capacity from 6.85 mmol g⁻¹ at 298 K and 1 bar to 14 mmol g⁻¹ at 298 K and 1 bar.^[130]

Porous materials are used for the storage of natural gas. The adsorption of methane was analyzed from a theoretical point of view. The three-dimensional COF-102 and COF-103 were predicted to store 230 and 234 v/v at 298 K and 1 bar, which would classify them as suitable methane storage materials according to the U.S. Department of Energy target for CH₄ storage.^[191] For COF-102, experiments found an uptake of 187 mg g⁻¹ at 298 K.^[182] Another broad computational study screened a database with 280 COFs in 12 different topologies and found the highest values (190 v/v at 298 K and 1 bar) for the 3D PI-COF-4. In the same study, 2D COFs were screened for an ideal π - π -stacking distance for methane adsorption, which was found to be as high as 6.8 Å.^[192]

From an environmental point of view, the capture of carbon dioxide is another important example as has been discussed in Chapter 1.2. A lot of research was done to find materials with high CO₂ capacities at low pressure. Different types of COFs have been used in CO₂ adsorption.^[180, 193-195] For example, a CO₂ uptake of 1180 mg g⁻¹ at 298 K was found for COF-102.^[182] A closer look into this field of research is given in Chapter 4.

1.4 References

- [1] *World Population Prospects: The 2017 Revision, Key Findings and Advanced Tables*.
- [2] *BP Statistical Review of World Energy 2018*.
- [3] F. Dimroth, M. Grave, P. Beutel, U. Fiedeler, C. Karcher, T. N. D. Tibbits, E. Oliva, G. Siefer, M. Schachtner, A. Wekkeli, A. W. Bett, R. Krause, M. Piccin, N. Blanc, C. Drazek, E. Guiot, B. Ghyselen, T. Salvétat, A. Tauzin, T. Signamarcheix, A. Dobrich, T. Hannappel, K. Schwarzburg, *Progress in Photovoltaics: Research and Applications* **2014**, *22*, 277-282.
- [4] A. Fujishima, K. Honda, *Nature* **1972**, *238*, 37-38.
- [5] R. Abe, M. Higashi, K. Domen, *J. Am. Chem. Soc.* **2010**, *132*, 11828-11829.
- [6] M. Higashi, K. Domen, R. Abe, *J. Am. Chem. Soc.* **2012**, *134*, 6968-6971.
- [7] H. Kato, K. Asakura, A. Kudo, *J. Am. Chem. Soc.* **2003**, *125*, 3082-3089.
- [8] K. Sivula, F. Le Formal, M. Grätzel, *ChemSusChem* **2011**, *4*, 432-449.
- [9] Y. Pihosh, I. Turkevych, K. Mawatari, J. Uemura, Y. Kazoe, S. Kosar, K. Makita, T. Sugaya, T. Matsui, D. Fujita, M. Tosa, M. Kondo, T. Kitamori, *Scientific Reports* **2015**, *5*, 11141.
- [10] K. Maeda, X. Wang, Y. Nishihara, D. Lu, M. Antonietti, K. Domen, *The Journal of Physical Chemistry C* **2009**, *113*, 4940-4947.
- [11] G. Zhang, G. Li, T. Heil, S. Zafeirotos, F. Lai, A. Savateev, M. Antonietti, X. Wang, *Angew. Chem. Int. Ed.* **2019**, *58*, 3433-3437.
- [12] V. W.-h. Lau, D. Klose, H. Kasap, F. Podjaski, M.-C. Pignié, E. Reisner, G. Jeschke, B. V. Lotsch, *Angew. Chem. Int. Ed.* **2017**, *56*, 510-514.
- [13] F. Podjaski, J. Kröger, B. V. Lotsch, *Adv. Mater.* **2018**, *30*, 1705477.
- [14] L. Stegbauer, K. Schwinghammer, B. V. Lotsch, *Chemical Science* **2014**, *5*, 2789-2793.
- [15] E. Rodriguez Acevedo, F. B. Cortés, C. A. Franco, F. Carrasco-Marín, A. F. Pérez-Cadenas, V. Fierro, A. Celzard, S. Schaefer, A. Cardona Molina, *Materials* **2019**, *12*, 2088.
- [16] A. Ghosh, K. S. Subrahmanyam, K. S. Krishna, S. Datta, A. Govindaraj, S. K. Pati, C. N. R. Rao, *The Journal of Physical Chemistry C* **2008**, *112*, 15704-15707.
- [17] K. S. W. Sing, D. H. Everett, R. A. W. Haul, L. Moscou, R. A. Pierotti, J. Rouquérol, T. Siemieniowska, *Pure & Applied. Chem.* **1985**, *57*, 603-619.
- [18] J. Rouquerol, D. Avnir, C. W. Fairbridge, D. H. Everett, J. M. Haynes, N. Pernicone, J. D. F. Ramsay, K. S. W. Sing, K. K. Unger, *Pure Appl. Chem.* **1994**, *66*, 1739.
- [19] *University of Oslo*, **2012**.
- [20] M. S. Onyango, D. Kuchar, M. Kubota, H. Matsuda, *Industrial & Engineering Chemistry Research* **2007**, *46*, 894-900.
- [21] A. Takahashi, R. T. Yang, C. L. Munson, D. Chinn, *Langmuir* **2001**, *17*, 8405-8413.
- [22] F. Su, C. Lu, S.-C. Kuo, W. Zeng, *Energy & Fuels* **2010**, *24*, 1441-1448.



- [23] J. C. Jansen, J. H. Koegler, H. van Bekkum, H. P. A. Calis, C. M. van den Bleek, F. Kapteijn, J. A. Moulijn, E. R. Geus, N. van der Puil, *Microporous Mesoporous Mater.* **1998**, *21*, 213-226.
- [24] W. Zhang, J. Wang, P. T. Tanev, T. J. Pinnavaia, *Chem. Commun.* **1996**, 979-980.
- [25] A. Corma, *Chem. Rev.* **1997**, *97*, 2373-2420.
- [26] T. C. Bowen, R. D. Noble, J. L. Falconer, *Journal of Membrane Science* **2004**, *245*, 1-33.
- [27] J. Caro, *Microporous Mesoporous Mater.* **2009**, *125*, 79-84.
- [28] D. W. Breck, W. G. Eversole, R. M. Milton, T. B. Reed, T. L. Thomas, *J. Am. Chem. Soc.* **1956**, *78*, 5963-5972.
- [29] H. Hayashi, A. P. Côté, H. Furukawa, M. O'Keeffe, O. M. Yaghi, *Nature Materials* **2007**, *6*, 501-506.
- [30] S. S. Kaye, A. Dailly, O. M. Yaghi, J. R. Long, *J. Am. Chem. Soc.* **2007**, *129*, 14176-14177.
- [31] N. L. Rosi, J. Eckert, M. Eddaoudi, D. T. Vodak, J. Kim, M. Keffe, O. M. Yaghi, *Science* **2003**, *300*, 1127.
- [32] M. P. Suh, H. J. Park, T. K. Prasad, D.-W. Lim, *Chem. Rev.* **2012**, *112*, 782-835.
- [33] C.-D. Wu, A. Hu, L. Zhang, W. Lin, *J. Am. Chem. Soc.* **2005**, *127*, 8940-8941.
- [34] J. Liu, K.-K. Yee, K. K.-W. Lo, K. Y. Zhang, W.-P. To, C.-M. Che, Z. Xu, *J. Am. Chem. Soc.* **2014**, *136*, 2818-2824.
- [35] H. Liu, Y. Liu, Y. Li, Z. Tang, H. Jiang, *The Journal of Physical Chemistry C* **2010**, *114*, 13362-13369.
- [36] Y. Hu, Z. Liu, J. Xu, Y. Huang, Y. Song, *J. Am. Chem. Soc.* **2013**, *135*, 9287-9290.
- [37] W. Morris, B. Leung, H. Furukawa, O. K. Yaghi, N. He, H. Hayashi, Y. Houndonougbo, M. Asta, B. B. Laird, O. M. Yaghi, *J. Am. Chem. Soc.* **2010**, *132*, 11006-11008.
- [38] L. Hao, P. Li, T. Yang, T.-S. Chung, *Journal of Membrane Science* **2013**, *436*, 221-231.
- [39] Y. Zhu, H. Long, W. Zhang, *Chem. Mater.* **2013**, *25*, 1630-1635.
- [40] J. Ma, M. Wang, Z. Du, C. Chen, J. Gao, J. Xu, *Polymer Chemistry* **2012**, *3*, 2346-2349.
- [41] A. P. Côté, A. I. Benin, N. W. Ockwig, M. O'Keeffe, A. J. Matzger, O. M. Yaghi, *Science* **2005**, *310*, 1166-1170.
- [42] A. P. Côté, H. M. El-Kaderi, H. Furukawa, J. R. Hunt, O. M. Yaghi, *J. Am. Chem. Soc.* **2007**, *129*, 12914-12915.
- [43] H. M. El-Kaderi, J. R. Hunt, J. L. Mendoza-Cortés, A. P. Côté, R. E. Taylor, M. O'Keeffe, O. M. Yaghi, *Science* **2007**, *316*, 268-272.
- [44] S. J. Rowan, S. J. Cantrill, G. R. L. Cousins, J. K. M. Sanders, J. F. Stoddart, *Angew. Chem. Int. Ed.* **2002**, *41*, 898-952.
- [45] S.-Y. Ding, W. Wang, *Chem. Soc. Rev.* **2013**, *42*, 548-568.
- [46] R. W. Tilford, S. J. Mugavero, P. J. Pellechia, J. J. Lavigne, *Adv. Mater.* **2008**, *20*, 2741-2746.
- [47] L. M. Lanni, R. W. Tilford, M. Bharathy, J. J. Lavigne, *J. Am. Chem. Soc.* **2011**, *133*, 13975-13983.
- [48] J. R. Hunt, C. J. Doonan, J. D. LeVangie, A. P. Côté, O. M. Yaghi, *J. Am. Chem. Soc.* **2008**, *130*, 11872-11873.
- [49] Y. Du, K. Mao, P. Kamakoti, P. Ravikovitch, C. Paur, S. Cundy, Q. Li, D. Calabro, *Chem. Commun.* **2012**, *48*, 4606-4608.

- [50] E. L. Spitler, B. T. Koo, J. L. Novotney, J. W. Colson, F. J. Uribe-Romo, G. D. Gutierrez, P. Clancy, W. R. Dichtel, *J. Am. Chem. Soc.* **2011**, *133*, 19416-19421.
- [51] B. T. Koo, W. R. Dichtel, P. Clancy, *J. Mater. Chem.* **2012**, *22*, 17460-17469.
- [52] L. Stegbauer, S. Zech, G. Savasci, T. Banerjee, F. Podjaski, K. Schwinghammer, C. Ochsenfeld, B. V. Lotsch, *Advanced Energy Materials* **2018**, *0*, 1703278.
- [53] F. Haase, K. Gottschling, L. Stegbauer, L. S. Germann, R. Gutzler, V. Duppel, V. S. Vyas, K. Kern, R. E. Dinnebier, B. V. Lotsch, *Materials Chemistry Frontiers* **2017**, *1*, 1354-1361.
- [54] S. Chandra, S. Kandambeth, B. P. Biswal, B. Lukose, S. M. Kunjir, M. Chaudhary, R. Babarao, T. Heine, R. Banerjee, *J. Am. Chem. Soc.* **2013**, *135*, 17853-17861.
- [55] I. Berlanga, M. L. Ruiz-Gonzalez, J. M. Gonzalez-Calbet, J. L. Fierro, R. Mas-Balleste, F. Zamora, *Small* **2011**, *7*, 1207-1211.
- [56] G. Li, K. Zhang, T. Tsuru, *ACS Appl Mater Interfaces* **2017**, *9*, 8433-8436.
- [57] B. J. Smith, L. R. Parent, A. C. Overholts, P. A. Beaucage, R. P. Bisbey, A. D. Chavez, N. Hwang, C. Park, A. M. Evans, N. C. Gianneschi, W. R. Dichtel, *ACS Central Science* **2017**, *3*, 58-65.
- [58] Y. Du, H. Yang, J. M. Whiteley, S. Wan, Y. Jin, S.-H. Lee, W. Zhang, *Angew. Chem. Int. Ed.* **2016**, *55*, 1737-1741.
- [59] B. J. Smith, W. R. Dichtel, *J. Am. Chem. Soc.* **2014**, *136*, 8783-8789.
- [60] A. M. Evans, L. R. Parent, N. C. Flanders, R. P. Bisbey, E. Vitaku, M. S. Kirschner, R. D. Schaller, L. X. Chen, N. C. Gianneschi, W. R. Dichtel, *Science* **2018**, *361*, 52-57.
- [61] F. J. Uribe-Romo, J. R. Hunt, H. Furukawa, C. Klöck, M. O’Keeffe, O. M. Yaghi, *J. Am. Chem. Soc.* **2009**, *131*, 4570-4571.
- [62] S.-Y. Ding, J. Gao, Q. Wang, Y. Zhang, W.-G. Song, C.-Y. Su, W. Wang, *J. Am. Chem. Soc.* **2011**, *133*, 19816-19822.
- [63] Y. Hou, X. Zhang, C. Wang, D. Qi, Y. Gu, Z. Wang, J. Jiang, *New J. Chem.* **2017**, *41*, 6145-6151.
- [64] S. Wan, F. Gándara, A. Asano, H. Furukawa, A. Saeki, S. K. Dey, L. Liao, M. W. Ambrogio, Y. Y. Botros, X. Duan, S. Seki, J. F. Stoddart, O. M. Yaghi, *Chem. Mater.* **2011**, *23*, 4094-4097.
- [65] N. Keller, M. Calik, D. Sharapa, H. R. Soni, P. M. Zehetmaier, S. Rager, F. Auras, A. C. Jakowetz, A. Görling, T. Clark, T. Bein, *J. Am. Chem. Soc.* **2018**, *140*, 16544-16552.
- [66] Y. Wu, H. Xu, X. Chen, J. Gao, D. Jiang, *Chem. Commun.* **2015**, *51*, 10096-10098.
- [67] L. Ascherl, E. W. Evans, M. Hennemann, D. Di Nuzzo, A. G. Hufnagel, M. Beetz, R. H. Friend, T. Clark, T. Bein, F. Auras, *Nature Communications* **2018**, *9*, 3802.
- [68] G. Lin, H. Ding, D. Yuan, B. Wang, C. Wang, *J. Am. Chem. Soc.* **2016**, *138*, 3302-3305.
- [69] S.-L. Cai, K. Zhang, J.-B. Tan, S. Wang, S.-R. Zheng, J. Fan, Y. Yu, W.-G. Zhang, Y. Liu, *ACS Macro Letters* **2016**, *5*, 1348-1352.
- [70] S. Dalapati, M. Addicoat, S. Jin, T. Sakurai, J. Gao, H. Xu, S. Irle, S. Seki, D. Jiang, *Nature Communications* **2015**, *6*, 7786.
- [71] R.-R. Liang, X. Zhao, *Organic Chemistry Frontiers* **2018**, *5*, 3341-3356.
- [72] Z.-F. Pang, T.-Y. Zhou, R.-R. Liang, Q.-Y. Qi, X. Zhao, *Chemical Science* **2017**, *8*, 3866-3870.
- [73] Z.-F. Pang, S.-Q. Xu, T.-Y. Zhou, R.-R. Liang, T.-G. Zhan, X. Zhao, *J. Am. Chem. Soc.* **2016**, *138*, 4710-4713.



- [74] C. Qian, Q.-Y. Qi, G.-F. Jiang, F.-Z. Cui, Y. Tian, X. Zhao, *J. Am. Chem. Soc.* **2017**, *139*, 6736-6743.
- [75] X. Chen, M. Addicoat, E. Jin, H. Xu, T. Hayashi, F. Xu, N. Huang, S. Irle, D. Jiang, *Scientific Reports* **2015**, *5*, 14650.
- [76] Y. Zeng, R. Zou, Z. Luo, H. Zhang, X. Yao, X. Ma, R. Zou, Y. Zhao, *J. Am. Chem. Soc.* **2015**, *137*, 1020-1023.
- [77] H. Li, Q. Pan, Y. Ma, X. Guan, M. Xue, Q. Fang, Y. Yan, V. Valtchev, S. Qiu, *J. Am. Chem. Soc.* **2016**, *138*, 14783-14788.
- [78] S. Kandambeth, A. Mallick, B. Lukose, M. V. Mane, T. Heine, R. Banerjee, *J. Am. Chem. Soc.* **2012**, *134*, 19524-19527.
- [79] M. C. Daugherty, E. Vitaku, R. L. Li, A. M. Evans, A. D. Chavez, W. R. Dichtel, *Chem. Commun.* **2019**, *55*, 2680-2683.
- [80] S. Chandra, T. Kundu, S. Kandambeth, R. BabaRao, Y. Marathe, S. M. Kunjir, R. Banerjee, *J. Am. Chem. Soc.* **2014**, *136*, 6570-6573.
- [81] Y. Zhang, X. Shen, X. Feng, H. Xia, Y. Mu, X. Liu, *Chem. Commun.* **2016**, *52*, 11088-11091.
- [82] C. R. DeBlase, K. E. Silberstein, T.-T. Truong, H. D. Abruña, W. R. Dichtel, *J. Am. Chem. Soc.* **2013**, *135*, 16821-16824.
- [83] C. R. DeBlase, K. Hernández-Burgos, K. E. Silberstein, G. G. Rodríguez-Calero, R. P. Bisbey, H. D. Abruña, W. R. Dichtel, *ACS Nano* **2015**, *9*, 3178-3183.
- [84] F. J. Uribe-Romo, C. J. Doonan, H. Furukawa, K. Oisaki, O. M. Yaghi, *J. Am. Chem. Soc.* **2011**, *133*, 11478-11481.
- [85] Z.-J. Li, S.-Y. Ding, H.-D. Xue, W. Cao, W. Wang, *Chem. Commun.* **2016**, *52*, 7217-7220.
- [86] Z. Kang, Y. Peng, Y. Qian, D. Yuan, M. A. Addicoat, T. Heine, Z. Hu, L. Tee, Z. Guo, D. Zhao, *Chem. Mater.* **2016**, *28*, 1277-1285.
- [87] G. Das, D. Balaji Shinde, S. Kandambeth, B. P. Biswal, R. Banerjee, *Chem. Commun.* **2014**, *50*, 12615-12618.
- [88] M. Wu, G. Chen, P. Liu, W. Zhou, Q. Jia, *J. Chromatogr. A* **2016**, *1456*, 34-41.
- [89] T. Kundu, J. Wang, Y. Cheng, Y. Du, Y. Qian, G. Liu, D. Zhao, *Dalton Transactions* **2018**, *47*, 13824-13829.
- [90] W. Liu, Q. Su, P. Ju, B. Guo, H. Zhou, G. Li, Q. Wu, *ChemSusChem* **2017**, *10*, 664-669.
- [91] S.-Y. Ding, X.-H. Cui, J. Feng, G. Lu, W. Wang, *Chem. Commun.* **2017**, *53*, 11956-11959.
- [92] B.-J. Yao, J.-T. Li, N. Huang, J.-L. Kan, L. Qiao, L.-G. Ding, F. Li, Y.-B. Dong, *ACS Applied Materials & Interfaces* **2018**, *10*, 20448-20457.
- [93] Z. Zhou, W. Zhong, K. Cui, Z. Zhuang, L. Li, L. Li, J. Bi, Y. Yu, *Chem. Commun.* **2018**, *54*, 9977-9980.
- [94] S.-Y. Ding, M. Dong, Y.-W. Wang, Y.-T. Chen, H.-Z. Wang, C.-Y. Su, W. Wang, *J. Am. Chem. Soc.* **2016**, *138*, 3031-3037.
- [95] K. Zhang, S.-L. Cai, Y.-L. Yan, Z.-H. He, H.-M. Lin, X.-L. Huang, S.-R. Zheng, J. Fan, W.-G. Zhang, *J. Chromatogr. A* **2017**, *1519*, 100-109.
- [96] X. Li, Q. Gao, J. Wang, Y. Chen, Z.-H. Chen, H.-S. Xu, W. Tang, K. Leng, G.-H. Ning, J. Wu, Q.-H. Xu, S. Y. Quek, Y. Lu, K. P. Loh, *Nature Communications* **2018**, *9*, 2335.
- [97] G. Chen, H.-H. Lan, S.-L. Cai, B. Sun, X.-L. Li, Z.-H. He, S.-R. Zheng, J. Fan, Y. Liu, W.-G. Zhang, *ACS Applied Materials & Interfaces* **2019**, *11*, 12830-12837.

- [98] Y. Li, C. Wang, S. Ma, H. Zhang, J. Ou, Y. Wei, M. Ye, *ACS Applied Materials & Interfaces* **2019**, *11*, 11706-11714.
- [99] S. Dalapati, S. Jin, J. Gao, Y. Xu, A. Nagai, D. Jiang, *J. Am. Chem. Soc.* **2013**, *135*, 17310-17313.
- [100] Z. Li, X. Feng, Y. Zou, Y. Zhang, H. Xia, X. Liu, Y. Mu, *Chem. Commun.* **2014**, *50*, 13825-13828.
- [101] L. Stegbauer, M. W. Hahn, A. Jentys, G. Savasci, C. Ochsenfeld, J. A. Lercher, B. V. Lotsch, *Chem. Mater.* **2015**, *27*, 7874-7881.
- [102] L. Zhongping, Z. Yongfeng, F. Xiao, D. Xuesong, Z. Yongcun, L. Xiaoming, M. Ying, *Chem. Eur. J.* **2015**, *21*, 12079-12084.
- [103] R. A. Maia, F. L. Oliveira, M. Nazarkovsky, P. M. Esteves, *Crystal Growth & Design* **2018**, *18*, 5682-5689.
- [104] J. Lu, F. Lin, Q. Wen, Q.-Y. Qi, J.-Q. Xu, X. Zhao, *New J. Chem.* **2019**, *43*, 6116-6120.
- [105] Y. Zhu, S. Wan, Y. Jin, W. Zhang, *J. Am. Chem. Soc.* **2015**, *137*, 13772-13775.
- [106] S. B. Alahakoon, G. Occhialini, G. T. McCandless, A. A. K. Karunathilake, S. O. Nielsen, R. A. Smaldone, *CrystEngComm* **2017**, *19*, 4882-4885.
- [107] H. Fan, A. Mundstock, A. Feldhoff, A. Knebel, J. Gu, H. Meng, J. Caro, *J. Am. Chem. Soc.* **2018**, *140*, 10094-10098.
- [108] Z. Li, Y. Zhang, H. Xia, Y. Mu, X. Liu, *Chem. Commun.* **2016**, *52*, 6613-6616.
- [109] V. S. Vyas, F. Haase, L. Stegbauer, G. Savasci, F. Podjaski, C. Ochsenfeld, B. V. Lotsch, *Nat Commun* **2015**, *6*.
- [110] F. Haase, T. Banerjee, G. Savasci, C. Ochsenfeld, B. V. Lotsch, *Faraday Discuss.* **2017**, *201*, 247-264.
- [111] Y. Fu, X. Zhu, L. Huang, X. Zhang, F. Zhang, W. Zhu, *Applied Catalysis B: Environmental* **2018**, *239*, 46-51.
- [112] A. Nagai, X. Chen, X. Feng, X. Ding, Z. Guo, D. Jiang, *Angew. Chem. Int. Ed.* **2013**, *52*, 3770-3774.
- [113] J. Guo, Y. Xu, S. Jin, L. Chen, T. Kajii, Y. Honsho, M. A. Addicoat, J. Kim, A. Saeki, H. Ihee, S. Seki, S. Irlle, M. Hiramoto, J. Gao, D. Jiang, *Nat Commun* **2013**, *4*.
- [114] S. Nandi, S. K. Singh, D. Mullangi, R. Illathvalappil, L. George, C. P. Vinod, S. Kurungot, R. Vaidhyanathan, *Advanced Energy Materials* **2016**, *6*, 1601189.
- [115] D. A. Pyles, J. W. Crowe, L. A. Baldwin, P. L. McGrier, *ACS Macro Letters* **2016**, *5*, 1055-1058.
- [116] D. A. Pyles, W. H. Coldren, Grace M. Eder, C. M. Hadad, P. L. McGrier, *Chemical Science* **2018**, *9*, 6417-6423.
- [117] A. F. M. El-Mahdy, Y.-H. Hung, T. H. Mansoure, H.-H. Yu, T. Chen, S.-W. Kuo, *Chemistry – An Asian Journal* **2019**, *14*, 1429-1435.
- [118] B. Zhang, M. Wei, H. Mao, X. Pei, S. A. Alshimri, J. A. Reimer, O. M. Yaghi, *J. Am. Chem. Soc.* **2018**, *140*, 12715-12719.
- [119] X. Guan, H. Li, Y. Ma, M. Xue, Q. Fang, Y. Yan, V. Valtchev, S. Qiu, *Nature Chemistry* **2019**.
- [120] X. Zhuang, W. Zhao, F. Zhang, Y. Cao, F. Liu, S. Bi, X. Feng, *Polymer Chemistry* **2016**, *7*, 4176-4181.
- [121] E. Jin, M. Asada, Q. Xu, S. Dalapati, M. A. Addicoat, M. A. Brady, H. Xu, T. Nakamura, T. Heine, Q. Chen, D. Jiang, *Science* **2017**, *357*, 673-676.
- [122] E. Jin, J. Li, K. Geng, Q. Jiang, H. Xu, Q. Xu, D. Jiang, *Nature Communications* **2018**, *9*, 4143.



- [123] S. Xu, G. Wang, B. P. Biswal, M. Addicoat, S. Paasch, W. Sheng, X. Zhuang, E. Brunner, T. Heine, R. Berger, X. Feng, *Angew. Chem. Int. Ed.* **2019**, *58*, 849-853.
- [124] R. Chen, J.-L. Shi, Y. Ma, G. Lin, X. Lang, C. Wang, *Angew. Chem. Int. Ed.* **2019**, *58*, 6430-6434.
- [125] Y. Zhao, H. Liu, C. Wu, Z. Zhang, Q. Pan, F. Hu, R. Wang, P. Li, X. Huang, Z. Li, *Angew. Chem. Int. Ed.* **2019**, *58*, 5376-5381.
- [126] B. F. Hoskins, R. Robson, *J. Am. Chem. Soc.* **1990**, *112*, 1546-1554.
- [127] Y. H. Kiang, G. B. Gardner, S. Lee, Z. Xu, E. B. Lobkovsky, *J. Am. Chem. Soc.* **1999**, *121*, 8204-8215.
- [128] K. K. Tanabe, S. M. Cohen, *Chem. Soc. Rev.* **2011**, *40*, 498-519.
- [129] J. L. Segura, S. Royuela, M. Mar Ramos, *Chem. Soc. Rev.* **2019**, *48*, 3903-3945.
- [130] Y. Yang, M. Faheem, L. Wang, Q. Meng, H. Sha, N. Yang, Y. Yuan, G. Zhu, *ACS Central Science* **2018**, *4*, 748-754.
- [131] H. Wang, F. Jiao, F. Gao, Y. Lv, Q. Wu, Y. Zhao, Y. Shen, Y. Zhang, X. Qian, *Talanta* **2017**, *166*, 133-140.
- [132] H. Vardhan, G. Verma, S. Ramani, A. Nafady, A. M. Al-Enizi, Y. Pan, Z. Yang, H. Yang, S. Ma, *ACS Applied Materials & Interfaces* **2019**, *11*, 3070-3079.
- [133] L.-H. Li, X.-L. Feng, X.-H. Cui, Y.-X. Ma, S.-Y. Ding, W. Wang, *J. Am. Chem. Soc.* **2017**, *139*, 6042-6045.
- [134] W. Leng, R. Ge, B. Dong, C. Wang, Y. Gao, *RSC Advances* **2016**, *6*, 37403-37406.
- [135] J. Wang, X. Yang, T. Wei, J. Bao, Q. Zhu, Z. Dai, *ACS Applied Bio Materials* **2018**, *1*, 382-388.
- [136] H. B. Aiyappa, J. Thote, D. B. Shinde, R. Banerjee, S. Kurungot, *Chem. Mater.* **2016**, *28*, 4375-4379.
- [137] M. Mu, Y. Wang, Y. Qin, X. Yan, Y. Li, L. Chen, *ACS Applied Materials & Interfaces* **2017**, *9*, 22856-22863.
- [138] X. Han, J. Zhang, J. Huang, X. Wu, D. Yuan, Y. Liu, Y. Cui, *Nature Communications* **2018**, *9*, 1294.
- [139] W. Zhang, P. Jiang, Y. Wang, J. Zhang, Y. Gao, P. Zhang, *RSC Advances* **2014**, *4*, 51544-51547.
- [140] W. Leng, Y. Peng, J. Zhang, H. Lu, X. Feng, R. Ge, B. Dong, B. Wang, X. Hu, Y. Gao, *Chemistry – A European Journal* **2016**, *22*, 9087-9091.
- [141] Y. Hou, X. Zhang, J. Sun, S. Lin, D. Qi, R. Hong, D. Li, X. Xiao, J. Jiang, *Microporous Mesoporous Mater.* **2015**, *214*, 108-114.
- [142] Q. Sun, B. Aguila, S. Ma, *Materials Chemistry Frontiers* **2017**, *1*, 1310-1316.
- [143] E. M. Johnson, R. Haiges, S. C. Marinescu, *ACS Applied Materials & Interfaces* **2018**, *10*, 37919-37927.
- [144] S. Yang, W. Hu, X. Zhang, P. He, B. Pattengale, C. Liu, M. Cendejas, I. Hermans, X. Zhang, J. Zhang, J. Huang, *J. Am. Chem. Soc.* **2018**, *140*, 14614-14618.
- [145] X. Wu, X. Han, Y. Liu, Y. Liu, Y. Cui, *J. Am. Chem. Soc.* **2018**, *140*, 16124-16133.
- [146] P. Pachfule, S. Kandambeth, D. Díaz Díaz, R. Banerjee, *Chem. Commun.* **2014**, *50*, 3169-3172.
- [147] P. Pachfule, M. K. Panda, S. Kandambeth, S. M. Shivaprasad, D. D. Díaz, R. Banerjee, *Journal of Materials Chemistry A* **2014**, *2*, 7944-7952.
- [148] S. Lu, Y. Hu, S. Wan, R. McCaffrey, Y. Jin, H. Gu, W. Zhang, *J. Am. Chem. Soc.* **2017**, *139*, 17082-17088.
- [149] H.-L. Qian, Y. Li, X.-P. Yan, *Journal of Materials Chemistry A* **2018**, *6*, 17307-17311.

- [150] Z. Li, X. Ding, Y. Feng, W. Feng, B.-H. Han, *Macromolecules* **2019**, *52*, 1257-1265.
- [151] P. J. Waller, S. J. Lyle, T. M. Osborn Popp, C. S. Diercks, J. A. Reimer, O. M. Yaghi, *J. Am. Chem. Soc.* **2016**, *138*, 15519-15522.
- [152] J.-M. Seo, H.-J. Noh, H. Y. Jeong, J.-B. Baek, *J. Am. Chem. Soc.* **2019**, *141*, 11786-11790.
- [153] P. J. Waller, Y. S. AlFaraj, C. S. Diercks, N. N. Jarenwattananon, O. M. Yaghi, *J. Am. Chem. Soc.* **2018**, *140*, 9099-9103.
- [154] F. Haase, E. Troschke, G. Savasci, T. Banerjee, V. Duppel, S. Dörfler, M. M. J. Grundei, A. M. Burow, C. Ochsenfeld, S. Kaskel, B. V. Lotsch, *Nature Communications* **2018**, *9*, 2600.
- [155] X. Li, C. Zhang, S. Cai, X. Lei, V. Altoe, F. Hong, J. J. Urban, J. Ciston, E. M. Chan, Y. Liu, *Nature Communications* **2018**, *9*, 2998.
- [156] A. Nagai, Z. Guo, X. Feng, S. Jin, X. Chen, X. Ding, D. Jiang, *Nat Commun* **2011**, *2*, 536.
- [157] H. Xu, X. Chen, J. Gao, J. Lin, M. Addicoat, S. Irlle, D. Jiang, *Chem. Commun.* **2014**, *50*, 1292-1294.
- [158] N. Huang, R. Krishna, D. Jiang, *J. Am. Chem. Soc.* **2015**, *137*, 7079-7082.
- [159] L. Chen, K. Furukawa, J. Gao, A. Nagai, T. Nakamura, Y. Dong, D. Jiang, *J. Am. Chem. Soc.* **2014**, *136*, 9806-9809.
- [160] D. N. Bunck, W. R. Dichtel, *Chem. Commun.* **2013**, *49*, 2457-2459.
- [161] S.-L. Ji, H.-L. Qian, C.-X. Yang, X. Zhao, X.-P. Yan, *ACS Applied Materials & Interfaces* **2019**.
- [162] Q. Sun, B. Aguila, J. Perman, L. D. Earl, C. W. Abney, Y. Cheng, H. Wei, N. Nguyen, L. Wojtas, S. Ma, *J. Am. Chem. Soc.* **2017**, *139*, 2786-2793.
- [163] Q. Sun, B. Aguila, J. A. Perman, T. Butts, F.-S. Xiao, S. Ma, *Chem* **2018**, *4*, 1726-1739.
- [164] M. S. Lohse, T. Stassin, G. Naudin, S. Wuttke, R. Ameloot, D. De Vos, D. D. Medina, T. Bein, *Chem. Mater.* **2016**, *28*, 626-631.
- [165] X. Li, J. Yu, J. Low, Y. Fang, J. Xiao, X. Chen, *Journal of Materials Chemistry A* **2015**, *3*, 2485-2534.
- [166] A. T. Montoya, E. G. Gillan, *ACS Omega* **2018**, *3*, 2947-2955.
- [167] X. Wang, L. Chen, S. Y. Chong, M. A. Little, Y. Wu, W.-H. Zhu, R. Clowes, Y. Yan, M. A. Zwijnenburg, R. S. Sprick, A. I. Cooper, *Nature Chemistry* **2018**, *10*, 1180-1189.
- [168] T. Sick, A. G. Hufnagel, J. Kampmann, I. Kondofersky, M. Calik, J. M. Rotter, A. Evans, M. Döblinger, S. Herbert, K. Peters, D. Böhm, P. Knochel, D. D. Medina, D. Fattakhova-Rohlfing, T. Bein, *J. Am. Chem. Soc.* **2018**, *140*, 2085-2092.
- [169] T. Banerjee, F. Haase, G. Savasci, K. Gottschling, C. Ochsenfeld, B. V. Lotsch, *J. Am. Chem. Soc.* **2017**, *139*, 16228-16234.
- [170] S. Hug, M. B. Mesch, H. Oh, N. Popp, M. Hirscher, J. Senker, B. V. Lotsch, *Journal of Materials Chemistry A* **2014**, *2*, 5928-5936.
- [171] C. J. Doonan, D. J. Tranchemontagne, T. G. Glover, J. R. Hunt, O. M. Yaghi, *Nat Chem* **2010**, *2*, 235-238.
- [172] S. S. Han, H. Furukawa, O. M. Yaghi, W. A. Goddard, *J. Am. Chem. Soc.* **2008**, *130*, 11580-11581.
- [173] G. Garberoglio, *Langmuir* **2007**, *23*, 12154-12158.
- [174] E. Klontzas, E. Tylianakis, G. E. Froudakis, *The Journal of Physical Chemistry C* **2008**, *112*, 9095-9098.



- [175] E. Klontzas, E. Tylianakis, G. E. Froudakis, *Nano Lett.* **2010**, *10*, 452-454.
- [176] E. Tylianakis, E. Klontzas, G. E. Froudakis, *Nanoscale* **2011**, *3*, 856-869.
- [177] J.-H. Guo, H. Zhang, Z.-P. Liu, X.-L. Cheng, *The Journal of Physical Chemistry C* **2012**, *116*, 15908-15917.
- [178] X.-D. Li, J.-H. Guo, H. Zhang, X.-L. Cheng, X.-Y. Liu, *RSC Advances* **2014**, *4*, 24526-24532.
- [179] Y. Li, R. T. Yang, *AIChE J.* **2008**, *54*, 269-279.
- [180] M. G. Rabbani, A. K. Sekizkardes, Z. Kahveci, T. E. Reich, R. Ding, H. M. El-Kaderi, *Chemistry – A European Journal* **2013**, *19*, 3324-3328.
- [181] B. Assfour, G. Seifert, *Chem. Phys. Lett.* **2010**, *489*, 86-91.
- [182] H. Furukawa, O. M. Yaghi, *J. Am. Chem. Soc.* **2009**, *131*, 8875-8883.
- [183] M. M. Wu, Q. Wang, Q. Sun, P. Jena, Y. Kawazoe, *The Journal of Chemical Physics* **2010**, *133*, 154706.
- [184] S. B. Kalidindi, H. Oh, M. Hirscher, D. Esken, C. Wiktor, S. Turner, G. Van Tendeloo, R. A. Fischer, *Chemistry – A European Journal* **2012**, *18*, 10848-10856.
- [185] J. L. Mendoza-Cortes, W. A. Goddard, H. Furukawa, O. M. Yaghi, *The Journal of Physical Chemistry Letters* **2012**, *3*, 2671-2675.
- [186] G. M. Psfogiannakis, G. E. Froudakis, *The Journal of Physical Chemistry C* **2011**, *115*, 4047-4053.
- [187] E. Ganz, M. Dornfeld, *The Journal of Physical Chemistry C* **2012**, *116*, 3661-3666.
- [188] L. Wang, R. T. Yang, *Energy & Environmental Science* **2008**, *1*, 268-279.
- [189] D. Britt, D. Tranchemontagne, O. M. Yaghi, *Proceedings of the National Academy of Sciences* **2008**, *105*, 11623-11627.
- [190] A. J. Rieth, M. Dincă, *ACS Central Science* **2018**, *4*, 666-667.
- [191] J. L. Mendoza-Cortés, S. S. Han, H. Furukawa, O. M. Yaghi, W. A. Goddard, *The Journal of Physical Chemistry A* **2010**, *114*, 10824-10833.
- [192] M. Tong, Y. Lan, Z. Qin, C. Zhong, *The Journal of Physical Chemistry C* **2018**, *122*, 13009-13016.
- [193] R. Dawson, E. Stockel, J. R. Holst, D. J. Adams, A. I. Cooper, *Energy & Environmental Science* **2011**, *4*, 4239-4245.
- [194] Z. Kahveci, T. Islamoglu, G. A. Shar, R. Ding, H. M. El-Kaderi, *CrystEngComm* **2013**, *15*, 1524-1527.
- [195] J.-R. Song, J. Sun, J. Liu, Z.-T. Huang, Q.-Y. Zheng, *Chem. Commun.* **2014**, *50*, 788-791.



2 Methods

In the following, an overview on the main analytical methods used for COFs will be given, namely physisorption analysis, powder x-ray diffraction (PXRD) and solid-state nuclear magnetic resonance (ssNMR). They cover for the most important features of COFs – defined porosity, crystallinity, and chemical integrity.

2.1 Gas adsorption

Adsorption at a solid/gas interface is defined as the enrichment of one or more components in an interfacial layer.^[1] Adsorption can be divided in chemi- and physisorption. Chemisorption results from a chemical bond formation between the adsorbate and the adsorbent. Thus, chemisorption is characterized by a relatively high heat of adsorption, typically between 80 and 400 kJ mol⁻¹. Chemisorption only occurs on chemically active sites of the material. Physisorption describes a merely physical process that is reversible with effectively no or only very low activation energies. It allows complete surface coverage and multilayered pore filling. Therefore, physisorption with inert adsorptives is a potent analysis technique for the characterization of porous materials identifying pore sizes and surface areas.

2.1.1 Physisorption isotherms

To analyze the porosity of micro-, meso-, and macroporous materials, the uptake over a wider range of relative pressures of an adsorptive is measured at a constant temperature. Typical adsorptives are argon, nitrogen, hydrogen, carbon dioxide, or water. By evaluation of the shape of the isotherm, conclusions about the interactions that occur in the system can be drawn and, hence, insights into the type and size of inter- and intraparticular pores. The adsorption of a gas by an adsorbate is quantitatively described by its adsorption isotherm. According to the IUPAC^[2], six physisorption isotherm types can be distinguished (see Figure 2-1) that are typical for microporous (type I), mesoporous (type IV, and V), or macroporous and nonporous materials (type I, III, and VI).

Type I shows a strong pore filling at low relative pressure with a plateau at increased relative pressure. This is very typical for microporous materials with small external surface area, where adsorbate-adsorbent interactions and capillary forces are dominant leading to early condensation of the adsorbative into the pores. Smaller pores lead to earlier pore filling, while in larger pore systems, the pore filling is shifted to higher relative pressures.

In type II isotherms, monolayer formation is observed in low pressure ranges. Above a certain pressure B , a linear rise indicates multilayer formation with a terminal rise at high relative pressure which is typical for textural pores. This isotherm type is very typical for macroporous and nonporous materials.

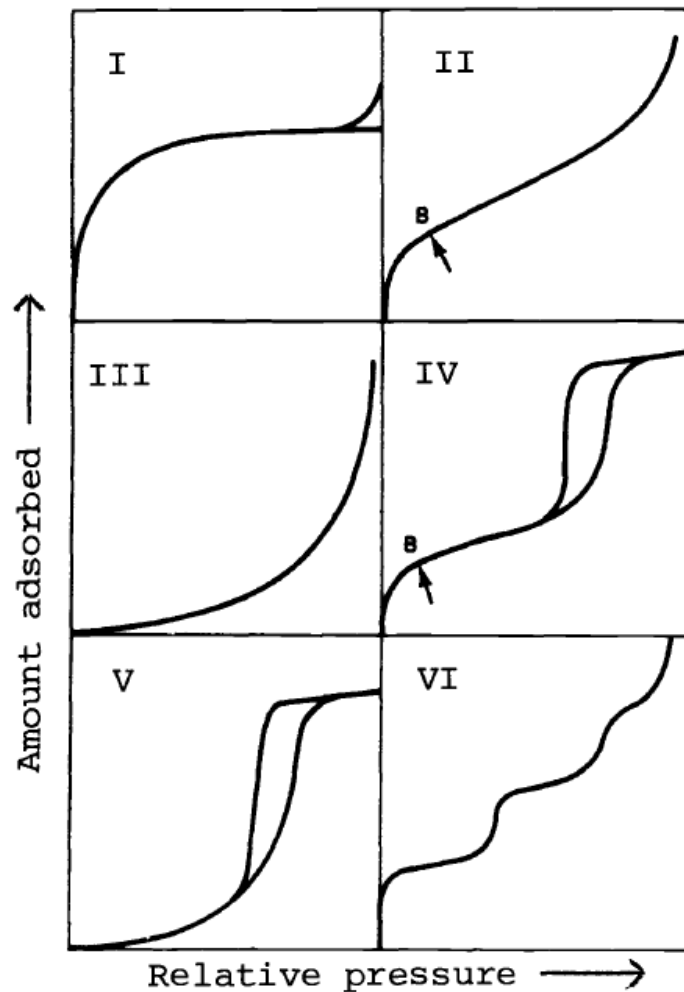


Figure 2-1: Types of physisorption isotherms according to IUPAC recommendation. Reprinted from [2].

Type III isotherms are indicative for very weak interactions of the adsorbate and the surface. Interactions occur mostly between the adsorbed molecules which leads to a convex shape of the isotherm. This type is rather uncommon, an example being the adsorption of water vapour on nonporous carbons.

The most common isotherm for mesoporous material is type IV. It is a combination of monolayer formation comparable to type II isotherms in the low-pressure region and multilayer formation at higher pressure. Pore filling becomes visible at a certain critical pressure where capillary condensation creates a steep rise of the adsorptive uptake. Typically, desorption creates a hysteresis at this stage, as it takes place at lower pressure



than the pore filling. If pore filling is fully reversible and hysteresis does not occur, the isotherm is referred to as type IVb.

Type V isotherms are closely related to type II and likewise uncommon. It is characteristic for weak adsorbate-adsorbent interactions.

Type VI shows stepwise multilayer adsorption where the step-height represents monolayer capacity for the adsorbed layers on nonporous surfaces.

2.1.2 Surface area determination

One of the most characteristic properties of a porous material is its surface area. It is determined from gas adsorption measurements according to the Langmuir or the BET theory. The Langmuir adsorption model describes adsorption of an ideal gas at isothermal conditions. It uses the following assumptions to describe the adsorption process: Formation of a monolayer on a completely homogeneous surface, where all binding sites are equal, and no additional interactions between adsorbate molecules occur.

From that, the following equation is deduced, where n is the amount of adsorbate, n_m the monolayer capacity, p the pressure and K the ratio between the constant of adsorption reaction k_{ad} and the constant of desorption reaction k_{des} :

$$\frac{n}{n_m} = \frac{Kp}{1+Kp} \quad (2.1)$$

More accurate is the 1938 published Brunauer-Emmet-Teller (BET) theory,^[3] which became the most widely used model to date. It is an extension of the Langmuir theory and assumes that the adsorptive is adsorbed on the surface in infinite layers without interlayer interactions. The Langmuir theory is applied to each individual layer (see eq. 2.2) with p and p_0 as the equilibrium and the saturation pressure, W and W_m as the adsorbed weight and monolayer weight and C as the BET constant.

$$\frac{1}{W\left[\frac{p_0}{p}-1\right]} = \frac{1}{W_m C} + \frac{C-1}{W_m C} \left(\frac{p}{p_0}\right) \quad (2.2)$$

To extract W_m and C , $1/W[(p_0/p)-1]$ against p/p_0 is plotted. Linear fitting in the range of approximately $0.05 \leq p_0/p \leq 0.35$ gives the slope s and the intercept i that are used as shown in eq. 2.3 and eq. 2.4. The standard BET procedure requires the measurement of at least three, but preferably more than five points in this pressure range on the N_2 or Ar adsorption isotherm at the respective boiling point of N_2 or Ar.

$$W_m = \frac{1}{s+i} \quad (2.3)$$

$$C = 1 + \frac{s}{i} \quad (2.4)$$

The values can now be used to calculate the total surface area S_t according to the Langmuir theory (see eq. 2.5), where N_A is Avogadro's number, A_x is the cross-sectional area and M is the molecular weight of the adsorbate. The specific BET surface area is obtained by dividing S_t by the sample weight.

$$S_t = \frac{W_m N_A A_x}{M} \quad (2.5)$$

2.1.3 Pore size analysis

The pore size distribution links the pore volume to pore size. With a number of assumptions made like ideal pore geometry, the pore shape (cylindrical or spherical), or a noncontinuous transition from meso- to macropores, a certain pore size range can be computed very accurately.

The Kelvin equation (equ. 2.6) is used to describe the radius of the curvature of the liquid meniscus in the pore to the relative vapour pressure $\frac{p}{p_0}$ at which condensation occurs. This radius is directly related to the pore width and is often referred to as the Kelvin radius r_K . In this equation, γ is the surface tension of the adsorbate and V_L is the molar volume.

$$r_K = \frac{-2\gamma V_L}{RT \ln \frac{p}{p_0}} \quad (2.6)$$

In addition to the Kelvin equation, the Barret-Joyner-Halenda (BJH) method includes the monolayer thickness t which leads to the following equation:

$$\ln \frac{p}{p_0} = \frac{2\gamma V_L}{(r_p - t)RT} \quad (2.7)$$

Where r_p is the pore radius, γ the surface tension of the liquid and V_L the molar volume.

In general, both models underestimate the pore volumes by up to 20 - 30% for pores smaller than 10 nm due to the disregard of enhanced surface forces.^[4] This deviation can be overcome by adapting the Kelvin equation to a series of very homogeneous and well-known pore diameters and using the empirically corrected version of the Kelvin equation.

In recent years, developments in density functional theory (DFT) and Monte Carlo (MC) simulations yielded more accurate descriptions and, hence, are the methods of choice for pore size determination today. Those methods are based on statistical mechanics and describe the adsorbed phase on a molecular level taking into account attractive and repulsive fluid-solid and fluid-fluid interactions, even at curved solid walls. This predicts the capillary condensation and evaporation of argon and nitrogen in silica and homogeneous carbons quantitatively. For the analysis of those material, non-local density functional theory

(NLDFT) kernels were developed^[5], while quenched solid density functional theory (QSDFT) describes PSDs for heterogeneous carbons well. This latter method takes into account surface roughness as well as chemical inhomogeneity.^[6] At the same time, those methods are known to exhibit good results for COFs.

The pore size distributions are calculated by the integration of equilibrium density profiles of the adsorbent in modeled pores. Kernels are used as theoretical references for the experimental systems. A kernel consists of isotherms calculated for a set of pore sizes for a given adsorbate. Comparison of calculated and experimental isotherms allows the validation of the method. An accurate analysis of pore sizes over the complete micro- and mesoporous range is possible with DFT methods, as long as the chosen kernel is compatible with the experimental system.

2.2 Powder x-ray diffraction

X-ray diffraction (XRD) is a nondestructive analytical method used for the analysis of the atomic and molecular structure of typically crystalline materials.

In 1912 Max von Laue was the first one to discover, that crystals act as 3D diffraction lattices for X-rays with a wavelength in the size of the d-spacing of the crystal lattice. The regular arrangement of atoms in a crystalline material causes a likewise regular, coherent scattering of an incoming monochromatic X-ray beam by the atom's electrons. The scattered beams of a crystalline material can interact and cause constructive or destructive interference. The specific directions in which the electromagnetic waves add constructively are defined by Bragg's law (see eq. 2.8).

$$n\lambda = 2d\sin\theta \quad (2.8)$$

where λ is the wavelength of the incident X-ray beam and n is an integer.

The diffracted X-rays are then detected and processed. The measured intensity is proportional to the square of the static structure factor F_{hkl} which is the Fourier transform of the electron density (see eq. 2.9 and 2.10) with a , b and c being the lattice parameters, x , y and z the coordinates in the unit cell and h , k and l the Miller indices.

$$I_{hkl} \sim |F_{hkl}|^2 \quad (2.9)$$

$$F_{hkl} = \int_0^a \int_0^b \int_0^c \rho(x,y,z) \exp \left[2\pi i \left(\frac{hx}{a} + \frac{ky}{b} + \frac{lz}{c} \right) \right] dx dy dz \quad (2.10)$$

The positions of the maxima of the electron density equal the atom positions in the unit cell. As the measured intensities only give the modulus of the structure factor, the problem of phase determination remains. After phase analysis, the structure can be refined. The structure factor F can be expressed by the sum of the atomic form factors f of the atoms in the unit cell (see eq. 2.11). The atomic form factor f is the Fourier transform of the electron

density of one atom. In structural refinement, the atom coordinates are altered until the difference between measured and calculated structure factors is minimized.

$$F_{hkl} = \sum_j^N f_j \exp [2\pi i(hx_j + ky_j + lz_j)] \quad (2.11)$$

In the case of COFs, direct structural refinement is usually very challenging. The number of single crystal analyses is little, as materials are usually obtained as nanocrystalline powders with crystallite dimensions below 100 nm. Additional real structure problems as anisotropy in crystallite size, strain, and solvent molecules remaining in the pores, impede direct structural analysis. Therefore, atomistic structure modelling was established as the main tool for the PXRD analysis of COFs. This allows to correlate modeled and experimentally obtained diffraction patterns and structure assignment.

2.3 Nuclear magnetic resonance spectroscopy

Solid state NMR is a powerful tool for the characterization of COFs. It provides structural and dynamic local information on the investigated system. It is based on the existence of a nuclear spin in NMR active nuclei, which is the case for spin $\frac{n+1}{2}$ systems. The most important nuclei in the context of COFs are ^1H , ^{13}C , $^{14/15}\text{N}$. By application of an external magnetic field, degenerated energy states are split up into energetically separated states, which is called Zeeman effect. The energy difference of the separated states is dependent on the local environment of the investigated system, especially on the spatial proximity of other spins and the shielding effect of chemical bonds. The effects are time and orientation dependent, which leads to a strong influence of anisotropic interactions in media with reduced mobility and therefore access to the dynamics of the system.

While in solution-based NMR very rapid processes based on Brownian motion are averaged out, thus leading to very sharp signals, ssNMR suffers from several effects leading to peak broadening and poor signal-to-noise ratio. Therefore, special ssNMR techniques like magic-angle spinning (MAS) are inevitable for a reliable evaluation of immobile samples. MAS was introduced by E. R. Andrew and I. L. Lowe to mimic the averaging orientation in solution. It uses a spinning rate equal or greater than the dipolar linewidth (ca. 1 – 100 kHz) at an angle β_M of 54.74° relative to the magnetic field B_0 to average anisotropic dipolar interactions. Chemical shift anisotropies can still be accessed from spinning sidebands. With cross polarization (CP), the polarization of abundant nuclei, often ^1H , is transferred to rare nuclei, so that the signal-to-noise ratio is strongly increased. This can also be achieved by transfer from radicals (added to the sample as polarizing agent or native) to rare nuclei. The so-called dynamic nuclear polarization (DNP) ssNMR is considered as a hyperpolarization technique. DNP uses the Overhauser effect, which is interactions between unpaired electrons

and NMR-sensitive nuclei. In DNP experiments, the NMR signal is detected from the NMR nucleus while the unpaired electron is excited by microwave irradiation. This results in a significant amplification of the signal-to-noise ratio. This technique was used in Chapter 4.2 to investigate the interaction of CO₂ with amine-modified COFs.

With advanced experimental techniques like the homonuclear 2D double quantum – single quantum correlation experiments, ¹H – ¹H distances can be probed. It generates double-quantum coherences by dipole-dipole coupling to gain through-space information of locally close protons. The spectrum only contains cross-peaks of protons with direct dipolar interactions due to the double-quantum filter, which is indicative of a proton-proton proximity of below 3.5 Å. This technique contributed substantially to the structural investigation of the COF sample in Chapter 3.4, where photocatalytic activities were compared with experimental as well as theoretical structural considerations based on advanced ssNMR techniques.

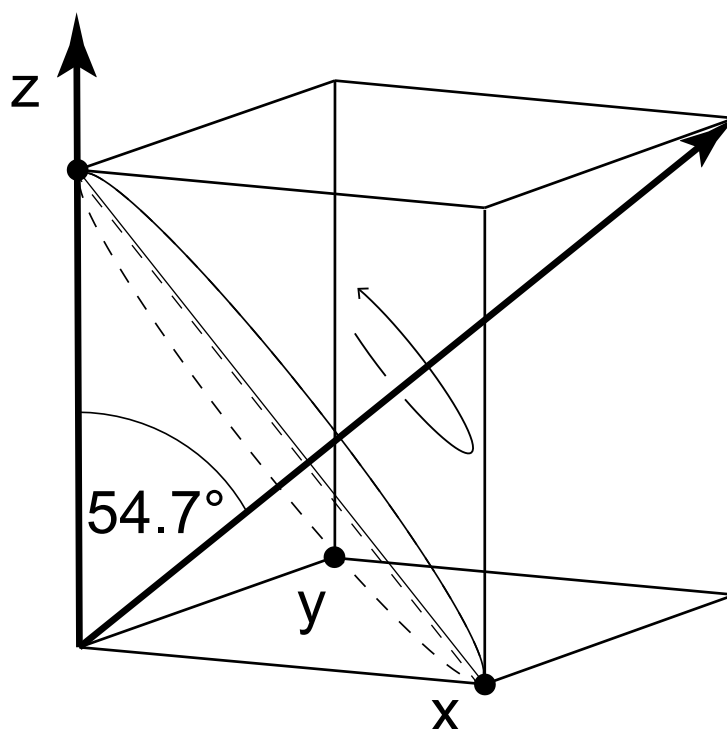


Figure 2-2: Schematic representation of the magic angle (54.7°). Rapid spinning of the sample about this axis averages the dipolar interactions.

2.4 Thin film synthesis

The synthesis of COF thin films and membranes has always been challenging. The insoluble powders that are created during COF synthesis are hardly processable with conventional thin film fabrication techniques like dip or spin coating limiting the applicability of COFs in practice. Both bottom-up and top-down approaches have been tested for COF thin film

fabrication.^[7] The following techniques have been successfully executed so far: exfoliation of COF powders by shear force^[8-10], solvent-assisted exfoliation^[11-14], solvothermal synthesis^[15-17], interfacial polymerization^[18-19], flow synthesis^[20], and vapor-assisted synthesis^[21].

In this thesis, two main methods were used for the synthesis of COF thin films on Si, glass or ITO wafers: solvothermal synthesis in autoclave reactors and interfacial synthesis between organic solvents and water. The methodology is briefly described in the following.

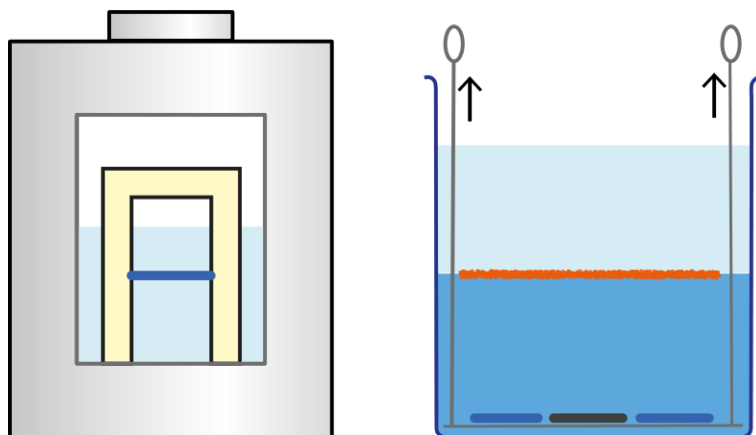


Figure 2-3: Schematic representation of thin film synthesis methods used in this thesis. Solvothermal synthesis in autoclave reactors (left), in which the wafer (dark blue) is placed floating in the synthetic mixture. Interfacial synthesis (right), where material deposition is carried out by lifting the substrate through the interface.

Solvothermal synthesis

For the synthesis of COF thin films, substrates can be directly added to the solvothermal reaction mixture that is used in traditional COF powder synthesis. It has been proven advantageous to use an inert Teflon holder to carry the substrates, as the substrates can be placed at an optimized height depending on the solvent volume and the adhesion of the COF powder on Teflon is low. This holder is placed into an autoclave with an appropriate inlet volume and subjected to the respective standard COF synthesis conditions, e. g. acid catalysis at 120 °C for 72 h. With this method, homogeneous coverage of the substrates is achieved. The number of substrates coated at the same time is limited due to limited space in the autoclaves as well as the fact, that the substrates should be placed at the same height in the solvent to achieve comparable film thicknesses. It was shown that so-synthesized films are formed homogeneously, crystalline and oriented parallel to the substrate surface.^[22-23]

Interfacial polymerization

This method confines the COF formation reaction to the interface between two immiscible solvents, e. g. water and dichloromethane. It is inspired by classical polymer thin film synthesis.^[24-26] By protonation with strong acids, imines are dissolved in water and the



corresponding aldehydes are added carefully as the top layer. The COF film forms within hours at room temperature, its thickness is adjustable by the reaction time. The transfer from the interface onto the substrate was achieved by keeping the substrates on the bottom of the reaction vessel during synthesis and lifting them up with a grid to minimize solvent turbulences as far as possible. Coverage of several substrates at the same time is easily achieved on a large area.

2.5 References

- [1] K. S. W. Sing, D. H. Everett, R. A. W. Haul, L. Moscou, R. A. Pierotti, J. Rouqu erol, T. Siemieniewska, *Pure & Applied. Chem.* **1985**, *57*, 603-619.
- [2] K. S. W. Sing, in *Pure Appl. Chem., Vol. 54*, **1982**, p. 2201.
- [3] S. Brunauer, P. H. Emmett, E. Teller, *J. Am. Chem. Soc.* **1938**, *60*, 309-319.
- [4] M. Thommes, *Chem. Ing. Tech.* **2010**, *82*, 1059-1073.
- [5] P. I. Ravikovitch, S. C. O. Domhnaill, A. V. Neimark, F. Schueth, K. K. Unger, *Langmuir* **1995**, *11*, 4765-4772.
- [6] P. I. Ravikovitch, A. V. Neimark, *Langmuir* **2006**, *22*, 11171-11179.
- [7] H. Wang, Z. Zeng, P. Xu, L. Li, G. Zeng, R. Xiao, Z. Tang, D. Huang, L. Tang, C. Lai, D. Jiang, Y. Liu, H. Yi, L. Qin, S. Ye, X. Ren, W. Tang, *Chem. Soc. Rev.* **2019**, *48*, 488-516.
- [8] B. P. Biswal, S. Chandra, S. Kandambeth, B. Lukose, T. Heine, R. Banerjee, *J. Am. Chem. Soc.* **2013**, *135*, 5328-5331.
- [9] S. Wang, Q. Wang, P. Shao, Y. Han, X. Gao, L. Ma, S. Yuan, X. Ma, J. Zhou, X. Feng, B. Wang, *J. Am. Chem. Soc.* **2017**, *139*, 4258-4261.
- [10] S. Chandra, S. Kandambeth, B. P. Biswal, B. Lukose, S. M. Kunjir, M. Chaudhary, R. Babarao, T. Heine, R. Banerjee, *J. Am. Chem. Soc.* **2013**, *135*, 17853-17861.
- [11] D. N. Bunck, W. R. Dichtel, *J. Am. Chem. Soc.* **2013**, *135*, 14952-14955.
- [12] I. Berlanga, M. L. Ruiz-Gonzalez, J. M. Gonzalez-Calbet, J. L. Fierro, R. Mas-Balleste, F. Zamora, *Small* **2011**, *7*, 1207-1211.
- [13] G. Li, K. Zhang, T. Tsuru, *ACS Appl Mater Interfaces* **2017**, *9*, 8433-8436.
- [14] H. Zhang, *ACS Nano* **2015**, *9*, 9451-9469.
- [15] D. D. Medina, V. Werner, F. Auras, R. Tautz, M. Dogru, J. Schuster, S. Linke, M. Doblinger, J. Feldmann, P. Knochel, T. Bein, *ACS Nano* **2014**, *8*, 4042-4052.
- [16] J. W. Colson, A. R. Woll, A. Mukherjee, M. P. Levendorf, E. L. Spitler, V. B. Shields, M. G. Spencer, J. Park, W. R. Dichtel, *Science* **2011**, *332*, 228-231.
- [17] E. L. Spitler, J. W. Colson, F. J. Uribe-Romo, A. R. Woll, M. R. Giovino, A. Saldivar, W. R. Dichtel, *Angew. Chem. Int. Ed. Engl.* **2012**, *51*, 2623-2627.
- [18] K. Dey, M. Pal, K. C. Rout, S. Kunjattu H, A. Das, R. Mukherjee, U. K. Kharul, R. Banerjee, *J. Am. Chem. Soc.* **2017**, *139*, 13083-13091.
- [19] M. Matsumoto, L. Valentino, G. M. Stiehl, H. B. Balch, A. R. Corcos, F. Wang, D. C. Ralph, B. J. Mari nas, W. R. Dichtel, *Chem* **2018**, *4*, 308-317.
- [20] R. P. Bisbey, C. R. DeBlase, B. J. Smith, W. R. Dichtel, *J. Am. Chem. Soc.* **2016**, *138*, 11433-11436.
- [21] D. D. Medina, J. M. Rotter, Y. Hu, M. Dogru, V. Werner, F. Auras, J. T. Markiewicz, P. Knochel, T. Bein, *J. Am. Chem. Soc.* **2015**, *137*, 1016-1019.

-
- [22] T. Sick, A. G. Hufnagel, J. Kampmann, I. Kondofersky, M. Calik, J. M. Rotter, A. Evans, M. Döblinger, S. Herbert, K. Peters, D. Böhm, P. Knochel, D. D. Medina, D. Fattakhova-Rohlfing, T. Bein, *J. Am. Chem. Soc.* **2018**, *140*, 2085-2092.
- [23] S.-L. Cai, Y.-B. Zhang, A. B. Pun, B. He, J. Yang, F. M. Toma, I. D. Sharp, O. M. Yaghi, J. Fan, S.-R. Zheng, W.-G. Zhang, Y. Liu, *Chem. Sci.* **2014**, *5*, 4693-4700.
- [24] I. J. Roh, A. R. Greenberg, V. P. Khare, *Desalination* **2006**, *191*, 279-290.
- [25] K. H. Mah, H. W. Yussof, M. N. A. Seman, A. W. Mohammad, *IOP Conference Series: Materials Science and Engineering* **2016**, 162.
- [26] S. Karan, Z. Jiang, A. G. Livingston, *Science* **2015**, *348*, 1347-1351.



3 Covalent organic frameworks as photosensitizers for photocatalytic hydrogen evolution

3.1 Summary

As stated before, COFs have been used as photosensitizers in the field of photocatalytic hydrogen evolution since 2014. Their evolution will be discussed in the following chapters. The first COF to be found to perform photocatalytic hydrogen evolution was the before-mentioned TFPT-COF followed by the N_x -COF series. Platinum nanoparticles were used as co-catalysts and sacrificial agents as triethanolamine (TEOA) or methanol as well as the solvent system were screened to find optimum working conditions for each individual system. This leads to hydrogen evolution rates of $1970 \mu\text{mol h}^{-1} \text{g}^{-1}$ for TFPT-COF with 10 vol% TEOA in water and $1703 \mu\text{mol h}^{-1} \text{g}^{-1}$ for N_3 -COF with 1 vol% TEOA in PBS-buffer at pH 7. In Chapter 3.2, the advances in the field will be stated and based on that, representative variables will be identified that need to be optimized to gain maximum efficiency in COF based photocatalytic hydrogen evolution systems. Those variables are the following: The robustness of the COF, which is mainly defined by its linkage stability, should be as high as possible. Good stacking and high crystallinity as well as porosity promotes the COFs activity. Both charge separation and axial charge transport need to be quick enough to prevent recombination. In-plane conjugation of the network supports good light harvesting ability. The interactions of the COF with the sacrificial electron donor as well as the co-catalyst need to be optimized.

In the second part of this project, the scope of proton reduction catalysts for COF photosensitizers was broadened significantly. We demonstrated the use of physisorbed molecular chloro(pyridine)cobaloxime co-catalysts with azine- and hydrazine-linked COFs. With N_2 -COF and TEOA as sacrificial donor, a hydrogen evolution rate of $782 \mu\text{mol h}^{-1} \text{g}^{-1}$ was achieved. By a combination of experimental results and quantum chemical calculations, a monometallic pathway of hydrogen evolution via an intermediate Co^{III} -hydride and/or Co^{II} -hydride species was identified. This leads way to an overall single-site, noble metal free COF-based photocatalytic system in a leaf-like architecture for solar fuel generation. Long-term stability of the system is still insufficient and needs to be addressed in further studies.

The last part of the project focused on the improvement of the interaction between the beforehand identified chloro(pyridine)cobaloxime co-catalyst and COF-42. For this purpose, the co-catalyst was functionalized with an azide group in different orientation (two

axial and one equatorial functionalization positions were realized) and COF-42 was modified by a copolymerization approach to carry propargyl units. This enabled the covalent attachment of the co-catalyst via Cu(I)-catalyzed click chemistry. The COF-co-catalyst hybrid shows improved and prolonged photocatalytic activity compared to the equivalent physisorbed system. By thorough analysis with a combination of solid-state NMR techniques and quantum chemical calculations, we found that a genuine interaction between the COF backbone and the co-catalyst facilitates the re-coordination of the cobaloxime during photocatalysis.

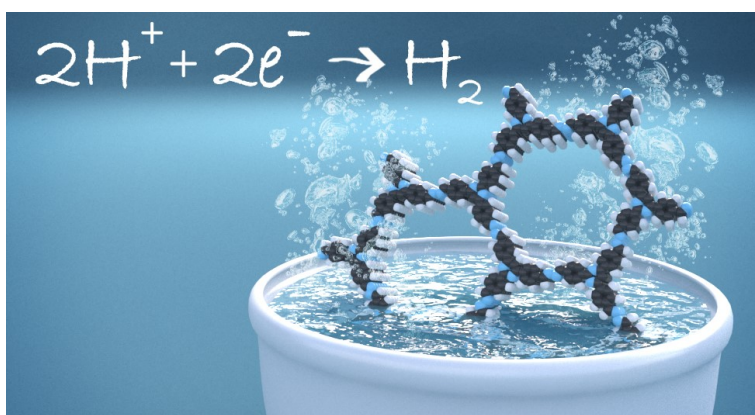
The concept of covalent hybridization of COFs and molecular hydrogen evolution co-catalysts for improved solar-fuel generation was developed and performed in the course of the presented thesis.

3.2 H₂ evolution with covalent organic framework photocatalysts

Tanmay Banerjee, Kerstin Gottschling, Gökçen Savasci, Christian Ochsenfeld, and Bettina V. Lotsch

published in
ACS Energy Lett., **2018**, 3(2), 400-409.
DOI: 10.1021/acseenergylett.7b01123
<https://pubs.acs.org/doi/abs/10.1021/acsenergylett.7b01123>
Formatting and numbering of figures were changed.
Adapted with permission from ACS

3.2.1 Abstract



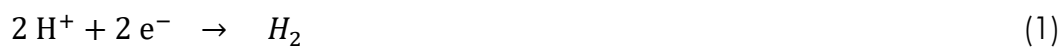
Covalent Organic Frameworks (COFs) are a new class of crystalline organic polymers that have garnered significant recent attention as highly promising H₂ evolution photocatalysts. The present article discusses the advances in this field of energy research while highlighting the

underlying peremptory factors for the rational design of the readily tunable COF backbone and hence optimal performance.

3.2.2 Introduction

Fossil fuels have been the driving force for economic growth in our world since the dawn of the industrial revolution. At present, more than 80% of the world energy requirement is derived from fossil fuels. However, overexploitation and hence the ever-increasing depletion of these natural resources, in addition to the anthropogenic climate change caused by the release of greenhouse gases by combustion of fossil fuels, is a matter of profound concern. Of the renewable alternative energy resources available, solar power is arguably the most promising one. However, solar energy is diffused and thus requires large collection areas for harvesting meaningful amounts. Also, solar energy is intermittent in nature. Thus, as a probable primary energy source, it would need to be coupled to energy storage mechanisms in an exceptional scale. In nature, photosynthesis converts solar energy into stored chemical energy in the form of carbohydrate fuels and oxygen. While too complex to duplicate in all its detail, it is an excellent inspiration to keep pace with the increasing energy demands on our planet, as it offers a blueprint for the design of artificial photosynthetic systems where the goal is to use (and hence convert) solar energy to make solar fuels like H₂ by driving

thermodynamically uphill chemical reactions like splitting of water (Figure 3-1), as shown in eq 1-3.^[1-9]



Under standard conditions, the free-energy change of 237.2 kJ/mol for the conversion of one molecule of water to H₂ and 1/2O₂ (eq 3) corresponds to $\Delta E = 1.23 \text{ V}$ per electron transferred. Thus, for a photosystem to drive this reaction upon photoexcitation, it must absorb light with photon energies $> 1.23 \text{ eV}$, corresponding to wavelengths $\sim \leq 1000 \text{ nm}$. This process should produce two and four electron-hole pairs per molecule of H₂ and O₂, respectively. An ideal photosystem, with its band gap larger than that required to split water, and with appropriately positioned conduction band and valence band energies with respect to E(H⁺/H₂) and E(O₂/H₂O), respectively, should be able to drive the hydrogen evolution (eq 1) and the oxygen evolution (eq 2) reactions using e⁻/h⁺ generated upon illumination. Honda and Fujishima were the first to report water splitting by band gap excitation of titanium dioxide in 1972.^[10] Substantial progress has been made in subsequent years, but the intense complications associated with the complete water-splitting reaction has led to only a handful of successful systems^[4] On the other hand, studying the oxidative and the reductive half reactions separately enables detailed investigations and optimizations and thus greatly facilitates the ultimate endeavor.

3.2.3 Results and discussion

A typical photocatalytic hydrogen production scheme (Figure 3-1) starts with absorption of light by the photosensitizer to generate electron-hole pairs. Charge separation occurs subsequently; a co-catalyst is usually added for carrying out the proton reduction reaction, while a sacrificial electron donor is added as a source of electrons, replacing water as a thermodynamically and kinetically challenging reducing agent. The sacrificial donor then regenerates the photosensitizer by undergoing irreversible decomposition and thus prevents back electron transfer. Direct photocatalytic hydrogen production following this mechanism has been explored under homogeneous conditions and using particulate photoabsorbers alike, each with their pros and cons. Molecular photocatalytic systems based on redox active metal complexes are highly tunable, but they are poorly stable and have comparatively low efficiencies.^[1, 11-14] Heterogeneous systems, on the other hand, have limited light-harvesting abilities and tunability.^[9, 15-18] However, they are robust and long-lived and show decent photocatalytic efficiencies.

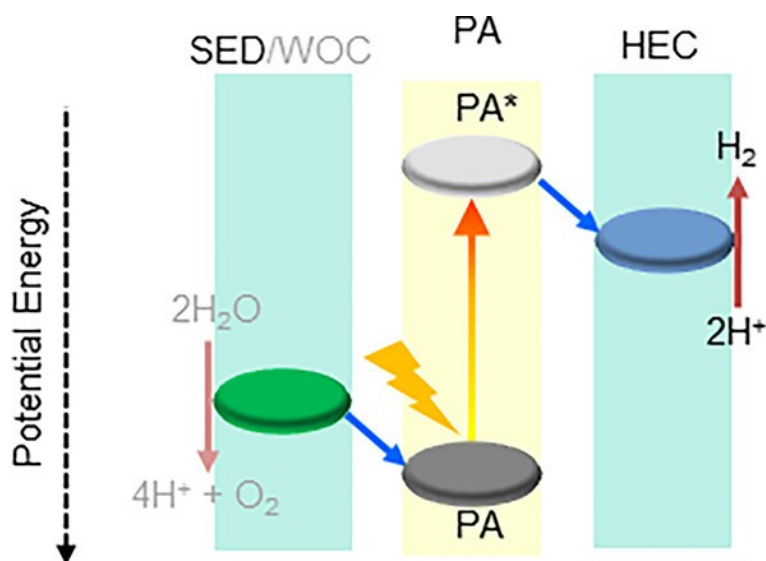


Figure 3-1: Artificial Photosynthetic Water Splitting. SED, sacrificial electron donor; WOC, water oxidation catalyst; PA, photoabsorber; HEC, hydrogen evolution catalyst.

The past few years have witnessed increasing interest in organic polymers for photocatalytic H_2 evolution, the study of which had been dominated by inorganic materials so far.^[17-20]

Graphitic carbon nitride, represented by Liebig's "Melon" is the most prominent example in this category.^[21-22] While it features good H_2 evolution activity, the scope for fine-tuning the structure and photophysical properties, and hence H_2 evolution activity, is rather limited and mechanistic insights are accordingly scarce.^[21-26] This is because carbon nitrides, made by polycondensation of the precursors at high temperatures, are mostly amorphous or semicrystalline 1D or 2D polymers with a large dispersity index. In addition, the molecular backbone of carbon nitrides is composed of either heptazine or triazine units, thus limiting their molecular tunability. The need to overcome these inherent limitations with carbon nitrides, while still retaining the well-defined molecular backbone in a heterogeneous system, marks the advent of covalent organic framework (COF) photocatalysis (Figure 3-2).

In 2005, Yaghi and co-workers showed the utility of topological design principles in reticulation of molecular building blocks via covalent bonds, to form *crystalline* COFs.^[27] COFs were thus a new class of highly porous organic polymers with 2D or 3D network topologies, similar to metal-organic frameworks, but composed solely of light elements and potentially more robust in nature. The suitably chosen functionalized molecular building units are linked to each other in a reversible fashion by thermodynamically controlled dynamic covalent chemistry.^[28-32] The reversibility in bond formation under the network-forming reaction conditions imparts self-healing ability for the repair of structural defects and facilitates reorganization of the framework structure to produce long-range order and crystallinity, not seen in typical organic polymers which are formed by kinetically driven, irreversible bond formation reactions such as C-C cross coupling.

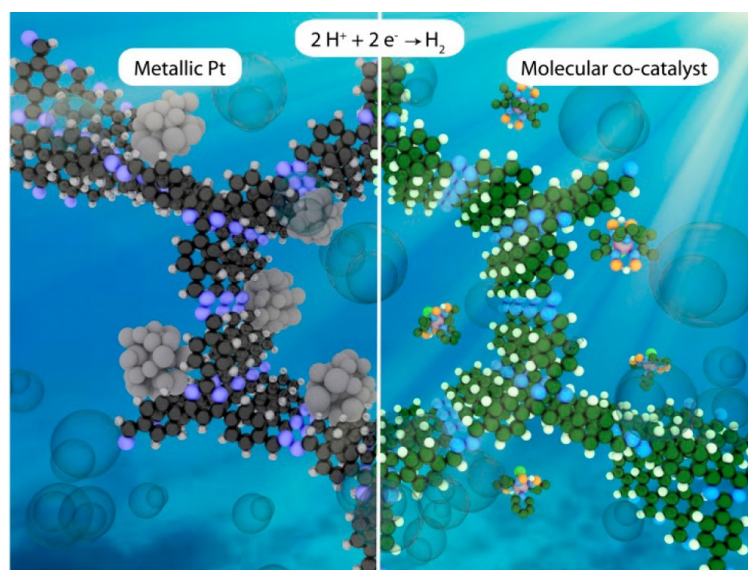


Figure 3-2: Photocatalytic H₂ evolution with metallic Pt (left) and molecular co-catalysts (right). The sacrificial electron donor molecules have been omitted for clarity.

COFs are one of the most significant discoveries pertaining to heterogeneous photocatalysis because (i) they are composed of molecular building blocks and hence possess almost unlimited chemical tunability of the different functions fundamental to the photocatalytic process, namely, light harvesting, charge separation, charge transport and electrocatalysis. (ii) They possess permanent, nanometer-sized structural pores which can be precisely tuned by choice of appropriate molecular building blocks and their reticulation. The high structural porosity entails high surface areas, enabling both rapid diffusion of charges to the surface and a very high interaction surface for enhanced accessibility of sensitizers, electrolytes, sacrificial components, and co-catalysts throughout the sample. (iii) Unlike molecular systems, the photoactive building blocks can be locked in a rigid architecture, and this can enhance the lifetimes of the excited states by preventing deactivation through collisions. Possible conjugation, both in-plane and in the stacking direction, can also contribute to increased charge carrier mobility. (iv) The crystallinity, in other words, the local and the long-range order in these systems, facilitates charge transport, can prevent recombination of charge carriers, and minimizes charge trapping at defect sites. (v) COFs are composed of covalent bonds and thus are very stable and robust. They are largely impermeable to solvents and, with appropriately chosen linking schemes, can be stable to hydrolysis, extremes of pH, and oxidative and reductive environments, and (vi) being composed of lightweight elements, COFs have an extremely low density and can offer high gravimetric performance. The exceptional blend of solid-state character together with modularity, porosity, and crystallinity

means that COFs actually have the potential to be avant-garde in photocatalysis research.^[18, 33-35]

In 2013, Jiang and co-workers synthesized a squaraine linked porphyrin COF featuring extended π -conjugation and charge-carrier mobility. With a 1,3-diphenylisobenzofuran label, this COF showed steady generation of singlet oxygen from molecular oxygen.^[36] Molecular oxygen being in the triplet state, this showed that a triplet excited state of the COF photocatalyst, which did not contain any noble metals, can be populated upon visible light excitation and can actually be harvested in a subsequent reaction.

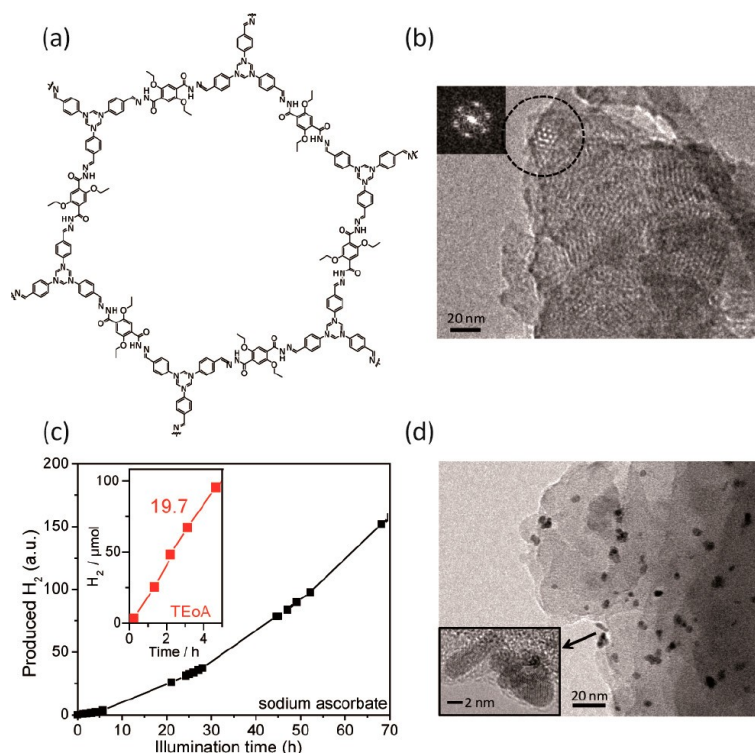


Figure 3-3: Molecular structure (a) of the TFPT-COF hexagonal pore as seen by TEM at 300 kV (b). Visible light-mediated H₂ evolution (c) with TFPT-COF using sodium ascorbate donor and Pt co-catalyst. The inset shows H₂ evolution using TEOA as an electron donor. Photodeposited Pt nanoparticles (d) on TFPT-COF after photocatalysis for 84 h. Adapted with permission from ref 36. Copyright 2014 Royal Society of Chemistry.

Indeed, this ability of COFs to harvest light energy laid the foundation for their development as platforms for photocatalytic hydrogen evolution. In 2014, we reported the first COF (Figure 3-3a) observed to produce H₂ in the presence of metallic platinum as the proton reduction catalyst when irradiated with visible light.^[37] The hydrazone-linked TFPT-COF, based on 1,3,5-tris(4-formyl-phenyl)triazine (TFPT) and 2,5-diethoxy-terephthalohydrazide building blocks, shows a much smaller dihedral angle of 7.7° between the central triazine and the peripheral phenyl rings as compared to its benzene analogue with a dihedral angle of 38.3°. This planarity of the molecular building block translates into a largely planar

structure, potentially enabling enhanced stacking interactions and thus charge transport in the axial direction as evident from the interlayer distance of 3.37 Å corresponding to typical van der Waals interactions between aromatic rings. The relatively small optical band gap of 2.8 eV enables significant light absorption in the visible region, thus rendering platinumized TFPT-COF an effective H₂-evolving photocatalytic system. With ascorbic acid as the sacrificial donor in water, H₂ evolved at a steady rate of 230 μmol h⁻¹ g⁻¹, and in 52 h (Figure 3-3c), the amount of H₂ produced was more than the amount of H₂ present in the COF itself, thus showing that H₂ production is photocatalytic and does not originate from the decomposition of the COF. The COF was also seen to be recyclable, at least three times, with no appreciable decrease in H₂ evolution activity. H₂ evolution at specific wavelengths of irradiation was found to follow the absorption spectrum of TFPT-COF, thus suggesting band gap excitation to be the source of charge carrier separation. H₂PtCl₆ was used as the platinum precursor, and TEM images of the COF post photocatalysis showed photodeposition of Pt nanoparticles of roughly 5 nm size (Figure 3-3d). While photoactivity was retained, the COF lost its crystallinity as seen in a 92 h postphotocatalysis sample, likely because of exfoliation in water. Interestingly though, the amorphous product filtered out of the photocatalysis reaction mixture could be reconverted to the crystalline and porous TFPT-COF by subjecting it to the original synthesis conditions without addition of new building blocks, thus suggesting that the connectivity of the COF remained intact throughout the catalytic conversion. The H₂ evolution activity could be improved by replacing the sacrificial electron donor ascorbic acid with triethanolamine (TEOA), however at an expense of a quicker deactivation of the COF. With 10 vol% TEOA, the H₂ evolution rate was 1970 μmol h⁻¹ g⁻¹ (Figure 3-3c) corresponding to a quantum efficiency of 2.2%. This rate was almost 3 times higher than those with benchmark photocatalytic systems such as Pt-modified amorphous melon,^[38] other carbon nitrides,^[39] and crystalline poly(triazine imide).^[38]

As discussed before, the most remarkable feature of COFs pertinent to photocatalysis research is their tunability down to the atomic level in an otherwise heterogeneous backbone.^[29-30, 32, 40] This was exemplified in the engineering of azine-linked N_x-COFs with triphenylaryl nodes for photocatalytic water reduction.^[41] Four COFs, with the number of nitrogen atoms in the central aryl ring increasing from 0 to 3, were synthesized by reaction of the corresponding aldehydes with hydrazine under reversible conditions (Figure 3-4a). Substitution of the C–H units with N atoms gradually decreased the dihedral angle between the central aryl ring and the peripheral phenyl rings in the COF nodes, thus increasing planarity. As a direct result, the peaks in the powder X-ray diffraction (PXRD) pattern become sharper and the stacking reflection at $2\theta = 26^\circ$ becomes more and more prominent along the series from N₀- to N₃-COF, thus indicating a gradual increase in crystallinity with

increasing nitrogen content (Figure 3-4b). This finding is significant in that it shows that a bulk property such as crystallinity can be controlled precisely by a modulation at the molecular, i.e., the building block level.

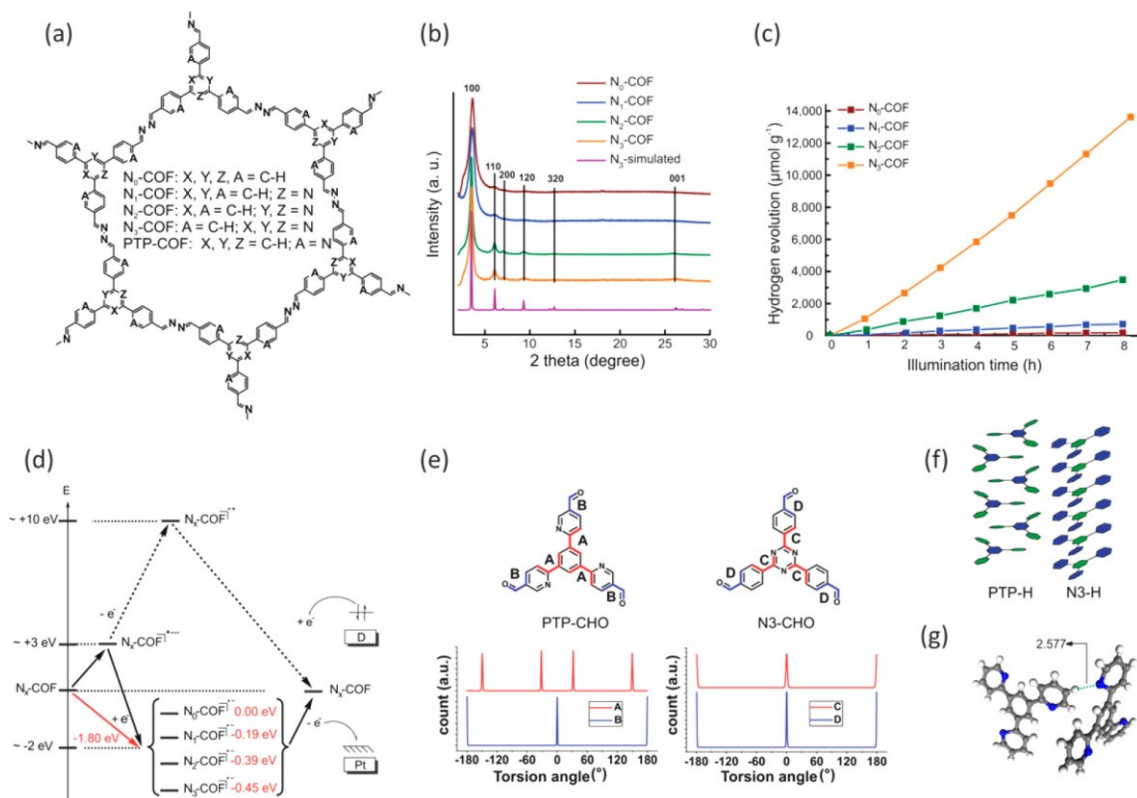


Figure 3-4: Molecular structure (a) of the hexagonal pore of N_x - and PTP-COF. For the N_x -COFs, the crystallinity increases gradually from N_0 - to N_3 -COF as seen in the PXRD pattern (b). The H_2 evolution rate with Pt co-catalyst and TEOA donor (c) analogously increases by 4 times for every additional N atom in the central aryl ring. The stability of the radical anion consistently increases (d) as one goes from N_0 - to N_3 -COF. Four different conformations are possible around torsion angle A in PTP-CHO (e) as opposed to only two around torsion angle C in N_3 -CHO. Additional D–A type interactions (f) and H-bonding interactions (g) can be seen in single-crystal structure solutions of PTP-H. All of these possibly contribute to the lower crystallinity of PTP-COF. Panels a–d are adapted with permission from [41]. Copyright 2015 by Nature Publishing Group. Panels e–g are adapted with permission from [42]. Copyright 2017 Royal Society of Chemistry.

The porosity of the COFs as measured by the BET surface area increased as well along this series, again reflecting the increasing degree of order with increasing nitrogen content. The increase in planarity and hence crystallinity can affect more facile exciton migration not only along the COF plane but also along the axial direction. The observed increase in planarity also leads to an obvious increase in electronic conjugation; however, with the simultaneous increase in the electron-deficient character of the central aryl ring acting against this trend, all four COFs were found to have essentially identical optical band gaps of around 2.6–2.7 eV. The light-harvesting ability of the COFs was therefore ruled out as a variable for the

photocatalytic water reduction activity which was studied under visible light irradiation using TEOA donor and photodeposited platinum nanoparticles as electrocatalyst. Interestingly, the H₂ evolution rate showed a 4-fold increase with each isolobal substitution of C–H with N atoms in the central aryl ring. Thus, the H₂ evolution rate increased from a mere 23 $\mu\text{mol h}^{-1} \text{g}^{-1}$ for N₀-COF to 90, 438, and finally to 1703 $\mu\text{mol h}^{-1} \text{g}^{-1}$ for N₁-, N₂-, and N₃-COFs, respectively (Figure 3-4c, Table 3-1). Unlike TFPT-COF, the postphotocatalysis samples did not show any significant structural change in the material; framework connectivity, structure, and crystallinity were nearly fully retained with only a slight loss in the long-range order. Also, upon replacing the sacrificial donor with ascorbic acid, long-term experiments with N₃-COF for over 120 h showed sustained H₂ evolution and thus evidence the remarkable stability of the COF under photocatalytic conditions.

Computational methods are a powerful tool in predicting and analyzing electronic properties of COF photocatalysts pertinent to their photocatalytic activity. Using representative semiextended model systems for the N_x-COF series, it was found that, in line with the observed H₂ evolution activities, the highest occupied molecular orbital (HOMO) was stabilized gradually from N₀- to N₃-COF, suggesting a progressive increase in the thermodynamic driving force for hole extraction by TEOA. The simultaneous decrease in the lowest unoccupied molecular orbital (LUMO) energy, however, indicated a gradual decrease in the driving force for electron transfer to Pt up the series, contrary to the increasing H₂ evolution rate.

Molecular orbital calculations in unit cells of N_x-COFs after optimization with periodic single-point conditions at the DFTB+/mio-1-0 level of theory reveal that the HOMO is localized only on the azine-linker moiety, thus suggesting it to be a possible hole-quenching site through hydrogen bonding interactions with TEOA. The LUMO was seen to be delocalized across the conjugated π system of the framework. For hydrazone-terminated model hexagons on the PBE0-D3/def2-SVP level of theory, electron affinities were of the order of -2 eV, rendering anionic quenching of the photoexcited COF as the likely reaction pathway. The ionization potential values were estimated to be very high, around $+10$ eV in vacuum. Thus, oxidative quenching of the photoexcited COF, i.e., the intermediate formation of a radical cationic COF by electron transfer to the co-catalyst, seems unlikely. Assuming the formation of the radical anion to be the rate-determining step in the overall photocatalytic process, the increasingly electron-poor character of the central aryl ring translated into a progressive increase in the stability of the radical anion, going from the N₀- to the N₃-COF model systems (Figure 3-4d), and this was found to be in line with the observed trend in the H₂ production activity of the COFs. Increased stability of the COF radical anion also suggests more effective charge separation. This highlights the importance of the interface between the COF and the electron donor, i.e., the necessity of efficient hole-



transfer reactivity by optimizing the COF–sacrificial donor interactions, for the design of a potent photocatalytic system.

Table 3-1: Summary of H₂ Evolution Activity of COF-Based Photocatalytic Systems.

COF	HEC	SED	other conditions	solvent	illumination	activity ($\mu\text{mol h}^{-1} \text{g}^{-1}$)	AQE	TON ^a	ref
TFPT-COF	Pt	1 wt% sodium ascorbate		water	>420 nm	230			36
TFPT-COF	Pt	10 vol % TEOA		water	>420 nm	1970	2.2–3.9% at 500 nm		36
N ₀ -COF	Pt	1 vol % TEOA		PBS buffer at pH 7	>420 nm	23	0.001% at 450 nm		40
N ₁ -COF	Pt	1 vol % TEOA		PBS buffer at pH 7	>420 nm	90	0.077% at 450 nm		40
N ₂ -COF	Pt	1 vol % TEOA		PBS buffer at pH 7	>420 nm	438	0.19% at 450 nm		40
N ₃ -COF	Pt	1 vol % TEOA		PBS buffer at pH 7	>420 nm	1703	0.44% at 450 nm		40
PTP-COF	Pt	1 vol % TEOA		PBS buffer at pH 7	AM 1.5	83.83			41
N ₂ -COF	Co-1 ^b	1 vol % TEOA	pH 8, 60 equ dmgH ₂	4:1 ACN/H ₂ O	AM 1.5	782	0.16% at 400 nm	54.4	60
N ₂ -COF	Co-2 ^c	1 vol % TEOA	pH 10	4:1 ACN/H ₂ O	AM 1.5	414		9.79	60
N ₁ -COF	Co-1	1 vol % TEOA	pH 8	4:1 ACN/H ₂ O	AM 1.5	100		2.03	60
N ₃ -COF	Co-1	1 vol % TEOA	pH 8	4:1 ACN/H ₂ O	AM 1.5	163		5.65	60
COF-42	Co-1	1 vol % TEOA	pH 8	4:1 ACN/H ₂ O	AM 1.5	233		5.79	60

a: Turnover number (TON) is based on the cobaloxime co-catalyst.

b: Co-1: [Co(dmgH)₂pyCl]. c: Co-2: Co(dmgBF₂)₂(OH)₂]

The complex interplay of structural, morphological, and electronic factors for photocatalytic H₂ evolution in COF-based systems is further demonstrated with PTP-COF, having the same

total number of N atoms as N₃-COF, but distributed instead on the peripheral rather than the central ring (Figure 3-4a).^[43] Under similar conditions as for the N_x-COFs, PTP-COF produces H₂ at a rate of only 83.83 μmol h⁻¹ g⁻¹ after an initial activation period corresponding to the photodeposition of Pt nanoparticles. The lower symmetry of PTP-COF, compared to that of N₃-COF, most likely leads to disorder in the former system due to a higher number of possible molecular conformations involving the torsion angle between the central and the peripheral aryl rings in the PTP nodes (Figure 3-4e). Such molecular arrangements could have a detrimental influence on the stacking interactions, thus causing stacking disorder. Further disorder can be induced into the PTP-system by a possible donor (phenyl)–acceptor (pyridyl) stacking interactions, as opposed to face-to-face interactions in the N₃- system (Figure 3-4f). Also, the higher basicity of pyridyl Ns in the PTP nodes, compared to that of the triazine Ns in the N₃-nodes, could lead to oligomers or molecules occluding the pores of PTP-COF (Figure 3-4g). As a consequence of a possible combination of these factors, the overall crystallinity of PTP-COF was seen to be very low as compared to that of N₃-COF, resulting in a BET surface area of only 84.21 m² g⁻¹ for the former, the theoretical surface area being 2147 m² g⁻¹. The low crystallinity and porosity further induce morphological changes: as compared to small, well-dispersible aggregates for N₃-COF, PTP-COF forms large spheres and macroscopic intergrown monoliths that are very hard to disperse in water during photocatalysis. Because dispersibility affects the efficiency of light absorption and scattering, the amount of COF photosensitizer needed to absorb all light now becomes a variable and puts comparison of the H₂ evolution rate with N₃-COF in perspective. Photophysical measurements and quantum chemical calculations call attention to additional factors responsible for the poor performance of PTP-COF: As compared to N₃-COF, measured fluorescence quantum yield and lifetime imply possibly a less efficient nonradiative deactivation of the photoexcited state of PTP-COF via charge-transfer pathways involved in H₂ evolution. That the nonradiative excited-state decay rates might actually correspond to these charge-transfer steps was confirmed in an analogous experiment where the emission quantum yield of PTP-COF was observed to be significantly lower and its luminescence decay significantly faster under photocatalytic conditions (i.e., with added TEOA and photodeposited Pt), compared to that in water. Interestingly, while all N_x-COFs have a band gap of around 2.6–2.7 eV, PTP-COF has a band gap of only 2.1 eV and thus a more extended absorption in the visible region. However, the undermining factors discussed above, which apparently challenge charge transport and the efficiency of light absorption in PTP-COF, seemingly emasculate this effect. In addition, from the calculations of frontier molecular orbitals for the PTP-CHO building block at the PBE0-D3/def2-TZVP level of theory, the HOMO and the LUMO were seen to have a similar spatial extent, thus rendering facile charge recombination another possible channel reducing the efficiency of



the photocatalytic system. In addition, the calculated vertical electron affinities of the N_x -CHO and the PTP-CHO units show that the anion radical of PTP-CHO is significantly destabilized compared to that of N_3 -CHO. This is because the pyridine moieties in the PTP motifs cannot stabilize the negative charges as effectively as the central triazine rings in the N_3 system.

It is thus evident that there are a myriad of variables that need to be modulated and orchestrated to have the “perfect” H_2 evolving COF photocatalyst. This includes structural factors such as crystallinity and porosity on the one hand and optoelectronic factors like charge separation, charge migration, charge recombination, and stability of the radical cationic or anionic intermediates on the other. Our research highlights the *structure–property–activity* relationship in such systems and accentuates the importance of the best possible optimization of the said factors for best performance. While these can be potential hurdles, they can be actually engineered to the desired extent at a molecular level in COFs, as mentioned at the beginning.

The development of robust COFs is the most basic step toward the development of photocatalytically active systems. In this context, it is important to remember that crystallinity in COFs is generated through *reversible* bond formation.^[29-30] Under conditions of dynamic covalent chemistry, bond breaking is thus as facile as the bond formation process, and stability and crystallinity act in opposite ways. The choice of the linkage in a COF, as well as the COF synthesis conditions (including choice of catalyst, solvent and temperature), is thus of significant importance, and linkages which are more prone to hydrolysis, such as boronic acid ones, might render the photocatalytic system unstable.^[30-31, 44] In that regard, supramolecular interactions to strengthen the intra- and interlayer interactions^[32, 45-48] and irreversible lock-in strategies such as post synthetic stabilization of crystalline COFs^[49] could be promising tactics to rigidify the framework with a desired complexity. The competition between stability and crystallinity quite reasonably generates COFs with structural disorder and defects,^[50-52] the roles of which in the charge-transfer processes during photocatalysis need to be explored in detail and precisely controlled, as this could be the key to establish a precise structure–property correlation.

COF as the photosensitizing scaffold has to be able to harvest light energy efficiently and transfer charges to the electrocatalyst. For optimal performance, this mandates extended absorption in the visible and near-infrared region while still maintaining the driving force necessary for proton reduction as well as the overpotential for electron transfer. Conjugation, in other words the delocalization of the π -electron system, both in the axial direction and *in-plane*, should lower the band gap and also render charge transport more efficient by quick dissipation of the excitation energy,^[53-54] thus emphasizing the importance of planar and conjugated chromophores as the building blocks. An appropriate choice of the linker is also

necessary for a fully conjugated COF layer. Achieving efficient charge separation is another challenge in such low dielectric constant polymers^[55] that typically show facile recombination of charges created upon photoexcitation. In that regard, our frontier molecular orbital calculations of model oligomeric systems indicate that electron-rich terminal groups could actually assist in charge separation.^[41] Another way to circumvent this issue would be to work with molecules having long-lived excited states to possibly increase the excited-state lifetimes of the COF. However, while systematic and thorough studies are yet to be done, our studies have generated examples where COFs with longer-lived excited states are less efficient as H₂ evolution photocatalysts.^[43] It must however be mentioned that it is very difficult to ascribe the H₂ evolution activity to a single variable, as discussed above.

The unique advantage of COFs over molecular systems is their ability to transport photogenerated charges efficiently, thus reducing the likelihood of recombination.^[56-57] An interesting research exemplifying the superior charge transport properties of COFs was reported by Banerjee and co-workers where the authors used the COF synthesized from 1,3,5-triformylphloroglucinol and 2,5-dimethyl-*p*-phenylenediamine as a support for CdS nanoparticles.^[58] For a CdS:COF ratio of 90:10, the authors observed a H₂ evolution rate of 3678 $\mu\text{mol h}^{-1} \text{g}^{-1}$, which was ascribed by emission quenching experiments and Mott–Schottky measurements to an efficient transport of the photogenerated electrons from the CdS photosensitizer via the COF layers, which further prevented charge recombination losses seen in bare CdS. A H₂ evolution rate of only 128 $\mu\text{mol h}^{-1} \text{g}^{-1}$ was observed for CdS alone under the same conditions. In more general terms, the charge transport and the carrier mobilities can be maximized in a COF by improving the overall crystallinity; by refining stacking interactions for optimal overlap of π -orbitals in the axial direction; and by increasing in-plane conjugation preferably with precursors having high native charge carrier mobilities, such as thiophene, perylene, etc.

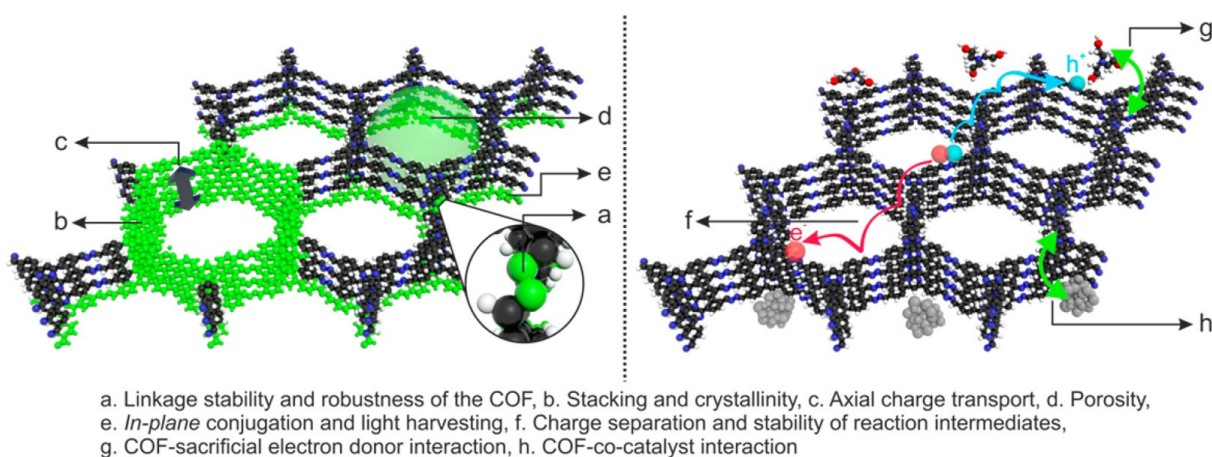


Figure 3-5: Representative variables that need to be optimized for maximizing photocatalytic H₂ evolution efficiency of COF-based systems



Optimization of the interaction of the COF with the sacrificial electron donor is necessary as well for optimal H₂ evolution photocatalysis (Figure 3-5). The appropriate choice of the donor could be very specific for a particular COF photosensitizer and has to be optimized for high cage escape yields (for reductive quenching) and faster degradation than charge recombination, in addition to the solvent, pH, concentrations, etc.^[59] While quantum chemical calculations point to a reductive quenching mechanism in the azine-based COF photocatalytic systems developed by us,^[41] a thorough photophysical investigation of the mechanism and identification of the reaction intermediates is necessary. This could be all the more important because of the possible role of these Lewis basic electron donors in some other steps in the intricate photocatalytic cycle or its possible role in poisoning the nanoparticulate electrocatalysts.

Optimization of the COF–electrocatalyst interface would be equally important for efficient H₂ evolution photocatalysis (Figure 3-5). This is because without an added electrocatalyst, COFs have not yet been observed to produce H₂. While charge recombination is an aspect, the major factor seems to be the kinetic overpotential associated with the charge-transfer and bond formation processes for H₂ evolution. Thus, in the absence of dedicated catalytic sites right at the COF backbone, suitable co-catalysts for hydrogen evolution need to be identified. Metallic Pt, with a large work function and a low Fermi level, is traditionally employed as the electron sink to trap electrons from the COF.^[60] It further provides effective proton reduction sites and makes H₂ formation facile. In this regard, coordination sites for platinum on the COF backbone might lead to more specific interaction of platinum with the COF and can result in improved charge transfer. This was observed in studies with phenyl-triazine oligomers (PTOs) where the smaller oligomers were observed to be more efficient H₂ evolution photocatalysts because of the increased number of terminal nitrile moieties which possibly act as coordination sites for platinum while also assisting in the dispersion of the photocatalyst by H-bonding.^[61] Unfortunately, platinum is an extremely rare element and hence very expensive. In the long run, it thus needs to be replaced with co-catalysts based on earth-abundant nonprecious elements.^[11-12] In our recent work we demonstrated the feasibility of this approach using N_x-COFs and the hydrazone-based COF-42 as photosensitizers and a series of molecular cobaloxime co-catalysts as biomimetic hydrogenase mimics (Figure 3-6a,b, Table 3-1).^[62] Composed entirely of molecular building blocks, this system represents the first single-site heterogeneous COF photocatalyst with a unique level of molecular tunability. H₂ evolution activity was found to be dependent on the solvent used, and acetonitrile was observed to be important for better performance. Further dependencies on reaction pH, choice of sacrificial donor, and the crystallinity and porosity of the COF were noted. Using N₂-COF as the photosensitizer and chloro(pyridine)-cobaloxime co-catalyst, H₂ evolution rates as high as 782 μmol h⁻¹ g⁻¹ were obtained,

corresponding to an apparent quantum efficiency (AQE) of 0.16% at 400 nm. The H₂ evolution rates were comparable to the previously discussed benchmark photocatalytic systems like Pt-modified amorphous melon,^[38] other graphitic carbon nitrides,^[39] and crystalline poly(triazine imide) (PTI).^[38] The turnover number (TON) was 54.4 at 20 h. Interestingly, for the same mol % of metallic Pt as the cobaloxime catalyst **Co-1**, a three times lower H₂ evolution rate was observed with the former when measured under the same conditions in 4:1 acetonitrile/water. However, the H₂ evolution rate of N₂-COF with Pt co-catalyst was more than 8 times higher in water than in 4:1 acetonitrile/water, and a poorer distribution of Pt nanoparticles on the COF surface and/or a poorer photodeposition from the hexachloroplatinic acid precursor in the latter solvent was observed to be the probable reason. Photodeposition of Pt nanoparticles,^[63] their distribution on the COF surface, as well as the sizes of the nanoparticle clusters, only the surface atoms of which are catalytically active, thus are important factors that affect the H₂ evolution rate in such cases and will need to be optimized.

The decisive role of the kinetics and thermodynamics of the charge-transfer processes between the COF photosensitizer and the co-catalyst was illustrated in the lower H₂ evolution rate with N₃-COF than N₂-COF, using **Co-1** co-catalyst (Figure 3-6b). With molecular co-catalysts, an important advantage will be the possibility of studying the photocatalytic processes in detail and resolving the reaction intermediates experimentally to further fine-tune the photocatalytic activity of the hybrid system. Using COF-42 photosensitizer and **Co-1** co-catalyst, successive reduction of Co^{III} to Co^{II} and then to Co^I and/or the final formation of the possible H₂ evolving Co^{III}-H species could be verified (Figure 3-6c,d). The Co^{III}-H and/or Co^{II}-H species were further observed to produce H₂ in a heterolytic pathway (Figure 3-6e). Characterization of the H₂ evolving species and optimization of its integrity during photocatalysis with molecular co-catalysts will be important. This is because many molecular co-catalysts are known to be photoreduced to the corresponding metallic species during photocatalysis which instead act as the heterogeneous H₂-evolving species.^[64] Furthermore, the deactivation of the catalyst, for example by formation of cobalt oxide from cobaloximes, could be a limiting factor in the long run.^[20] With co-catalysts like cobaloximes featuring labile ligands and the molecular heterogeneous structure of COFs having potential coordinating framework atoms, it is important to probe whether the complex actually binds to the COF, because if it binds it can mediate an inner sphere electron transfer to the catalyst. As studied for the N₂-COF system with **Co-1** co-catalyst, we could confirm that neither metallic Co nor cobalt oxide nanoparticles were formed during photocatalysis, nor does the catalyst bind chemically to the COF at any stage during photocatalysis. Improving upon this weak and nonspecific interaction between the co-catalyst and the COF by covalently binding the two could be the next step forward. A more directional binding is expected to optimize

the kinetics of electron transfer to the co-catalyst and surpass the diffusion-controlled limits. Our work also shows that the simpler path of optimizing the COF and the co-catalyst as independent modules has potential as well. With molecular co-catalysts the biggest challenge is however the search for a system that is stable and has limited photodecomposition over time.

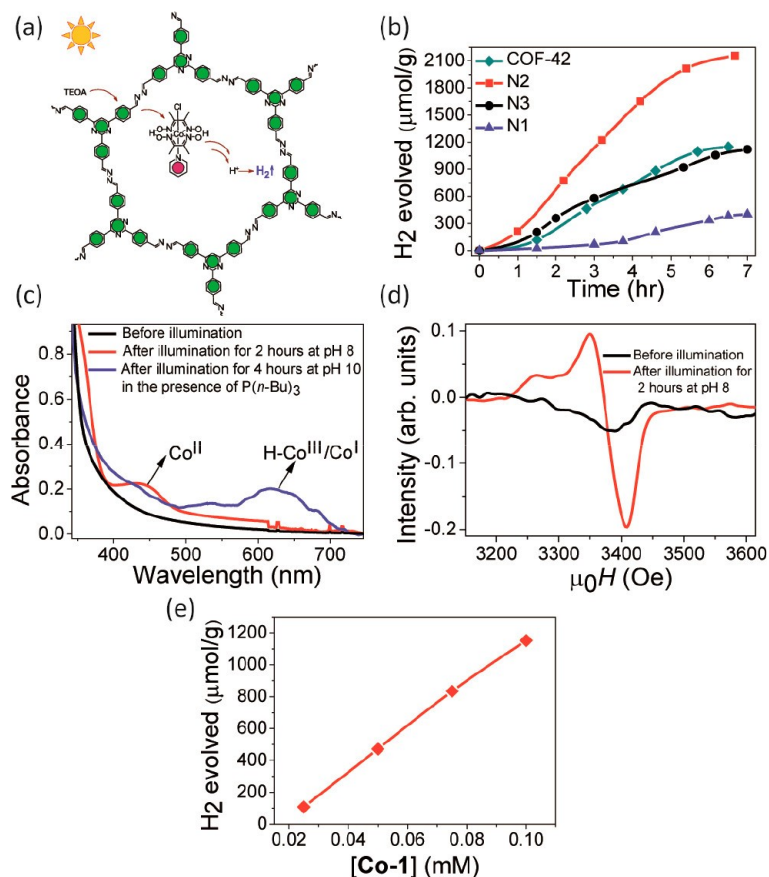


Figure 3-6: (a) Photocatalytic H₂ evolution with N₂-COF and **Co-1**, (b) H₂ evolution rates with the N_x-COFs and with COF-42 photosensitizers using **Co-1** co-catalyst and TEOA donor, and (c) spectrophotometrically monitoring the reduced Co^{II} state and subsequent formation of the Co^I and/or H-Co^{III} state using COF-42 and **Co-1** co-catalyst. (d) The paramagnetic Co^{II} state formed during photocatalysis can be observed in the X-band EPR spectrum. (e) The Co^{III}-H and/or the Co^{II}-H species are shown to produce H₂ by a heterolytic pathway involving a single cobalt center in the reaction involving N₂-COF and **Co-1** co-catalyst. Reprinted from [60]. Copyright 2017 American Chemical Society.

3.2.4 Conclusion

In conclusion, the molecular and hence the modular nature of the heterogeneous COF backbone creates enormous prospects for H₂ evolution photocatalysis as demonstrated by the first promising steps outlined above. However, these results mark just the beginning of a prospering area of research, and every aspect of these complex architectures needs to be scrutinized to push the limits of COF photocatalysis further. Optimization of the solid-state factors such as robustness, crystallinity, porosity, and defect engineering of COFs will be

important and are expected to ameliorate the desired *bottom-up* design for enhancing the light-harvesting and charge transport properties of such materials (Scheme 3). Thus, the development of this field will be driven by the overall progress in COF research; its success will be contingent on our ability to engineer ordered complexity within a stable, photoactive COF framework.

The authors declare no competing financial interest.

3.2.5 Acknowledgment

Financial support was provided by an ERC Starting Grant (Project COF Leaf, Grant Number 639233), the Max Planck Society, the cluster of excellence Nanosystems Initiative Munich, and the Center for Nanoscience (CeNS). C.O. acknowledges financial support by the excellence cluster EXC114 (DFG).

3.2.6 Author contributions

Tanmay Banerjee wrote the manuscript. Kerstin Gottschling edited the figures and helped writing the manuscript. Gökçen Savasci helped writing the manuscript. Christian Ochsenfeld and Bettina V. Lotsch supervised the project. All authors worked on and revised the manuscript.

3.2.7 References

- [1] S. Berardi, S. Drouet, L. Francàs, C. Gimbert-Suriñach, M. Guttentag, C. Richmond, T. Stoll, A. Llobet, *Chem. Soc. Rev.* **2014**, *43*, 7501-7519.
- [2] Y. Tachibana, L. Vayssieres, J. R. Durrant, *Nature Photonics* **2012**, *6*, 511.
- [3] T. Jafari, E. Moharreri, A. S. Amin, R. Miao, W. Song, S. L. Suib, *Molecules* **2016**, *21*, 900.
- [4] S. Chen, T. Takata, K. Domen, *Nature Reviews Materials* **2017**, *2*, 17050.
- [5] C. Jiang, S. J. A. Moniz, A. Wang, T. Zhang, J. Tang, *Chem. Soc. Rev.* **2017**, *46*, 4645-4660.
- [6] I. Roger, M. A. Shipman, M. D. Symes, *Nature Reviews Chemistry* **2017**, *1*, 0003.
- [7] X. Li, X. Hao, A. Abudula, G. Guan, *Journal of Materials Chemistry A* **2016**, *4*, 11973-12000.
- [8] M. K. Brennaman, R. J. Dillon, L. Alibabaei, M. K. Gish, C. J. Dares, D. L. Ashford, R. L. House, G. J. Meyer, J. M. Papanikolas, T. J. Meyer, *J. Am. Chem. Soc.* **2016**, *138*, 13085-13102.
- [9] P. D. Tran, L. H. Wong, J. Barber, J. S. C. Loo, *Energy & Environmental Science* **2012**, *5*, 5902-5918.
- [10] A. Fujishima, K. Honda, *Nature* **1972**, *238*, 37-38.
- [11] P. Du, R. Eisenberg, *Energy & Environmental Science* **2012**, *5*, 6012-6021.
- [12] W. T. Eckenhoff, W. R. McNamara, P. Du, R. Eisenberg, *Biochimica et Biophysica Acta (BBA) - Bioenergetics* **2013**, *1827*, 958-973.
- [13] F. Wang, W.-G. Wang, H.-Y. Wang, G. Si, C.-H. Tung, L.-Z. Wu, *ACS Catalysis* **2012**, *2*, 407-416.
- [14] E. Deponti, M. Natali, *Dalton Transactions* **2016**, *45*, 9136-9147.



- [15] R. D. Tentu, S. Basu, *Current Opinion in Electrochemistry* **2017**, *5*, 56-62.
- [16] H. Ahmad, S. K. Kamarudin, L. J. Minggu, M. Kassim, *Renewable and Sustainable Energy Reviews* **2015**, *43*, 599-610.
- [17] G. Zhang, Z.-A. Lan, X. Wang, *Angew. Chem. Int. Ed.* **2016**, *55*, 15712-15727.
- [18] V. S. Vyas, V. W.-h. Lau, B. V. Lotsch, *Chem. Mater.* **2016**, *28*, 5191-5204.
- [19] C. B. Meier, R. S. Sprick, A. Monti, P. Guiglion, J.-S. M. Lee, M. A. Zwijnenburg, A. I. Cooper, *Polymer* **2017**, *126*, 283-290.
- [20] S.-W. Cao, X.-F. Liu, Y.-P. Yuan, Z.-Y. Zhang, J. Fang, S. C. J. Loo, J. Barber, T. C. Sum, C. Xue, *PCCP* **2013**, *15*, 18363-18366.
- [21] W.-J. Ong, L.-L. Tan, Y. H. Ng, S.-T. Yong, S.-P. Chai, *Chem. Rev.* **2016**, *116*, 7159-7329.
- [22] S. Cao, J. Low, J. Yu, M. Jaroniec, *Adv. Mater.* **2015**, *27*, 2150-2176.
- [23] K. L. Corp, C. W. Schlenker, *J. Am. Chem. Soc.* **2017**, *139*, 7904-7912.
- [24] J. Ehrmaier, T. N. V. Karsili, A. L. Sobolewski, W. Domcke, *The Journal of Physical Chemistry A* **2017**, *121*, 4754-4764.
- [25] V. W.-h. Lau, V. W.-z. Yu, F. Ehrat, T. Botari, I. Moudrakovski, T. Simon, V. Duppel, E. Medina, J. K. Stolarczyk, J. Feldmann, V. Blum, B. V. Lotsch, *Advanced Energy Materials* **2017**, *7*, 1602251.
- [26] V. W.-h. Lau, I. Moudrakovski, T. Botari, S. Weinberger, M. B. Mesch, V. Duppel, J. Senker, V. Blum, B. V. Lotsch, *Nature Communications* **2016**, *7*, 12165.
- [27] A. P. Côté, A. I. Benin, N. W. Ockwig, M. O'Keeffe, A. J. Matzger, O. M. Yaghi, *Science* **2005**, *310*, 1166-1170.
- [28] C. S. Diercks, O. M. Yaghi, *Science* **2017**, *355*, eaal1585.
- [29] J. Jiang, Y. Zhao, O. M. Yaghi, *J. Am. Chem. Soc.* **2016**, *138*, 3255-3265.
- [30] X. Feng, X. Ding, D. Jiang, *Chem. Soc. Rev.* **2012**, *41*, 6010-6022.
- [31] S.-Y. Ding, W. Wang, *Chem. Soc. Rev.* **2013**, *42*, 548-568.
- [32] N. Huang, P. Wang, D. Jiang, *Nature Reviews Materials* **2016**, *1*, 16068.
- [33] T. Banerjee, T. Bennett, K. Butler, T. L. Easun, M. Eddaoudi, R. Forgan, L. Gagliardi, C. Hendon, M. Jorge, C. Lamberti, J.-S. M. Lee, K. Leus, J. Li, W. Lin, M. Ranocchiari, N. Rosi, J. G. Santaclara, S. Shevlin, K. Svane, V. Ting, M. van der Veen, P. Van Der Voort, A. Walsh, D. Woods, O. M. Yaghi, G. Zhu, *Faraday Discuss.* **2017**, *201*, 87-99.
- [34] S. Nandi, S. K. Singh, D. Mullangi, R. Illathvalappil, L. George, C. P. Vinod, S. Kurungot, R. Vaidhyanathan, *Advanced Energy Materials* **2016**, *6*, 1601189.
- [35] D. Mullangi, V. Dhavale, S. Shalini, S. Nandi, S. Collins, T. Woo, S. Kurungot, R. Vaidhyanathan, *Advanced Energy Materials* **2016**, *6*, 1600110.
- [36] A. Nagai, X. Chen, X. Feng, X. Ding, Z. Guo, D. Jiang, *Angew. Chem. Int. Ed.* **2013**, *52*, 3770-3774.
- [37] L. Stegbauer, K. Schwinghammer, B. V. Lotsch, *Chemical Science* **2014**, *5*, 2789-2793.
- [38] K. Schwinghammer, B. Tuffy, M. B. Mesch, E. Wirnhier, C. Martineau, F. Taulelle, W. Schnick, J. Senker, B. V. Lotsch, *Angew. Chem. Int. Ed.* **2013**, *52*, 2435-2439.
- [39] J. Zhang, X. Chen, K. Takane, K. Maeda, K. Domen, J. D. Epping, X. Fu, M. Antonietti, X. Wang *Angew. Chem. Int. Ed.* **2010**, *49*, 441-444.
- [40] R. P. Bisbey, W. R. Dichtel, *ACS Central Science* **2017**, *3*, 533-543.
- [41] V. S. Vyas, F. Haase, L. Stegbauer, G. Savasci, F. Podjaski, C. Ochsenfeld, B. V. Lotsch, *Nat Commun* **2015**, *6*.

- [42] F. Haase, T. Banerjee, G. Savasci, C. Ochsenfeld, B. V. Lotsch, *Faraday Discuss.* **2017**, *201*, 247-264.
- [43] F. Haase, T. Banerjee, G. Savasci, C. Ochsenfeld, B. V. Lotsch, *Faraday Discuss.* **2017**, *201*, 247-264.
- [44] C. R. DeBlase, W. R. Dichtel, *Macromolecules* **2016**, *49*, 5297-5305.
- [45] X. Chen, M. Addicoat, S. Irle, A. Nagai, D. Jiang, *J. Am. Chem. Soc.* **2013**, *135*, 546-549.
- [46] S. Kandambeth, D. B. Shinde, M. K. Panda, B. Lukose, T. Heine, R. Banerjee, *Angew. Chem. Int. Ed.* **2013**, *52*, 13052-13056.
- [47] X. Chen, M. Addicoat, E. Jin, L. Zhai, H. Xu, N. Huang, Z. Guo, L. Liu, S. Irle, D. Jiang, *J. Am. Chem. Soc.* **2015**, *137*, 3241-3247.
- [48] S. Kandambeth, A. Mallick, B. Lukose, M. V. Mane, T. Heine, R. Banerjee, *J. Am. Chem. Soc.* **2012**, *134*, 19524-19527.
- [49] P. J. Waller, S. J. Lyle, T. M. Osborn Popp, C. S. Diercks, J. A. Reimer, O. M. Yaghi, *J. Am. Chem. Soc.* **2016**, *138*, 15519-15522.
- [50] B. Lukose, A. Kuc, T. Heine, *Chemistry – A European Journal* **2011**, *17*, 2388-2392.
- [51] N. A. A. Zwaneveld, R. Pawlak, M. Abel, D. Catalin, D. Gimes, D. Bertin, L. Porte, *J. Am. Chem. Soc.* **2008**, *130*, 6678-6679.
- [52] R. Gutzler, H. Walch, G. Eder, S. Klotz, W. M. Heckl, M. Lackinger, *Chem. Commun.* **2009**, 4456-4458.
- [53] C. Butchosa, T. O. McDonald, A. I. Cooper, D. J. Adams, M. A. Zwiijnenburg, *The Journal of Physical Chemistry C* **2014**, *118*, 4314-4324.
- [54] J. Guo, Y. Xu, S. Jin, L. Chen, T. Kajii, Y. Honsho, M. A. Addicoat, J. Kim, A. Saeki, H. Ihee, S. Seki, S. Irle, M. Hiramoto, J. Gao, D. Jiang, *Nat Commun* **2013**, *4*.
- [55] D. D. Medina, M. L. Petrus, A. N. Jumabekov, J. T. Margraf, S. Weinberger, J. M. Rotter, T. Clark, T. Bein, *ACS Nano* **2017**, *11*, 2706-2713.
- [56] X. Ding, J. Guo, X. Feng, Y. Honsho, J. Guo, S. Seki, P. Maitarad, A. Saeki, S. Nagase, D. Jiang, *Angew. Chem. Int. Ed.* **2011**, *50*, 1289-1293.
- [57] S. Wan, F. Gándara, A. Asano, H. Furukawa, A. Saeki, S. K. Dey, L. Liao, M. W. Ambrogio, Y. Y. Botros, X. Duan, S. Seki, J. F. Stoddart, O. M. Yaghi, *Chem. Mater.* **2011**, *23*, 4094-4097.
- [58] J. Thote, H. B. Aiyappa, A. Deshpande, D. Díaz Díaz, S. Kurungot, R. Banerjee, *Chemistry – A European Journal* **2014**, *20*, 15961-15965.
- [59] Y. Pellegrin, F. Odobel, *Comptes Rendus Chimie* **2017**, *20*, 283-295.
- [60] J. Yang, D. Wang, H. Han, C. Li, *Acc. Chem. Res.* **2013**, *46*, 1900-1909.
- [61] K. Schwinghammer, S. Hug, M. B. Mesch, J. Senker, B. V. Lotsch, *Energy & Environmental Science* **2015**, *8*, 3345-3353.
- [62] T. Banerjee, F. Haase, G. Savasci, K. Gottschling, C. Ochsenfeld, B. V. Lotsch, *J. Am. Chem. Soc.* **2017**, *139*, 16228-16234.
- [63] Z. Jiang, Z. Zhang, W. Shangguan, M. A. Isaacs, L. J. Durndell, C. M. A. Parlett, A. F. Lee, *Catalysis Science & Technology* **2016**, *6*, 81-88.
- [64] P. Lei, M. Hedlund, R. Lomoth, H. Rensmo, O. Johansson, L. Hammarström, *J. Am. Chem. Soc.* **2008**, *130*, 26-27.

3.3 Single site photocatalytic H₂ evolution from covalent organic frameworks with molecular cobaloxime co-catalysts

Tanmay Banerjee, Frederik Haase, Gökçen Savasci, Kerstin Gottschling, Christian Ochsenfeld, and Bettina V. Lotsch

published in

J. Am. Chem. Soc. **2017**, *139*, 16228-16234

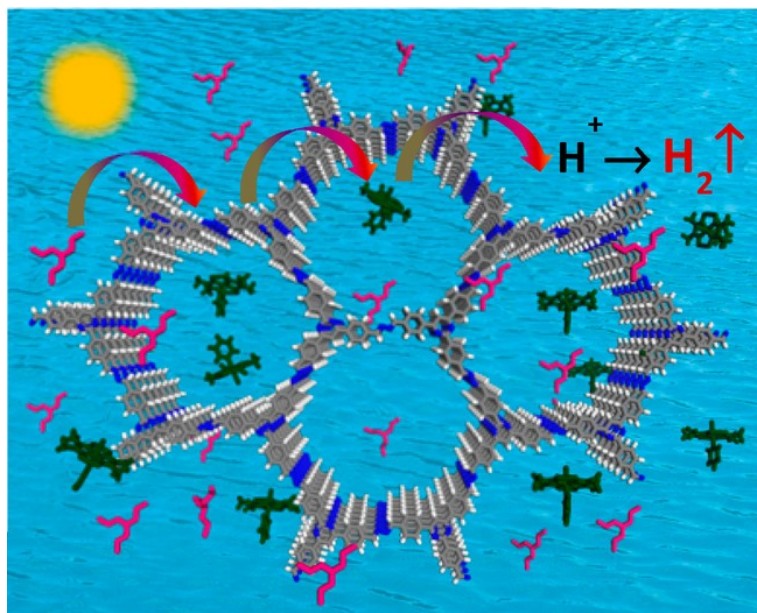
DOI: 10.1021/jacs.7b07489

<https://pubs.acs.org/doi/10.1021/jacs.7b07489>

Formatting and numbering of figures were changed.

Adapted with permission from ACS

3.3.1 Abstract



We demonstrate photocatalytic hydrogen evolution using COF photosensitizers with molecular proton reduction catalysts for the first time. With azine-linked N₂-COF photosensitizer, chloro-(pyridine)cobaloxime co-catalyst, and TEOA donor, H₂ evolution rate of 782 $\mu\text{mol g}^{-1} \text{h}^{-1}$ and TON of 54.4 has been obtained in a water/acetonitrile mixture. PXRD, solid-state spectroscopy,

EM analysis, and quantum chemical calculations suggest an outer sphere electron transfer from the COF to the co-catalyst which subsequently follows a monometallic pathway of H₂ generation from the Co^{III}-hydride and/or Co^{II}-hydride species.

3.3.2 Introduction

With fossil fuel reserves dwindling every day, there is an urgent need for clean and sustainable alternative energy sources. Artificial photosynthesis, the conversion of solar energy into energy stored in the bonds of “solar fuels” like hydrogen, could be one of the most viable and nonintermittent solution in this regard.^[1-2] Development of efficient photocatalytic systems for hydrogen evolution via photoinduced water splitting is thus a very active field of energy research. In this context, covalent organic frameworks (COFs) have recently emerged as a new class of photoactive materials for light-induced hydrogen evolution.^[3] Similar to related polymeric carbon nitrides, but even more so, COFs are modular, versatile, and adaptive as they are characterized by an easy tunability of

(opto)electronic properties, structure, crystallinity, and porosity.^[4-5] In addition, COFs are solely composed of light elements and thus have enormous prospects as earth-abundant and synthetically versatile platforms for modular, heterogeneous photocatalysis.^[2-6] The π -electron conjugation in-plane together with the possibility of axial charge transport in the stacking direction by the overlap of π -orbitals can result in high charge carrier mobilities, thus making COFs promising supramolecular architectures for efficient light harvesting and charge transport.^[7-8] Already, even with the very limited number of reports of H₂ evolution with COFs, hydrogen evolution rates as high as 1700 $\mu\text{mol g}^{-1} \text{h}^{-1}$ have been achieved.^[9-12] However, in all such studies platinum has been used as the co-catalyst to reduce the overpotential of H₂ generation. Despite the excellent activity of metallic platinum, it is rare and expensive and should thus be replaced by earth-abundant, non-precious-metal-based co-catalysts in the long run.^[13-15] The combination of a COF as the molecularly defined photoabsorber with an earth-abundant molecular co-catalyst could provide a highly tunable, single-site heterogeneous photocatalytic platform which is fully accessible to the toolbox of organic synthesis. It would thus be an important steppingstone toward sustainable and inexpensive photocatalytic systems. However, development of such a system is challenging because of the limited photostability of molecular co-catalysts and generally slow multielectron diffusion-controlled proton reduction processes which need to be coupled efficiently to the light-harvesting and charge-percolation processes on the COF.

We report here, for the first time, light-induced proton reduction catalysis with COFs using cobaloximes as noble-metal-free molecular co-catalysts (Figure 3-7). Efficient hydrogen evolution is seen with an azine-linked COF (N₂) and a chloro(pyridine)cobaloxime co-catalyst (**Co-1**) in the presence of triethanolamine (TEOA) as a sacrificial electron donor in a water/acetonitrile mixture under AM 1.5 illumination. The methodology can also be extended to other azine- and hydrazone-based COFs and other cobaloximes as co-catalysts. The results lead way to the development of efficient and robust, noble-metal-free, single-site heterogenized systems for artificial photosynthesis that offer a precise control over the nature, density, and arrangement of the photocatalytically active sites.

3.3.3 Results and discussion

Photocatalysis

The azine-based N_x-COFs were chosen as the photoabsorber, owing to their robustness and efficient hydrogen evolution activity with metallic platinum.^[16] All our primary investigations have been carried out with N₂-COF (Figure 3-7) because of a relatively easier synthesis protocol as compared to that of the most active member of the series, N₃-COF.

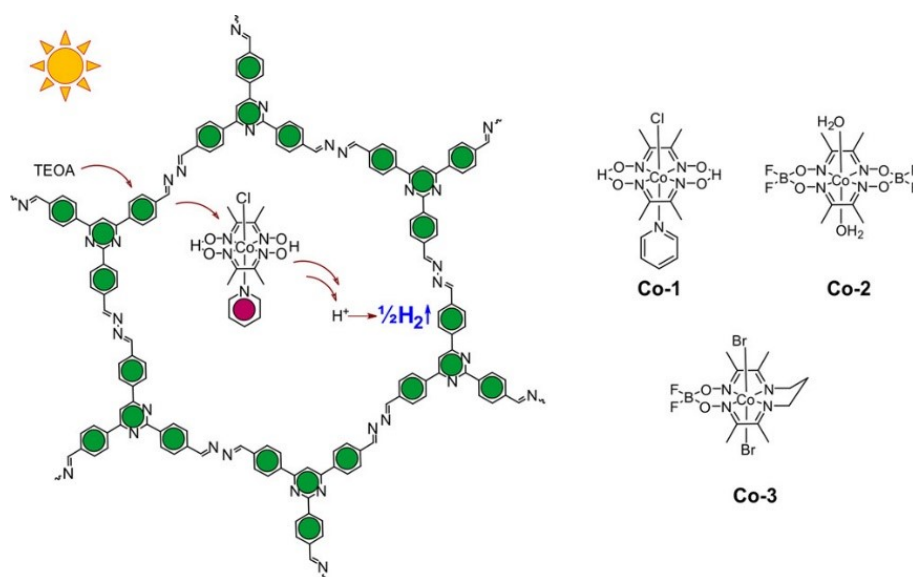


Figure 3-7: Structures of N₂-COF and the cobaloxime co-catalysts used in this study. Schematic representation of photocatalytic H₂ evolution with N₂-COF and Co-1 is shown on the left.

Of the different transition metal based co-catalysts reported for proton transfer catalysis, cobalt complexes with dimethylglyoxime ligands, also known as cobaloximes, are among the most efficient. They feature low overpotentials for H₂ generation, easy synthesis, and oxygen tolerance, and can be easily incorporated covalently into natural and artificial photocatalytic systems.^[14-15, 17] Cobaloximes have been used as earth abundant molecular H₂ evolution co-catalysts, e. g., with MOF^[18] and carbon nitride photosensitizers.^[19-20] We thus chose the complex chloro(pyridine)cobaloxime(III) (**Co-1**, Figure 3-7) for our studies. In a typical photocatalytic experiment, 5 mg of N₂-COF was dispersed in 10 mL of 4:1 ACN/H₂O solvent together with 100 μL of TEOA (0.075 M final concentration) as the sacrificial electron donor and 400 μL of a 2.48 mM solution of **Co-1** in acetonitrile (0.1 mM final concentration). When irradiated with 100 mW/cm² AM 1.5 radiation, the resulting mixture produces hydrogen actively at a rate of 160 μmol g⁻¹ h⁻¹ over a period of 7 h (Figure 1a) with a peak hydrogen as high as 701 μmol g⁻¹ corresponding to a turnover number (TON) of 3.54 (based on **Co-1**), after which the activity of the system levels off. An induction period of about 1.5 h is however seen at the onset, which possibly corresponds to the photogeneration of Co^{II} and then finally Co^I and Co^{III}-H and/or Co^{II}-H species from the initial Co^{III} for H₂ evolution to occur (*vide infra*).^[13-15, 17, 21-23] In control experiments without either the COF or TEOA, no H₂ evolution was observed in a period of 3 h. The control experiment without **Co-1** produced only 5 μmol g⁻¹ h⁻¹ in 3 h. This implies that all the aforementioned three components are necessary for the photocatalytic system to work and that there is a charge transfer in the ensemble. The negative Gibbs free energy of the photoinduced electron transfer reaction (Table 3-2), from either the conduction band of N₂-

COF or the reduced radical anion species to either Co^{III} or to Co^I calculated according to the Weller equation^[24-25] suggests that electron transfer is thermodynamically feasible.

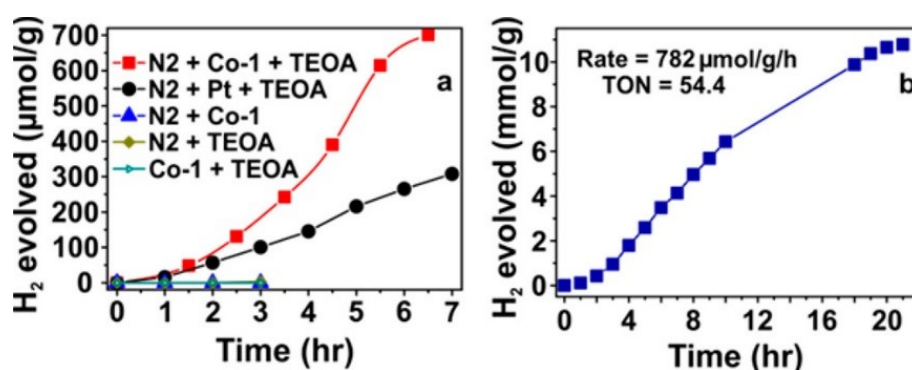


Figure 3-8: (a) H₂ evolution using N₂-COF and Co-1 (see text for details) as well as N₂-COF and metallic platinum (5 μL of 8 wt% H₂PtCl₆ solution in water) in the presence of TEOA, when irradiated with 100 mW cm⁻² AM 1.5 light. Control experiments in absence of either of the three components, with all other conditions being the same, show no H₂ evolution in 3 h. (b) H₂ evolution using optimized parameters, 5 mg of N₂-COF dispersed in 10 mL of 4:1 ACN/H₂O solvent together with 100 μL of TEOA, 400 μL of a 2.48 mM solution of Co-1 in ACN, and 4.69 mM dmgH₂ at a final pH of 8. The reaction mixture is illuminated with 100 mW cm⁻² AM 1.5 light.

After photocatalysis, the COF sample was then fully characterized to check for any decomposition. The framework structure and crystallinity is fully retained after photocatalysis, as seen in the PXRD pattern of the post photocatalysis N₂-COF sample (Figure 6-1). FTIR and ssNMR spectra (Figure 3-10 and Figure 6-2) again remain unchanged, demonstrating that molecular connectivity and hence the structure of the COF remains intact after photocatalysis. SEM images evidence that the rod-like morphology of N₂-COF is unchanged (Figure 6-3), and TEM images confirm retention of the hexagonally ordered crystalline domains after photocatalysis (Figure 6-4). Also, no trace of cobalt oxide or metallic cobalt was seen on the surface of the COF.

Table 3-2: Gibbs Free Energy of formation of Co^{II} and Co^I by Oxidative and Reductive Electron Transfer Pathways. The N₂-COF energy levels are the calculated values for a model hexagon with hydrazone termination.^[9] $E(\text{Co}^{\text{III}}/\text{Co}^{\text{II}})$ and $E(\text{Co}^{\text{II}}/\text{Co}^{\text{I}})$ potential values have been obtained from ref 25.

$E_{\text{CB}}^{\text{N}_2}, \text{V (NHE)}$ in vacuum	$E(\text{N}_2^{\bullet-}), \text{V (NHE)}$ in vacuum	$E(\text{Co}^{\text{III}}/\text{Co}^{\text{II}}), \text{V (NHE)}$ in ACN	$E(\text{Co}^{\text{II}}/\text{Co}^{\text{I}}), \text{V (NHE)}$ in ACN	$\Delta G_1^\circ,$ eV ^a	$\Delta G_2^\circ,$ eV ^a	$\Delta G_3^\circ,$ eV ^a	$\Delta G_4^\circ,$ eV ^a
-1.52	-2.31	-0.43	-0.88	-1.09	-0.64	-1.88	-1.43

a. Calculations are as follows: $\Delta G_1^\circ = E_{\text{CB}}^{\text{N}_2} - E(\frac{\text{Co}^{\text{III}}}{\text{Co}^{\text{II}}})$, $\Delta G_2^\circ = E_{\text{CB}}^{\text{N}_2} - E(\frac{\text{Co}^{\text{II}}}{\text{Co}^{\text{I}}})$, $\Delta G_3^\circ = E(\text{N}_2^{\bullet-}) - E(\frac{\text{Co}^{\text{III}}}{\text{Co}^{\text{II}}})$, $\Delta G_4^\circ = E(\text{N}_2^{\bullet-}) - E(\frac{\text{Co}^{\text{II}}}{\text{Co}^{\text{I}}})$.

We then tried to find the optimum working conditions for the hybrid photocatalytic system. Solvent variation was found to have a profound influence on H₂ production.^[26] Different



solvents have different coordination abilities for binding to cobalt; they have different polarities and dielectric constants which differently stabilize the reduction intermediates. Also, the solvent dependence of the $\text{Co}^{\text{II}}/\text{Co}^{\text{I}}$ redox potential, and/or the reduction of the Co^{III} and/or Co^{II} -hydride intermediate greatly affects the driving force for the H_2 generation reaction. While in DMF/ H_2O 4:1, H_2 evolution is seen at a rate of $22.6 \mu\text{mol g}^{-1} \text{h}^{-1}$; most efficient H_2 evolution is seen with ACN/ H_2O 4:1 ($160 \mu\text{mol g}^{-1} \text{h}^{-1}$) (Figure 6-5). H_2 evolves at a rate of only $4.75 \mu\text{mol g}^{-1} \text{h}^{-1}$ in a THF/ H_2O 4:1 system. The ratio of ACN to H_2O in the solvent was found to have an influence on the H_2 evolution efficiency as well and the rate of hydrogen production increases when the ratio is increased from 2:3 to 3:2 and to finally 4:1 where it reaches a maximum (Figure 6-6). The induction period also seems to be somewhat shortened when using a higher ACN content.

As seen commonly for many H_2 production systems, the pH of the reaction mixture was also found to have a profound influence on H_2 evolution efficiency.^[21] The amount of H_2 generated from the photochemical reaction is maximum at around pH 8. Significantly less H_2 evolution is seen at lower pH values because TEOA is either protonated or else due to inhibition of proton loss from TEOA^+ .^[21] Likewise, very little H_2 evolution is seen at pH 12 (Figure 6-7) because of the reduced thermodynamic driving force and because of protonation of the cobalt catalyst becoming greatly unfavorable.

Next, we varied the sacrificial donor. Triethylamine (TEA) as the electron donor led to significantly reduced hydrogen generation ($17 \mu\text{mol g}^{-1} \text{h}^{-1}$) as compared to TEOA ($160 \mu\text{mol g}^{-1} \text{h}^{-1}$, Figure S8). Interestingly, a TEOA concentration as low as 0.075 M led to the most efficient H_2 production in our system. When [TEOA] was increased to 0.375 M, H_2 evolution was reduced ($110 \mu\text{mol g}^{-1} \text{h}^{-1}$), most likely as a result of an increase in pH.

Cobaloxime complexes are unstable because of the labile dimethylglyoxime ligands which undergo exchange with free dimethylglyoxime in solution.^[14-15, 27] We thus added 8 equivalents of dmgH_2 to the photocatalytic reaction mixture when absolutely no further H_2 evolution was seen with the initially added **Co-1**. H_2 evolution duly renewed and continued for an additional 9 h at the rate $170 \mu\text{mol g}^{-1} \text{h}^{-1}$ in comparison to H_2 evolution for only 6 h with a slightly lower rate of $150 \mu\text{mol g}^{-1} \text{h}^{-1}$ before dmgH_2 addition (Figure 6-9). The improvement in the efficiency of H_2 production with dimethylglyoxime led us to explore its use as the sacrificial electron donor, replacing TEOA, for long-term hydrogen evolution. With 0.05 M dimethylglyoxime (this is the limit of solubility of dmgH_2 in 4:1 ACN/ H_2O solvent), H_2 however evolves at an extremely poor rate of $0.63 \mu\text{mol g}^{-1} \text{h}^{-1}$ for 24 h after an initial induction period of about 3 h (Figure 6-10).

Crystallinity and porosity of the COF also seem to have an effect on the efficiency of H_2 evolution. Poorly crystalline samples (with typically lower porosity) led to poorer H_2 generation. This is most likely because of a smaller extension of the π -system in the less

crystalline sample and/or stacking faults which could impede lateral and/or vertical charge carrier transport in the COF photosensitizer and likely also the interfacial charge transfer from the COF to the cobaloxime. We would also expect a less porous COF sample to impede accessibility to **Co-1** and thus limit effective transfer of charges.

With all the above variables optimized, a H₂ evolution rate of 782 $\mu\text{mol g}^{-1} \text{h}^{-1}$ is achieved corresponding to a TON of 54.4 at 20 h (Figure 3-9b) and an initial TOF of 3.96 h^{-1} . The amount of H₂ evolved thus makes this system competitive with carbon nitride based benchmark photocatalytic systems such as Pt-modified amorphous melon (720 $\mu\text{mol g}^{-1} \text{h}^{-1}$),^[28] g-C₃N₄ (840 $\mu\text{mol g}^{-1} \text{h}^{-1}$),^[29] or crystalline poly(triazine imide) (864 $\mu\text{mol g}^{-1} \text{h}^{-1}$).^[28] The TONs obtained are comparable to that obtained for a homogeneous photocatalytic system comprising of a Pt-terpyridyl acetylide chromophore and **Co-1** co-catalyst in MeOH/H₂O 3:2 (TON of 56).^[26] Even higher TONs may be attained in our system by adding dmgh₂ periodically because, as shown above, the COF photosensitizer is quite stable under photocatalytic conditions. In fact, our previous report shows it to be stable for more than 120 h under photocatalytic conditions.^[16] The apparent quantum efficiency (AQE) in the present system was estimated to be 0.027% under AM 1.5 illumination. Under 400 nm irradiation, the AQE is estimated to be as high as 0.16%. To put this into perspective, the AQE of the photocatalytic reaction of the Ni bis(diphosphine) catalyst, NiP, in combination with the heptazine carbon nitride polymer melon in water is (0.04 \pm 0.01)% using 460 nm irradiation.^[30]

In order to further optimize the hydrogen evolution efficiency of N₂-COF with cobaloximes, we tried to circumvent the instability of the dimethylglyoxime ligands. Indeed, a higher H₂ evolution rate (414 $\mu\text{mol g}^{-1} \text{h}^{-1}$) and a higher TON of 9.79 are obtained with the more stable BF₂-annulated complex **Co-2** as compared to that with **Co-1** (160 $\mu\text{mol g}^{-1} \text{h}^{-1}$, TON 3.54) under the same conditions (Figure 3-9a and Table 6-1).^[25] However, cobaloxime **Co-3**, despite the stable tetradentate diimine-dioxime ligand, produces very little hydrogen (20 $\mu\text{mol g}^{-1}$ in 6 h).^[31] The low activity could arise from the difficulty of **Co-3** to undergo protonation at the oxime moieties since they are linked covalently to the boron atom. This makes adjustment of the redox potentials to the acido-basic conditions of the reaction mixture difficult and thus probably disfavors proton reduction in this system.^[32] As compared to **Co-2**, which is also a BF₂-annulated complex, H₂ evolution with **Co-3** is further hindered because of the single diimine dioxime ligand, whose other diimine end cannot be protonated. Interestingly, the H₂ evolution efficiency of N₂-COF with **Co-1** (160 $\mu\text{mol g}^{-1} \text{h}^{-1}$) is higher as compared to that in the presence of colloidal platinum (52 $\mu\text{mol g}^{-1} \text{h}^{-1}$) (Figure 1a, the mol % of platinum being the same as **Co-1**). As seen from our previous report, photocatalytic hydrogen evolution with N₂-COF in the presence of platinum takes place with much higher efficiency in water (438 $\mu\text{mol g}^{-1} \text{h}^{-1}$).^[9, 33] The lower H₂ evolution efficiency of



N_2 -COF in this report is thus probably a reflection of the choice of solvent (4:1 ACN/ H_2O , instead of pure water). TEM images of the post photocatalysis (with Pt in 4:1 ACN/ H_2O) N_2 -COF sample shows a distribution of ~ 2 nm nanoparticles on the surface of the COF (Figure 6-11). Such distributions were however seen only in some areas. In comparison, well-distributed, though larger, nanoparticle clusters of 10–15 nm size were seen when the reaction was done in water where a significantly higher H_2 evolution was observed. Thus, while smaller nanoparticles indeed form in 4:1 ACN/ H_2O and should make H_2 evolution more efficient because of a higher availability of surface Pt atoms, the overall poorer distribution and/or poorer photodeposition of Pt nanoparticles in this solvent probably reverses the trend in H_2 evolution reaction. The energetics of the charge transfer processes involved, in 4:1 ACN/ H_2O vs H_2O , might also vary and could also contribute to the lower H_2 evolution efficiency in the former solvent. A comparison between the activities of N_2 -COF with **Co-1** and with platinum in 4:1 ACN/ H_2O is thus difficult. **Co-1** is insoluble in pure water, whereas **Co-2** is soluble. However, no hydrogen evolution is seen with N_2 -COF in the presence of **Co-2** in water.

We also measured the activity of other COFs which are known to produce H_2 photocatalytically with metallic platinum, namely, the azine-linked COFs N_1 and N_3 , and the hydrazone linked COF-42 (Figure 3-9b, Figure 6-12, Figure 6-13, and Table 6-2). With COFs N_1 and N_3 , nonoptimized TONs of 2.03 and 5.65 could be obtained at pH 8 with **Co-1** co-catalyst, respectively, while a TON of 5.79 was obtained with COF-42 under similar conditions. The reaction methodology can thus be extended to different types of COFs producing H_2 under photocatalytic conditions.

Interestingly, the H_2 evolution rate of N_3 -COF ($163 \mu\text{mol g}^{-1} \text{h}^{-1}$) is lower than that of N_2 -COF ($390 \mu\text{mol g}^{-1} \text{h}^{-1}$) with **Co-1** at pH 8 in 4:1 ACN/ H_2O . This is contrary to our previously reported results with Pt co-catalyst in water where N_3 -COF was seen to be 4 times as active as N_2 -COF (1703 vs $438 \mu\text{mol g}^{-1} \text{h}^{-1}$, respectively).^[9] However, the H_2 evolution rate of N_3 -COF ($175 \mu\text{mol g}^{-1} \text{h}^{-1}$) with metallic Pt in 4:1 ACN/ H_2O is still about 3.5 times higher than that of N_2 -COF ($52 \mu\text{mol g}^{-1} \text{h}^{-1}$) with Pt under the same conditions (Table 6-3). Therefore, the charge transfer processes between the COF and **Co-1** seem to dictate the lower reaction rate of N_3 -COF with **Co-1** as compared to N_2 -COF.

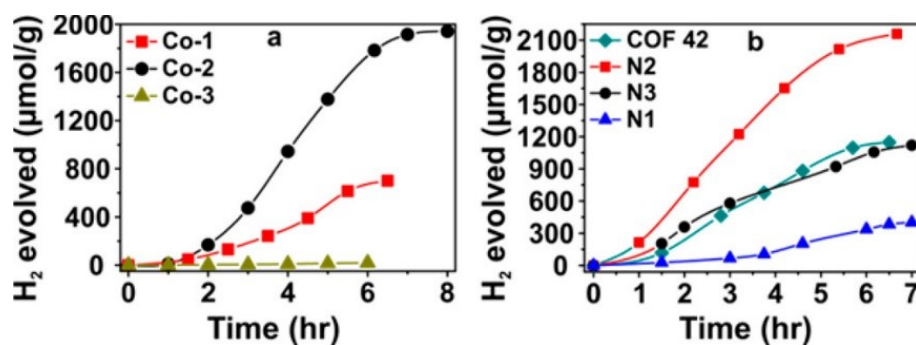


Figure 3-9: (a) H₂ evolution with N₂-COF and different co-catalysts. The co-catalyst concentration is 0.1 mM in all measurements. All other conditions are the same including a pH of 10. (b) H₂ evolution with different COFs at pH 8. 5 mg COF sample has been used in all the measurements. All other conditions are the same. Rates are 233, 390, 163, and 100 μmol g⁻¹ h⁻¹ for COF-42, N₂, N₃ and N₁ COFs, respectively. TON for the reaction with N₂-COF is 10.89 at 6.5 h.

Outer versus Inner Sphere Electron Transfer

Cobaloximes, as discussed before, are known to be quite labile complexes, more so under photocatalytic conditions. The dimethylglyoxime ligands as well as the axial pyridine ligands exchange readily and this limits the long-term usability of such catalysts.^[27] This ligand exchange could have far reaching implications in the present photocatalytic system in terms of what the actual proton reduction catalyst is or what way the electron is actually transferred from the COF photosensitizer to the cobalt center. The lability of the dimethylglyoxime ligands might lead to the formation of an entirely different H₂ evolution catalyst, with the primary coordination sphere of cobalt being occupied by N atoms of the azine linkers (the N atoms of the pyrimidine nodes might be too sterically hindered to interact). However, this seems unlikely looking at the importance of the dimethylglyoxime ligands in keeping the catalyst active for proton reduction.^[13-15, 26-27] A quite possible alternative could be axial coordination of a N atom of the azine linker to the cobalt center after the labile pyridine is lost. This would mean that the COF backbone forms a part of the coordination sphere of the co-catalyst and electrons are transferred from the COF photosensitizer to the catalyst in an inner sphere mechanism.^[34]

In order to probe any interaction between N₂-COF and **Co-1**, we recorded ¹³C cross-polarization magic angle spinning (CPMAS) NMR spectra of N₂-COF post photocatalysis and found it absolutely identical to pristine N₂-COF including the signal for the azine carbon at 162 ppm (Figure 3-10a and Figure 6-14), thus suggesting no chemical interaction between the COF and **Co-1**. Neither peaks corresponding to **Co-1** could be seen, nor were effects due to the presence of any paramagnetic cobalt species such as line broadening or loss of signal intensity observed. No interactions could again be seen in an illuminated and dried mixture of N₂-COF and 8 or 35 wt% **Co-1** in ACN. This time, while peaks

corresponding to **Co-1** are seen owing to higher amounts of **Co-1** in the sample, the chemical shifts again remain unchanged. No interactions were observed in the ^1H MAS NMR spectra as well (Figure S2). ATR-IR spectra of the COF sample before and after photocatalysis are again identical, including the $\nu(\text{C}=\text{N})_{\text{stretch}}$ appearing at 1620 cm^{-1} , as is the IR spectrum of an illuminated and dried mixture of $\text{N}_2\text{-COF}$ and 8 wt% **Co-1** in acetonitrile. In the latter sample, the new features arising can easily be assigned to **Co-1** and the spectrum is simply additive (Figure 3-10b). Energy-dispersive X-ray (EDX) spectroscopic analysis in TEM shows no trace of cobalt in the post-photocatalysis sample (Figure 6-16). However, in the illuminated and dried mixture of $\text{N}_2\text{-COF}$ and 8 wt% **Co-1**, cobalt and chlorine can easily be detected (Figure 6-17). Also, the filtered, washed, and thus recovered $\text{N}_2\text{-COF}$ sample after photocatalysis does not produce any H_2 in the presence of TEOA without **Co-1**, all other conditions being exactly the same as before. These results combined prove beyond doubt that (i) **Co-1** rather than the photochemically decomposed metallic cobalt is the catalytically active species and (ii) that it does not chemically interact with $\text{N}_2\text{-COF}$. Also, physisorption, if any, is weak enough for **Co-1** to be washed away very easily with standard solvents.

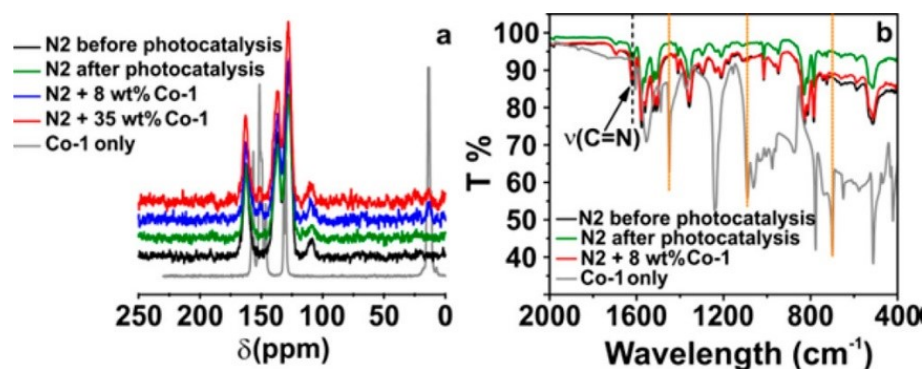


Figure 3-10: (a) ^{13}C CPMAS NMR spectra of $\text{N}_2\text{-COF}$ under different conditions. No change in chemical shift in the COF signals is seen. Please see Figure S12 for peak assignments. (b) ATR-IR spectra of $\text{N}_2\text{-COF}$ under different conditions. Again, no shift in the frequencies of the bands is seen.

Quantum chemical calculations with **Co-1** and model compounds further confirm this argument. Four different cobaloxime-COF composites were modeled in order to mimic possible binding sites of the cobalt co-catalyst to the framework (Figure 3-11 and Quantum chemical Calculations section). Two different cobaloximes with pyridine and ACN as the axial N donor ligands (Figure 6-18 and Figure 6-19) were also modeled in order to compare cobalt–axial nitrogen bond lengths of these optimized compounds against the corresponding distances in cobaloxime-COF models, in order to estimate their binding strength. For cobaloxime-COF models, the shortest cobalt–nitrogen distance obtained is 2.79 \AA for the surface-diazene cobaloxime-COF model (Table 6-5), which is still significantly

larger than the longest cobalt–axial nitrogen bond distance of 1.96 Å observed among the modeled cobaloximes (Table 6-4). A distance-based approximation thus suggests that cobalt tends to form more stable complexes with its axial N donor ligands in the parent complexes, pyridine or ACN, than with a N center on the COF framework. Interaction energies were also calculated on PBE0-D3/def2-TZVP level of theory^[35-40] using the FermiONs++ program package^[41-42] and, as anticipated from the analysis of cobalt–nitrogen distances, all four COF-cobaloxime models, especially pore-diazene and pore-diazene-90°, were seen to be distinctly unfavored in comparison to the parent complexes with either pyridine, ACN or H₂O as the axial ligands (Table 6-6). Combined experimental and quantum chemical investigations thus refute the possibility of an inner sphere electron transfer from the COF to the co-catalyst via covalent interactions and suggest possibly an outer sphere collisional electron transfer mechanism.

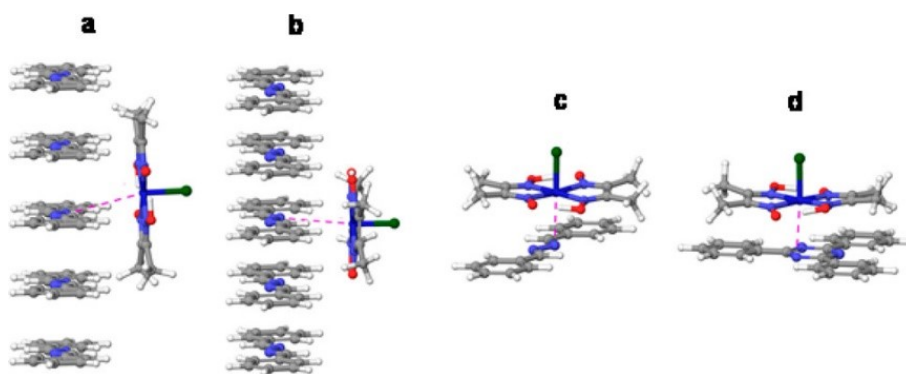


Figure 3-11: Constrained optimized geometry of (a) pore-diazene, (b) pore-diazene-90°, (c) surface-diazene, and (d) surface-triazine cobaloxime-COF models, obtained on the PBE0-D3/def2-SVP level of theory using the Turbomole program package. The surface-diazene and triazine models are for possible interactions on the surface of the COF microstructure. Other details of the calculations can be found in the Supporting Information. The dashed pink lines show the shortest Co–N distance obtained and are 4.197, 4.082, 2.792, and 3.00 Å, respectively, in panels a–d.

Mechanism

A general mechanism of proton reduction by cobalt complexes involves stepwise reduction of the Co^{III} complex to the resting state of the complex, Co^{II}, then to Co^I which is then protonated to form a Co^{III} hydride intermediate.^[14-15, 17, 21, 23, 27] A direct proton coupled electron transfer step from Co^{II} to H–Co^{III} has also been proposed.^[22] Likewise, in the present COF-cobaloxime photocatalytic system, Co^{II} and the Co^I intermediates can actually be identified in the photolysis solutions owing to their unique spectroscopic signatures.

Prior to irradiation of the reaction mixture containing COF-42 as the photosensitizer and Co-1 as the co-catalyst, cobalt is only present in the +3 oxidation state and has no significant absorption in the visible region. After irradiation for 2 h at pH 8, an absorption



band centered at 440 nm corresponding to Co^{II} can be seen, and the reaction mixture is visibly dark yellow (Figure 5a).^[21, 25-26, 32, 43-44] Measurements were impeded by the use of N_2 -COF, since the COF particles took an extraordinarily long time to settle down for us to be able to record an absorption spectrum of the supernate. This problem could be avoided with COF-42. We also recorded an X-band EPR spectrum of this photocatalytic reaction mixture before and after illumination and could observe formation of the one electron reduced paramagnetic Co^{I} species with Lorentzian line broadening corresponding to $g_{\text{eff}} = 2.006$ (Figure 3-12b) as has been reported previously.^[18-19, 45-47] Before illumination there seems to be a weak signal at $g_{\text{eff}} = 2.058$ possibly corresponding to paramagnetic impurities in the starting complex **Co-1**.^[18-19] At low pH the formation rate of Co^{I} is itself very low. At high pH, H_2 production is supposed to be greatly decreased and photoaccumulation of the Co^{I} state should be possible.^[21] Nevertheless, our efforts to spectroscopically monitor the Co^{I} state at pH 12 proved unsuccessful. However, a 4 h illumination of the reaction mixture at pH 10 with 5 equivalents of added $\text{P}(n\text{-Bu})_3$ led to an intense blue color corresponding to an absorption band at 500–700 nm (Figure 5a). The blue color which disappears immediately upon air exposure can have three possible origins. It can be attributed to the phosphine coordinated Co^{I} species,^[32, 48] namely, $[\text{Co}^{\text{I}}(\text{dmgH})_2(\text{P}(n\text{-Bu})_3)]^-$ or bridge protonated $[\text{Co}^{\text{I}}(\text{dmgH})(\text{dmgH}_2)(\text{P}(n\text{-Bu})_3)]$. It could also be attributed to a solvent stabilized charge-transfer state of $[\text{Co}^{\text{III}}\text{H}(\text{dmgH})_2(\text{P}(n\text{-Bu})_3)]$, i.e., the H-Co^{III} species,^[48-49] as all of these have a similar absorption spectrum. However, an initially formed photoreduced Co^{I} species uncoordinated to $\text{P}(n\text{-Bu})_3$ or the Co^{II} -hydride species can safely be ruled out.^[21-22, 25-26, 32, 43-44] $\text{P}(n\text{-Bu})_3$ is actually reported to increase the efficiency in some hydrogen evolving photocatalytic systems by stabilizing the aforesaid intermediate Co^{I} state.^[32, 50] However, the fact that no hydrogen evolution is seen in our system with added $\text{P}(n\text{-Bu})_3$ makes us believe that it is the Co^{III} hydride $[\text{CoH}(\text{dmgH})_2(\text{P}(n\text{-Bu})_3)]$, known to produce H_2 only on thermolysis at $150\text{ }^\circ\text{C}$,^[51] which is actually formed.

The cobalt^{III} and/or cobalt^{II} hydride formed in the reaction mixture can produce hydrogen by either a homolytic/bimetallic pathway involving two cobalt centers or a kinetically distinguishable heterolytic/monometallic pathway involving a single cobalt center.^[14-15, 17, 26, 52-53] In order to distinguish between these two pathways for the present photocatalytic system, we studied the amount of hydrogen evolved for different concentrations of **Co-1**, while keeping all other conditions the same. From Figure 3-12c it can be seen that H_2 evolution after 3 h of photolysis exhibits a linear dependence on $[\text{Co-1}]$, thus supporting a single cobalt mechanism for hydrogen generation (Figure 6-26).^[14, 26, 53]

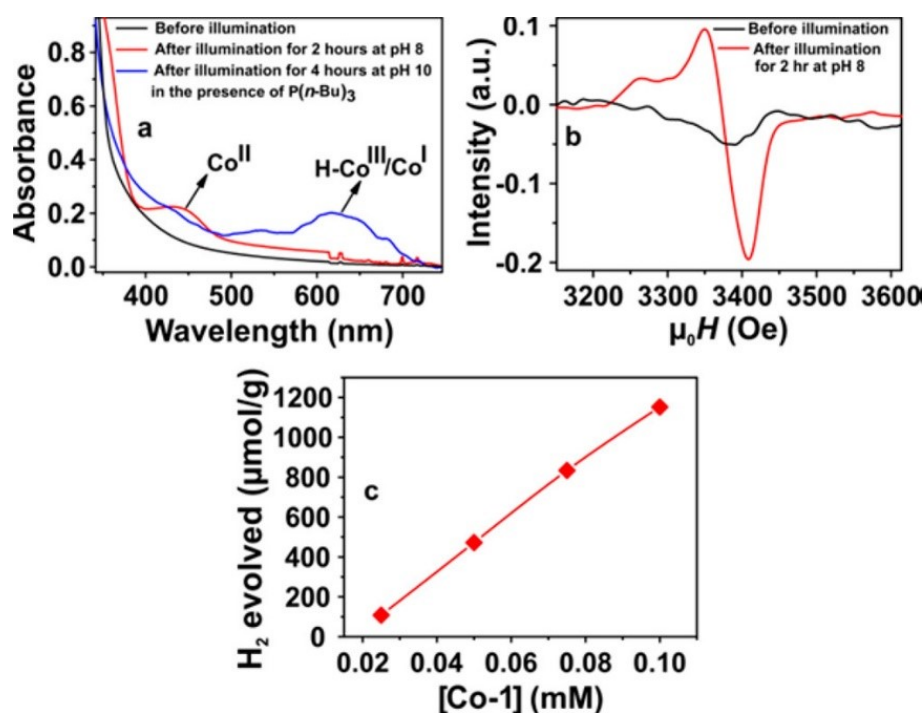


Figure 3-12: (a) Red trace: UV-vis spectra of the degassed photocatalytic reaction dispersion containing 2.5 mg of COF-42, 50 μL of TEOA and 200 μL of Co-1 (2.48 mM in ACN) in 5 mL 4:1 ACN/H₂O mixture at pH 8 illuminated with 100 mW cm^{-2} AM 1.5 light. The reaction mixture was allowed to stand for 1 h after illumination before a spectrum was recorded. Blue trace: similar reaction conditions as before except at pH 10 of the reaction mixture and 5 equiv of externally added P(n-Bu)₃. The noise in the spectra is from the still suspended COF particles. (b) X-band EPR spectrum at 4K of the photocatalytic reaction dispersion containing COF-42 before and after illumination. The microwave frequencies are 9.47614 GHz in both cases. The reaction conditions are identical to those in Figure 5a. (c) H₂ evolution at 3 h after illumination under different [Co-1]. In all measurements, 5 mg of N₂-COF and 100 μL of TEOA in 10 mL of 4:1 ACN/H₂O has been used. The reaction pH is 8.

The other reversible cycle, i.e., the photochemical COF cycle, can proceed along either oxidative or reductive quenching of the COF upon photoexcitation. Our previously published theoretical studies on the N_x-COFs show that the formation of a radical cation intermediate during the photocatalytic cycle is less likely for these COFs for energetic reasons.^[9] In fact, a radical anionic state has been identified in an ongoing experimental study. This speculation however does not undermine the importance of a correct identification of the reaction pathway adopted in our COF-cobaloxime photocatalytic system. Detailed transient absorption measurements are underway in this regard and will be reported elsewhere.

We also tried to explore the charge transfer pathways in our photocatalytic system by photoluminescence measurements. Unfortunately, N₂-COF is scarcely emissive; thus, it was not possible to collect reproducible emission spectra or quantum yields of the photolysis dispersions to check whether Co-1 or TEOA quench emission. Measurements were further



impeded by simultaneous absorption of **Co-1**. Photoluminescence lifetimes recorded using time-correlated single-photon counting method (TCSPC), however, show almost no change in the decay of N₂-COF in the presence of either TEOA, **Co-1** or both (Figure 6-27 and Table 6-8), which probably suggests a different time scale of the electron transfer process from TEOA and to **Co-1** under these conditions.^[54]

3.3.4 Conclusion

Photocatalytic hydrogen evolution with COF photosensitizers using molecular, earth-abundant co-catalysts has been demonstrated with large H₂ evolution rates and good TONs, as exemplified with the N_x-COF series and COF-42 with **Co-1** and other cobaloximes. No external proton source is required for H₂ evolution. Metallic cobalt, which could possibly form by photodecomposition of **Co-1**, could be ruled out as the hydrogen evolving co-catalyst; **Co-1** in solution thus acts as the proton reduction catalyst transferring reducing equivalents from the photosensitizer to the protons. Experimental results and quantum chemical calculations suggest an outer sphere electron transfer from N₂-COF to co-catalyst **Co-1** and a monometallic, i.e., a single cobalt pathway was identified in the present system for H₂ generation from the intermediate Co^{III}- and/or Co^{II}-hydride. Long-term stability needs to be further addressed with other more stable and efficient H₂ evolving co-catalysts or by engineering the COF so as to prevent ligand dissociation.^[18] A possible improvement of the H₂ evolution efficiency by optimizing the electron transfer process between the COF and the co-catalyst by covalently linking the molecular co-catalyst to the COF backbone also needs to be explored and is currently underway.

To conclude, it is important to understand the implications of the results presented in this article. The quest for earth abundant molecular replacements of co-catalyst platinum for photocatalytic H₂ evolution using COF photosensitizers is a big challenge because: (i) COFs that produce H₂ photocatalytically are themselves rare. A number of factors come into play such as crystallinity, porosity, rigidity, and stability on the one hand and light harvesting, charge separation/recombination, and charge transport on the other, which have to be retained throughout the course of the photocatalytic reaction. (ii) Electron transfer from the COF to the co-catalyst has to be thermodynamically and kinetically favorable. There needs to be an efficient coupling of single-photon electron events with the multielectron redox reactions necessary for H₂ evolution. (iii) Molecular co-catalysts, unlike metallic platinum, possess limited photostability and could have slow multielectron diffusion controlled rates. The observation of photocatalytic H₂ evolution from COFs with molecular cobaloxime based co-catalysts is thus the first step in overcoming these challenges. The results presented herein lead way to the development of efficient "COF-molecular co-catalyst" based photocatalytic systems entirely free of noble metals which, with the robustness and tunability of the COF

backbone, enables a precise control over the nature, the arrangement and the density of photocatalytically active sites for optimal competence.^[55] The results show that water splitting or CO₂ reduction catalysts could be combined with COF-based light-harvesting systems in a “leaf”-like architecture for stable generation of solar fuels in future. While covalently linked COF-co-catalyst architectures could be envisaged for better performance, our results also show that design and optimization of the COF photosensitizer and the co-catalyst as independent components is another worthwhile avenue.

3.3.5 Acknowledgments

B.V.L. acknowledges financial support by an ERC Starting Grant (project COF Leaf, grant number 639233), the Max Planck Society, the cluster of excellence Nanosystems Initiative Munich (NIM), and the Center for Nanoscience (CeNS). We thank Viola Duppel for recording the SEM and TEM images, Igor Moudrakovski for the measurement of the solid-state NMR, Marie-Luise Schreiber for recording the ATR-IR spectra, and Prof. Reinhard Kremer for recording the EPR spectra.

3.3.6 Author contributions

Tanmay Banerjee conceptualized, designed and performed the experiments and wrote the manuscript. Frederik Haase assisted in synthesis of initial samples. Gökçen Savasci designed and performed all quantum chemical calculations. Kerstin Gottschling had the initial idea for the project and provided additional samples that enabled more detailed analysis of the reaction mechanism. Christian Ochsenfeld and Bettina V. Lotsch supervised the project. All authors worked on and revised the manuscript.

3.3.7 References

- [1] Y. Tachibana, L. Vayssieres, J. R. Durrant, *Nature Photonics* **2012**, *6*, 511.
- [2] S. Berardi, S. Drouet, L. Francàs, C. Gimbert-Suriñach, M. Guttentag, C. Richmond, T. Stoll, A. Llobet, *Chem. Soc. Rev.* **2014**, *43*, 7501-7519.
- [3] V. S. Vyas, V. W.-h. Lau, B. V. Lotsch, *Chem. Mater.* **2016**, *28*, 5191-5204.
- [4] S.-Y. Ding, W. Wang, *Chem. Soc. Rev.* **2013**, *42*, 548-568.
- [5] R. P. Bisbey, W. R. Dichtel, *ACS Central Science* **2017**, *3*, 533-543.
- [6] N. Huang, P. Wang, D. Jiang, *Nature Reviews Materials* **2016**, *1*, 16068.
- [7] X. Ding, J. Guo, X. Feng, Y. Honsho, J. Guo, S. Seki, P. Maitarad, A. Saeki, S. Nagase, D. Jiang, *Angew. Chem. Int. Ed.* **2011**, *50*, 1289-1293.
- [8] C. Butchosa, T. O. McDonald, A. I. Cooper, D. J. Adams, M. A. Zwiijnenburg, *The Journal of Physical Chemistry C* **2014**, *118*, 4314-4324.
- [9] V. S. Vyas, F. Haase, L. Stegbauer, G. Savasci, F. Podjaski, C. Ochsenfeld, B. V. Lotsch, *Nat Commun* **2015**, *6*.
- [10] L. Stegbauer, K. Schwinghammer, B. V. Lotsch, *Chemical Science* **2014**, *5*, 2789-2793.
- [11] F. Haase, T. Banerjee, G. Savasci, C. Ochsenfeld, B. V. Lotsch, *Faraday Discuss.* **2017**, *201*, 247-264.



- [12] J. Thote, H. B. Aiyappa, A. Deshpande, D. Díaz Díaz, S. Kurungot, R. Banerjee, *Chemistry – A European Journal* **2014**, *20*, 15961-15965.
- [13] P. Du, R. Eisenberg, *Energy & Environmental Science* **2012**, *5*, 6012-6021.
- [14] V. Artero, M. Chavarot-Kerlidou, M. Fontecave, *Angew. Chem. Int. Ed.* **2011**, *50*, 7238-7266.
- [15] W. T. Eckenhoff, W. R. McNamara, P. Du, R. Eisenberg, *Biochimica et Biophysica Acta (BBA) - Bioenergetics* **2013**, *1827*, 958-973.
- [16] V. S. Vyas, F. Haase, L. Stegbauer, G. Savasci, F. Podjaski, C. Ochsenfeld, B. V. Lotsch, *Nature Communications* **2015**, *6*, 8508.
- [17] J. L. Dempsey, B. S. Brunschwig, J. R. Winkler, H. B. Gray, *Acc. Chem. Res.* **2009**, *42*, 1995-2004.
- [18] M. A. Nasalevich, R. Becker, E. V. Ramos-Fernandez, S. Castellanos, S. L. Veber, M. V. Fedin, F. Kapteijn, J. N. H. Reek, J. I. van der Vlugt, J. Gascon, *Energy & Environmental Science* **2015**, *8*, 364-375.
- [19] L.-F. Gao, Z.-Y. Zhu, W.-S. Feng, Q. Wang, H.-L. Zhang, *The Journal of Physical Chemistry C* **2016**, *120*, 28456-28462.
- [20] S.-W. Cao, X.-F. Liu, Y.-P. Yuan, Z.-Y. Zhang, J. Fang, S. C. J. Loo, J. Barber, T. C. Sum, C. Xue, *PCCP* **2013**, *15*, 18363-18366.
- [21] P. Du, K. Knowles, R. Eisenberg, *J. Am. Chem. Soc.* **2008**, *130*, 12576-12577.
- [22] J. T. Muckerman, E. Fujita, *Chem. Commun.* **2011**, *47*, 12456-12458.
- [23] B. H. Solis, S. Hammes-Schiffer, *Inorg. Chem.* **2011**, *50*, 11252-11262.
- [24] G. J. Kavarnos, N. J. Turro, *Chem. Rev.* **1986**, *86*, 401-449.
- [25] P. Zhang, M. Wang, J. Dong, X. Li, F. Wang, L. Wu, L. Sun, *The Journal of Physical Chemistry C* **2010**, *114*, 15868-15874.
- [26] P. Du, J. Schneider, G. Luo, W. W. Brennessel, R. Eisenberg, *Inorg. Chem.* **2009**, *48*, 4952-4962.
- [27] T. M. McCormick, Z. Han, D. J. Weinberg, W. W. Brennessel, P. L. Holland, R. Eisenberg, *Inorg. Chem.* **2011**, *50*, 10660-10666.
- [28] K. Schwinghammer, B. Tuffy, M. B. Mesch, E. Wirnhier, C. Martineau, F. Taulelle, W. Schnick, J. Senker, B. V. Lotsch, *Angew. Chem. Int. Ed.* **2013**, *52*, 2435-2439.
- [29] J. Zhang, X. Chen, K. Takane, K. Maeda, K. Domen, J. D. Epping, X. Fu, M. Antonietti, X. Wang *Angew. Chem. Int. Ed.* **2010**, *49*, 441-444.
- [30] C. A. Caputo, M. A. Gross, V. W. Lau, C. Cavazza, B. V. Lotsch, E. Reisner, *Angew. Chem. Int. Ed.* **2014**, *53*, 11538-11542.
- [31] P.-A. Jacques, V. Artero, J. Pécaut, M. Fontecave, *Proceedings of the National Academy of Sciences* **2009**, *106*, 20627-20632.
- [32] P. Zhang, P.-A. Jacques, M. Chavarot-Kerlidou, M. Wang, L. Sun, M. Fontecave, V. Artero, *Inorg. Chem.* **2012**, *51*, 2115-2120.
- [33] It needs to be mentioned that a comparison between the activities with a co-catalyst in solution versus photodeposited metallic platinum is not reasonable in any case, even in the absence of all the factors discussed above. This is because only a fraction of atoms on the surface of the nanoparticles are photocatalytically active; the rest, in the bulk of the nanoparticles, are inactive.
- [34] V. Balzani, *Electron Transfer in Chemistry, Vol. 1*, WILEY-VCH Verlag GmbH, Weinheim, **2008**.
- [35] C. Adamo, V. Barone, *The Journal of Chemical Physics* **1999**, *110*, 6158-6170.
- [36] M. Ernzerhof, G. E. Scuseria, *The Journal of Chemical Physics* **1999**, *110*, 5029-5036.

- [37] S. Grimme, J. Antony, S. Ehrlich, H. Krieg, *The Journal of Chemical Physics* **2010**, 132, 154104.
- [38] A. Schäfer, H. Horn, R. Ahlrichs, *The Journal of Chemical Physics* **1992**, 97, 2571-2577.
- [39] R. Ahlrichs, M. Bär, M. Häser, H. Horn, C. Kölmel, *Chem. Phys. Lett.* **1989**, 162, 165-169.
- [40] A. Schäfer, C. Huber, R. Ahlrichs, *The Journal of Chemical Physics* **1994**, 100, 5829-5835.
- [41] J. Kussmann, C. Ochsenfeld, *The Journal of Chemical Physics* **2013**, 138, 134114.
- [42] J. Kussmann, C. Ochsenfeld, *Journal of Chemical Theory and Computation* **2015**, 11, 918-922.
- [43] X. Hu, B. S. Brunschwig, J. C. Peters, *J. Am. Chem. Soc.* **2007**, 129, 8988-8998.
- [44] T. Lazarides, T. McCormick, P. Du, G. Luo, B. Lindley, R. Eisenberg, *J. Am. Chem. Soc.* **2009**, 131, 9192-9194.
- [45] M. Baumgarten, W. Lubitz, C. J. Winscom, *Chem. Phys. Lett.* **1987**, 133, 102-108.
- [46] D. M. Cropek, A. Metz, A. M. Muller, H. B. Gray, T. Horne, D. C. Horton, O. Poluektov, D. M. Tiede, R. T. Weber, W. L. Jarrett, J. D. Phillips, A. A. Holder, *Dalton Transactions* **2012**, 41, 13060-13073.
- [47] W. Lubitz, C. J. Winscom, H. Diegruber, R. Mösel, in *Zeitschrift für Naturforschung A*, Vol. 42, **1987**, p. 970.
- [48] A. Bhattacharjee, M. Chavarot-Kerlidou, E. S. Andreiadis, M. Fontecave, M. J. Field, V. Artero, *Inorg. Chem.* **2012**, 51, 7087-7093.
- [49] E. Szajna-Fuller, A. Bakac, *Eur. J. Inorg. Chem.* **2010**, 2010, 2488-2494.
- [50] J. Hawecker, J. M. Lehn, R. Ziessel, *New J. Chem.* **1983**, 7, 271-277.
- [51] G. N. Schrauzer, R. J. Holland, *J. Am. Chem. Soc.* **1971**, 93, 1505-1506.
- [52] F. Wen, J. Yang, X. Zong, B. Ma, D. Wang, C. Li, *J. Catal.* **2011**, 281, 318-324.
- [53] A. Fihri, V. Artero, A. Pereira, M. Fontecave, *Dalton Transactions* **2008**, 5567-5569.
- [54] V. W.-h. Lau, V. W.-z. Yu, F. Ehrat, T. Botari, I. Moudrakovski, T. Simon, V. Duppel, E. Medina, J. K. Stolarczyk, J. Feldmann, V. Blum, B. V. Lotsch, *Advanced Energy Materials* **2017**, 7, 1602251.
- [55] C. S. Diercks, O. M. Yaghi, *Science* **2017**, 355, eaal1585.



3.4 Rational design of covalent cobaloxime-COF hybrids for enhanced photocatalytic hydrogen evolution

Kerstin Gottschling, Gökçen Savasci, Hugo Vignolo-González, Sandra Schmidt, Phillip Mauker, Tanmay Banerjee, Petra Rovó, Christian Ochsenfeld, and Bettina V. Lotsch

published in

J. Am. Chem. Soc. **2020**, *142* (28), 12146–12156

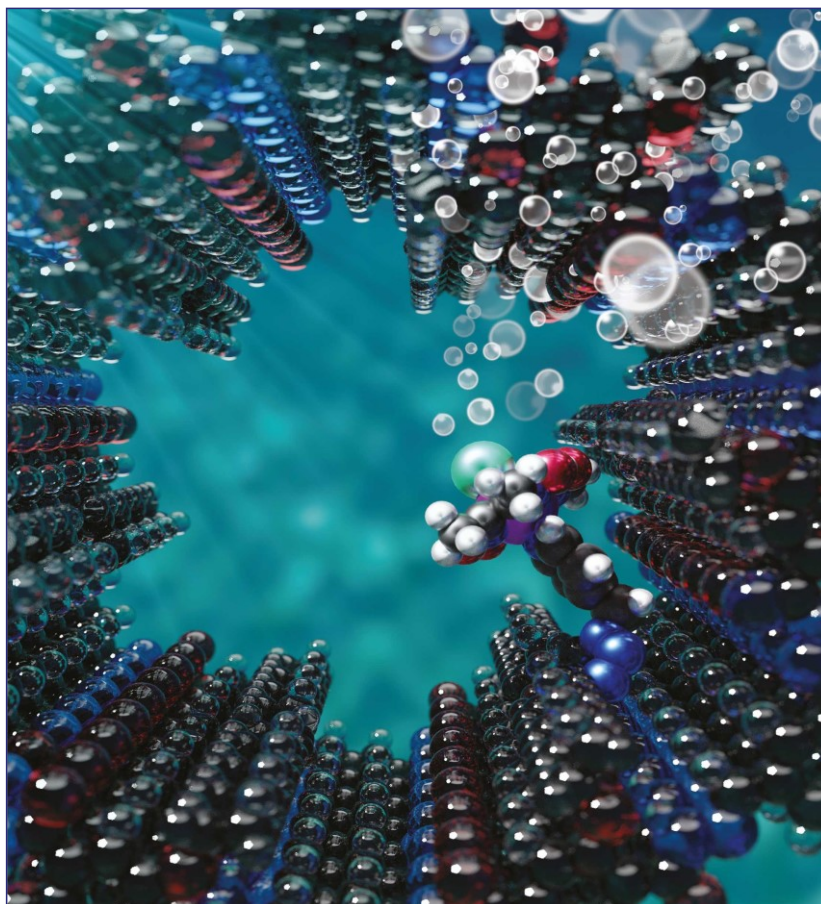
DOI: 10.1021/jacs.0c02155

<https://pubs.acs.org/doi/10.1021/jacs.0c02155>

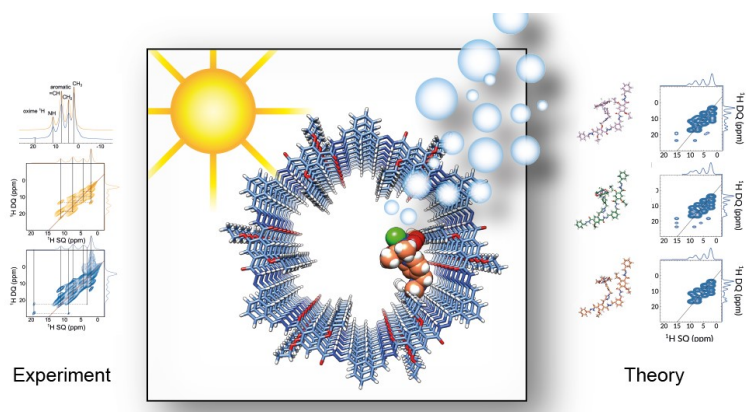
Formatting and numbering of figures were changed.

Adapted with permission from ACS

This project was highlighted as a supplementary cover image of the journal Chemistry of Materials, the cover image was designed by Kerstin Gottschling.



3.4.1 Abstract



Covalent organic frameworks (COFs) represent promising materials for the field of nanosciences due to their unique combination of chemical tunability, structural diversity, high porosity, nanoscale regularity, and extreme thermal stability. Covalent organic

frameworks (COF) display a unique combination of chemical tunability, structural diversity, and porosity. Recent efforts in the field are directed at using such frameworks as tunable scaffolds for chemical reactions. Owing to their built-in photoactivity and nanoscale regularity, COFs have emerged as viable platforms for mimicking natural photosynthesis. While previous approaches have focused on platinum nanoparticle or molecular co-catalysts physisorbed in the COF pores, controlling interfacial charge transfer through close COF-co-catalyst contact remains an open challenge. Here, we present a covalently bound COF-co-catalyst hybrid based on an earth-abundant azide-functionalized cobaloxime hydrogen evolution catalyst immobilized on a hydrazone-linked COF-42 backbone. This single-site heterogeneous catalyst shows improved and prolonged photocatalytic activity with respect to the corresponding physisorbed systems. Advanced solid-state NMR and quantum chemical methods reveal details of the improved photocatalytic activity and the structural composition of the involved active site. We found that a genuine interaction between the COF backbone and the cobaloxime facilitates charge transfer and re-coordination of the co-catalyst during the photoreaction, thereby improving the reactivity and hindering degradation of the catalyst. This study highlights the importance of engineering the COF-co-catalyst interface and at the same time provides pertinent design principles for improved polymeric photocatalysts in general.

3.4.2 Introduction

Identifying competitive alternatives to fossil-fuel-based energy constitutes one of the main research goals of this decade. Nature-inspired processes, like artificial photosynthesis, guide the way to a green and sustainable solution. Much effort was put into research for different material classes like porous conjugated polymers^[1] or metal organic frameworks^[2] and processes like carbon dioxide reduction^[3] and photocatalytic hydrogen evolution. Covalent organic frameworks (COFs) are emerging as new materials for the conversion of sunlight into energetic materials like hydrogen.^[4-5] COFs consist of light-elements only and their



bottom-up synthesis enables high versatility and tunability on a molecular level while benefiting from high stability and crystallinity due to covalent bonding in plane and via π - π stacking out of plane.^[6-9] Most reports of COFs as photosensitizers for light-driven hydrogen evolution use platinum as a co-catalyst;^[10-12] hydrogen evolution rates up to 16.3 mmol h⁻¹ g⁻¹ have been reported in this context.^[13] Recent studies showed that the precious metal platinum can be replaced by earth-abundant molecular co-catalysts, namely chloro(pyridine)cobaloxime and related complexes.^[14-16] These co-catalysts are well-known and well-defined while offering high tunability, which facilitate their incorporation into photoactive organic and inorganic systems.^[17-19] Cobaloximes feature low overpotential for the hydrogen evolution reaction and have been used in heterogeneous systems with MOFs^[20-21] and carbon nitrides^[22-23], as well as physisorbed to COFs.^[14] A major drawback of molecular proton reduction catalysts physisorbed to photosensitizers is their photodeactivation over time^[24-26] and rate limitations due to diffusion-controlled mechanisms. While previous attempts^[14] used molecular cobaloxime catalysts in solution, in this work we report photocatalytic hydrogen evolution with molecular cobaloxime catalysts covalently tethered to the COF backbone, yielding unprecedented insights into the nature of the active site and the COF-co-catalyst interface. By comparison with equivalent unbound, i.e. physisorbed systems we show how the modification of the hydrazone-based COF-42 and attachment of functionalized chloro(pyridine)cobaloxime lead to more efficient hydrogen evolution in a water/acetonitrile mixture under visible light illumination in the presence of a sacrificial electron donor. The structural composition of the photoreaction is verified by computational and experimental methods including advanced high-resolution solid-state NMR techniques. These results combine the advantages of fully heterogeneous systems with the tunability of molecular co-catalysts and lead the way towards true single-site COF-based photocatalytic systems with a high level of interfacial control.

3.4.3 Results and discussion

COF characterization

In previous studies, COF-42^[27] has been shown to be active in photocatalytic hydrogen evolution reactions with conventional hydrogen evolution co-catalysts such as platinum nanoparticles or molecular chloro(pyridine)cobaloxime.^[14] At the same time, this COF is a well-known and versatile platform that is chemically robust due to its hydrazone-linked structure.^[28-29] In this study, we used COF-42 as a platform for covalent post-synthetic modification with cobaloxime complexes. The synthesis of COF-42 by solvothermal acid-catalyzed condensation of 1,3,5-triformylbenzene (TFB) and 2,5-diethoxyterephthalohydrazide (DETH) followed published protocols.^[27] In order to provide functional sites for the covalent attachment of the co-catalyst, 10 mol% of DETH was replaced by the

propargyl-containing 2,5-bis(prop-2-yn-1-yloxy)terephthalohydrazide (DPTH) to obtain the propargyl-modified pCOF₁₀. The COFs were characterized by FT-IR spectroscopy, sorption analysis, powder X-ray diffraction (PXRD), magic-angle-spinning solid-state NMR (ssNMR), and quantum-chemical calculations.

The successful transformation of the starting materials to pCOF₁₀ was proved by the lack of residual aldehyde stretches in its FT-IR spectrum. Characteristic C=O stretching vibrations and signals originating from the hydrazone bonds overlap at 1680 cm⁻¹ (see Figure 6-42). New vibrations emerged at 2250 cm⁻¹ which could be assigned to the propargyl groups confirming the successful incorporation of DPTH building blocks into the COF backbone. This was further supported by a 1D {¹H}¹³C ssNMR spectrum where signals at 79 and 58 ppm can be assigned to the propargyl functional group (Figure 3-13C). These shifts match the corresponding chemical shift of the liquid state NMR of the DPTH linker (see Chapter 6.1.2 for experimental details) and are also confirmed by quantum chemical calculations (see Table 6-12).

PXRD analysis confirmed the crystalline structure of pCOF₁₀. The PXRD pattern shows a strong reflection at 3.3° 2θ followed by smaller ones at 5.9, 7.0, 9.1 and a very broad one at 26° 2θ. The experimental powder pattern was compared to a simulated one (see Figure 3-13E) and the diffraction peaks assigned as the 100, 101, 200, 201 and 001 reflection, respectively. The peaks are broadened due to small domain sizes in the COF particles, especially in the z direction, where the interlayer interactions are defined by π-π-stacking only. Different possible orientations for the propargyl functionality as well as slightly shifted AA' stacking modes lead to very similar powder patterns; due to broadening of the reflections in the experimental data, the different orientations cannot be distinguished, one of these possible structural models is shown in Figure 3-13B. This model presents an AA stacking mode with an interlayer distance of 3.5 Å, which is typical for structurally similar COFs.^{[10]27^[30-31]} Note that in the underlying structural model, one out of six DETH linkers per pore was replaced by DPTH which results in a functionalization degree of 16.6% instead of the statistically distributed 10% in the experimentally prepared pCOF₁₀.

Pawley refinement of the structure in the idealized AA stacking mode suggests the *P2/m* symmetry. For the modeled structure, the resulting cell parameters are $a = 51.09 \text{ \AA}$, $b = 3.50 \text{ \AA}$, $c = 29.48 \text{ \AA}$ and $\alpha = \gamma = 90.00^\circ$ and $\beta = 89.94^\circ$. Sorption analysis revealed a mesoporous structure of the material with pore size of 2.3 nm and a Brunauer-Emmett-Teller (BET) surface area of 1839 m² g⁻¹, which matches the theoretically expected values of the structural model (see Figure 3-13D).

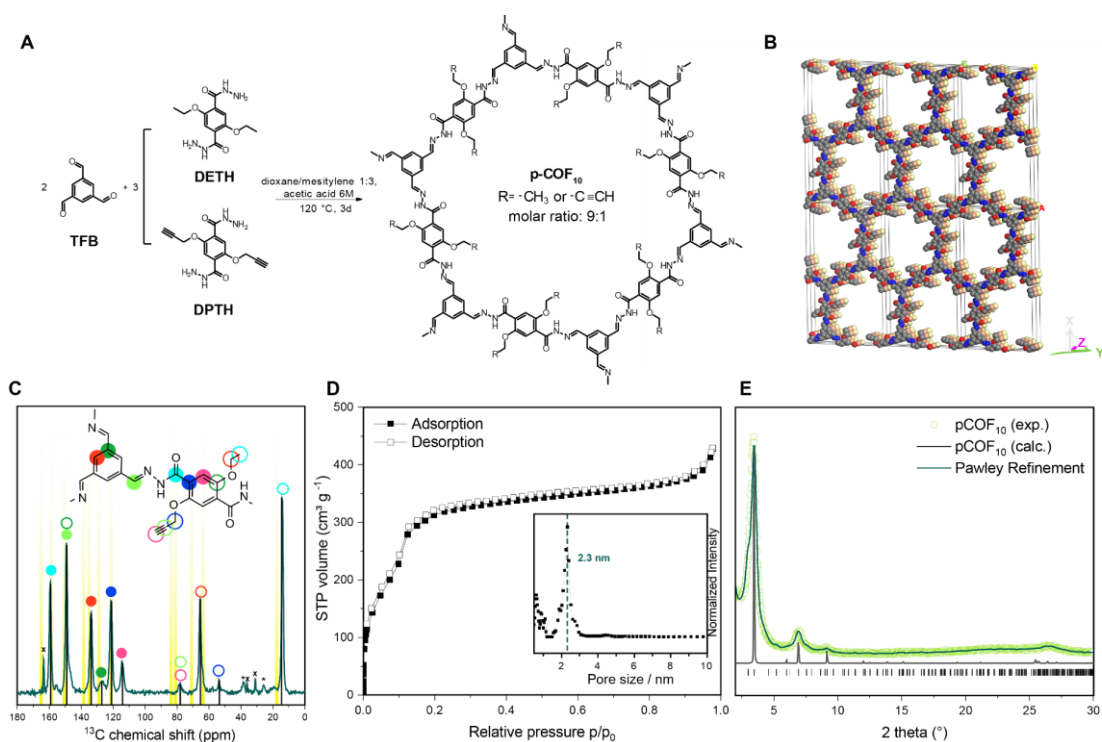


Figure 3-13: (A) Synthesis of pCOF₁₀ by solvothermal condensation of triformyl benzene (TFB) and a 9:1 mixture of 2,5-diethoxyterephthalohydrazide (DETH) and 2,5-bis(prop-2-yn-1-yloxy)terephthalohydrazide (DPTH). (B) Eclipsed stacking model for pCOF₁₀. C, N and O atoms are represented in grey, blue and red. H atoms are omitted, the second and third layer are represented in orange and yellow for clarity. (C) Solid state $1D^{13}C\{^1H\}$ CP-MAS NMR spectrum of pCOF₁₀ acquired at 11.7 T, 12 kHz MAS, 298 K, and using cross-polarization times of 5 ms. Spinning side bands are marked with asterisks. Calculated shifts are marked with yellow bars. The narrow signals labelled with crosses at 164 ppm, 37 ppm, and 32 ppm correspond to residual dimethylformamide. (D) Argon adsorption isotherm of pCOF₁₀. Inlet: Pore size distribution from NLDFT calculations with cylindrical pores in equilibrium mode. Resulting main pore size is 2.3 nm. (E) PXRD pattern of pCOF₁₀ (open, green circles), Pawley refined profile (blue line) and calculated XRD pattern for the idealized AA stacking (black line).

Postsynthetic modification and choice of ligands

For the covalent attachment of the cobaloxime catalyst to pCOF₁₀, a postsynthetic click-chemistry approach was chosen. The copper(II)-catalyzed Huisgen-type cycloaddition of azides and alkynes is known to be broadly applicable with high yields and a high tolerance for functional groups.^[32-36] Therefore, the pyridine which acts as axial cobaloxime ligand was functionalized with an azide group to yield the para-functionalized pyridine 1a, which forms the azide-functionalized complex [Co-1a] and likewise, the meta-functionalized analogues 1b and [Co-1b] were synthesized, as depicted in

Figure 3-14. It forms the azide-functionalized catalyst [Co-2] by metal complexation as before. Two strategies were tested for the attachment of the cobaloxime complex to pCOF₁₀: i) metal complexation of azide-functionalized ligands with subsequent COF-modification by

click-reaction with the azide-functionalized complexes, termed route I; ii) COF-modification by click-reaction with azide-functionalized ligands with subsequent complexation, termed route II (see Chapter 6.1.2 for experimental details). The resulting COF-cobaloxime hybrid samples are labeled as follows with the respective numbering according to Figure 3-14: **[1a]**-COF for clicked ligands; **[Co-1a]**-COF for COF-cobaloxime hybrid samples.

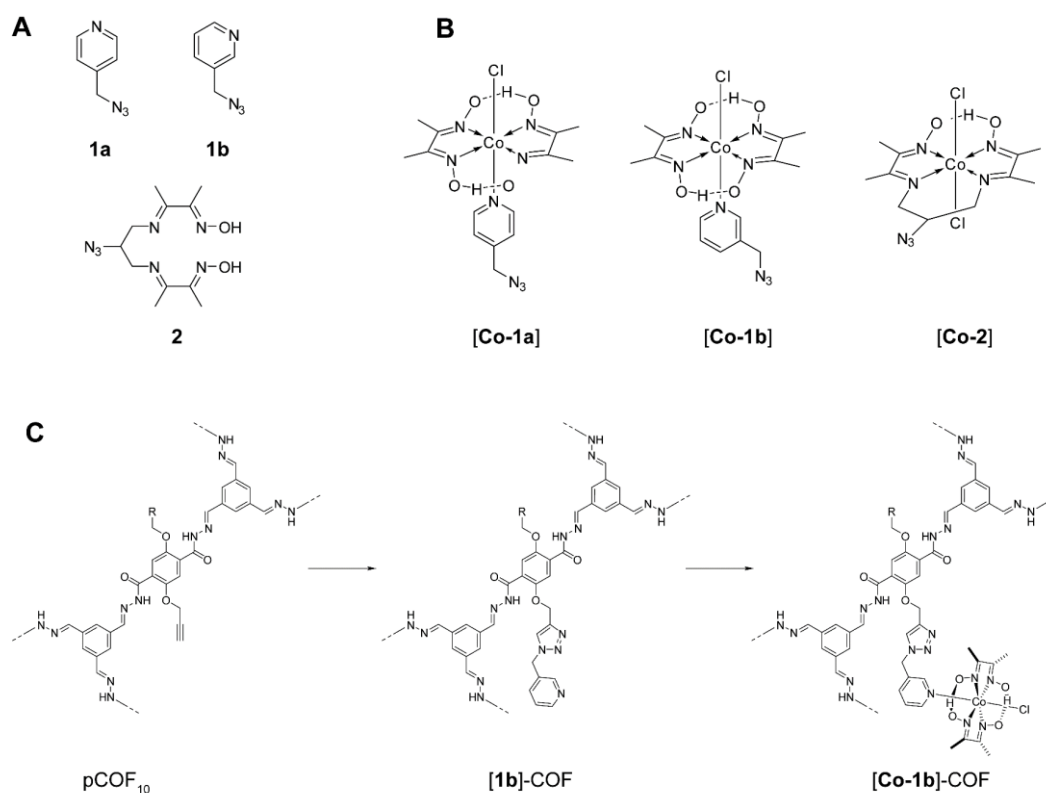


Figure 3-14:(A) Structure of the azide-functionalized ligands **1a**, **1b**, **2** and (B) the azide-functionalized complexes **[Co-1a]**, **[Co-1b]**, and **[Co-2]**. (C) Exemplary postsynthetic COF modification towards **[Co-1b]**-COF. Synthesis conditions can be found in Chapter 6.1.2.

Characterization of the COF-cobaloxime hybrid systems

To verify the success of the tethering of the cobaloxime and the unperturbed structural integrity of the covalently modified hybrid COF-cobaloxime systems we performed the same systematic experimental analysis as for the intact pCOF₁₀. PXRD shows that the crystallinity of the COF is preserved and the stacking mode does not change with respect to pCOF₁₀ (Figure 6-35). Sorption analysis shows the expected reduction of the surface area according to Table 6-9. Pore size distributions for the clicked samples were calculated from Ar sorption isotherms as shown in Figure 6-34. In all samples, the 2.3 nm pore size, as found in pCOF₁₀, is preserved with lower pore volume fraction while additional smaller pores up to 1.9 nm



occur as seen from optimized pore models (see Figure 6-47). FT-IR spectra display all expected vibrations of the COF including propargyl vibrations at ca. 3300 and 2300 cm^{-1} . These vibrations are still visible in ligand-tethered samples which hints to partial transformation. New triazole peaks are hidden in the region around 3100 cm^{-1} due to low intensity. The success of the click reaction was further confirmed by the reduced intensity of the propargyl signals relative to the other signals in the 1D $\{^1\text{H}\} \text{ }^{13}\text{C}$ CP ssNMR spectrum upon addition of the azide compounds. We did not observe any additional signals arising from the clicked compound, which is probably due to signal superposition, especially in the aromatic region, and due to lower signal intensity caused by a low functionalization degree. UV-Vis diffuse reflectance spectra show two additional broad absorption bands at 500 and 600 nm for the cobaloxime containing samples (Figure 6-44). These bands are due to the electronic transitions of the azide-functionalized cobaloximes. Depending on the reaction conditions (see Chapter 6.1.2 for more details), the cobaloxime loading can be adjusted within limits. For all samples, the total cobaloxime amount was determined by ICP analysis, and for [Co-1a]-COF it was additionally confirmed by fast-MAS -detected NMR spectra. The values range from 0.47 to 2.4 wt% for route II, while route I resulted in higher cobaloxime amounts between 1.2 and 8.5 wt%. The highest cobaloxime content was found for [Co-1a]-COF as can be seen in Table 6-11. The resulting functionalization degrees ranging from 2.0 to 15% are also listed there.

ssNMR of the COF-cobaloxime hybrid systems

While powder diffraction analysis provides long-range spatial information such as approximate interlayer separations, ssNMR provides us with short-range interatomic proximities, and hints about the position of the cobaloxime inside the pore. To this end, we performed an in-depth structural analysis of the clicked samples **1a**-COF and [Co-1a]-COF using ^1H -detected, fast-MAS ssNMR at $\nu_{\text{rot}} = 55.55$ kHz at 700 MHz ^1H Larmor frequency (16.4 T). The samples based on [Co-1a] were chosen due to higher molecular symmetry compared to [Co-1b]. Both **1a**-COF and [Co-1a]-COF were studied by 1D and 2D ^1H and ^{13}C solid-state NMR techniques. All 2D measurements were ^1H -detected, which significantly improved the sensitivity of the natural abundance measurements. In addition to the sensitivity gain, we could exploit the ^1H chemical shifts as well as the ^1H - ^1H correlations as sources of structural information. Figure 3-15B compares the 1D ^1H spectra of **1a**-COF (yellow) and [Co-1a]-COF (blue). The high structural order of these two-dimensional crystalline polymers is reflected in the good resolution of the ^1H signals (^1H line widths vary between 800 and 1300 Hz for **1a**-COF and between 1000 and 2000 Hz for [Co-1a]-COF). In the ^1H spectra, we could directly observe four (**1a**-COF) and five ([Co-1a]-COF) distinct proton resonances which correspond to the amide proton (10.9 ppm), aromatic protons overlapping with the

olefin proton (7.2 ppm), methylene protons (3.9 ppm), methyl protons (1.7 ppm), and for [Co-1a]-COF, we also observe a well-separated, downfield-shifted, low-intensity peak that belongs to the strongly hydrogen-bonded oxime proton (19.1 ppm). Note that all signals are broader in the spectrum of [Co-1a]-COF relative to 1a-COF which indicates that the cobaloxime functionalization process disrupted the overall COF crystallinity to some extent. Cobaloxime contains Co(III) which is, unlike Co(II), diamagnetic, therefore the observed line broadening of [Co-1a]-COF cannot be a consequence of paramagnetic relaxation enhancement; also residual salt is washed out during the sample preparation process. It is more likely that the post-synthetic modification reduced the crystalline domain size and increased the sample's inhomogeneity leading to a wider range of chemical shifts for each site.

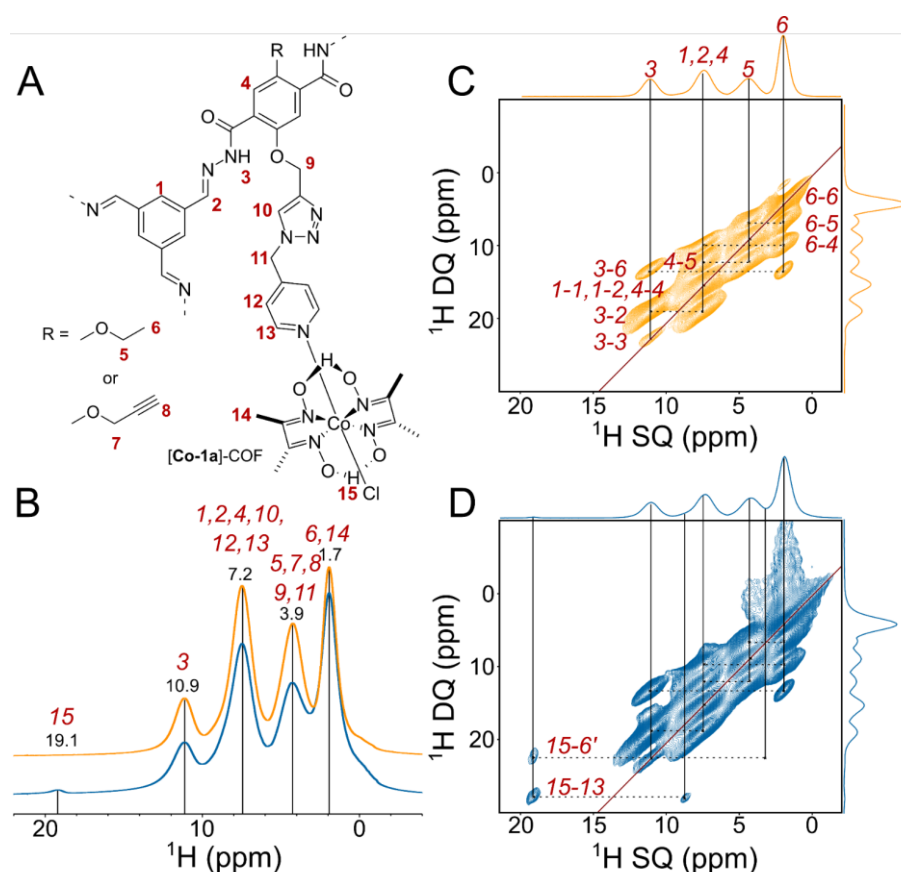


Figure 3-15: Solid-state NMR comparison of the ^1H spectra of [1a]-COF (yellow) and [Co-1a]-COF (blue) measured at 700 MHz ^1H Larmor frequency at $\nu_{\text{rot}} = 55.55$ kHz. (A) Schematic structure of the subsection of [Co-1a]-COF with proton labeling. (B) 1D ^1H spectra of [1a]-COF (yellow) and [Co-1a]-COF (blue). Distinct ^1H resonances are given in ppm and labelled with the corresponding atom labels as displayed in (A). (C) and (D) ^1H - ^1H DQ-SQ correlation spectra of [1a]-COF (yellow) and [Co-1a]-COF (blue). Horizontal dashed lines indicate the ^1H - ^1H connectivities, and vertical solid lines reflect the individual ^1H SQ resonances. Assignments are given next to the dashed lines. In (D) the assignment for only the two new connectivities are shown. The sky-line projection of both dimensions are also shown.



The good ^1H resolution of the fast-MAS ^1H spectrum prompted us to measure 2D homonuclear correlation experiments to gain deeper insight into the intramolecular interaction between the COF backbone and the cobaloxime co-catalyst. We probed the relative ^1H - ^1H distances using a 2D double quantum-single quantum (DQ-SQ) correlation experiment employing the R-symmetry-based $\text{R}14_4^{-2}$ homonuclear recoupling sequence.^[37] The $\text{R}14_4^{-2}$ is a γ -encoded symmetry sequence which suppresses all heteronuclear dipole-dipole couplings and chemical shift terms in the first-order Hamiltonian. We used a $R = \pi_0$ element as the basic R-symmetry block with a nutation frequency of 97.22 kHz ($3.5 \times \nu_{\text{rot}}$). The homonuclear 2D ^1H - ^1H DQ-SQ recoupling experiment relies on the generation of double quantum coherences *via* homonuclear dipole-dipole coupling to obtain through-space information of nearby protons. Due to the double-quantum filter, the spectrum exhibits cross-peaks only between protons that are in direct dipolar interactions with each other and thus no relayed magnetization transfer occurs. For protonated organic solid materials, such as the COFs of this study, the observation of a DQ peak is indicative of a proton-proton proximity that is $\leq 3.5 \text{ \AA}$.^[38-39] The relative signal intensities could well approximate interatomic distances.^[39]

Figure 3-15C and D show the ^1H - ^1H DQ-SQ correlation spectra of **1a**-COF (yellow) and [**Co-1a**]-COF (blue). The spectra reveal double quantum correlations between both distinct and identical environments, appearing at the off-diagonal and diagonal positions, respectively. Diagonal peaks are expected for the signals of the methyl and methylene group, as well as between the resonances of the chemically equivalent aromatic sites. However, the weak diagonal peak for the NH protons corresponds to an NH-NH autopeak which is indicative of the dipolar interaction between COF layers; the separation of NH protons within one layer is $< 7 \text{ \AA}$, while the layer-to-layer distance is 3.5 \AA according to powder crystal analysis. The two spectra look almost identical, the only considerable difference being the ^1H cross-peaks of the oxime at 19.1 ppm with resonances at 8.7 and 3.4 ppm. In order to assign these two peaks, and thus uncover the position of Co-oxime inside the pore, we performed a detailed quantum chemical study (*vide infra*). Based on these studies we conclude the resonances at 8.7 and 3.4 ppm to belong to the pyridine aromatic proton (H13), as well as to a downfield shifted methyl proton of a neighboring ethoxy group with which the cobaloxime is in close contact.

Next, we assessed the relative flexibility of the two compounds using 1D ^{13}C NMR spectroscopy. Three different 1D ^{13}C MAS spectra of [**1a**]-COF and [**Co-1a**]-COF are given in Figure 3-16A and B, respectively. These spectra include $^{13}\text{C} \{^1\text{H}\}$ cross-polarization (CP) MAS, and T_1 -weighted, direct-polarization (DP) ^{13}C spectra recorded with short (1 s) and long (25 s) recycle delay times. These latter spectra were used to elucidate the relative mobility of certain sites in the COF samples. In the ^{13}C spectra recorded with $d_1 = 1 \text{ s}$ those

signals are more intense that have considerably shorter ^{13}C longitudinal relaxation time constants ($T_1 < 1$ s), since the signal recovery is proportional to $1 - \exp(-d_1/T_1)$. Such short T_1 is indicative of motions occurring on the inverse of the Larmor frequency (few nanoseconds). The longitudinal relaxation constant depends not only on the amplitude of ns time-scale motion but also on the number of directly attached protons: the more protons are directly bound to a carbon the faster it relaxes via heteronuclear dipolar relaxation. This is reflected in the relative change of signal intensities among the aromatic carbons. Besides, the methyl resonance relaxes rapidly due to the free rotation around the C-C axis in the ethyl group. The methyl resonance line shape in the DP spectrum of [Co-1a]-COF is markedly distorted presenting a shoulder at lower resonances. This signal could be assigned to the methyl carbons of the cobaloxime ligand. Otherwise, the signals of the covalently tethered ligand does not show any obvious sign of increased fast time-scale flexibility, neither for [1a]-COF nor for [Co-1a]-COF. In the spectrum of [Co-1a]-COF recorded with $d_1 = 1$ s the intensified resonances at 128 ppm indicate rather flexible aromatic sites, but due to strong overlaps in this region we could not identify if this signal belongs to the ligand or to some residual impurities which tend to show up stronger in T_1 -weighted experiments. Selective ^{13}C or ^{15}N labeling at specified positions at the ligand would help us to quantify the amplitude and time scale of the ligand motion.

The apparent lack of high-amplitude fast time-scale dynamics of the two COF frameworks were further validated by comparing ^1H -detected 2D CP-based ^1H - ^{13}C correlation spectra with INEPT-based 2D HSQC spectra (Figure 3-16D, E). High-amplitude ns time-scale motion results in inherent decoupling and thus leads to increased coherent lifetimes in INEPT-based experiments and to decreased transfer efficiencies in CP-based experiments. In the HSQC spectrum of both [1a]-COF and [Co-1a]-COF we observe only a single methyl peak indicating that the COF backbone is generally rigid on the ns time scale.

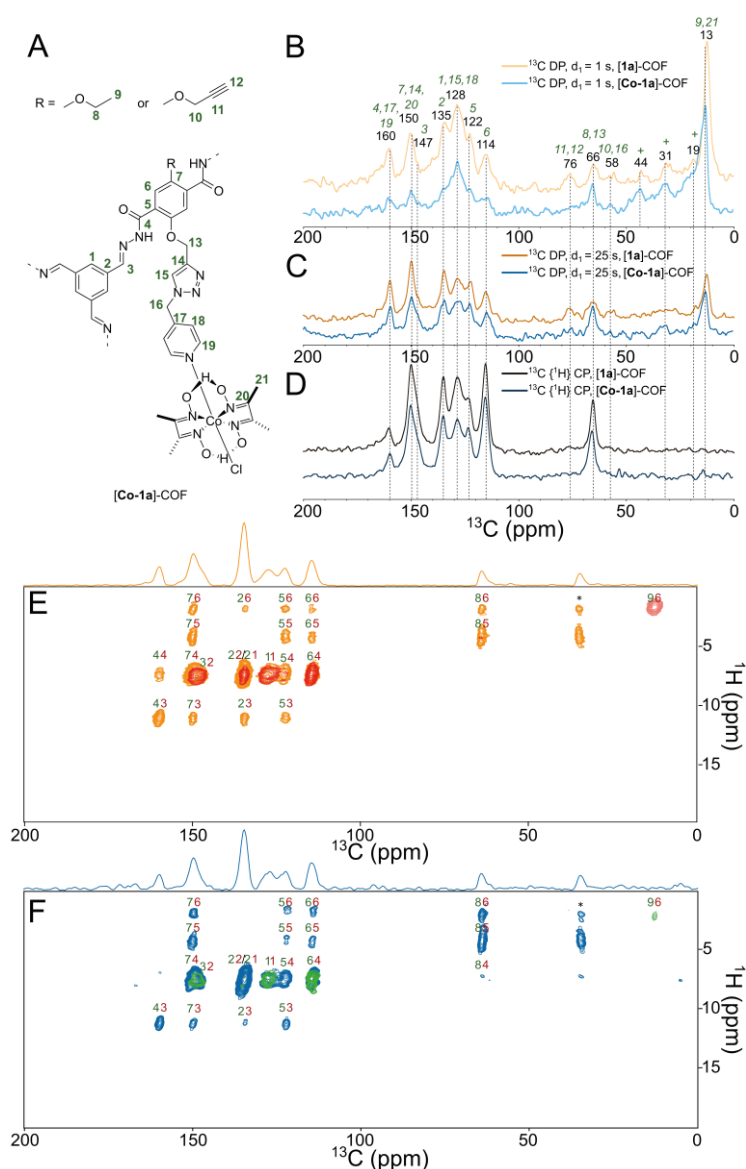


Figure 3-16: (A) Schematic structure of the subsection of **[Co-1a]-COF** with carbon labeling. (B), (C) and (D) Comparison of the natural abundance ^{13}C one-dimensional solid-state NMR spectra of **[1a]-COF** (blue shades) and **[Co-1a]-COF** (orange shades) measured at 700 MHz Larmor frequency at $\nu_{\text{rot}} = 55.55$ kHz. Direct polarization spectra recorded with $d_1 = 1$ s (B) or with long $d_1 = 25$ s (C) are compared with CP MAS spectra (D). For the CP MAS experiment, the carrier was centered at 130 ppm and the CP was optimized to transfer magnetization to the aromatic region. The CP contact time was 500 μs . Signals with short longitudinal relaxation times are enhanced in the ^{13}C direct MAS spectrum measured with 1 s recycle delay. The assignment of the ^{13}C resonances was obtained from 2D ^1H - ^{13}C , and ^1H - ^1H correlation experiments, and from the quantum chemical calculations. The signals marked with crosses correspond to impurities, e.g. to residual solvent signals. (E) and (F) ^1H -detected 2D ^1H - ^{13}C correlation spectra of **[1a]-COF** (E) and **[Co-1a]-COF** (F) recorded with 500 μs (red and green), or with 2250 μs (orange and blue) CP contact times. The CP-based spectra are overlaid with INEPT-based HSQC spectra which display only one methyl cross-peak displayed with blue (E) and magenta (F) colors. For each cross peak the ^1H and ^{13}C assignments are displayed with red and green colors, respectively. Signals marked with an asterisk are measurement artefacts and they do not appear in 1D ^{13}C -detected $^1\text{H}\{^{13}\text{C}\}$ CP spectra.

Computational studies

In order to provide a structural model for the position and the orientation of the covalently tethered cobaloxime co-catalyst inside the pore, a detailed *in silico* structural investigation of [1a]-COF and [Co-1a]-COF was conducted. Atom positions and lattices of the periodic COF structure of [1a]-COF were optimized on RI-PBE-D3/def2-TZVP^[40-43] level of theory using an acceleration scheme based on the resolution of the identity (RI) technique and the continuous fast multipole method (CFMM)^[44-46] implemented^[47-48] in Turbomole version V7.1.^[49] The obtained structure for the [1a]-COF was then used to prepare parameters for molecular dynamics simulations using antechamber.^[50] Force field minimizations and subsequent dynamics were performed using the NAMD program package^[51-52] using GAFF parameters^[53] afterwards. NMR chemical shifts were then calculated on B97-2/pcSseg-1.^[54-55] level of theory using the FermiONs++^[56-57] program package, using cut models of obtained structures to compare with experimentally obtained chemical shifts and establish the assignment of peaks.

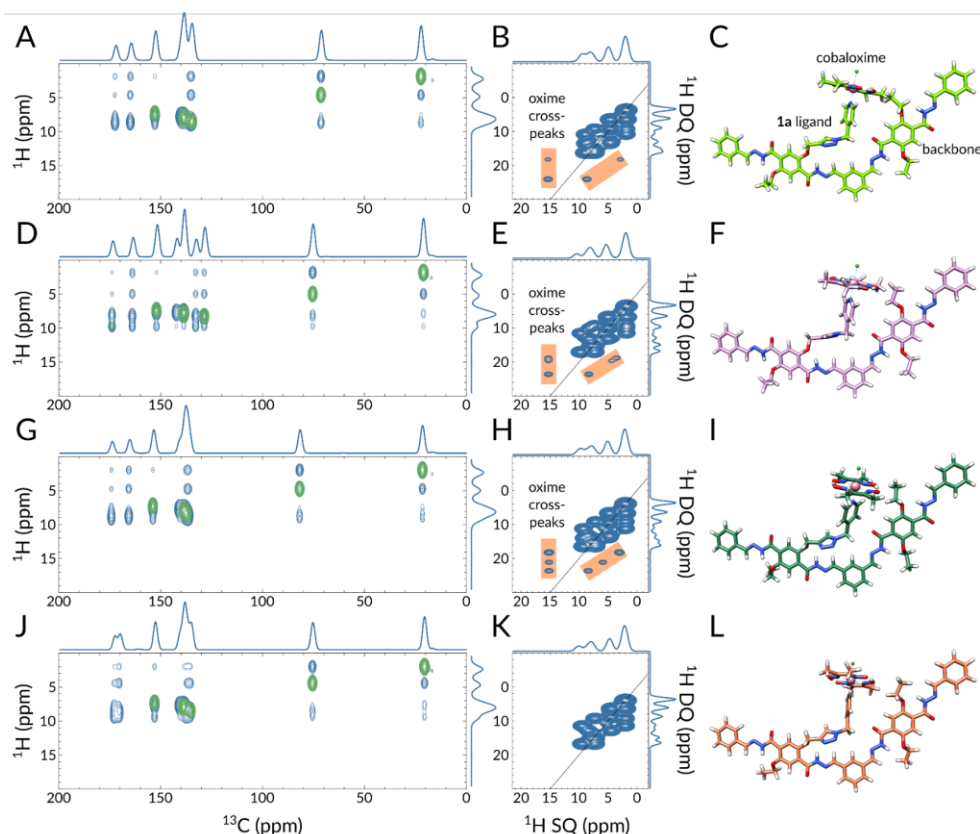


Figure 3-17: Direct comparison of quantum-chemically obtained ^1H - ^{13}C (A, D, G, J) and ^1H - ^1H DQ-SQ (B, E, H, K) 2D ssNMR spectra with corresponding structural models of [Co-1a]-COF on the right (C, F, I, L). For a better comparison, the same NMR chemical shift region is displayed as in the experimentally obtained spectra (Fig. 3C, D and Fig. 4D, E). In the ^1H - ^{13}C 2D spectra blue and green colors represent ^1H - ^{13}C atom pairs that are within 6 and 2 Å, respectively. In the ^1H - ^1H DQ-SQ spectra, the orange color highlights the oxime proton cross-peaks. In C, F, I, and L the Co, Cl, O, N, and H atoms are displayed with pink, lime, red, blue, and white colors, respectively.

Using this data, we prepared 200 *in silico* ^1H - ^1H DQ-SQ and ^1H - ^{13}C 2D correlation spectra (see Chapter 6.1.2 for details) and used them to identify features that are also present in the experimentally obtained ssNMR spectra. Such features include the number of cross-peaks, especially cross-peaks of the oxime proton, their relative intensity ratios, and their peak positions. The most distinctive factor in the simulated ^1H - ^1H DQ-SQ spectra is the presence of oxime (H15) cross-peaks with resonances at around 8.7 and 3.4 ppm, which was used to categorize the simulated spectra. These distinct chemical shifts suggest that the oxime proton is interacting with an aromatic proton (at 8.7 ppm), and with either an upfield shifted methylene proton or with a downfield shifted methyl proton (at 3.4 ppm). There are four different aromatic protons in [Co-1a]-COF: H1, H4, H12, and H13, out of which only H4 and H13 can get closer than 3.5 Å to H15.

To decide which resonance lead to the 3.4 ppm cross-peak with H15, we analyzed the shielding effects of the glyoxime group on the nearby ethoxy methyl and methylene protons. The approach of the glyoxime oxygen towards the ethoxy group induces a deshielding effect, consequently, both the methyl and the methylene protons resonate at higher frequencies (see Figure 6-55 and Chapter 6.1.2 for more details), this rules out the possibility that the cross-peak at 3.4 ppm would stem from an upfield shifted methylene proton and leaves only a downfield shifted methyl proton as a possible interaction partner. Besides, we excluded the possibility that the oxime proton shows a trivial intra-ligand cross-peak with the glyoxime methyl protons, since (i) the distance between the H15 and H16 protons are > 3.5 Å, and (ii) the calculated chemical shift are below 2.9 ppm.

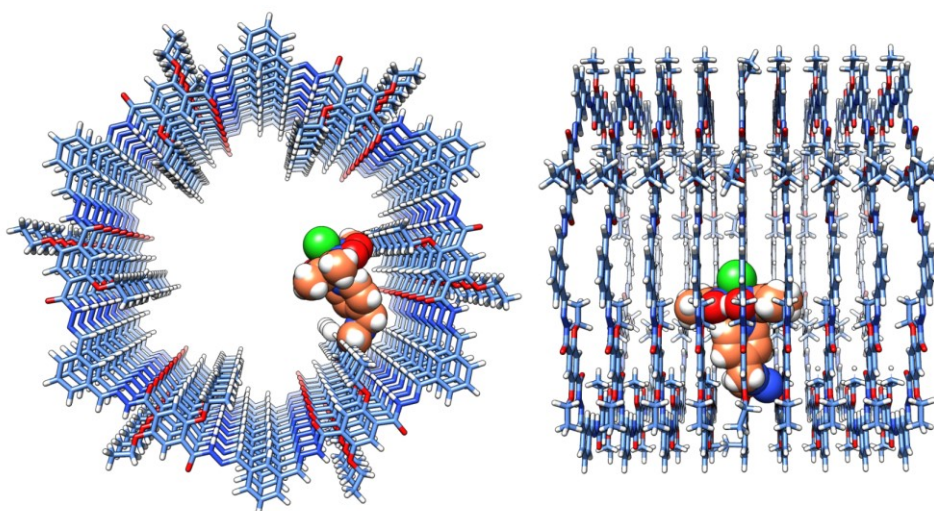


Figure 3-18: Front and side views of the MD simulated structural model of [Co-1a]-COF showing a possible arrangement of the co-catalyst. The linker and the cobaloxime group are depicted by spheres and their carbon atoms are displayed with orange color. Co, Cl, O, N, and H atoms are displayed with pink, lime, red, blue, and white colors, C atoms of the backbone is light blue.

Out of the 200 simulated ^1H - ^1H DQ-SQ spectra 27 (13) contained two (three) oxime cross-peaks, among which 22 spectra have these peaks in the expected ppm range. By considering the relative peak intensity ratios between the oxime cross-peaks only 15 spectra have a more intense than a methyl-oxime cross peak. Two of such spectra, together with the simulated ^1H - ^{13}C spectra and corresponding structures, are displayed in Figure 3-17A-F. As counter-examples, Figure 3-17G-H and J-K display the spectra of such structures (Figure 3-17I and L) where three equally intense peaks (Figure 3-17H) or no oxime proton cross peak (Figure 3-17K) appear in the simulated DQ-SQ spectra. The possibility that in reality, in a fraction of the [Co-1a]-COF pores the cobaloxime does not interact with the pore wall cannot be ruled out, nonetheless, our current data suggests that when it does, it gets in close contact with the nearby ethoxy group. It is also likely that this genuine interaction stabilizes the complex and restricts the co-catalyst's degradation during the photocatalytic cycles. Note that at this stage, both the ssNMR measurements and the *in silico* calculations were performed in a solvent-free environment. Future ssNMR measurements with added acetonitrile/water mixture accompanied with simulations in explicit solvent could reveal if the cobaloxime stays attached to the pore wall or whether it gains more flexibility and drifts towards the pore center.

To inspect the spacial arrangement inside the pore, we modelled [Co-1a]-COF including one tethered co-catalyst based on the MD simulated structures (Figure 3-18). The displayed ligand has the same orientation as in Figure 3-17C. From the side and front views, it is apparent that the ligand spreads over multiple layers and occupies a substantial portion of the pore. Due to spacial confinements our model suggests that no more than three [Co-1a] over three layers can fit into the backbone, i.e. the maximum number of [Co-1a] per layer is one. In our case, we have 13 mol% functionalization which translates into one [Co-1a] for every seven layers.

Photocatalytic activity

To probe whether there is a possible benefit of covalent co-catalyst immobilization over simple physisorption,^[14-15] the COF-cobaloxime hybrid samples were tested for photocatalytic activity. In a typical photocatalysis experiment, 5 mg of COF hybrid were suspended in 10 mL of acetonitrile and water in a ratio of 4:1 at pH 8 containing 100 μL tri-ethanolamine (TEOA) as sacrificial donor. A housed Xe lamp was used to illuminate the suspension interface with a nominal beam spectral distribution similar to AM1.5G. The beam intensity before experiments was then adjusted to 100 mW cm^{-1} . See Chapter 6.1.2 for more details. Photocatalytic hydrogen evolution reaction (HER) rates were quantified in a continuous flow reactor as previously reported^[15] (Figure 3-19A). As a reference system, we compared the hybrid systems to samples where [Co-1a] or [Co-1b] were added to the

suspension and physisorbed to COF-42 with a BET surface area of $2336 \text{ m}^2 \text{ g}^{-1}$ during photocatalysis. As different lamps were used for different measurements, photonic efficiencies were calculated to guarantee comparability of the numbers. The maximum photonic efficiencies after *in situ* photoactivation of the samples ranging from 2 to 8 wt% cobaloxime catalyst according to ICP results can be found in Figure 3-19A. In the physisorbed samples, an increase of the photonic efficiency was found when increasing the catalyst amount from 2 to 4 wt% with a maximum efficiency of 0.06% for [Co-1a] and 0.07% for [Co-1b] at 4.0 wt%, while the efficiency is fairly constant at higher percentages (0.06% to 0.08% at 5.0 and 8.0 wt% for [Co-1b]). This behaviour is expected for the system as in the low-loading region, the photocatalytic activity scales linearly with the co-catalyst amount while it reaches a maximum in the higher-loading region where the availability of the co-catalyst is not limiting anymore.

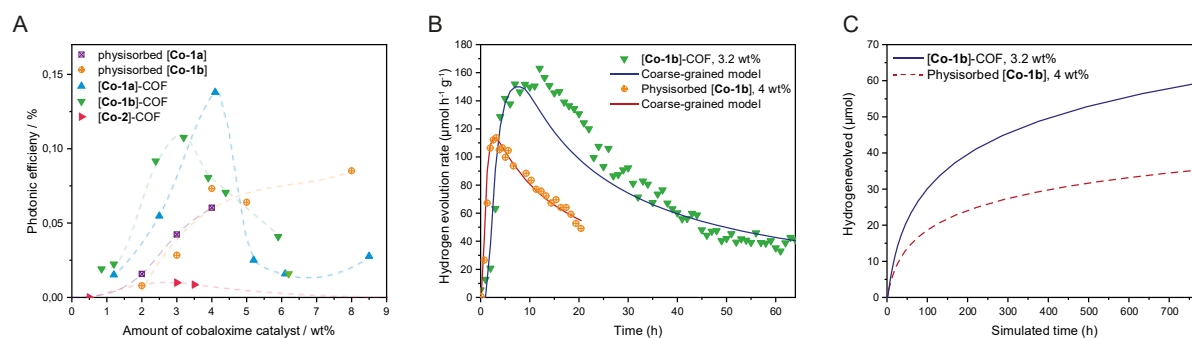


Figure 3-19: (A) Comparison of photonic efficiencies for hybrid samples and COF-42 with physisorbed [Co-1a] and [Co-1b]. (B) Comparison of the hydrogen evolution rate of [Co-1b]-COF containing 3.2 wt% [Co-1b] and COF-42 with 4.0 wt% physisorbed [Co-1b] and coarse-grained model fits of both systems. (C) Projection of the hydrogen evolution of [Co-1b]-COF containing 3.2 wt% [Co-1b] and COF-42 with 4.0 wt% physisorbed [Co-1b] based on the coarse-grained models.

In the hybrid samples, an activity maximum rather than a constant behavior is found for each hybrid type. For the para-functionalized [Co-1a], the highest photonic efficiency was found at 4.1 wt%, while for the meta-functionalized [Co-1b] the maximum was found at 3.2 wt%. As before, a linear increase of the photonic efficiency in the low-loading regime was observed. However, further increase in cobaloxime loading resulted in lower activity in the immobilized samples. We attribute this to a predominant pore clogging effect of the active sites with increasing functionalization. In general, the highest photonic efficiency was achieved with [Co-1a]-COF with 0.14% followed by [Co-1b]-COF with 0.11%. Compared to the physisorbed samples with the corresponding cobaloxime content, the activity doubles for both systems. Additionally, to emphasize the role of the complex environment of the cobaloxime over the pure presence of Co(II) we performed a measurement where we added to a suspension of pCOF₁₀ and triethanolamine in the photocatalysis medium as well as

experiments where one of the components (COF, TEOA) was excluded (Figure 3-19B). None of the reference samples showed hydrogen evolution after several hours of irradiation. For the hybrid samples, the close contact between the cobaloxime and the COF pore wall - revealed by representative solid state NMR and computational studies (*vide supra*) - might facilitate charge transfer to the cobaloxime catalyst from the COF pore wall as also observed from photoluminescence measurements (see Figure 6-40 and Figure 6-41). The meta-functionalized equivalent ([Co-1b]-COF) is expected to have less interaction with the pore wall which would account for its decreased photocatalytic activity. [Co-2]-COF shows a significantly lower activity in which is a known effect for cobaloximes that lack equatorial protons. The protonation of the oxime oxygen, which is necessary for the catalytic process, is hindered in those cases.^[58]^[59] The catalytic activity could not be improved by lowering the pH to 4. In this case, different acids (ascorbic acid, acetic acid, and citric acid) were tested which simultaneously served as sacrificial electron donors instead of the amine base TEOA. Even though the stability of [Co-2]-COF is predicted to be higher than for the other tested cobaloximes, the complex proved not to be appropriate in our case. We compared the best performing [Co-1b]-COF sample (containing 3.2 wt% cobaloxime) to COF-42 physisorbed with [Co-1b]. A sample with the same amount of physisorbed cobaloxime was qualitatively active in photocatalytic hydrogen evolution, but for precise quantification we increased the catalyst amount to 4.0 wt%. Even though it contained 20% less catalyst, the hybrid sample was 47% more active than the physisorbed one (163 vs. $111 \mu\text{mol h}^{-1} \text{g}^{-1}$), see Figure 3-19A. Additionally, the long-term stability increased significantly. After 20 h, the physisorbed sample shows 52% of its initial activity, while the hybrid sample maintains 80% of its initial activity. To get an estimate of the longevity of the systems, we fitted the hydrogen evolution rates of both samples with a coarse-grained model (Figure 3-19C) that was established in an earlier study on photocatalysis with COFs and a Nickel-based oligomer as co-catalyst.^[15] The model resulted in very precise fitting for the physisorbed catalyst because of similarities to the original Nickel-based system from where the coarse-grain fitting model was obtained, while the hybrid sample showed a more complex behaviour that is not perfectly mapped with this simplified model. Based on the coarse-grained fits, we projected the total amount of hydrogen evolved by the samples at full depletion (see Figure 3-19C). After 780 h, the projection of the physisorbed sample reaches $35 \mu\text{mol}$ hydrogen evolved while the value is $59 \mu\text{mol}$ for the hybrid sample, which is a gain of 69%. Comparing the estimated turnover number (TON) of both systems, the deviation gets even more obvious. While the TON after 780 h is simulated to be 81 for the physisorbed sample, it increases by 110% to a value of 170 in the hybrid sample. We attribute this activity enhancement to the local confinement in the COF-hybrid samples as supported by MD simulations.



Cobaloximes are known to slowly decompose under photocatalytic conditions. The labile axial pyridine ligand decoordinates in the catalytic cycle due to a square-planar Co(II) transition state. The catalyst in solution can then possibly be reduced which limits its stability. Due to the confinement between ligand and catalyst in the COF pores, the re-coordination might be enhanced, hence counteracting degradation, which leads to reactivation of the catalyst. Additionally, charge transfer is favored in the case of spatial proximity of the co-catalyst and the pore wall. Both effects result in higher overall activity as well as longevity. Interestingly, the activation period for the hybrid samples is significantly longer than for the physisorbed ones. This may be attributed to the time-delayed accessibility of the catalyst in the pores. Both limitations could be addressed via a method that was recently published by Thomas and coworkers^[60-61], where silica spheres were used to create an inverse-opal architecture in the COF material. The so created macropores could serve as channels for reagents and products. Also, immobilization of the co-catalyst in a COF with larger pores might have a similar effect.

3.4.4 Conclusion

In summary, we have developed a platform derived from COF-42 as a support for the immobilization of cobaloxime catalysts. The post-synthetic modification of propargyl-functionalized COF-42 enabled the covalent tethering of three different cobaloximes to form COF-cobaloxime hybrid systems. This tethering significantly enhanced the photocatalytic activity of the system by more than 100% compared to the physisorbates with the corresponding cobaloxime amount. The high crystallinity of our materials allowed for an in-depth solid-state 2D NMR characterization using fast MAS and proton detection. In the 1D ^1H spectrum of [Co-1a]-COF we could clearly identify the resonance corresponding to the oxime proton based on its highly downfield shifted resonance. The 2D ^1H - ^1H Dq-Sq experiment showed two cross-peaks for the oxime proton consistent with the incorporation of the co-catalyst into the COF material. MD simulations with subsequent quantum-chemical NMR chemical shift calculations allowed us to locate the position of the tethered ligand inside the pore based on the experimentally observed oxime proton cross peaks. Our analysis suggests that the cobaloxime in [Co-1a]-COF closely interacts with the pore wall. We surmise this interaction is responsible both for the improved photocatalytic activity and for the prolonged activity of the hybrid samples with respect to the physisorbed variant. We anticipate that larger pore channels or the addition of dedicated transport pores will further improve the pore accessibility and prevent back-reaction via local confinement of the products, thereby further increasing the hydrogen evolution activity of the system even further.

3.4.5 Acknowledgements

Financial support is gratefully acknowledged from the Max Planck Society, an ERC Starting Grant (project COF Leaf, grant number 639233), the Deutsche Forschungsgemeinschaft (DFG) via the SFB 1333 (project A03), the Cluster of Excellence e-conversion, and the Center for Nanoscience. PR acknowledges the Deutsche Forschungsgemeinschaft (DFG, German Research Foundation) SFB 1309 – 325871075, project A3 and Fonds der Chemischen Industrie. We thank Prof. T. Bein and Prof. W. Schnick (University of Munich, LMU) for granting access to the XRD facility and V. Duppel and M.-L. Schreiber for the assistance with material analysis.

3.4.6 Author contributions

Kerstin Gottschling had the initial idea for the project and designed and performed the experiments as well as the evaluation of analytical data. Gökçen Savasci designed and performed all quantum chemical calculations and evaluated analytical data, esp. NMR data. Hugo Vignolo-González performed photocatalysis measurements and corresponding analytic evaluation including numerical calculation of photocatalysis rates. Sandra Schmidt and Phillip Mauker helped with sample preparation. Tanmay Banerjee performed additional experiments (PL, XRD) for revision. Petra Rovó supervised the NMR study and performed all NMR experiments and analytical evaluation. Christian Ochsenfeld and Bettina V. Lotsch supervised the project. All authors worked on and revised the manuscript.

3.4.7 References

- [1] L. Li, Z. Cai, Q. Wu, W.-Y. Lo, N. Zhang, L. X. Chen, L. Yu, *J. Am. Chem. Soc.* **2016**, *138*, 7681-7686.
- [2] Y. Zhang, F. Mao, L. Wang, H. Yuan, P. F. Liu, H. G. Yang, *Solar RRL* **2019**, *n/a*, 1900438.
- [3] C. S. Diercks, Y. Liu, K. E. Cordova, O. M. Yaghi, *Nature Materials* **2018**, *17*, 301-307.
- [4] V. S. Vyas, V. W.-h. Lau, B. V. Lotsch, *Chem. Mater.* **2016**, *28*, 5191-5204.
- [5] T. Sick, A. G. Hufnagel, J. Kampmann, I. Kondofersky, M. Calik, J. M. Rotter, A. Evans, M. Döblinger, S. Herbert, K. Peters, D. Böhm, P. Knochel, D. D. Medina, D. Fattakhova-Rohlfing, T. Bein, *J. Am. Chem. Soc.* **2017**, *140*, 2085-2092.
- [6] A. P. Côté, A. I. Benin, N. W. Ockwig, M. O'Keeffe, A. J. Matzger, O. M. Yaghi, *Science* **2005**, *310*, 1166-1170.
- [7] R. W. Tilford, S. J. Mugavero, P. J. Pellechia, J. J. Lavigne, *Adv. Mater.* **2008**, *20*, 2741-2746.
- [8] S.-Y. Ding, W. Wang, *Chem. Soc. Rev.* **2013**, *42*, 548-568.
- [9] M. S. Lohse, T. Bein, *Adv. Funct. Mater.* **2018**, *28*, 1705553-1705553.
- [10] L. Stegbauer, K. Schwinghammer, B. V. Lotsch, *Chemical Science* **2014**, *5*, 2789-2793.
- [11] F. Haase, T. Banerjee, G. Savasci, C. Ochsenfeld, B. V. Lotsch, *Faraday Discuss.* **2017**, *201*, 247-264.



- [12] L. Stegbauer, S. Zech, G. Savasci, T. Banerjee, F. Podjaski, K. Schwinghammer, C. Ochsenfeld, B. V. Lotsch, *Advanced Energy Materials* **2018**, *8*, 1703278.
- [13] X. Wang, L. Chen, S. Y. Chong, M. A. Little, Y. Wu, W.-H. Zhu, R. Clowes, Y. Yan, M. A. Zwiijnenburg, R. S. Sprick, A. I. Cooper, *Nature Chemistry* **2018**, *10*, 1180-1189.
- [14] T. Banerjee, F. Haase, G. Savasci, K. Gottschling, C. Ochsenfeld, B. V. Lotsch, *J. Am. Chem. Soc.* **2017**, *139*, 16228-16234.
- [15] B. P. Biswal, H. A. Vignolo-Gonzalez, T. Banerjee, L. Grunenberg, G. Savasci, K. Gottschling, J. Nuss, C. Ochsenfeld, B. V. Lotsch, *J. Am. Chem. Soc.* **2019**, *141*, 11082-11092.
- [16] T. Banerjee, K. Gottschling, G. Savasci, C. Ochsenfeld, B. V. Lotsch, *ACS Energy Letters* **2018**, *3*, 400-409.
- [17] J. L. Dempsey, B. S. Brunshwig, J. R. Winkler, H. B. Gray, *Acc. Chem. Res.* **2009**, *42*, 1995-2004.
- [18] V. Artero, M. Chavarot-Kerlidou, M. Fontecave, *Angew. Chem. Int. Ed.* **2011**, *50*, 7238-7266.
- [19] N. M. Muresan, J. Willkomm, D. Mersch, Y. Vaynzof, E. Reisner, *Angew. Chem. Int. Ed.* **2012**, *51*, 12749-12753.
- [20] M. A. Nasalevich, R. Becker, E. V. Ramos-Fernandez, S. Castellanos, S. L. Veber, M. V. Fedin, F. Kapteijn, J. N. H. Reek, J. I. van der Vlugt, J. Gascon, *Energy & Environmental Science* **2015**, *8*, 364-375.
- [21] L.-F. Gao, Z.-Y. Zhu, W.-S. Feng, Q. Wang, H.-L. Zhang, *The Journal of Physical Chemistry C* **2016**, *120*, 28456-28462.
- [22] S.-W. Cao, X.-F. Liu, Y.-P. Yuan, Z.-Y. Zhang, J. Fang, S. C. J. Loo, J. Barber, T. C. Sum, C. Xue, *PCCP* **2013**, *15*, 18363-18366.
- [23] X. Li, A. F. Masters, T. Maschmeyer, *ChemCatChem* **2014**, *7*, 121-126.
- [24] T. Lazarides, T. McCormick, P. Du, G. Luo, B. Lindley, R. Eisenberg, *J. Am. Chem. Soc.* **2009**, *131*, 9192-9194.
- [25] F. Lakadamyali, E. Reisner, *Chem. Commun.* **2011**, *47*, 1695-1695.
- [26] M. Yin, S. Ma, C. Wu, Y. Fan, *RSC Advances* **2015**, *5*, 1852-1858.
- [27] F. J. Uribe-Romo, C. J. Doonan, H. Furukawa, K. Oisaki, O. M. Yaghi, *J. Am. Chem. Soc.* **2011**, *133*, 11478-11481.
- [28] K. Gottschling, L. Stegbauer, G. Savasci, N. A. Prisco, Z. J. Berkson, C. Ochsenfeld, B. F. Chmelka, B. V. Lotsch, *Chem. Mater.* **2019**, *31*, 1946-1955.
- [29] Y. Zhang, X. Shen, X. Feng, H. Xia, Y. Mu, X. Liu, *Chem. Commun.* **2016**, *52*, 11088-11091.
- [30] X. Chen, M. Addicoat, E. Jin, H. Xu, T. Hayashi, F. Xu, N. Huang, S. Irle, D. Jiang, *Scientific Reports* **2015**, *5*, 14650.
- [31] Z.-J. Li, S.-Y. Ding, H.-D. Xue, W. Cao, W. Wang, *Chem. Commun.* **2016**, *52*, 7217-7220.
- [32] F. Himo, T. Lovell, R. Hilgraf, V. V. Rostovtsev, L. Noodleman, K. B. Sharpless, V. V. Fokin, *J. Am. Chem. Soc.* **2005**, *127*, 210-216.
- [33] V. V. Rostovtsev, L. G. Green, V. V. Fokin, K. B. Sharpless, *Angew. Chem. Int. Ed.* **2002**, *41*, 2596-2599.
- [34] C. D. Hein, X.-M. Liu, D. Wang, *Pharm. Res.* **2008**, *25*, 2216-2230.
- [35] F. Amblard, J. H. Cho, R. F. Schinazi, *Chem. Rev.* **2009**, *109*, 4207-4220.
- [36] M. Meldal, C. W. Tornøe, *Chem. Rev.* **2008**, *108*, 2952-3015.
- [37] M. H. Levitt, American Cancer Society, **2007**, pp. 1-31.

- [38] S. P. Brown, A. Lesage, B. Elena, L. Emsley, *J. Am. Chem. Soc.* **2004**, *126*, 13230-13231.
- [39] J. P. Bradley, C. Tripon, C. Filip, S. P. Brown, *PCCP* **2009**, *11*, 6941-6941.
- [40] J. P. Perdew, K. Burke, M. Ernzerhof, *Phys. Rev. Lett.* **1996**, *77*, 3865-3868.
- [41] S. Grimme, J. Antony, S. Ehrlich, H. Krieg, *The Journal of Chemical Physics* **2010**, *132*, 154104.
- [42] A. Schäfer, C. Huber, R. Ahlrichs, *The Journal of Chemical Physics* **1994**, *100*, 5829-5835.
- [43] K. Eichkorn, F. Weigend, O. Treutler, R. Ahlrichs, *Theoretical Chemistry Accounts: Theory, Computation, and Modeling (Theoretica Chimica Acta)* **1997**, *97*, 119-124.
- [44] A. M. Burow, M. Sierka, F. Mohamed, *The Journal of Chemical Physics* **2009**, *131*, 214101-214101.
- [45] L. Grajciar, *J. Comput. Chem.* **2015**, *36*, 1521-1535.
- [46] A. M. Burow, M. Sierka, *Journal of Chemical Theory and Computation* **2011**, *7*, 3097-3104.
- [47] R. Łazarski, A. M. Burow, M. Sierka, *Journal of Chemical Theory and Computation* **2015**, *11*, 3029-3041.
- [48] R. Łazarski, A. M. Burow, L. Grajciar, M. Sierka, *J. Comput. Chem.* **2016**, *37*, 2518-2526.
- [49] TURBOMOLE, developer version based on version V7.1 2017, a development of University of Karlsruhe and Forschungszentrum Karlsruhe GmbH, 1989-2007, TURBOMOLE GmbH, since 2007; available from <http://www.turbomole.com>.
- [50] J. Wang, W. Wang, P. A. Kollman, D. A. Case, *J. Mol. Graphics Modell.* **2006**, *25*, 247-260.
- [51] J. C. Phillips, R. Braun, W. Wang, J. Gumbart, E. Tajkhorshid, E. Villa, C. Chipot, R. D. Skeel, L. Kalé, K. Schulten, *J. Comput. Chem.* **2005**, *26*, 1781-1802.
- [52] in D.A. Case, R.M. Betz, D.S. Cerutti, T.E. Cheatham, III, T.A. Darden, R.E. Duke, T.J. Giese, H. Gohlke, A.W. Goetz, N. Homeyer, S. Izadi, P. Janowski, J. Kaus, A. Kovalenko, T.S. Lee, S. LeGrand, P. Li, C. Lin, T. Luchko, R. Luo, B. Madej, D. Mermelstein, K.M. Merz, G. Monard, H. Nguyen, H.T. Nguyen, I. Omelyan, A. Onufriev, D.R. Roe, A. Roitberg, C. Sagui, C.L. Simmerling, W.M. Botello-Smith, J. Swails, R.C. Walker, J. Wang, R.M. Wolf, X. Wu, L. Xiao and P.A. Kollman (2016), AMBER 2016, University of California, San Francisco.
- [53] J. Wang, R. M. Wolf, J. W. Caldwell, P. A. Kollman, D. A. Case, *J. Comput. Chem.* **2004**, *25*, 1157-1174.
- [54] P. J. Wilson, T. J. Bradley, D. J. Tozer, *The Journal of Chemical Physics* **2001**, *115*, 9233-9242.
- [55] F. Jensen, *Journal of Chemical Theory and Computation* **2014**, *11*, 132-138.
- [56] J. Kussmann, C. Ochsenfeld, *Journal of Chemical Theory and Computation* **2015**, *11*, 918-922.
- [57] J. Kussmann, C. Ochsenfeld, *The Journal of Chemical Physics* **2013**, *138*, 134114.
- [58] A. Bhattacharjee, E. S. Andreiadis, M. Chavarot-Kerlidou, M. Fontecave, M. J. Field, V. Artero, *Chemistry - A European Journal* **2013**, *19*, 15166-15174.
- [59] N. Kaeffer, M. Chavarot-Kerlidou, V. Artero, *Acc. Chem. Res.* **2015**, *48*, 1286-1295.
- [60] X. Zhao, P. Pachfule, S. Li, T. Langenhahn, M. Ye, C. Schlesiger, S. Praetz, J. Schmidt, A. Thomas, *J. Am. Chem. Soc.* **2019**, *141*, 6623-6630.



- [61] X. Zhao, P. Pachfule, S. Li, T. Langenhahn, M. Ye, G. Tian, J. Schmidt, A. Thomas, *Chem. Mater.* **2019**, *31*, 3274-3280.



4 Covalent organic frameworks for carbon capture and storage

4.1 Summary

Functional porous solids have gained significant attention in the context of carbon capture and storage (CCS) during the last years. Heterogeneous adsorbents such as activated carbons, MOFs, or COFs offer an alternative solution to the growing problem of CO₂ emission to the atmosphere. The potential of easily adjustable COFs is huge and has still not been fully explored yet. For the rational development of a compatible COF system, a thorough understanding of the underlying processes is key.

Thus, in this project the interaction of CO₂ with a specifically designed COF system was investigated. Two isostructural hydrazone-linked COFs with different polarities (COF-H and COF-OH) have been synthesized and modified by a co-polymerization approach of varying amounts of a tertiary-amine-functionalized building block. The affinity to CO₂ was investigated by thorough analysis of CO₂ sorption properties of the frameworks including the determination of the heats of adsorption at zero coverage. With increasing amine content, an increasing heat of adsorption at zero coverage (Q_{st}) was found up to a value of 72.4 kJ mol⁻¹. By a combination of solid-state 2D ¹³C{¹H} NMR analyses and quantum chemical calculations, we analyzed the mechanism of CO₂ binding in the COF pores and observed the formation of a bicarbonate species along with strongly retained water. This was supported by water sorption experiments.

The promotion of CO₂ solvation was found to be a good candidate for further enhancement of the CO₂ adsorption properties of porous systems.

4.2 Molecular insights into carbon dioxide sorption in hydrazone-based covalent organic frameworks with tertiary amine moieties

Kerstin Gottschling, Linus Stegbauer, Gökçen Savasci, Nathan A. Prisco, Zachariah J. Berkson, Christian Ochsenfeld, Bradeley F. Chmelka, and Bettina V. Lotsch

published in

Chemistry of Materials **2019**, *31* (6), 1946–1955

DOI: 10.1021/acs.chemmater.8b04643

<https://pubs.acs.org/doi/10.1021/acs.chemmater.8b04643>

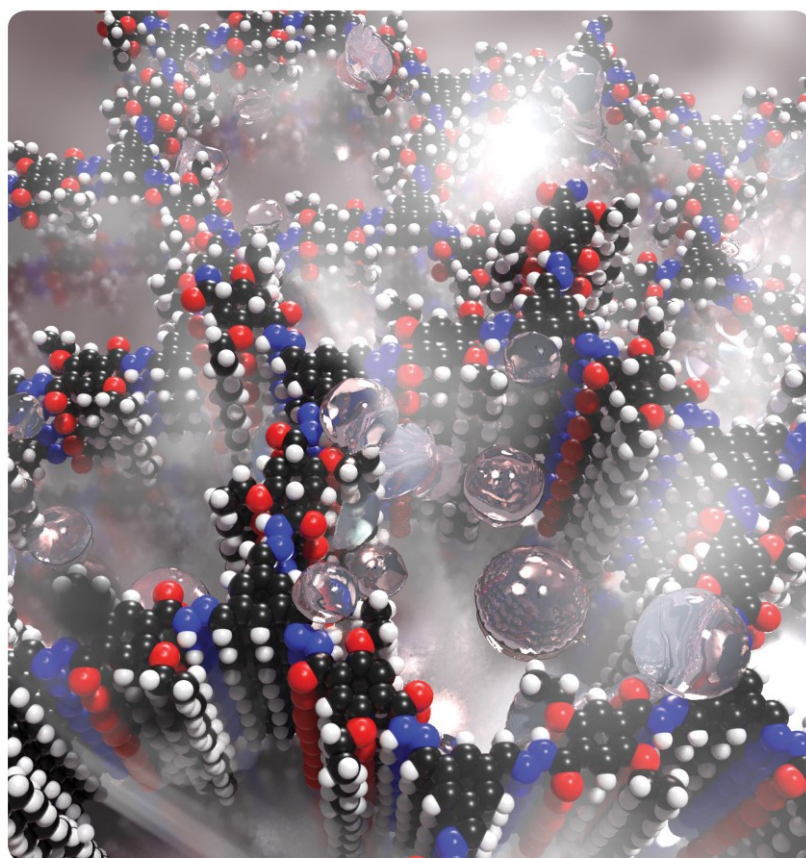
Formatting and numbering of figures were changed.

Adapted with permission from ACS

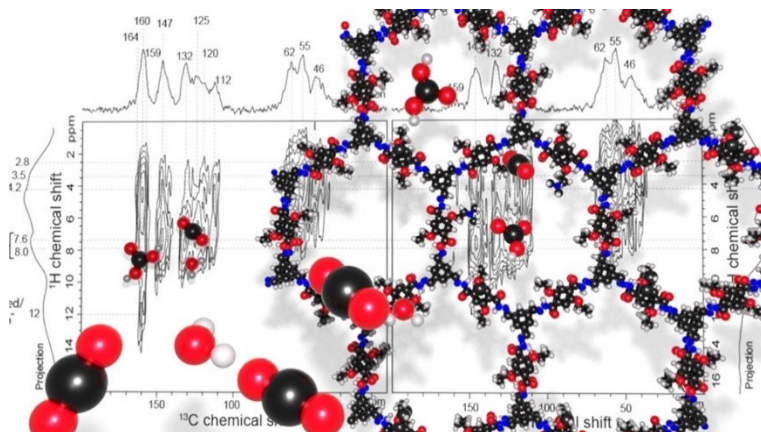
This project was highlighted as a supplementary cover image of the journal Chemistry of Materials, the cover image was designed by Kerstin Gottschling.

cm CHEMISTRY OF
MATERIALS

MARCH 26, 2019 | VOLUME 31 | NUMBER 6 | pubs.acs.org/cm



4.2.1 Abstract



Tailorable sorption properties at the molecular level are key for efficient carbon capture and storage and a hallmark of covalent organic frameworks (COFs). Although amine functional groups are known to facilitate CO₂ uptake, atomistic insights into CO₂ sorption by

COFs modified with amine-bearing functional groups are scarce. Herein, we present a detailed study of the interactions of carbon dioxide and water with two isostructural hydrazone-linked COFs with different polarities based on the 2,5-diethoxyterephthalohydrazide linker. Varying amounts of tertiary amines were introduced in the COF backbones by means of a copolymerization approach using 2,5-bis(2-(dimethylamino)ethoxy)terephthalohydrazide in different amounts ranging from 25 to 100% substitution of the original DETH linker. The interactions of the frameworks with CO₂ and H₂O were comprehensively studied by means of sorption analysis, solid-state NMR spectroscopy, and quantum chemical calculations. We show that the addition of the tertiary amine linker increases the overall CO₂ sorption capacity normalized by the surface area and of the heat of adsorption, whereas surface areas and pore size diameters decrease. The formation of ammonium bicarbonate species in the COF pores is shown to occur, revealing the contributing role of water for CO₂ uptake by amine-modified porous frameworks.

4.2.2 Introduction

Covalent organic frameworks (COFs) are a recently developed class of porous polymers with high chemical and thermal stability and well-defined crystal structures. COFs are promising for a range of applications, for example, in gas storage and separation,^[1-2]^[3] optoelectronics,^[4-5] and energy conversion.^[6-7] COFs are formed by condensation reactions of organic linkers that are covalently bound under reversible conditions, which provides a mechanism of error correction.^[8] All but a few COFs reported to date have two-dimensional (2D) network topologies, where the COF sheets are held together in the third dimension by noncovalent van der Waals interactions. The structure of COFs and their versatility allows for engineering these systems and their properties in a targeted manner.^[9-11] One way to do so is by pore-surface engineering, where the surface of preformed pores carrying specific functional sites can be further transformed postsynthetically, if desired.^[12] Another possibility is to modify the organic linkers presynthetically according to the targeted properties. A linker

that is suitable for diverse transformations and has been successfully used in several COF syntheses is 2,5-diethoxyterephthalohydrazide (DETH)).^[7, 13-14] An example is the DETH-based COF-JLU4 which is synthesized by condensation with triformylphloroglucinol (TFG)) and has been used in fluorescent pH sensing systems for aqueous solutions.^[15] Another chemically strongly related COF containing methoxy instead of ethoxy groups in the hydrazide linker, NUS-3, has been reported for the use in mixed-matrix membranes with high H₂/CO₂ permselectivity.^[16]

Utilization of functional porous solids with custom-made pores has seen a burst of activity over the past decades, specifically in the context of carbon capture and storage (CCS)). Carbon dioxide emissions are known to be the major source of global warming, and in order to reduce this effect, technically viable solutions for the capture and long-term storage of the greenhouse gas CO₂ are needed and actively sought. The chemisorption of CO₂ into aqueous alkanolamine solutions - known as amine scrubbing - is widely practiced in the downstream processing of flue gases produced at the mega ton scale by coal-fired fire plants.^[17] Primary or secondary amines form carbamates with CO₂, whereas tertiary or sterically hindered amines act as bases accepting a proton from carbonic acid formed by dissolution of CO₂ in water.^[18-20] It is worth noting that unhindered alkanolamines absorb only half a mole of CO₂ per mole of amine by a zwitterion mechanism, whereas tertiary amines undergo base-catalyzed hydration of CO₂ to form bicarbonate ions which increases the theoretical capacity to 1 mol of CO₂ per mole of amine.^[18] The amine solutions that are used decompose over time, and their CO₂ capturing ability decreases significantly.^[21] Additional problems are the corrosivity and toxicity of these amine solutions. Key goals in CCS are high adsorption capacity and cycle stability as well as full reversibility and adequate heats of adsorption. Materials such as activated carbons,^[22-23] metal organic frameworks (MOFs),^[24-25] or COFs^[26-27] are, in contrast to the standard method, easy to regenerate at moderate temperatures and allow a great variety of functional designs. In this context, heterogeneous adsorbents such as COFs with precisely tunable pores decorated with functional groups are attracting increasing interest in the field. Another challenge in this context is the presence of small amounts of water, which can be competitively adsorbed by hydrophilic adsorbents, thus reducing the overall CO₂ sorption capacity.^[28-30] Although mesoporous materials such as zeolites and activated carbons were already tested in pilot plants,^[31-32] the potential of COFs as alternative sorbents in the CCS technology has not been explored. However, to fully develop the potential of heterogeneous sorbents in CCS, understanding the interactions that account for CO₂ adsorption at the molecular level is key.^[33-35]

Here, we address this challenge by studying CO₂ sorption in tertiary amine-functionalized COFs by a combination of adsorption isotherm measurements and solid-state nuclear



magnetic resonance (NMR) spectroscopy, complemented by quantum chemical calculations, obtained on B97-2/pcS-2/PBE0-D3/def2-TZVP level of theory^[36-41] using the Turbomole^[42-43] program package for geometries and the FermiONs++^[44-45] program package for the calculation of NMR chemical shifts. DETH linker molecules were modified by insertion of a terminal tertiary amine group and integrated into two different hydrazone-linked COF systems. To adjust the linker functionalization level and study the influence of linker modification on the structural and sorption properties of the COF, a three-linker approach was developed inspired by classical copolymerization. We show that CO₂ sorption capacities as well as heats of adsorptions can be increased by this strategy. To the best of our knowledge, this is the first time the molecular interaction of CO₂ with a COF material was studied. CO₂ was found to adsorb at tertiary amine sites through water-mediated formation of a bicarbonate species.

4.2.3 Results and discussion

Synthesis and structural characterization

Two COF systems with different amounts of the amine-functionalized linker of 2,5-bis(2-(dimethylamino)ethoxy)terephthalohydrazide (DtATH, see Figure 4-1) were synthesized by a copolymerization approach using two generic COF systems.

The first system, named amine-coCOF-OH, is based on the hydrazone-linked HTFG-COF (coCOF-OH) that is synthesized by solvothermal condensation of DETH (see Figure 4-1) and 2,4,6-trihydroxybenzene-1,3,5-tricarbaldehyde (TFG), see Figure 4-1). The second system, COF-42 (coCOF-H), was synthesized similarly by condensation of DETH and 1,3,5-triformylbenzene (TFB), see Figure 4-1) and is referred to as amine-coCOF-H in the following.

For the synthesis of DtATH-containing samples, various amounts of DETH (25, 50, 75, and 100% substitution of the original DETH linker) were substituted by the respective amount of DtATH and the mixed linkers exposed to the initial COF synthesis protocol of the underlying coCOF systems coCOF-OH and coCOF-H. The solvent compositions were optimized to obtain high surface area and crystallinity in the modified samples.

COFs were characterized by Fourier transform infrared (FT-IR) spectroscopy, sorption analysis, powder X-ray diffraction (PXRD), and solid-state NMR. As seen in Figure 6-56, the FT-IR spectrum of coCOF-OH shows the characteristic C=O stretching vibrations of the β -ketoenamine carbonyl group at 1680 cm⁻¹. No residual aldehyde stretches are visible, indicating the complete transformation of the starting material. Comparison with the monomers corroborates the formation of the hydrazone bond. The same was found in coCOF-H as well as in the amine-containing samples. Addition of the tertiary amine linker further leads to color deepening in the samples from light yellow to orange in coCOF-OH

and from orange to reddish-brown in coCOF-H as is also visible in the solid-state UV/vis absorption spectra (see Figure 6-58).

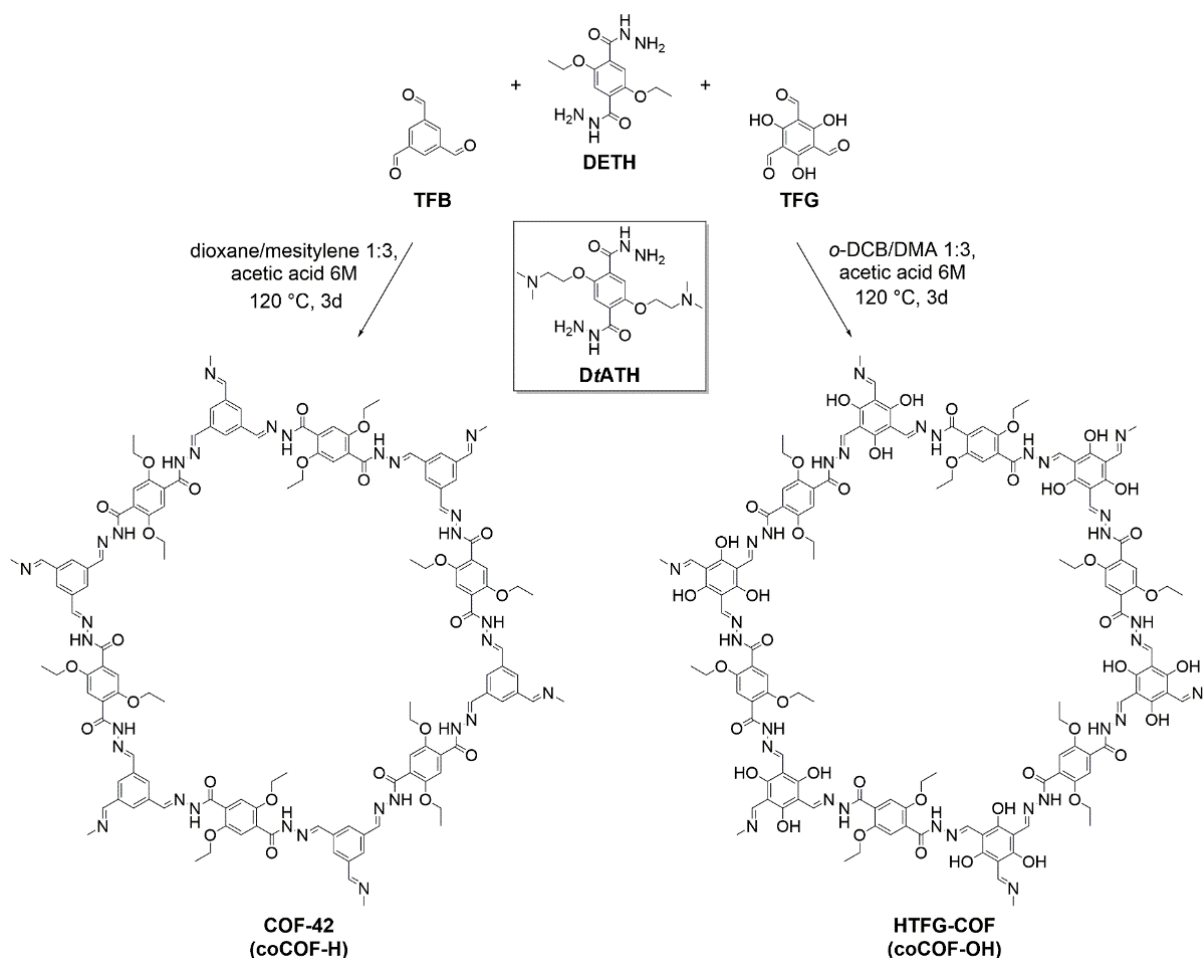


Figure 4-1: Synthesis of COF-42 (coCOF-H) from 2,5-diethoxyterephthalohydrazide (DETH) and 1,3,5-triformylbenzene (TFB, left) and HTFG-COF (coCOF-OH) from DETH and 2,4,6-trihydroxybenzene-1,3,5-tricarbaldehyde (TFG, right). Structure of 2,5-bis(2-(dimethylamino)ethoxy)terephthalohydrazide (DtATH), center.

Solid-state 1D $^{13}\text{C}\{^1\text{H}\}$ CP-MAS NMR further supports the bond formation and linker integration in both systems. The ^{13}C NMR signals are assigned to the different carbon atoms shown schematically in Figure 4-2a,e as indicated by the labels in Figure 4-2b,f.^[46] The signals assigned to the ethoxy group were observed at 66 and 15 ppm. Amine-containing samples show additional peaks at 45 and 57 ppm (Figure 4-2c,d,g,h) that can be attributed to the aminoethoxy and dimethylamine groups, respectively, as corroborated by quantum chemical calculations for a model compound (see Table 6-15). In the molecular linker, the respective carbon center shows a ^{13}C chemical shift of 45.1 ppm (see Chapter 6.1.3) The relative intensity of the ^{13}C NMR signal at 45 ppm increases with higher amount of amine in the synthesis mixture, consistent with greater incorporation of the amine linker into the COF framework.

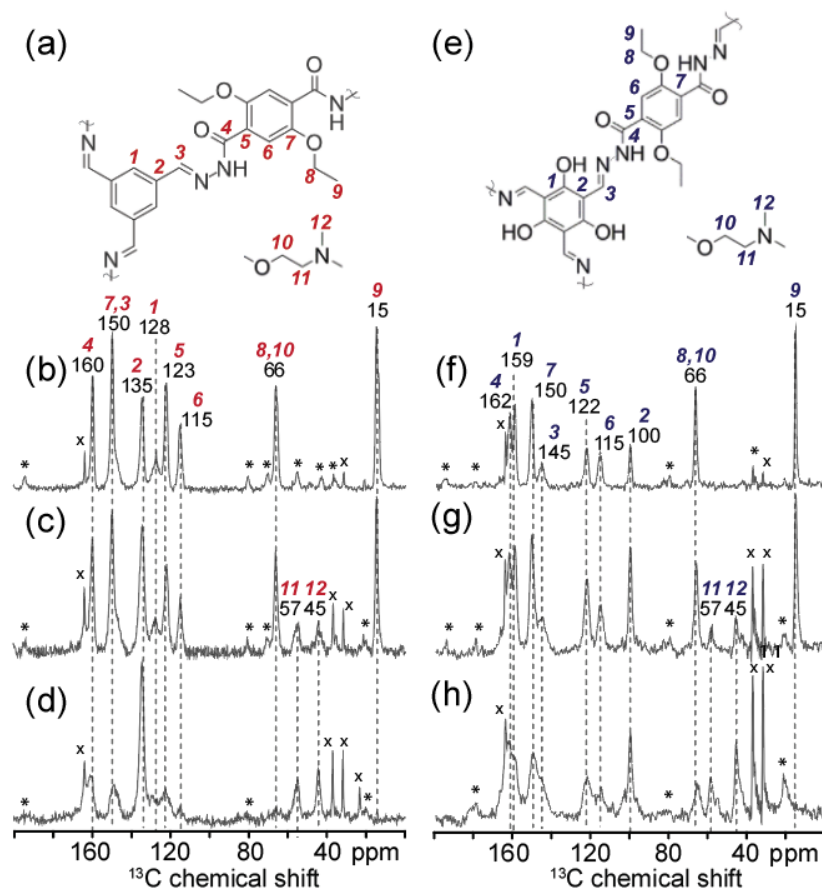


Figure 4-2: Schematic structural diagrams showing subsections of the (a) coCOF-H framework, (e) coCOF-OH framework, and the tertiary amine linker DtATH. Solid state 1D $^{13}\text{C}\{^1\text{H}\}$ CP-MAS NMR spectra of (b-d) coCOF-H and (f-h) coCOF-OH with (b, f) 0%, (c, g) 50%, and (d, h) 100% of DtATH substitution of the original DETH linker. The spectra in (b-d) and (f-h) were acquired at 11.7 T, 10 kHz MAS, 298 K, using cross-polarization contact times of 5 ms. The NMR spectrum (d) was acquired at 11.7 T, 12 kHz MAS, 298 K, and using cross-polarized contact times of 5 ms. Spinning sidebands are marked with asterisks. Distinct carbon atoms in the schematic structures in (a) and (e) are numbered and their associated ^{13}C NMR signals labeled accordingly in (b-d) and (f-h) respectively. The narrow signals labelled with crosses at 164 ppm, 37 ppm and 32 ppm correspond to residual dimethylformamide and at 25 ppm to residual tetrahydrofuran.

PXRD confirms the formation of crystalline COF networks with unit cell dimensions being consistent with the structural models shown in Figure 3c. For coCOF-OH, a strong reflection at 3.4° and weaker ones at 5.5 , 7.0 , and 26.2° are assigned to the 100, 110, 200, and 001 Miller indices, respectively (see Figure 4-3a). The PXRD data match well with an AA eclipsed stacking structure with an interlayer distance of 3.48 \AA because of π - π -stacking interactions (see Figure 3c). It should be noted that a lateral offset of 1.7 – 1.8 \AA is expected but cannot be distinguished from the AA eclipsed stacking structure because of broadening of the reflections.^[47-48] Further investigations were carried out with the AA eclipsed model.

Pawley refinement on the simulated structure suggests a $P6/m$ space group with $a = b = 29.6 \text{ \AA}$ and $\alpha = \beta = 90^\circ, \gamma = 120^\circ$.

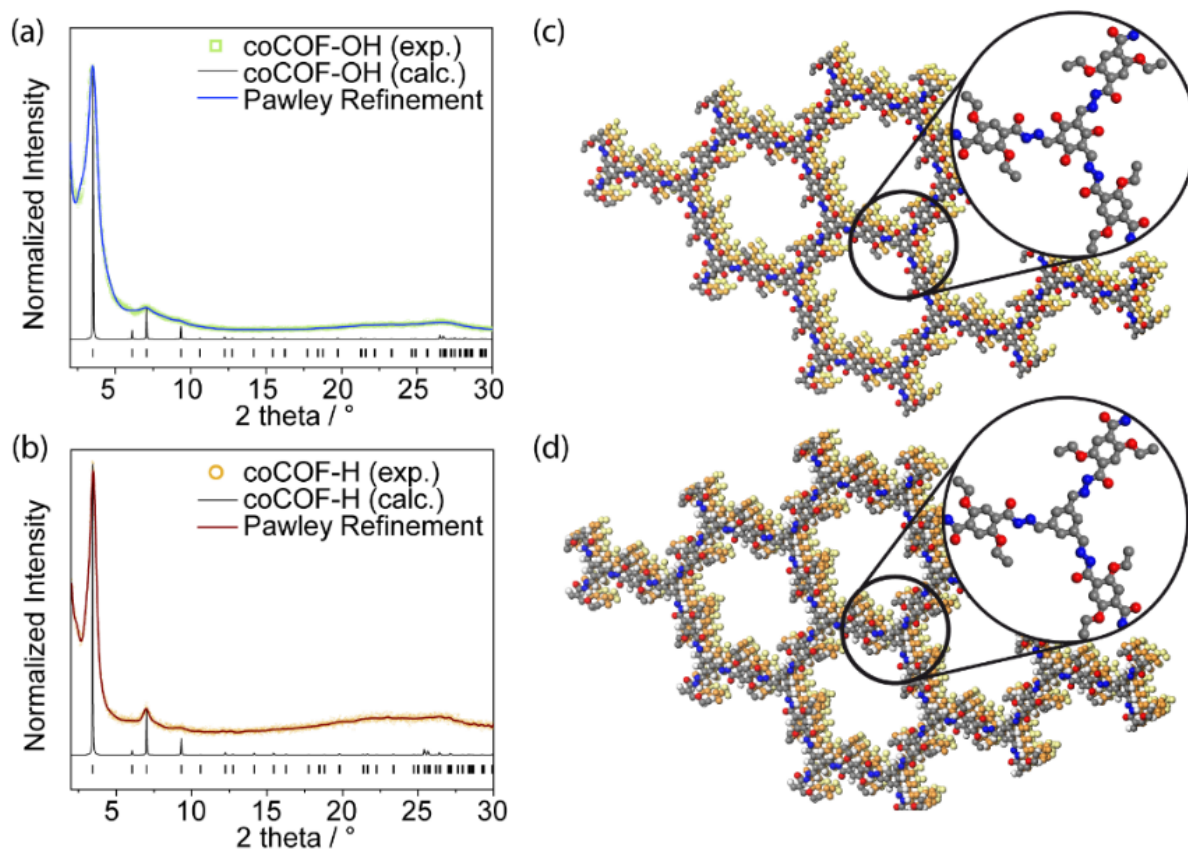


Figure 4-3: (a) PXR D pattern of coCOF-OH (open green squares), Pawley refined profile (blue line), calculated XRD pattern for the idealized eclipsed (AA) stacking (black line). (b) PXR D pattern of coCOF-H (open orange circles), Pawley refined profile (red line), calculated XRD pattern for the idealized eclipsed (AA) stacking (black line). (c) and (d) Eclipsed stacking model for coCOF-OH and coCOF-H, respectively. C, N and O atoms are represented in grey, blue and red. h atoms are omitted. The second and third layers are represented in orange and yellow for clarity.

In general, coCOF-H appears more crystalline than coCOF-OH. Introducing the modified linker leads to a further loss in crystallinity, whereas the architecture and dimensions of the unit cell are maintained. The 100, 110, 200, and 001 reflections of 100%-amine-coCOF-OH are found at 3.4, 5.7, 6.9, and 26.3°, respectively, which suggests retention of the stacking structure discussed above. The crystallinity decreases with higher amine content (see Figure 6-57). The loss of crystallinity is more distinct in amine-coCOF-OH which we attribute to a loss of reversibility in the bond formation and the coexistence of different tautomeric forms which is known for COFs based on the TFG linker.^[49]



Adsorption performance

According to argon sorption measurements at 87 K, both systems show characteristic type IV isotherms that are typical for mesoporous materials (see Figure 4-4). Brunauer–Emmett–Teller (BET) surface areas were calculated to be $998 \text{ m}^2 \text{ g}^{-1}$ for coCOF–OH and $2336 \text{ m}^2 \text{ g}^{-1}$ for coCOF–H, which surpasses the published values for both COFs (757 and $710 \text{ m}^2 \text{ g}^{-1}$ for coCOF–OH and coCOF–H, respectively^[46]). Pore size distributions (PSD) were derived from experimental data using nonlocal density functional theory and quenched solid-state functional theory calculations.^[50] In coCOF–H, the experimental pore size of 2.4 nm is in agreement with the theoretical value based on the structural model. Additionally, micropores of 0.92 and 0.61 nm are observed which points to structural effects such as mismatch stacking, leading to reduced pore sizes or pore blocking. The mesopores with 2.4 nm diameter account for 65% of the pore volume, whereas the smaller micropores represent 7.4% (for 0.92 nm) and 8.3% (for 0.61 nm) of the total pore volume. A similar trend is observed in coCOF–OH with a broader distribution of mesopores at 2.3 nm (55% pore volume) caused by the loss of long-range order because of tautomerism (see Figure 6-60). The smaller pores are found at 0.91 nm (26% pore volume) and 0.61 nm (16% pore volume).

For amine-containing samples, BET surface areas decrease linearly with an increasing amount of tertiary amine. Respective values for all samples are listed in Table 4-1. We derived PSDs from Ar isotherms for the samples containing 50 and 100% modified linker for both systems (see Figure 6-59 and Figure 6-60). Although the mean pore size of the pristine COFs is around 2.4 nm, additional smaller pores in the range of 1.4–1.8 nm are found for the amine-containing samples. This is in agreement with theoretical values for amine-modified pores, which vary between 1.6 and 2.2 nm depending on the amine conformation. A stochastic distribution of the different linkers in the systems along with stacking faults will lead to pores with different amounts of amine and therefore to different pore sizes, especially in the mixed systems. A broader distribution of pore sizes with more regular distribution of pore volumes is found in the 50% amine samples (see Table 6-14). In the 100% amine samples, two distinct pore sizes of 2.2 and 1.6 nm are found which are attributed to different pore surface architectures with amines either at the pore wall or protruding into the pore (see Figure 6-61).

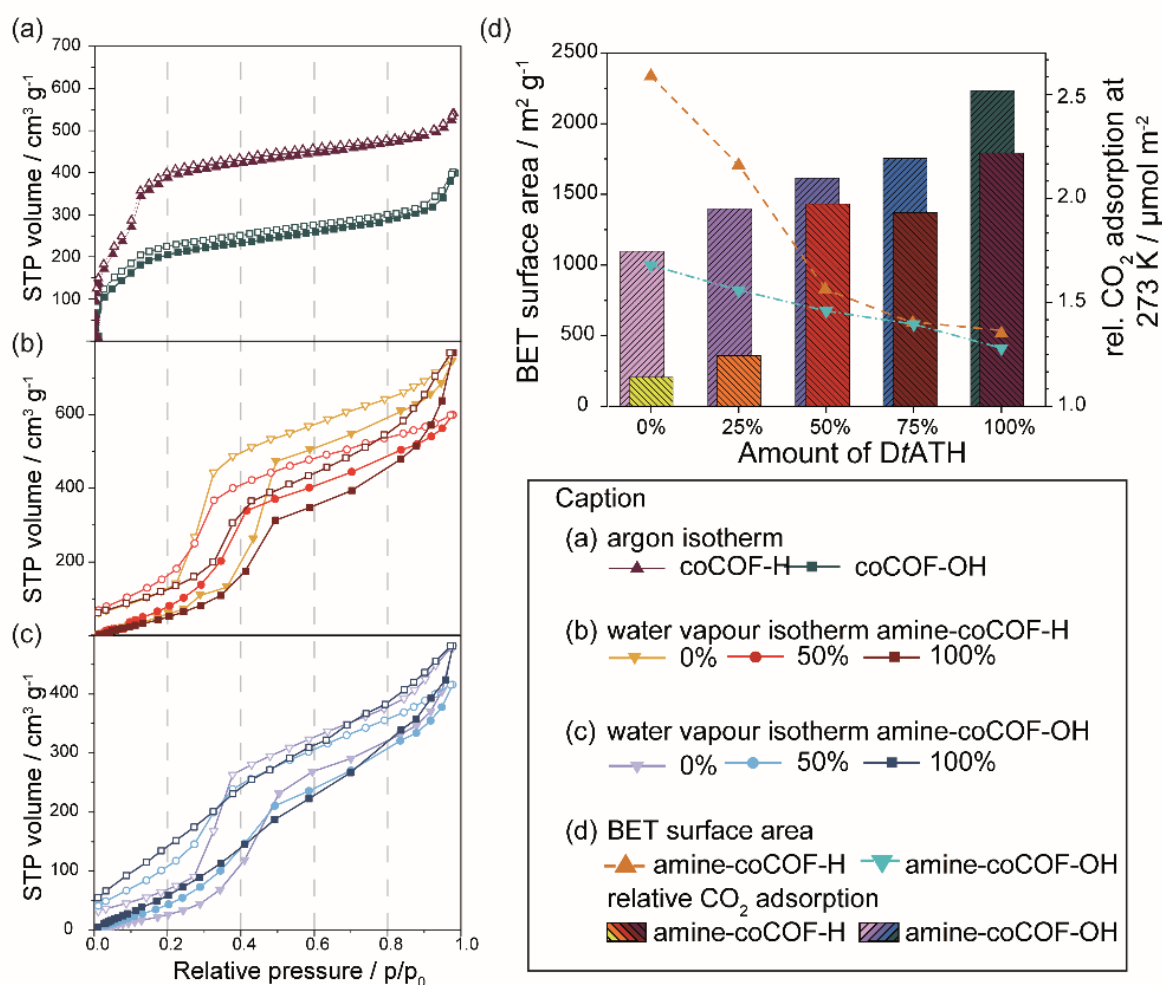


Figure 4-4: (a) Argon adsorption isotherms of coCOF-H (red) and coCOF-OH (blue). Water sorption at 273 K of (b) amine-coCOF-H and (c) amine-coCOF-OH with 0%, 50%, 100% DtATH substitution of the original DETH linker. Adsorption is represented by filled symbols, desorption by open symbols. (d) Relative CO₂ adsorption capacities at 273 K and BET surface areas of amine-coCOF-OH (blue and purple) and amine-coCOF-H (red and orange). BET surface area is indicated by triangles.

With respect to the CO₂ sorption isotherms of both systems, a linear decrease was observed for the uptake capacity ranging from 2.66 to 1.14 mmol g⁻¹ for coCOF-H (0–100% modification) and from 1.74 to 1.04 mmol g⁻¹ for coCOF-OH (0–100% modification; see Table 4-1). Interestingly, the loss in uptake capacity with increasing amine functionalization is significantly less than the decrease of surface area. Normalizing the CO₂ uptake to the BET surface area of the samples (see Table 4-1) to obtain relative rather than absolute CO₂ capacities, the uptake increases from 1.14 to 2.22 μmol m⁻² (0–100% modification) for the amine-coCOF-H. For amine-coCOF-OH, the relative CO₂ adsorption increases from 1.75 to 2.52 μmol m⁻² (see Figure 4-4b). Whereas at 50% amine loading, the uptake is fairly similar for both systems (2.10 μmol m⁻² for amine-coCOF-OH and 1.93 μmol m⁻² for



amine-coCOF-H), in the other amine loading regimes, the relative CO₂ capacity of the more polar amine-coCOF-OH distinctly surpasses amine-coCOF-H.

Table 4-1: BET surface areas, CO₂ uptake at 273 K, relative CO₂ adsorption at 273 K and heats of CO₂ adsorption of the presented COFs.

COF system	Amount of DtATH	BET SA ^a [m ² g ⁻¹]	CO ₂ uptake at 273 K [mmol g ⁻¹]	Relative CO ₂ adsorption [μmol m ⁻²]	Q _{st} ^b [kJ mol ⁻¹]
Amine-coCOF-H	0%	2336	2.66	1.14	24.0
	25%	1705	2.12	1.24	37.0
	50%	811	1.60	1.97	40.4
	75%	573	1.11	1.93	54.0
	100%	514	1.14	2.22	72.4
Amine-coCOF-OH	0%	998	1.74	1.75	36.7
	25%	822	1.60	1.95	47.9
	50%	675	1.42	2.10	49.6
	75%	581	1.27	2.19	66.0
	100%	412	1.04	2.52	48.5

^a From Ar sorption measurements. ^b At zero coverage.

Even though water is present in most applications, the behavior of COFs in water sorption experiments has rarely been studied systematically. Most studies have been performed on MOFs or porous carbons that show very different behaviors. Hydrophilicity is more pronounced in the case of MOFs because of their metal sites than on the nonpolar hydrophobic surface of carbon materials. However, MOFs are often not stable in water which leads to their degradation under humid conditions.^[51] COFs are expected to exhibit hydration properties that are intermediate between MOFs and carbons, where a more polar surface due to heteroatoms in the framework gives rise to a type IV sorption isotherm and a fully reversible hysteresis at lower relative pressures compared to nonpolar surfaces.

The two pristine COF systems in this study show similar behavior in water sorption measurements. The water uptake capacity is higher for amine-coCOF-H, ranging from 598 to 768 cm³ g⁻¹ (47–61 wt%) and 416–481 cm³ g⁻¹ (33 to 38 wt%). In both systems, the highest capacity is found for the 100%-amine samples and the lowest for the 50%-amine samples. This is likely due to a higher degree of disorder because of the distribution of modified and unmodified linkers in the 50%-amine samples. The adsorption isotherms of both systems show a step in the range of 0.30–0.45 p/p_0 with a strong hysteresis; the same step is found in the desorption isotherm at 0.20–0.30 p/p_0 . This behavior is indicative of

capillary condensation of water in the COF pores. By increasing the amine content in the samples, in both systems, the adsorption step flattens out up to an almost linear sorption isotherm in 100%-amine-coCOF-OH. This continuous pore filling might be due to a slightly higher polarity in the system. Interestingly, water sorption is not fully reversible. Fractions ranging from 6.8% (for pristine coCOF-OH) up to 11.4% (in the case of 100%-amine-coCOF-OH) of the maximum water uptake remain in the pores after desorption. The addition of amines in close proximity to the pore walls leads to higher hydrophilicity and thus increased water sorption capacities.

Isosteric heats of adsorption (Q_{st}) at zero coverage were calculated for all samples from the CO₂ sorption isotherms at 273, 288, and 298 K (see Table 4-1). Typical values for classical physisorption range between 8 and 25 kJ mol⁻¹ for van der Waals forces and up to 50 kJ mol⁻¹ for dipole-dipole interactions, whereas chemisorption is associated with heats of adsorption between 80 and 500 kJ mol⁻¹. The values obtained in our unmodified coCOFs are 24.0 kJ mol⁻¹ for coCOF-H and 36.7 kJ mol⁻¹ for coCOF-OH. Upon modification, the Q_{st} values increase drastically with maximum values of 72.4 kJ mol⁻¹ in 100%-amine-coCOF-H and 66.0 kJ mol⁻¹ in 75%-amine-coCOF-OH. Those values approach the chemisorption regime and are much higher than that for comparable COFs, such as COF-JLU2 (31 kJ mol⁻¹),^[52] TRIPTA (56.77 kJ mol⁻¹),^[53] [HO2C]100%-H2P-COF (43. kJ mol⁻¹),^[27] ACOF-1 (27.6 kJ mol⁻¹),^[54] TpPA-COF (34.1 kJ mol⁻¹),^[55] or other porous materials such as FCTF-1 (35.0 kJ mol⁻¹),^[56] mgMOF-74 (42 kJ mol⁻¹),^[57] and imine-linked porous organic cages (20.4 kJ mol⁻¹).^[58]

Amine-modification of the coCOF-H framework

To understand the improved CO₂ sorption properties of 100%-amine-coCOF-H, advanced 1D and 2D ¹H, ¹³C, and ¹⁵N solid-state NMR techniques were used to elucidate atomic-level structures and interactions in the modified COF framework and compared with findings from quantum chemical calculations. The ¹⁵N chemical shift interaction is highly sensitive to local bonding environments,^[59-60] however, ¹⁵N NMR experiments are severely limited for low-density and low-nitrogen content materials by the low natural isotopic abundance (0.4%) and low gyromagnetic ratio of the ¹⁵N nuclei. These limitations are partially overcome by dynamic nuclear polarization (DNP)-enhanced NMR spectroscopy, which uses microwave excitation of nitroxide biradical polarizing agents to achieve a potential ¹⁵N sensitivity gain of $\gamma_e/\gamma^{15}\text{N} \approx 6500$.^[61] Here, DNP-NMR enables the acquisition of natural-abundance ¹⁵N spectra as demonstrated in Figure 4-5.

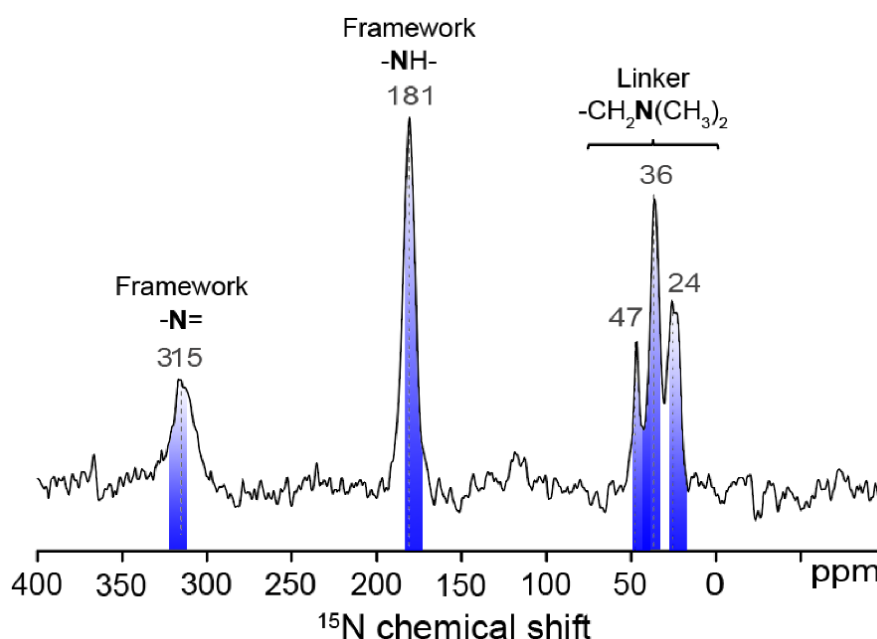


Figure 4-5: Solid-state 1D $^{15}\text{N}\{^1\text{H}\}$ DNP-CP-MAS spectra of 100%-amine-coCOF-H without CO_2 exposure. The spectrum was acquired at 9.4 T, 8 kHz MAS, 95 K, in the presence of 16 mM AMUPol biradical in 60:30:10 d_8 -glycerol: D_2O : H_2O , under microwave irradiation at 263 GHz, and using cross-polarization contact times of 5 ms. Blue markings correspond to values obtained by quantum chemical calculations (See Table 6-16, Table 6-17, and Table 6-19).

Although amine-functionalized nanoporous or mesoporous solids typically exhibit broad ^{15}N signals due to structural disorder,^[62-64] the ^{15}N signals from the DtATH linker exhibit narrow ^{15}N line shapes, which indicates relatively uniform local environments in the COF framework. The ^{15}N signals at 315 and 181 ppm are assigned to framework hydrazone ($-\text{N}=\text{N}-$) and ($-\text{NH}-$) moieties, respectively, as supported by quantum chemical calculations (see Figure 6-66, Figure 6-67, and Table 6-16) for a coCOF-H sub-structure and literature.^[59] A hydrogen bond to water causes displacement of the imine signal to lower frequency by approximately 12 ppm compared to the bare imine bond (see Figure 6-68 and Table 6-16). The presence of these signals, in addition to quantum chemical data, strongly suggest that after incorporation of DtATH into the COF framework the hydrazone ($-\text{N}=\text{N}-$) and ($-\text{NHCO}-$) linkages are intact and retain an atomic structure similar to unmodified coCOF-H. In 100%-amine-coCOF-H, there are three additional ^{15}N signals at 24, 36, and 47 ppm, which arise from the DtATH linker. For tertiary amines, the ^{15}N chemical shift may be influenced by local bonding environments, which can be influenced by temperature, solvent effects, or hydrogen-bonding interactions to varying extents and which can displace ^{15}N signals by as much as 40 ppm.^[60] In polar or acidic solvents, tertiary amines often exhibit partial deshielding of ^{15}N nuclei, as manifested by displacement of their isotropic chemical shifts to higher values.^[60] Consequently, the ^{15}N signal at 47 ppm is assigned to protonated

tertiary amine linker groups, consistent with quantum chemical calculations (see Figure 6-69 and Table 6-19). The ^{15}N signals at 24 and 36 ppm are attributed to unprotonated DtATH tertiary amine moieties also on the basis of quantum chemical calculations (Figure 6-68), with the former assigned to unhydrated linkers. The ^{15}N signal at 36 ppm is attributed to DtATH tertiary amine moieties that interact strongly with water.

CO₂ interactions with amine-coCOF-H moieties

Molecular-level insights on specific interactions between CO₂ and 100%-amine-coCOF-H are obtained from 2D $^{13}\text{C}\{^1\text{H}\}$ -heteronuclear correlation (HETCOR) analyses that establish spatial proximities of adsorbed CO₂ and the COF sorbent. Previously, site-specific CO₂ adsorption in tertiary amide (–NHCO)–containing mesoporous materials has been investigated by inelastic neutron spectroscopy for which subtle differences in local chemical environments are difficult to resolve.^[65] By comparison, the 2D $^{13}\text{C}\{^1\text{H}\}$ low-temperature magic-angle-spinning (LTMAS)–HETCOR spectra (Figure 4-6) of 100%-amine-coCOF-H can detect and resolve atomic-level interactions of specific COF framework moieties with adsorbed water and with adsorbed CO₂.

Specifically, 2D $^{13}\text{C}\{^1\text{H}\}$ -HETCOR methods rely on through-space dipole-dipole interactions to selectively detect ^{13}C nuclei which are in molecular-level proximity (<1 nm) to ^1H nuclei of both directly bound and neighboring moieties. The resulting 2D $^{13}\text{C}\{^1\text{H}\}$ spectrum represents a correlated intensity map that resolves spatially from molecularly near moieties on the basis of their isotropic ^1H and ^{13}C chemical shifts, which are sensitive to local bonding environments. For example, the 2D $^{13}\text{C}\{^1\text{H}\}$ HETCOR spectra in Figure 4-6a,b acquired for 100%-amine-coCOF-H, after exposure to ^{13}C -enriched CO₂ and then after subsequent degassing, respectively, both show intensity correlations arising from intramolecular correlations within the coCOF-H framework. These include the strong ^{13}C signals at 46, 55, and 62 ppm from alkyl carbon atoms in the DtATH linker which are correlated with ^1H signals from alkyl protons at 2.0–3.5 ppm; and ^{13}C signals ranging from 112 to 147 ppm from aromatic carbon atoms in the 100%-amine-coCOF-H backbone that are strongly correlated with ^1H signals at 7.0–8.0 ppm from aromatic protons. The framework amide moieties exhibit a ^1H chemical shift at 11.7 ppm, which is consistent with a 2D $^{15}\text{N}\{^1\text{H}\}$ DNP–HETCOR spectrum of 100%-amine-coCOF-H (Figure 6-65b) and a 1D solution-state ^1H NMR spectrum of a small-molecular analogue (see Chapter 6.1.3). A correlated 2D intensity is also observed between the ^{13}C signal at ca. 160 ppm and a new ^1H signal in the range 12–14 ppm, which is assigned to intramolecular HCO₃[–] interactions (green band).^[66] Nearly all of the ^{13}C signals are correlated with ^1H intensity centered at 4.2 ppm from adsorbed H₂O. More interestingly, for 100%-amine-coCOF-H exposed to ^{13}C -enriched CO₂ (Figure 4-6a), the ^{13}C intensity in the range 160–164 ppm is also strongly

correlated with ^1H signals at 4.2 and 7.0–8.0 and 11.7 ppm, which are assigned to adsorbed H_2O (blue band) and hydrazone and/or aromatic ^1H moieties (beige band), and amide groups (purple band), respectively. Such 2D intensity correlations unambiguously establish that chemisorption of CO_2 occurs in close molecular proximities to these moieties, which are consistent with the isotropic ^{13}C chemical shifts that have been reported for the formation of bicarbonate species in tertiary amine solutions.^[67] The breadth of the ^{13}C intensity reflects a distribution of solvated neutral (160 ppm)^[68] and ionic bicarbonate species (171 ppm from quantum chemical calculations, see Table 6-18). The 2D NMR results thus establish that HCO_3^- strongly interacts with adsorbed H_2O and amide and/or aromatic ^1H moieties in the 100%-amine-coCOF-H framework.

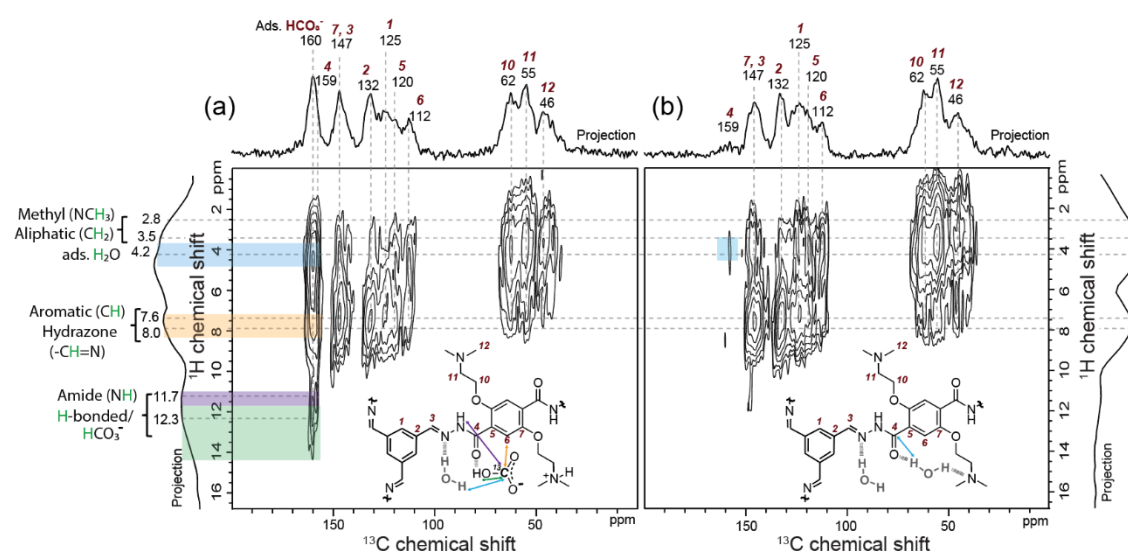


Figure 4-6: Solid-state 2D $^{13}\text{C}\{^1\text{H}\}$ LTMAS-HETCOR spectra of vacuum-dried 100%-amine-coCOF-H (a) after exposure to 100% ^{13}C -enriched CO_2 for 12 h at 1 bar pressure and 298 K, and (b) after desorption of CO_2 for 48 h by vacuum heating at 0.1 bar and 363 K. The spectra were acquired at 9.4 T, 8 kHz MAS, 95 K using short cross-polarization contact times of 500 μs . 1D ^{13}C projections are shown along the horizontal axes for comparison with the 2D spectra, and 1D ^1H projections are shown along the vertical axes. Strong correlated ^{13}C signal intensity (ca. 160 ppm) with ^1H signal at 12 - 14 ppm establishes that CO_2 chemisorbs to form a bicarbonate (HCO_3^-) species

As shown by the 1D $^{13}\text{C}\{^1\text{H}\}$ DNP-CP MAS spectra in Figure 6-64a,b, the ^{13}C amide signal (orange overbar) has stronger intensity for the longest CP contact time of 5 ms. Although ^{13}C -depleted glycerol was used in the DNP solvent formulation, there is a small intensity shoulder ranging from 65 to 80 ppm from glycerol. By comparison, the 1D $^{13}\text{C}\{^1\text{H}\}$ LTMAS-CP MAS spectra in Figure 6-64c,d were acquired on vacuum-dried 100%-amine-coCOF-H upon exposure to dry 100% ^{13}C -enriched CO_2 and after subsequent degassing step. As discussed in the experimental section, these materials were characterized without DNP to minimally influence adsorbed CO_2 . Under otherwise identical conditions, there is

significantly more ^{13}C signal at 160 ppm for the material exposed to ^{13}C -enriched CO_2 . In the 1D spectra, the adsorbed bicarbonate (red overbar) and amide have overlapping signal intensity at 160 ppm. By comparison, for the short contact time (500 μs) used in Figure 4-6, only the strongest $^{13}\text{C}\{\text{H}\}$ dipole-dipole-coupled moieties are expected to yield correlated intensity, which is consistent with the reduced signals from the amide moieties, the carbon atoms of which lack a directly bonded ^1H atom.

Despite degassing and drying the sorbent prior to CO_2 adsorption, 100%-amine-coCOF-H strongly retains adsorbed H_2O , which favors the formation of bicarbonates. Evidence for hydrogen-bonding interactions between H_2O and the framework amide ($-\text{NH}-$) moieties was also observed in a 2D $^{15}\text{N}\{\text{H}\}$ DNP-HETCOR spectrum (see Figure 6-63). After desorption of the CO_2 100% ^{13}C -enriched CO_2 , the ^{13}C signal (ca. 160 ppm) from bicarbonate completely disappears. However, there are still strong intensity correlations associated with ^{13}C moieties in 100%-amine-coCOF-H and ^1H moieties from adsorbed H_2O at ca. 4.2 ppm (blue band) and only very weak correlated intensity associated with the amide ^{13}C signal remains at ca. 159 ppm, which is consistent with the observed water desorption behavior of the samples. The retention of H_2O in 100%-amine-coCOF-H likely contributes to the reduction in the apparent BET surface area. Stronger interactions with CO_2 are usually attributed to a higher amount of heteroatoms, mostly nitrogen and oxygen, on the pore walls of porous framework materials, because of the higher interaction affinity of the heteroatoms to CO_2 .^[3, 69-70] In the context of the aminated COF materials, the interaction with water cannot be neglected. In addition to CO_2 adsorption functionality, the amine groups impart hydrophilicity that leads to increased water uptake by the framework. The increased network hydrophilicity promotes H_2O adsorption and deprotonation near the basic amine side chains, which promotes CO_2 coadsorption as bicarbonate species in the 100%-amine-coCOF-H pores. Note that increasing amounts of adsorbed water in the pores with increasing degree of amine functionalization is consistent with the water isotherms discussed above.

4.2.4 Conclusion

In this study, a mixed linker strategy was used to modify coCOF-H and coCOF-OH with a tertiary amine functionality by copolymerization of isostructural linkers. Addition of the functionalized linker species yields a higher affinity to CO_2 as shown by an increased relative CO_2 adsorption capacity, along with an increase of the heat of adsorption at zero coverage up to a value of 72.4 kJ mol^{-1} . We demonstrate by solid-state 2D $^{13}\text{C}\{\text{H}\}$ NMR analyses, supplemented by quantum chemical NMR calculations, that CO_2 sorption in the 100%-amine-coCOF-H pores proceeds via formation of a bicarbonate species adsorbed within the COF- CO_2 pores, along with water which is strongly retained. Thus, the hydrophilicity of



the COF framework appears to promote increased CO₂ sorption capacity, with different hydrophilicities leading to distinctly different adsorption behaviors of water in the pores. This is likely the reason that increased extents of framework functionalization with amine species lead to increased CO₂ affinity because of the formation of bicarbonate species. Such effects are partially offset by decreased surface area because of steric effects associated with the linkers, as well as strongly retained water in the pores. Tuning the COF's inherent water sorption properties by introducing functional groups such as tertiary amines or amides that promote CO₂ solvation^[71] is expected to further enhance CO₂ adsorption in porous systems.

4.2.5 Acknowledgments

Financial support is gratefully acknowledged from the Max Planck Society, the ERC Starting Grant (project COF Leaf, grant number 639233), the cluster of excellence "Nanosystems Initiative München" (NIM), the Center for NanoScience (CeNS), and for the UCSB group, the U.S. National Science Foundation (award no. CBET-1335694). We thank Prof. T. Bein and Prof. W. Schnick (University of Munich, LMU) for granting access to the XRD facility and V. Duppel for the assistance with material analysis. The solid-state NMR measurements were conducted using the MRL Shared Experimental Facilities supported by the MRSEC Program of the U.S. NSF under award no. DMR 1720256, a member of the NSF-funded Materials Research Facilities Network (www.mrhn.org). Z.J.B. acknowledges funding from the BASF corporation. C.O. acknowledges also support as Max-Planck-Fellow at MPI-FKF Stuttgart.

4.2.6 Author contributions

Kerstin Gottschling designed and performed the experiments as well as the evaluation of analytical data. Linus Stegbauer had the initial idea for the project. Gökçen savasci designed and performed all quantum chemical calculations and helped with data evaluation. Nathan A. Prisco and Zachariah J. Berkson performed NMR experiments and the corresponding data evaluation. Bradeley F. Chmelka supervised the NMR study. Christian Ochsenfeld and Bettina V. Lotsch supervised the project. All authors worked on and revised the manuscript.

4.2.7 References

- [1] S. Hug, M. B. Mesch, H. Oh, N. Popp, M. Hirscher, J. Senker, B. V. Lotsch, *Journal of Materials Chemistry A* **2014**, *2*, 5928-5936.
- [2] C. J. Doonan, D. J. Tranchemontagne, T. G. Glover, J. R. Hunt, O. M. Yaghi, *Nat Chem* **2010**, *2*, 235-238.
- [3] Z. Li, X. Feng, Y. Zou, Y. Zhang, H. Xia, X. Liu, Y. Mu, *Chem. Commun.* **2014**, *50*, 13825-13828.
- [4] S. Wan, J. Guo, J. Kim, H. Ihee, D. Jiang, *Angew. Chem. Int. Ed.* **2008**, *47*, 8826-8830.
- [5] S. Wan, J. Guo, J. Kim, H. Ihee, D. Jiang, *Angew. Chem. Int. Ed.* **2009**, *48*, 5439-5442.

- [6] M. Dogru, M. Handloser, F. Auras, T. Kunz, D. Medina, A. Hartschuh, P. Knochel, T. Bein, *Angew. Chem. Int. Ed.* **2013**, *52*, 2920-2924.
- [7] L. Stegbauer, K. Schwinghammer, B. V. Lotsch, *Chemical Science* **2014**, *5*, 2789-2793.
- [8] A. P. Côté, A. I. Benin, N. W. Ockwig, M. O'Keeffe, A. J. Matzger, O. M. Yaghi, *Science* **2005**, *310*, 1166-1170.
- [9] S.-Y. Ding, W. Wang, *Chem. Soc. Rev.* **2013**, *42*, 548-568.
- [10] R. W. Tilford, S. J. Mugavero, P. J. Pellechia, J. J. Lavigne, *Adv. Mater.* **2008**, *20*, 2741-2746.
- [11] L. Stegbauer, S. Zech, G. Savasci, T. Banerjee, F. Podjaski, K. Schwinghammer, C. Ochsenfeld, B. V. Lotsch, *Advanced Energy Materials* **2018**, *0*, 1703278.
- [12] A. Nagai, Z. Guo, X. Feng, S. Jin, X. Chen, X. Ding, D. Jiang, *Nat Commun* **2011**, *2*, 536.
- [13] Z.-J. Li, S.-Y. Ding, H.-D. Xue, W. Cao, W. Wang, *Chem. Commun.* **2016**, *52*, 7217-7220.
- [14] X. Chen, M. Addicoat, E. Jin, H. Xu, T. Hayashi, F. Xu, N. Huang, S. Irle, D. Jiang, *Scientific Reports* **2015**, *5*, 14650.
- [15] Y. Zhang, X. Shen, X. Feng, H. Xia, Y. Mu, X. Liu, *Chem. Commun.* **2016**, *52*, 11088-11091.
- [16] Z. Kang, Y. Peng, Y. Qian, D. Yuan, M. A. Addicoat, T. Heine, Z. Hu, L. Tee, Z. Guo, D. Zhao, *Chem. Mater.* **2016**, *28*, 1277-1285.
- [17] A. A. Olajire, *Journal of CO2 Utilization* **2017**, *17*, 137-161.
- [18] F. A. Chowdhury, H. Yamada, T. Higashii, K. Goto, M. Onoda, *Industrial & Engineering Chemistry Research* **2013**, *52*, 8323-8331.
- [19] Y. G. Ko, S. S. Shin, U. S. Choi, *J. Colloid Interface Sci.* **2011**, *361*, 594-602.
- [20] R. Zhang, Z. Liang, H. Liu, W. Rongwong, X. Luo, R. Idem, Q. Yang, *Industrial & Engineering Chemistry Research* **2016**, *55*, 3710-3717.
- [21] G. T. Rochelle, *Science* **2009**, *325*, 1652-1654.
- [22] J. Wang, L. Huang, R. Yang, Z. Zhang, J. Wu, Y. Gao, Q. Wang, D. O'Hare, Z. Zhong, *Energy & Environmental Science* **2014**, *7*, 3478-3518.
- [23] M.-M. Titirici, R. J. White, N. Brun, V. L. Budarin, D. S. Su, F. del Monte, J. H. Clark, M. J. MacLachlan, *Chem. Soc. Rev.* **2015**, *44*, 250-290.
- [24] K. Sumida, D. L. Rogow, J. A. Mason, T. M. McDonald, E. D. Bloch, Z. R. Herm, T.-H. Bae, J. R. Long, *Chem. Rev.* **2012**, *112*, 724-781.
- [25] J. Liu, P. K. Thallapally, B. P. McGrail, D. R. Brown, J. Liu, *Chem. Soc. Rev.* **2012**, *41*, 2308-2322.
- [26] X. Zhang, J. Lu, J. Zhang, *Chem. Mater.* **2014**, *26*, 4023-4029.
- [27] N. Huang, X. Chen, R. Krishna, D. Jiang, *Angew. Chem.* **2015**, *127*, 3029-3033.
- [28] A. C. Kizzie, A. G. Wong-Foy, A. J. Matzger, *Langmuir* **2011**, *27*, 6368-6373.
- [29] J. Liu, Y. Wang, A. I. Benin, P. Jakubczak, R. R. Willis, M. D. LeVan, *Langmuir* **2010**, *26*, 14301-14307.
- [30] Z. Liang, M. Marshall, A. L. Chaffee, *Energy & Fuels* **2009**, *23*, 2785-2789.
- [31] S. Krishnamurthy, V. R. Rao, S. Guntuka, P. Sharratt, R. Haghpanah, A. Rajendran, M. Amanullah, I. A. Karimi, S. Farooq, *AIChE J.* **2014**, *60*, 1830-1842.
- [32] P. A. Webley, *Adsorption* **2014**, *20*, 225-231.
- [33] X. Kong, E. Scott, W. Ding, J. A. Mason, J. R. Long, J. A. Reimer, *J. Am. Chem. Soc.* **2012**, *134*, 14341-14344.



- [34] L.-C. Lin, J. Kim, X. Kong, E. Scott, T. M. McDonald, J. R. Long, J. A. Reimer, B. Smit, *Angew. Chem. Int. Ed.* **2013**, *52*, 4410-4413.
- [35] T. M. McDonald, J. A. Mason, X. Kong, E. D. Bloch, D. Gygi, A. Dani, V. Crocellà, F. Giordanino, S. O. Odoh, W. S. Drisdell, B. Vlasisavljevich, A. L. Dzubak, R. Poloni, S. K. Schnell, N. Planas, K. Lee, T. Pascal, L. F. Wan, D. Prendergast, J. B. Neaton, B. Smit, J. B. Kortright, L. Gagliardi, S. Bordiga, J. A. Reimer, J. R. Long, *Nature* **2015**, *519*, 303.
- [36] P. J. Wilson, T. J. Bradley, D. J. Tozer, *The Journal of Chemical Physics* **2001**, *115*, 9233-9242.
- [37] F. Jensen, *Journal of Chemical Theory and Computation* **2006**, *2*, 1360-1369.
- [38] J. P. Perdew, K. Burke, M. Ernzerhof, *Phys. Rev. Lett.* **1996**, *77*, 3865-3868.
- [39] S. Grimme, J. Antony, S. Ehrlich, H. Krieg, *The Journal of Chemical Physics* **2010**, *132*, 154104.
- [40] F. Weigend, M. Häser, H. Patzelt, R. Ahlrichs, *Chem. Phys. Lett.* **1998**, *294*, 143-152.
- [41] F. Weigend, *PCCP* **2006**, *8*, 1057-1065.
- [42] TURBOMOLE, developer version based on version V7.1 2017, a development of University of Karlsruhe and Forschungszentrum Karlsruhe GmbH, 1989-2007, TURBOMOLE GmbH, since 2007; available from <http://www.turbomole.com>.
- [43] R. Ahlrichs, M. Bär, M. Häser, H. Horn, C. Kölmel, *Chem. Phys. Lett.* **1989**, *162*, 165-169.
- [44] J. Kussmann, C. Ochsenfeld, *The Journal of Chemical Physics* **2013**, *138*, 134114.
- [45] J. Kussmann, C. Ochsenfeld, *Journal of Chemical Theory and Computation* **2015**, *11*, 918-922.
- [46] F. J. Uribe-Romo, C. J. Doonan, H. Furukawa, K. Oisaki, O. M. Yaghi, *J. Am. Chem. Soc.* **2011**, *133*, 11478-11481.
- [47] E. L. Spitler, B. T. Koo, J. L. Novotney, J. W. Colson, F. J. Uribe-Romo, G. D. Gutierrez, P. Clancy, W. R. Dichtel, *J. Am. Chem. Soc.* **2011**, *133*, 19416-19421.
- [48] F. Haase, K. Gottschling, L. Stegbauer, L. S. Germann, R. Gutzler, V. Duppel, V. S. Vyas, K. Kern, R. E. Dinnebier, B. V. Lotsch, *Materials Chemistry Frontiers* **2017**, *1*, 1354-1361.
- [49] L. Stegbauer, M. W. Hahn, A. Jentys, G. Savasci, C. Ochsenfeld, J. A. Lercher, B. V. Lotsch, *Chem. Mater.* **2015**, *27*, 7874-7881.
- [50] S. Lowell, J. E. Shields, M. A. Thomas, M. Thommes, *Characterization of porous solids and powders: surface area, pore size and density*, Springer, **2012**.
- [51] S. J. Datta, C. Khumnoon, Z. H. Lee, W. K. Moon, S. Docao, T. H. Nguyen, I. C. Hwang, D. Moon, P. Oleynikov, O. Terasaki, K. B. Yoon, *Science* **2015**, *350*, 302-306.
- [52] L. Zhongping, Z. Yongfeng, F. Xiao, D. Xuesong, Z. Yongcun, L. Xiaoming, M. Ying, *Chem. Eur. J.* **2015**, *21*, 12079-12084.
- [53] R. Gomes, A. Bhaumik, *RSC Advances* **2016**, *6*, 28047-28054.
- [54] M. Shan, B. Seoane, E. Rozhko, A. Dikhtiarenko, G. Clet, F. Kapteijn, J. Gascon, *Chemistry – A European Journal* **2016**, *22*, 14467-14470.
- [55] S. Kandambeth, A. Mallick, B. Lukose, M. V. Mane, T. Heine, R. Banerjee, *J. Am. Chem. Soc.* **2012**, *134*, 19524-19527.
- [56] Y. Zhao, K. X. Yao, B. Teng, T. Zhang, Y. Han, *Energy & Environmental Science* **2013**, *6*, 3684-3692.

- [57] J. A. Mason, K. Sumida, Z. R. Herm, R. Krishna, J. R. Long, *Energy & Environmental Science* **2011**, *4*, 3030-3040.
- [58] Z. Lei, X. Long, H. Cheng, L. Wenlong, H. Wei, P. Yichang, *Angew. Chem. Int. Ed.* **2017**, *56*, 7787-7791.
- [59] M. Radek, L. Antonin, K. Erkki, S. Elina, T. Jaromir, *Curr. Org. Chem.* **2007**, *11*, 1154-1205.
- [60] G. J. Martin, M. L. Martin, J.-P. Gouesnard, *¹⁵N-NMR Spectroscopy*, Springer-Verlag, **1981**.
- [61] T. Kobayashi, S. Gupta, M. A. Caporini, V. K. Pecharsky, M. Pruski, *The Journal of Physical Chemistry C* **2014**, *118*, 19548-19555.
- [62] M. L. Pinto, L. Mafrá, J. M. Guil, J. Pires, J. Rocha, *Chem. Mater.* **2011**, *23*, 1387-1395.
- [63] C.-H. Chen, D. Shimon, J. J. Lee, S. A. Didas, A. K. Mehta, C. Sievers, C. W. Jones, S. E. Hayes, *Environmental Science & Technology* **2017**, *51*, 6553-6559.
- [64] E. G. Moschetta, M. A. Sakwa-Novak, J. L. Greenfield, C. W. Jones, *Langmuir* **2015**, *31*, 2218-2227.
- [65] O. Benson, I. da Silva, S. P. Argent, R. Cabot, M. Savage, H. G. W. Godfrey, Y. Yan, S. F. Parker, P. Manuel, M. J. Lennox, T. Mitra, T. L. Easun, W. Lewis, A. J. Blake, E. Besley, S. Yang, M. Schröder, *J. Am. Chem. Soc.* **2016**, *138*, 14828-14831.
- [66] H. Nebel, M. Neumann, C. Mayer, M. Epple, *Inorg. Chem.* **2008**, *47*, 7874-7879.
- [67] P. V. Kortunov, M. Siskin, L. S. Baugh, D. C. Calabro, *Energy & Fuels* **2015**, *29*, 5940-5966.
- [68] J. Seravalli, S. W. Ragsdale, *Biochemistry* **2008**, *47*, 6770-6781.
- [69] Z. Yongfei, Z. Ruqiang, Z. Yanli, *Adv. Mater.* **2016**, *28*, 2855-2873.
- [70] A. Sharma, A. Malani, N. V. Medhekar, R. Babarao, *CrystEngComm* **2017**, *19*, 6950-6963.
- [71] H. M. Lee, I. S. Youn, M. Saleh, J. W. Lee, K. S. Kim, *PCCP* **2015**, *17*, 10925-10933.



5 Conclusion and outlook

In this thesis, the concept of COF photocatalysis has been extended from the traditional Pt nanoparticle based hydrogen evolution systems as presented in 2014 towards molecular hydrogen evolution catalysts.

Cobaloximes were established as co-catalysts for azine- and hydrazone-based COFs. The combination of chloro-(pyridine)cobaloxime and azine-linked N_2 -COF produced hydrogen with a rate of $782 \mu\text{mol g}^{-1} \text{h}^{-1}$ and a TON of 54.4 in a water/acetonitrile mixture with TEOA as sacrificial donor. The photocatalysis mechanism was found to follow a monometallic pathway via a Co^{III} -hydride and/or Co^{II} -hydride species.

A true single-site photocatalytic system was generated by the covalent attachment of a modified cobaloxime catalyst to a COF photosensitizer. The photocatalytic activity of the system was more than doubled compared to the physisorbed COF/catalyst system. The single-site character of the interaction allowed for the in-depth solid-state NMR characterization which was supported by quantum chemical methods. The structural details of the improved photoreactivity was ascribed to an enhanced interaction of the co-catalyst and the pore wall.

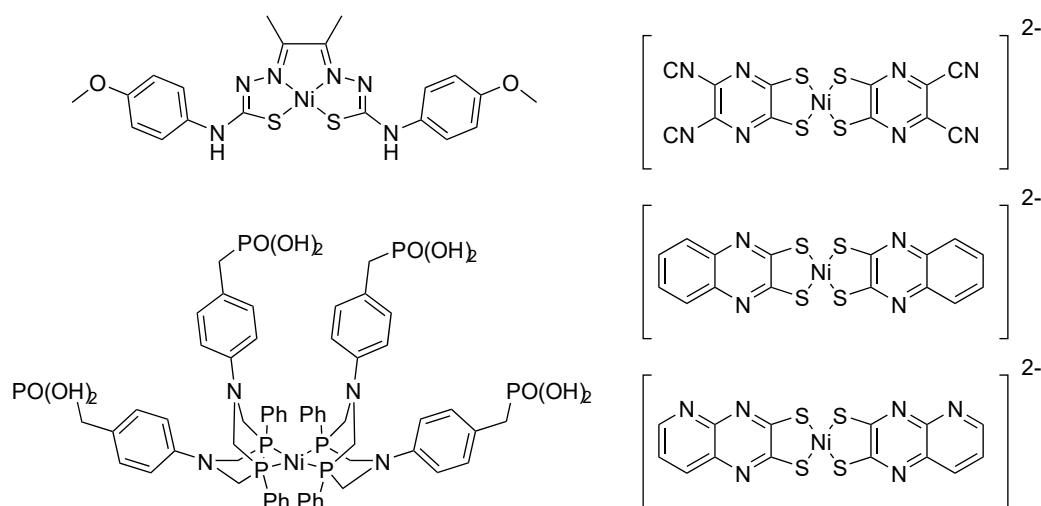


Figure 5-1: Chemical structures of different Ni-based hydrogen evolution co-catalysts.

This system lays the foundation for the development of a modular photocatalysis platform by providing the possibility for the integration of any functionalized molecular catalyst. For example, we showed that Ni-thiolate clusters perform well when physisorbed to a thiazole-linked COF.^[1] A covalent integration of a similar or other Ni-based HEC to a COF should

be studied as they are at the same time robust and earth-abundant. Other examples of Ni-based HECs that could be hybridized with a COF are shown in Figure 5-1.^[2-4] The covalent integration of water oxidation catalysts (WOC) like Ru-based^[5-7] or Ir-phenylpyridine complexes^[8-9] might be possible using the same strategy. Examples for such WOCs is shown in Figure 5-2. After matching the energy levels of the COF and introducing both WOC and HEC, a fully heterogeneous single-site system for overall water-splitting could be created, which would act like an artificial leaf. This concept was described in the ERC Starting Grant *COFLeaf* (Grant Number 639233).

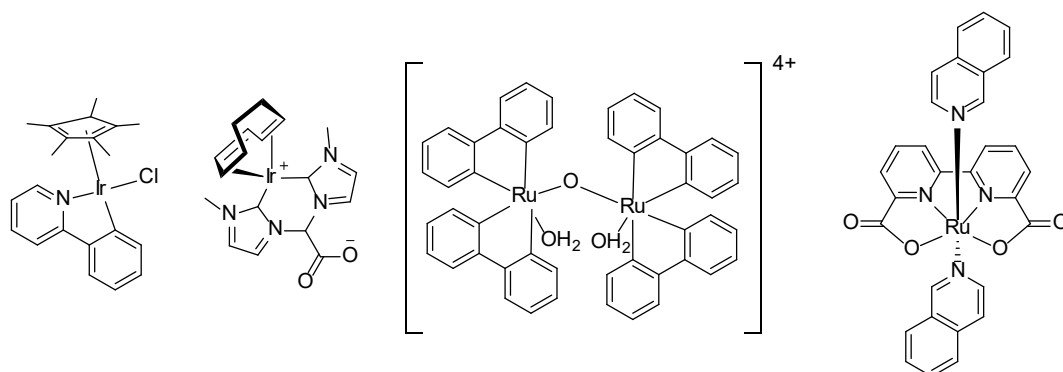


Figure 5-2: Chemical structures of different Ru- and Ir-based water oxidation co-catalysts.

The integration of the co-catalysts directly into the COF pore walls should be targeted. That would counteract the problem of pore clogging that was observed in this thesis. One possible approach is the integration of [FeFe] hydrogenase inspired catalysts as has been shown in the MOF field in 2013.^[10-11] The molecular co-catalyst [FeFe](dcbdt)(CO)₆ (dcbdt = 1,4-dicarboxylbenzene-2,3-dithiolate, Figure 5-3) was integrated into the Zr(IV)-based MOF UiO-66 and showed photocatalytic hydrogen evolution in the presence of a photosensitizer and an electron donor. For this purpose, the catalyst was modified with carboxyl groups. Selective reduction to the corresponding dialdehyde or synthesis of the hydrazine or amine analogue would be needed to integrate such a linker into a stable nitrogen-bonded COF.

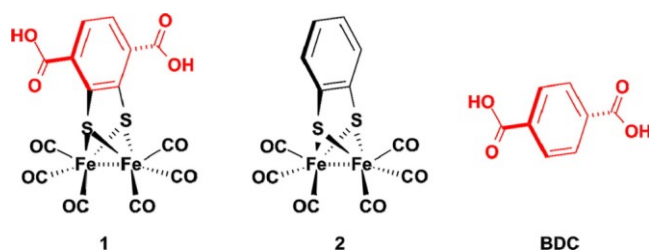


Figure 5-3: [FeFe] hydrogenase active site model complexes [FeFe](dcbdt)(CO)₆ (**1**) and [FeFe](bdt)(CO)₆ (**2**) and the BDC ligand. Reprinted from [10].

Also, the integration of an Ir-based WOC into the pore wall of MOFs has been demonstrated by coordination of the Ir to bipyridine units of UiO-67.^[12-13] The synthesis conditions and the choice of WOCs is shown in Figure 5-4. A similar approach or a combination of the methods mentioned in this thesis could be possible in the context of COFs as well.

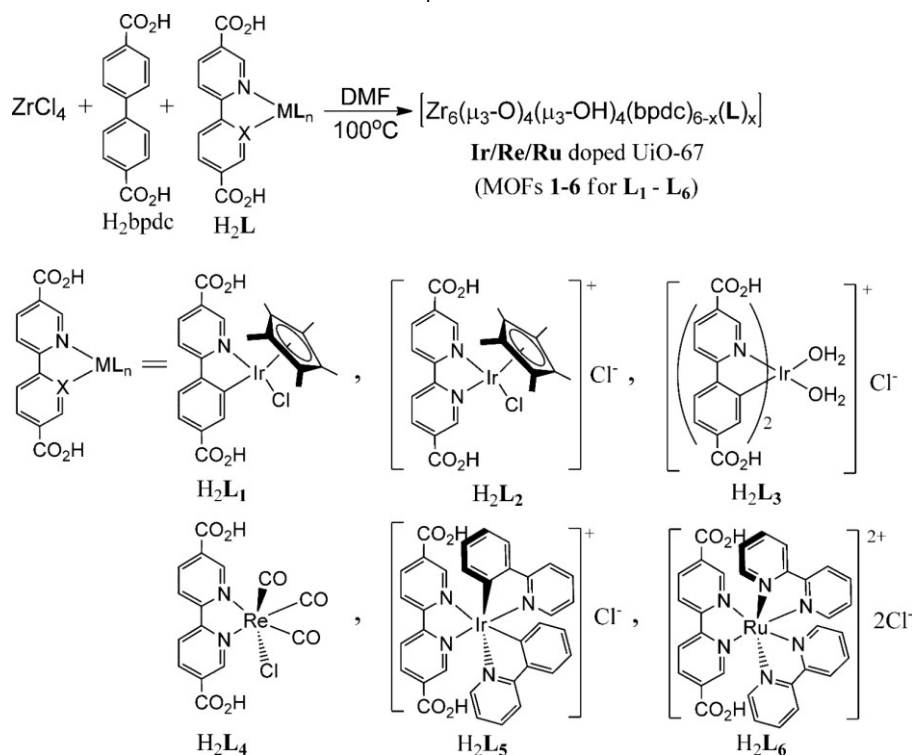
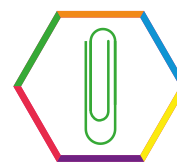


Figure 5-4: Synthesis of doped UiO-67. Reprinted from [12].

The versatility of COF systems was also used in the context of CCS. Hydrazone-based COF systems with varying amount of tertiary amine functionalization were synthesized. According to their inherent polarity, the solvation of CO₂ in the COF pores was modulated and with that its CO₂ and H₂O adsorption properties. The Q_{st} could be increased to up to 72.4 kJ mol⁻¹, which is higher than for most heterogeneous CCS systems. By means of solid-state 2D ¹³C{¹H} NMR and quantum chemical calculations it was found that the CO₂ binding mechanism is based on the formation of bicarbonate species. An expansion of the understanding of the basic mechanisms and principles in the context of COFs in CCS is key to the evaluation of the materials' suitability for this application. Also, the capture of nitric oxide should be investigated, as COFs could offer solutions in this area as well.

This thesis underlines the tunability of COF systems. According to the demands of the specific applications, COF systems can readily be designed to meet the desired requirements. Not only pore sizes, but also surface chemistry and polarity need to be considered in that context. This will help paving the way for this exceptional material class into innovative applications conquering the challenges of the anthropocene.

-
- [1] B. P. Biswal, H. A. Vignolo-Gonzalez, T. Banerjee, L. Grunenber, G. Savasci, K. Gottschling, J. Nuss, C. Ochsenfeld, B. V. Lotsch, *J. Am. Chem. Soc.* **2019**, *141*, 11082-11092.
- [2] S. Panagiotakis, G. Landrou, V. Nikolaou, A. Putri, R. Hardre, J. Massin, G. Charalambidis, A. G. Coutsolelos, M. Orio, *Front Chem* **2019**, *7*, 405.
- [3] Y. Aimoto, K. Koshiba, K. Yamauchi, K. Sakai, *Chem Commun (Camb)* **2018**, *54*, 12820-12823.
- [4] M. A. Gross, A. Reynal, J. R. Durrant, E. Reisner, *J. Am. Chem. Soc.* **2014**, *136*, 356-366.
- [5] S. W. Gersten, G. J. Samuels, T. J. Meyer, *J. Am. Chem. Soc.* **1982**, *104*, 4029-4030.
- [6] B. Zhang, L. Sun, *J. Am. Chem. Soc.* **2019**, *141*, 5565-5580.
- [7] C. J. Richmond, S. Escayola, A. Poater, *Eur. J. Inorg. Chem.* **2019**, *2019*, 2101-2108.
- [8] J. F. Hull, D. Balcells, J. D. Blakemore, C. D. Incarvito, O. Eisenstein, G. W. Brudvig, R. H. Crabtree, *J. Am. Chem. Soc.* **2009**, *131*, 8730-8731.
- [9] R. Puerta-Oteo, M. V. Jiménez, J. J. Pérez-Torrente, *Catalysis Science & Technology* **2019**, *9*, 1437-1450.
- [10] S. Pullen, H. Fei, A. Orthaber, S. M. Cohen, S. Ott, *J. Am. Chem. Soc.* **2013**, *135*, 16997-17003.
- [11] C. Bozal-Ginesta, S. Pullen, S. Ott, L. Hammarström, *ChemPhotoChem* **2020**.
- [12] C. Wang, Z. Xie, K. E. deKrafft, W. Lin, *J. Am. Chem. Soc.* **2011**, *133*, 13445-13454.
- [13] C. Wang, J. L. Wang, W. Lin, *J. Am. Chem. Soc.* **2012**, *134*, 19895-19908.



6 Appendix

6.1 Supporting information

6.1.1 Materials and methods for Chapter 3.3

Materials

Co-1 was obtained from Sigma-Aldrich and used without further purification. Co-2 and Co-3 were synthesized following reported procedures.^{1,2} All other chemicals were obtained from either Sigma-Aldrich or Fluka. Solvents were obtained from Merck and Roth.

Photocatalysis

Photocatalysis experiments were performed in a double walled glass reactor kept at a constant temperature (25 °C) with water circulated through a thermostat. The reactor was irradiated from the top through a quartz window with a xenon lamp (Newport, 300 W) equipped with a water filter and a dichroic mirror and subsequently through an AM1.5 filter. A power density of 100 mW/cm² (Thorlabs Thermo power sensor) was maintained at the surface of the photocatalysis reaction mixture. After all the components for the reaction were put in, residual oxygen and nitrogen were removed by three cycles of evacuation and backfill with argon. For the determination of evolved hydrogen, the headspace of the reactor was sampled periodically with a gas chromatograph (Thermo Scientific TRACE GC Ultra) equipped with a thermal conductivity detector (TCD) using argon as the carrier gas. AQE was calculated using the equation $AQE = [(average H_2 \text{ evolution rate} \times 2) / \text{incident photon flux}]$. TON based on **Co-1** was calculated using the equation $TON = \text{moles of evolved } H_2 / \text{moles of co-catalyst used}$. TOF was calculated using the equation $TOF = TON / \text{time(h)}$. The H₂ evolution rates under different experimental conditions correspond to a fit of the linear regime in the plot of H₂ evolved vs time, after the initial induction period.

PXRD

PXRD pattern were collected at room temperature on a Stoe Stadi P diffractometer (Cu-K α 1, Ge(111)) in Debye-Scherrer geometry. The sample was measured inside a sealed glass capillary (0.7 mm). For improved particle statistics the sample was spun.

IR

Infrared spectra were recorded in attenuated total reflection (ATR) geometry on a PerkinElmer UATR Two equipped with a diamond crystal. The spectra were background corrected.

ssNMR

ssNMR was recorded on a Bruker 400 MHz spectrometer. For ssNMR spectroscopy, the sample was filled in a 4 mm ZrO₂ rotor, which was mounted in a standard double resonance MAS probe (Bruker). Chemical shift was referenced relative to tetramethylsilane. ¹H spectrum was obtained using decoupling channel for detection. The spinning rate was 14 kHz for both ¹H and ¹³C NMR. A standard cross-polarization sequence with a 2 ms ramped contact pulse was used for ¹³C and a total of 4096 scans were accumulated. ¹H NMR was recorded with a common Bloch decay sequence and 16 scans were accumulated.

SEM

SEM images were obtained on a Zeiss Merlin instrument with SE (secondary electron) detector.

TEM

TEM was performed with a Philips CM30 ST (300kV, LaB₆ cathode). The samples were prepared dry onto a copper lacey carbon grid (Plano). EDX was obtained on a Nooan System Seven (NSS) Si(Li) detector.

UV-Vis

UV-Vis absorption spectra were recorded on Agilent Cary 60 UV-Vis spectrometer.

Steady-State and Time-Resolved Emission

The dynamics of emission decay were monitored at room temperature using FLS980 spectrometer's time-correlated single-photon counting capability (1024 channels; 50 ns window) with data collection for 3000 counts. Excitation was provided by an Edinburgh EPL-375 picosecond pulsed laser diode (375 ± 6 nm, pulse width – 68 ps). A cooled microchannel plate photomultiplier tube (MCP-PMT) was used as the detector. Kinetics were fit with a two-exponential function by using Edinburgh software package.

EPR

Continuous wave X-band EPR measurements were done using a commercial Bruker EMXmicro spectrometer equipped with a variable temperature control system (4-300K) and a Bruker ER 083 C magnet. All spectra were acquired at 4 K. Photocatalysis reaction dispersion was thoroughly degassed and then transferred to a glove bag and a standard Suprasil tube with 3 mm outer diameter was filled and then sealed outside. For the post-illumination sample, the degassed reaction dispersion was irradiated in a quartz cuvette for 2 hours and then the supernate was transferred to the EPR tube in a glove bag and sealed.



Quantum chemical calculations

Structures for all investigated geometries were optimized at the PBE0-D3/def2-SVP level of theory. Cobaloxime-COF model systems were optimized by optimizing the cobalt complex and the COF fragment in separate calculations, optimizing the cobaloxime-COF model afterwards with constraints on the COF fragment.

Interaction energies were calculated on PBE0-D3/def2-TZVP level of theory by including counterpoise corrections to account for basis set superposition errors. Differences of interaction energies were calculated relative to the **Co-1** model system.

Geometry optimizations were done using the Turbomole program package in version 7.0.2. Computation of interaction energies were performed using the FermiONs++ program package.

Additional characterization

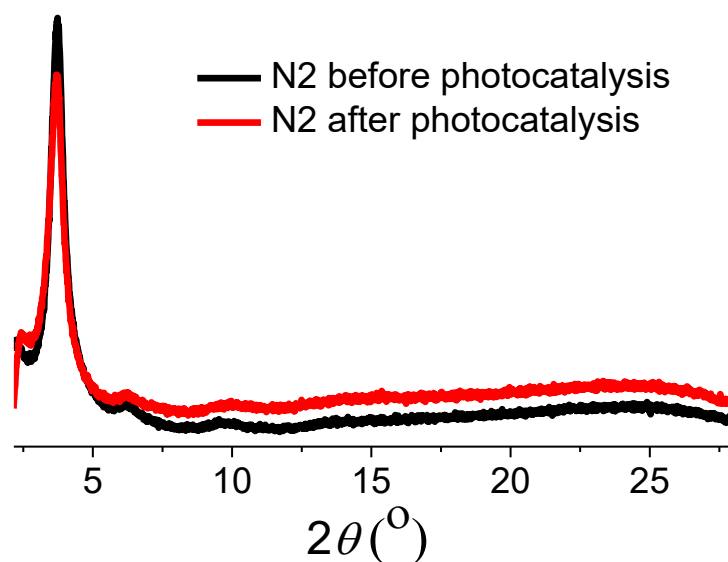


Figure 6-1: PXRD pattern of N₂-COF before and after photocatalysis showing retention of crystallinity.

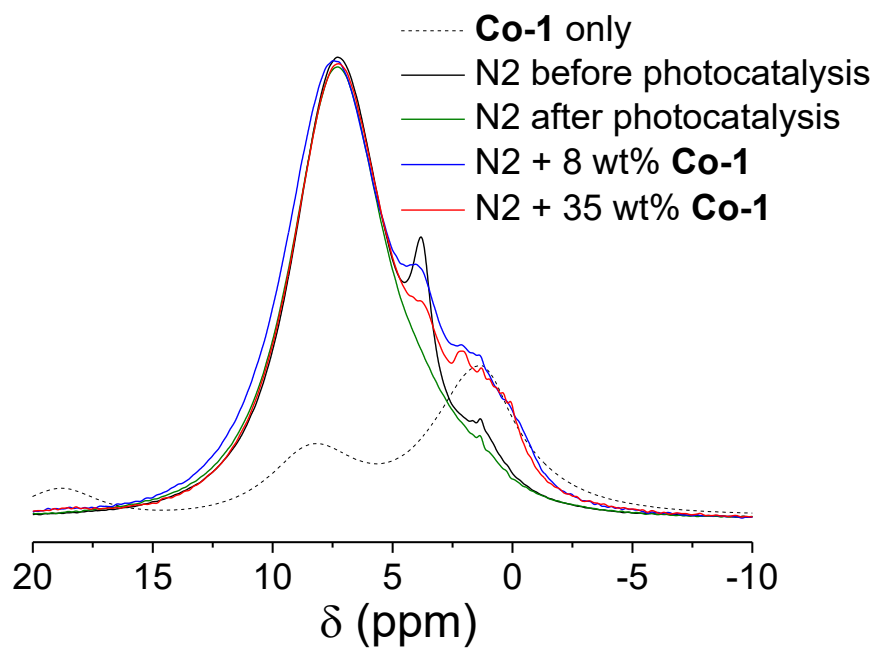


Figure 6-2: ¹H MAS spectra of N₂-COF before and after photocatalysis showing no change in the chemical shift values. The peak at 3.7 ppm is due to water, probably in the pores. Also shown are the illuminated and dried COF samples with 8 and 35 wt% Co-1 with the broad peak around 1.4 ppm due to large amounts of Co-1.

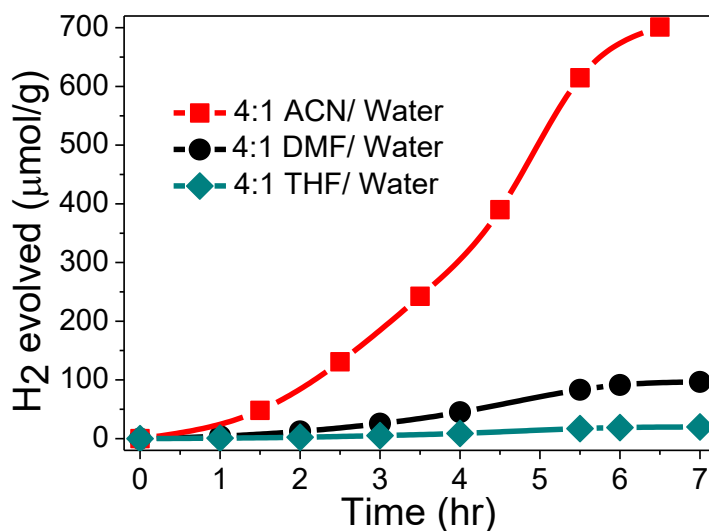


Figure 6-5: Variation of H₂ evolution rates in different solvents. For all measurements 5 mg of N₂-COF was dispersed in 10 ml of the solvent together with 100 μL of TEOA and 400 μL of a 2.48 mM solution of Co-1 in acetonitrile. 100 mW/cm² AM 1.5 radiation was used for illumination.

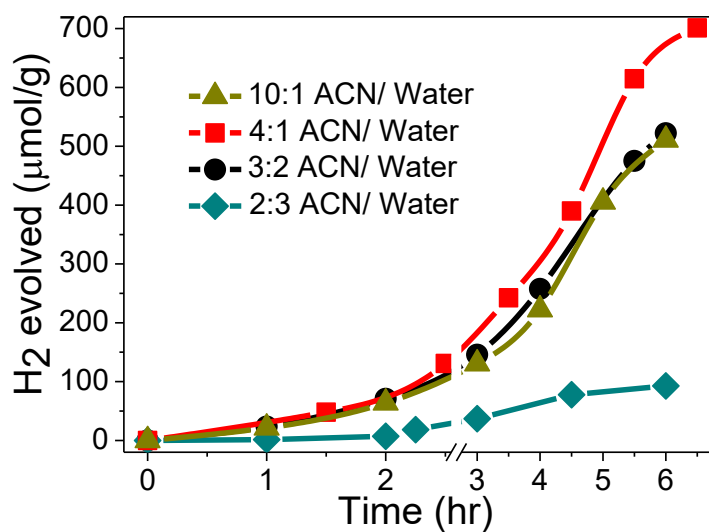


Figure 6-6: Variation of H₂ evolution rates with ratio of ACN/water in the photocatalytic reaction mixture. All conditions were the same as in Figure S5 caption. With increase in ACN content, the H₂ evolution rate increases from 27 μmolg⁻¹h⁻¹ to 130 μmolg⁻¹h⁻¹ and finally to 160 μmolg⁻¹h⁻¹ for 4:1 ACN/water. For 10:1 ACN/water the rate again drops to 130 μmolg⁻¹h⁻¹.

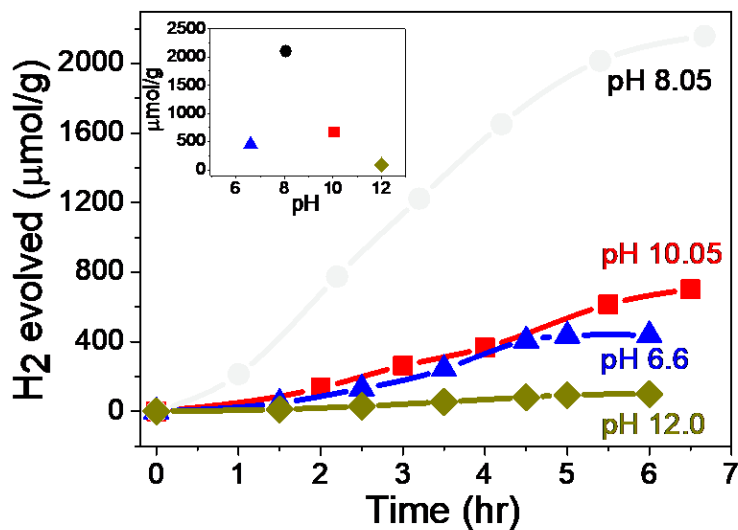


Figure 6-7: Variation of H₂ evolution rates with the pH of the photocatalytic reaction mixture. pH was adjusted by addition of 0.1 M aqueous HCl or NaOH dropwise. All other conditions were the same as before with 4:1 ACN/water as the solvent. The H₂ evolution rates are 138 µmolg⁻¹h⁻¹ at pH 6.6, 390 µmolg⁻¹h⁻¹ at pH 8.05, 160 µmolg⁻¹h⁻¹ at pH 10.05 and 26 µmolg⁻¹h⁻¹ at pH 12. The inset shows the amount of H₂ generated after 6h at different pH values.

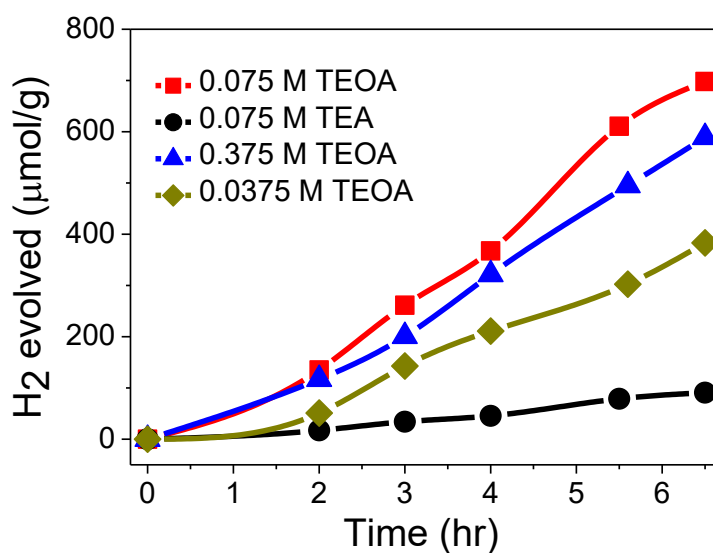


Figure 6-8: Variation of H₂ evolution rates with TEA and different concentrations of TEOA as the electron donor.

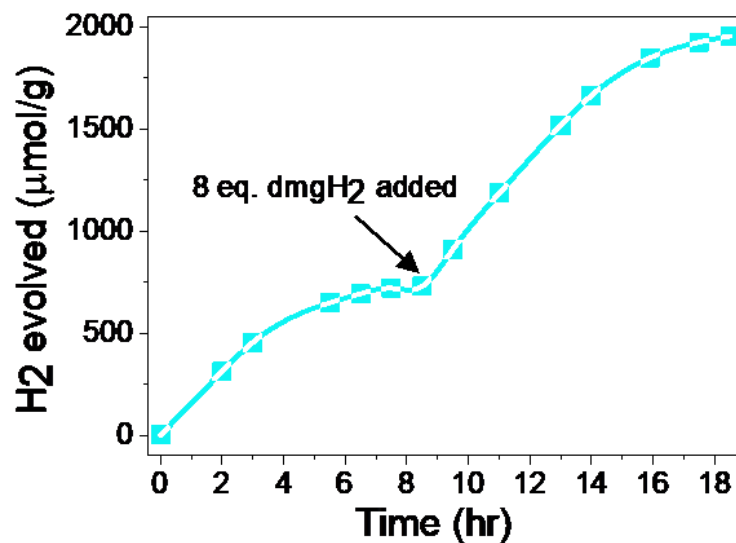


Figure 6-9: H₂ evolution is restored after addition of 8 equivalents of dmgH₂ to the reaction mixture. Initially, 5 mg of N₂-COF was dispersed in 10 ml of 4:1 ACN/H₂O solvent together with 100 µL of TEOA and 400 µL of a 2.48 mM solution of Co-1 in acetonitrile. The reaction mixture is irradiated with 100 mW/cm² AM 1.5 radiation.

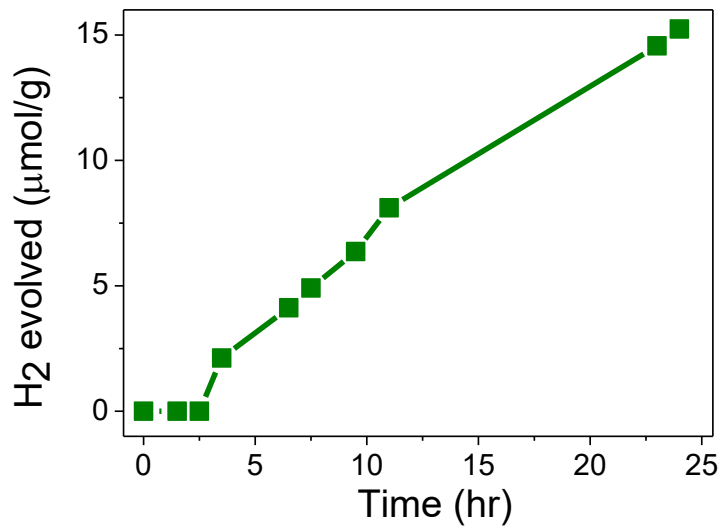


Figure 6-10: H₂ evolution with 0.05 M dmgH₂ as the electron donor. 5 mg of N₂-COF was dispersed in 10 ml of 4:1 ACN/H₂O solvent together with 400 µL of a 2.48 mM solution of Co-1 in acetonitrile. The reaction mixture is irradiated with 100 mW/cm² AM 1.5 radiation. No TEOA was added to the reaction mixture.

Table 6-1: Gibbs free energy of formation of Co^{II} and Co^I in the reaction of N₂ with **Co-2** and **Co-3** by oxidative and reductive electron transfer pathways. The N₂ energy levels are for a model hexagon with hydrazone termination. The Co(III)/Co(II) and Co(II)/Co(I) reduction potential values have been obtained from literature.^{2,3}

	$E(\text{Co}^{\text{III}}/\text{Co}^{\text{II}}), \text{V (NHE)}$ in ACN	$E(\text{Co}^{\text{II}}/\text{Co}^{\text{I}}), \text{V (NHE)}$ in ACN	$\Delta G_1^\circ, \text{eV}$	$\Delta G_2^\circ, \text{eV}$	$\Delta G_3^\circ, \text{eV}$	$\Delta G_4^\circ, \text{eV}$
Co-2		-0.29		-1.23		-2.02
Co-3	0.25	-0.21	-1.77	-1.31	-2.56	-2.1

$$E_{\text{CB}}^{\text{N}_2} = -1.52 \text{ V vs NHE in vacuum,}$$

$$E(\text{N}_2^{\bullet-}) = -2.31 \text{ V vs NHE in vacuum,}$$

$$\Delta G_1^\circ = E_{\text{CB}}^{\text{N}_2} - E(\text{Co}^{\text{III}}/\text{Co}^{\text{II}}),$$

$$\Delta G_2^\circ = E_{\text{CB}}^{\text{N}_2} - E(\text{Co}^{\text{II}}/\text{Co}^{\text{I}}),$$

$$\Delta G_3^\circ = E(\text{N}_2^{\bullet-}) - E(\text{Co}^{\text{III}}/\text{Co}^{\text{II}}),$$

$$\Delta G_4^\circ = E(\text{N}_2^{\bullet-}) - E(\text{Co}^{\text{II}}/\text{Co}^{\text{I}})$$

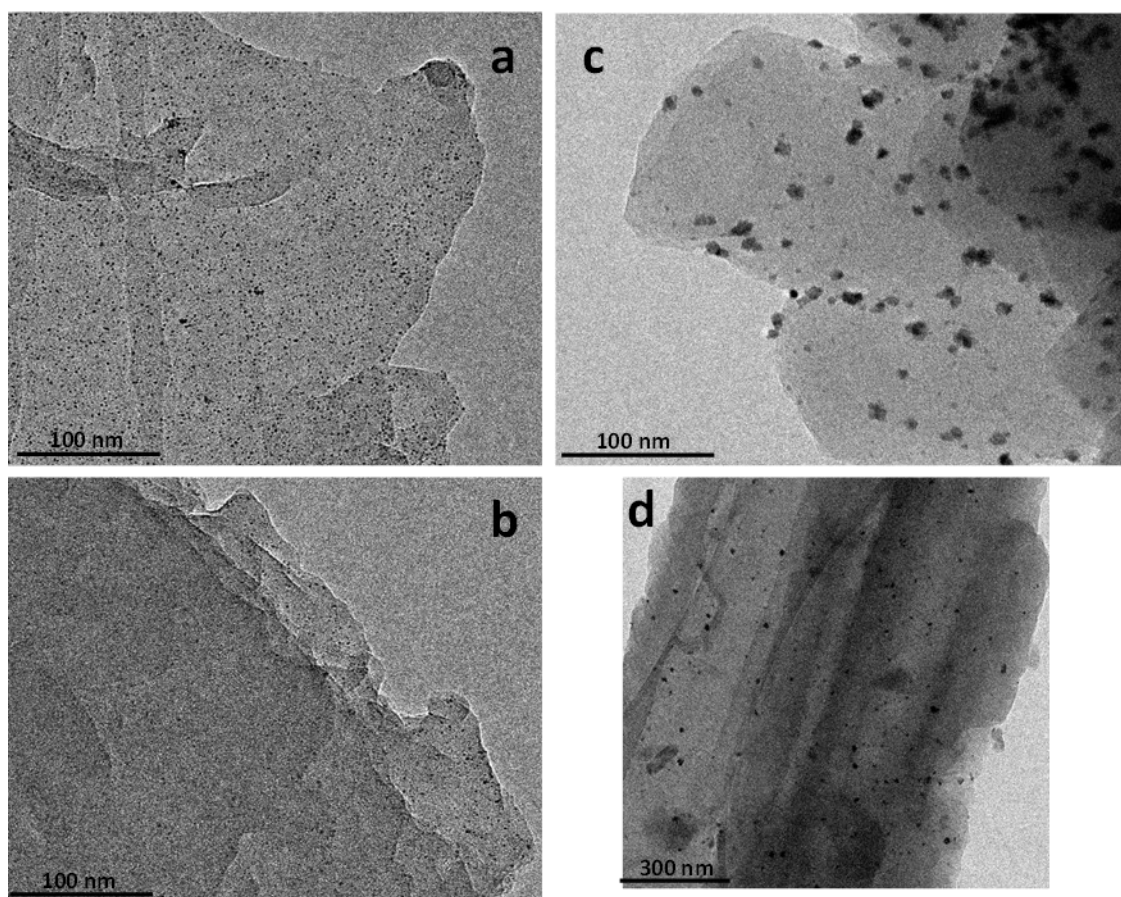


Figure 6-11: TEM micrographs of post photocatalysis sample of N₂-COF showing (a) even distribution of ~2 nm Pt nanoparticles on one section of the COF sample. (b) no appreciable Pt deposition can be seen on another section of the same sample. Photocatalysis was carried out in 4:1 ACN/water solvent with metallic platinum co-catalyst.

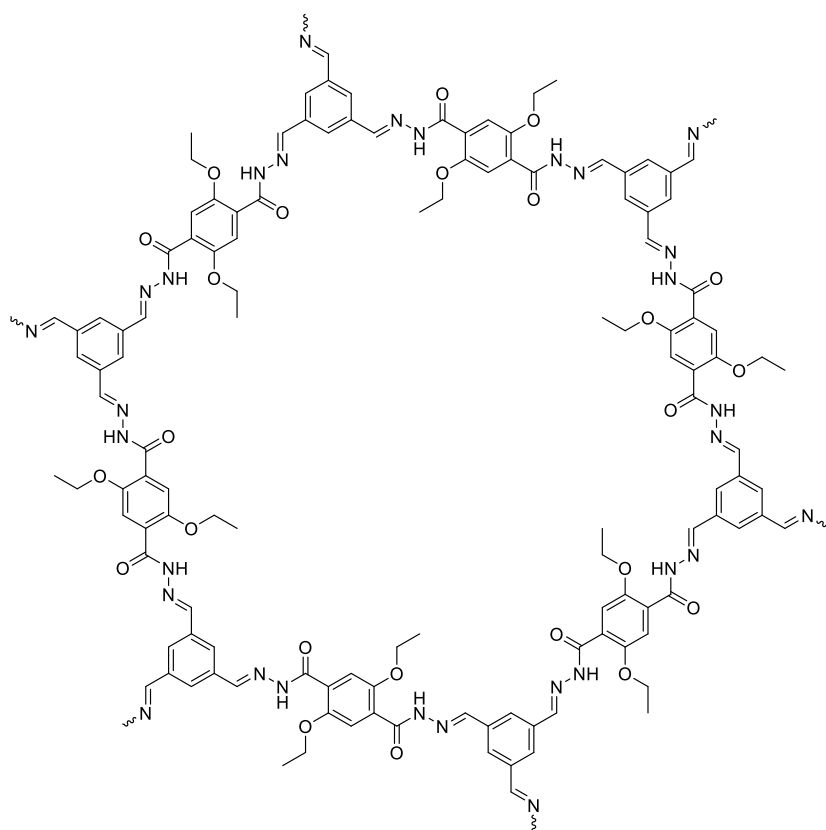
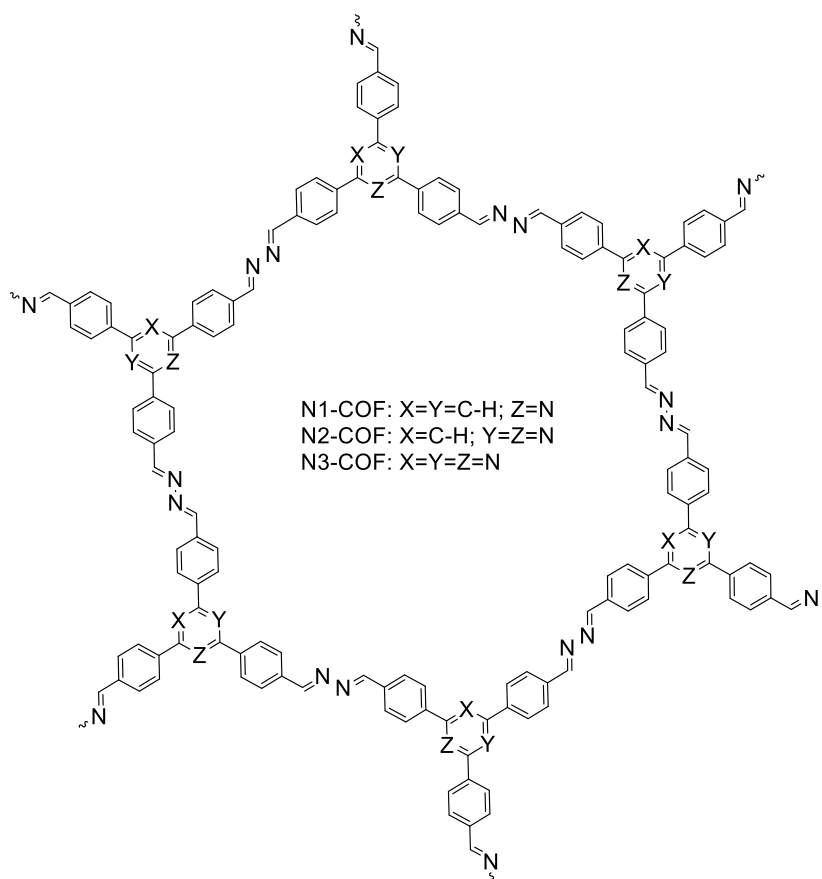


Figure 6-12: Structure of COF-42.

Figure 6-13: Structure of N_x -COFs.Table 6-2: Gibbs free energy of formation of Co^{II} and Co^{I} in the reaction of N1, N3 and COF 42 with **Co-1** by oxidative and reductive electron transfer pathways. The COF 42 energy levels are for a model with methyl terminations, unlike model hexagons with hydrazone termination for the N_x COFs.⁴

	$E_{\text{CB}}, \text{V (NHE) in vacuum}$	$E(\text{COF}^{\bullet-}), \text{V (NHE) in vacuum}$	$\Delta G_1^\circ, \text{eV}$	$\Delta G_2^\circ, \text{eV}$	$\Delta G_3^\circ, \text{eV}$	$\Delta G_4^\circ, \text{eV}$
N1	-1.73	-2.51	-1.3	-0.85	-2.08	-1.63
N3	-1.42	-2.25	-0.99	-0.54	-1.82	-1.37
COF 42	-2.45		-2.02	-1.57		

$$E(\text{Co}^{\text{III}}/\text{Co}^{\text{II}})_{\text{Co-1}} = -0.43 \text{ vs NHE in ACN}, E(\text{Co}^{\text{II}}/\text{Co}^{\text{I}})_{\text{Co-1}} = -0.88 \text{ vs NHE in ACN},$$

$$\Delta G_1^\circ = E_{\text{CB}} - E(\text{Co}^{\text{III}}/\text{Co}^{\text{II}}),$$

$$\Delta G_2^\circ = E_{\text{CB}} - E(\text{Co}^{\text{II}}/\text{Co}^{\text{I}}),$$

$$\Delta G_3^\circ = E(\text{COF}^{\bullet-}) - E(\text{Co}^{\text{III}}/\text{Co}^{\text{II}}),$$

$$\Delta G_4^\circ = E(\text{COF}^{\bullet-}) - E(\text{Co}^{\text{II}}/\text{Co}^{\text{I}})$$

Table 6-3: H₂ evolution rate ($\mu\text{molg}^{-1}\text{h}^{-1}$) for N2 and N3 COFs with platinum and Co-1 co-catalysts under different conditions.

	N2	N3
Pt in H₂O	438	1703
Pt in 4:1 ACN/Water	52	175
Co-1 in 4:1 ACN/Water at pH 8	390	163

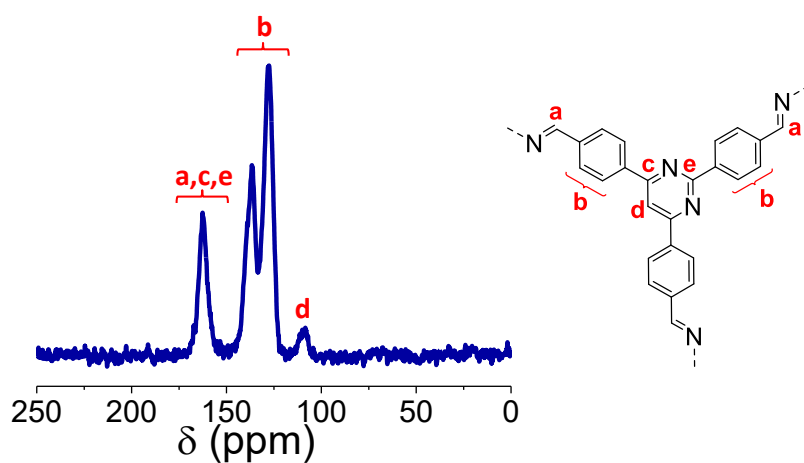


Figure 6-14: ¹³C CPMAS NMR spectra of N₂-COF and the peak assignments.

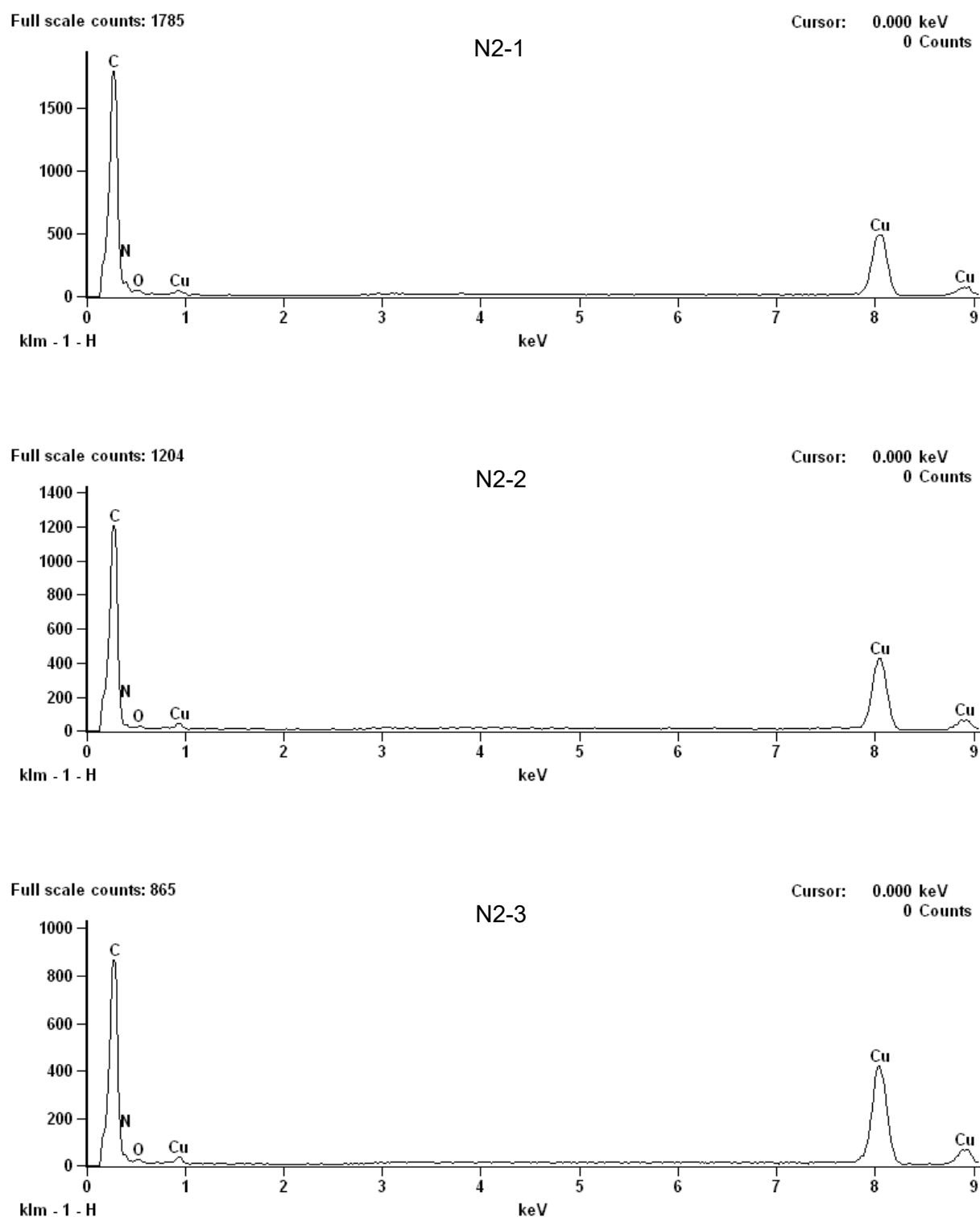


Figure 6-15: TEM energy dispersive X-ray (EDX) spectroscopic analysis of N₂-COF before photocatalysis. Three positions were sampled.

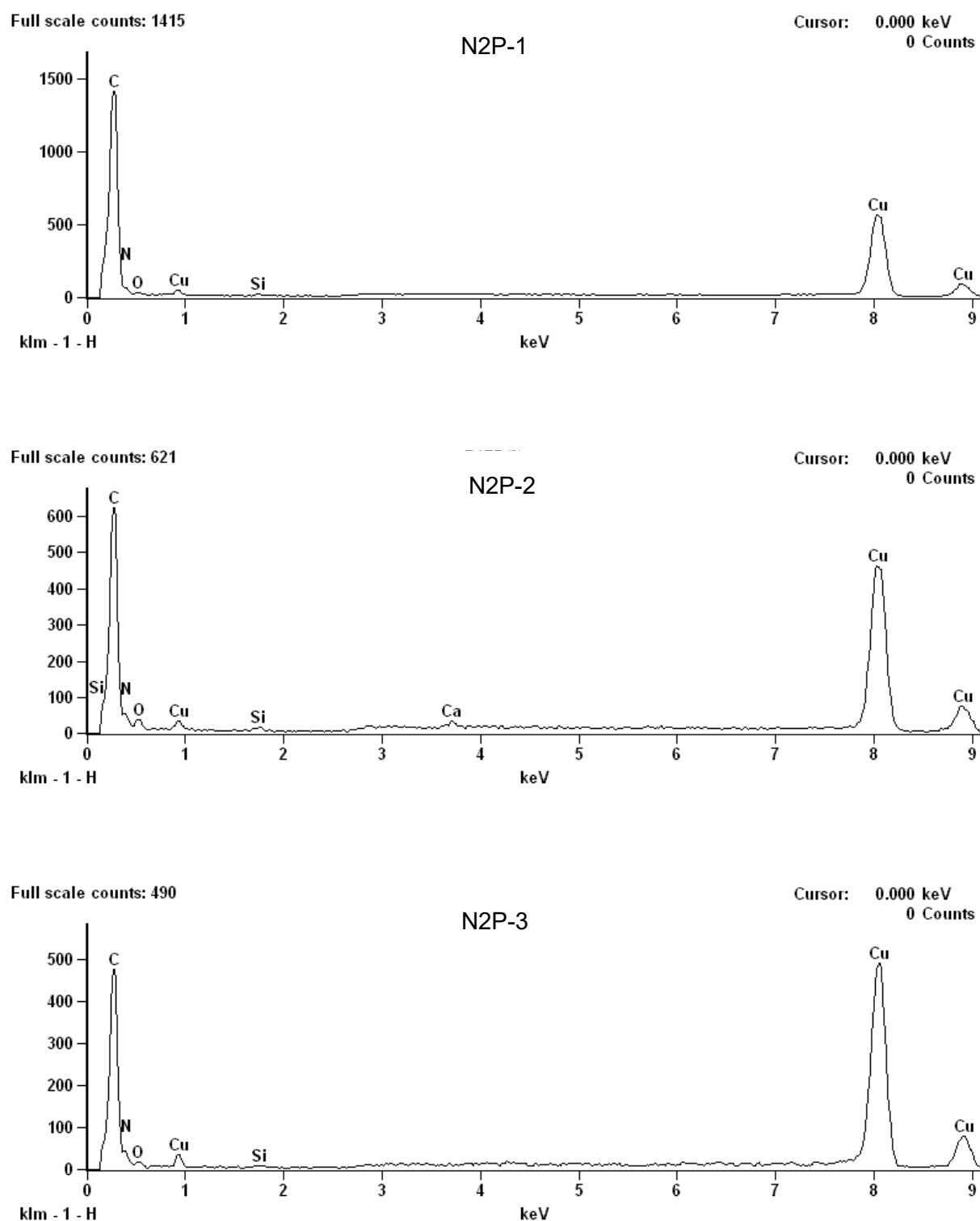


Figure 6-16: TEM energy dispersive X-ray (EDX) spectroscopic analysis of N₂-COF after photocatalysis showing no cobalt present. Three positions were sampled

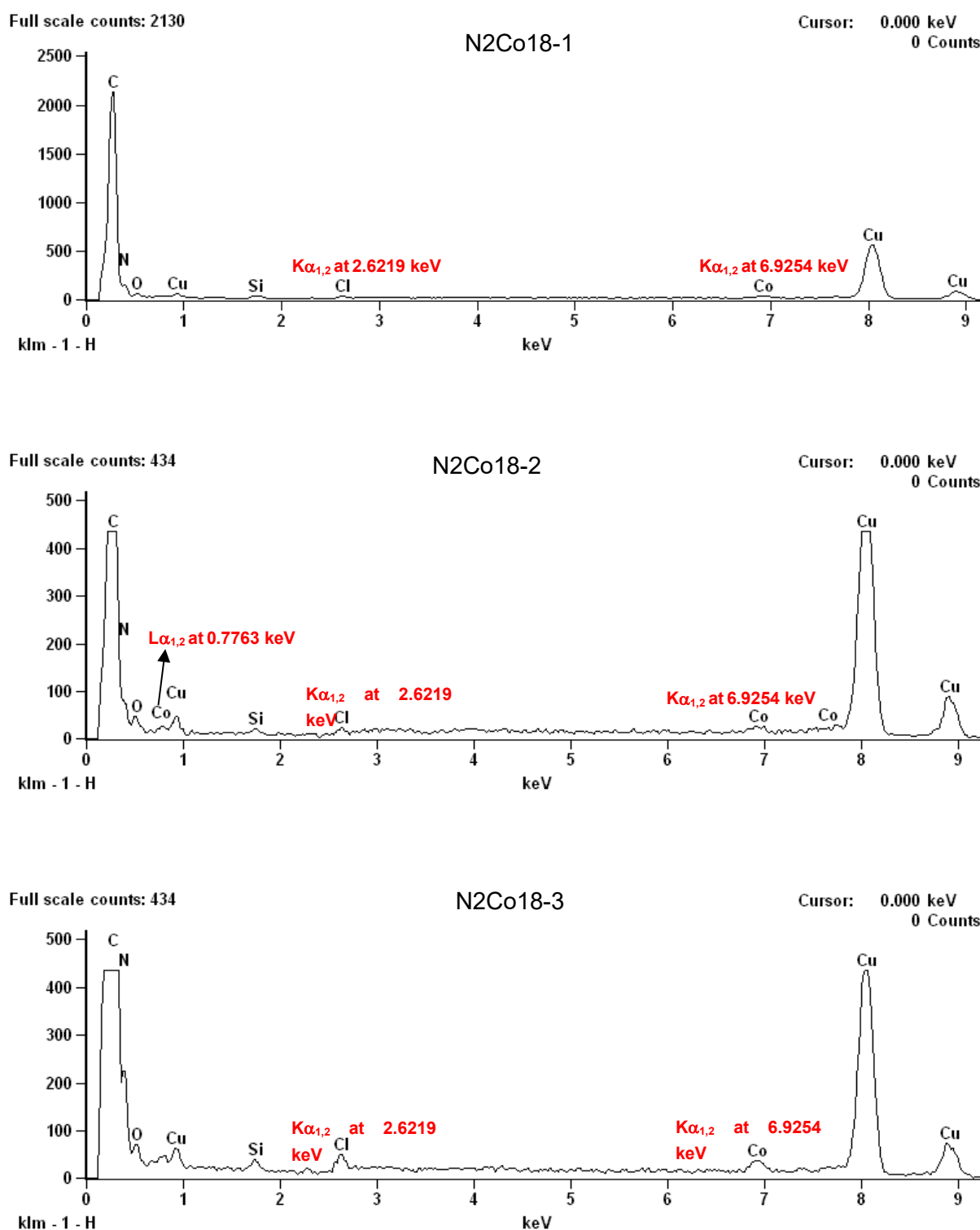


Figure 6-17: TEM energy dispersive X-ray (EDX) spectroscopic analysis of an illuminated and dried N₂ COF + 8 wt% Co-1 sample showing characteristic peaks of cobalt. Three positions were sampled.

Quantum chemical Calculations

The interactions between the co-catalyst and the COF were modelled with **Co-1**, with Co in a +3 oxidation closed-shell low-spin state. We did not investigate different spin-states on which there have been many discussions in the literature.⁵ It has to be stressed that these calculations only serve as model calculations involving the probable structure before photo-reduction and not the resting state of the co-catalyst i.e. the reduced Co(II) state.^{1,6} The axial pyridine ligand in **Co-1** is known to be quite labile and therefore this 6th position of the cobalt coordination sphere was used for probable binding to the COF fragments. For the same reason, the axial pyridine ligand was replaced with ACN (**Co-1-acn**) and with water (**Co-1-h2o**) to arrive at 3 possible parent cobaloxime structures existing in the reaction mixture, **Co-1**, **Co-1-acn** and **Co-1-h2o** (Figure 6-18, Figure 6-19, and Figure 6-20).

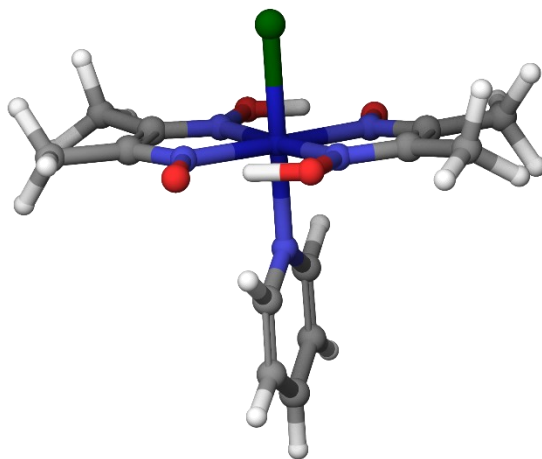


Figure 6-18: Geometry of **Co-1** optimized on PBE0 D3/def2-SVP level of theory

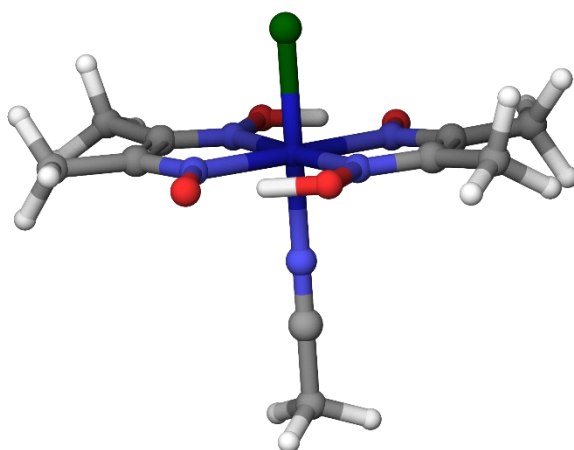


Figure 6-19: Geometry of **Co-1-acn** model compound, optimized on PBE0 D3/def2-SVP level of theory

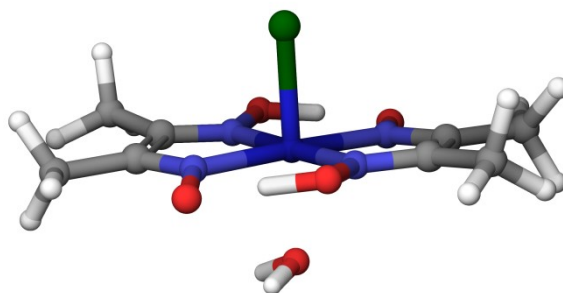


Figure 6-20: Geometry of **Co-1-h2o** model compound, optimized on PBE0 D3/def2-SVP level of theory

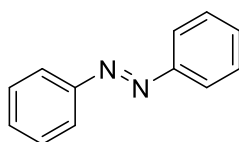


Figure 6-21: Diphenyl diazene model used for modelling the interaction of the co-catalyst with the COF in the pore walls.

Diphenyl diazene (Figure 6-21) was used for modelling the interaction of N₂-COF with **Co-1** in the pores with the N atoms of the azine linkage coordinating, if possible, to cobalt. Five layers of diphenyl diazene were stacked on top of each other, in order to hinder the formation of a π -stacked dimer. Thus, two possible binding modes were arrived at, the **pore-diazenes** (Figure 6-22) and the **pore-diazenes-90°** (Figure 6-23).

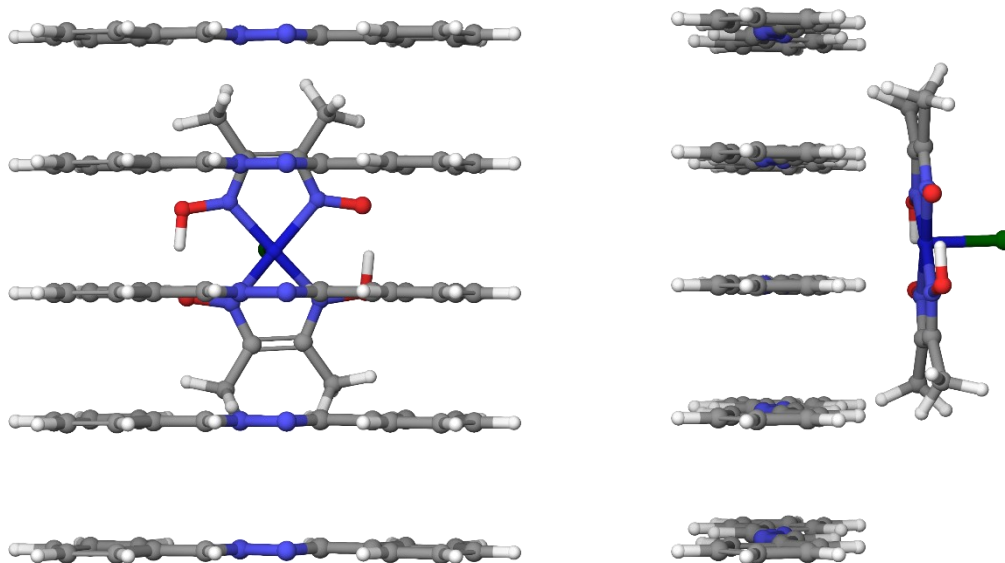


Figure 6-22: Constrained optimized geometry of the **pore-diazenes** cobaloxime-COF model obtained on PBE0-D3/def2-SVP level of theory.

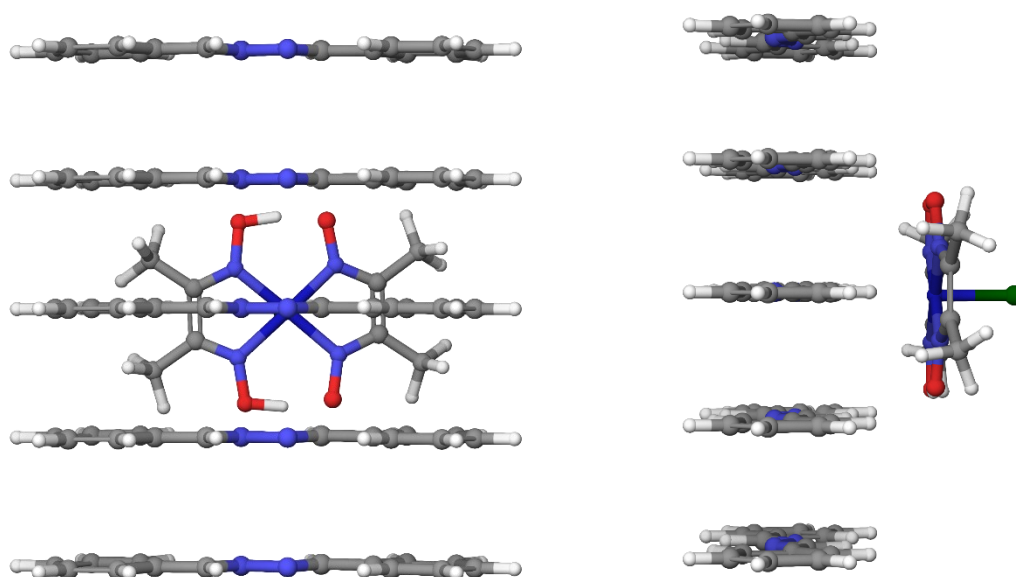


Figure 6-23: Constrained optimized geometry of the **pore-diazene-90°** cobaloxime-COF model obtained on PBE0-D3/def2-SVP level of theory.

A possible binding of **Co-1** to the surface of the COF crystal was also envisaged which led to the binding models **surface-diazene** and **surface-triazine**, for binding to the azine-linkage Ns and, as in the N3-COF, the triazine Ns, respectively (Figure 3-11).

Table 6-4: Calculated cobalt-axial nitrogen bond distances for cobaloxime model systems, obtained on PBE0-D3/def2-SVP level of theory.

Compound	Axial ligand	Cobalt - axial N bond distance [Å]
Co-1	Pyridine	1.965
Co-1-acn	Acetonitrile	1.903

Table 6-5: Calculated cobalt-nitrogen bond distances for cobaloxime-COF model systems, obtained on PBE0-D3/def2-SVP level of theory. For the pore-diazene and the pore-diazene-90° models, the distances to the four nearest N atoms are shown.

Cobaloxime-COF Model	Cobalt - N distance [Å]			
pore-diazene	6.525	5.053	4.197	4.628
pore-diazene-90°	5.438	5.695	4.082	4.419
surface-diazene	2.792			
surface-triazine	3.000			

Table 6-6: Comparison of calculated interaction energies, obtained on PBE0-D3/def2-TZVP level of theory. Interaction Energies (IAE) and Counterpoise Corrected Interaction Energies (CPC-IAE) are listed, as well as differences between Counterpoise Corrected Interaction Energies (Δ CPC-IAE) with respect to the **Co-1** model.

	IAE [kcal/mol]	CPC-IAE [kcal/mol]	Δ CPC-IAE [kcal/mol]
pore-diazene	-23.37	-21.45	25.77
pore-diazene-90°	-20.88	-18.90	28.32
surface-diazene	-18.79	-16.85	30.37
surface- triazine	-21.12	-19.09	28.14
Co-1	-49.21	-47.23	0.00
Co-1-acn	-34.20	-32.97	14.26
Co-1-h2o	-35.35	-26.50	20.73

Optimized geometries for selected reference compounds with available crystal structure data (Figure 6-24 and Figure 6-25) yield < 1 % errors for the cobalt- axial nitrogen bond distance for the selected level of theory (Table 6-7).⁷ Hence, this level of theory was employed throughout for comparison between presented model systems.

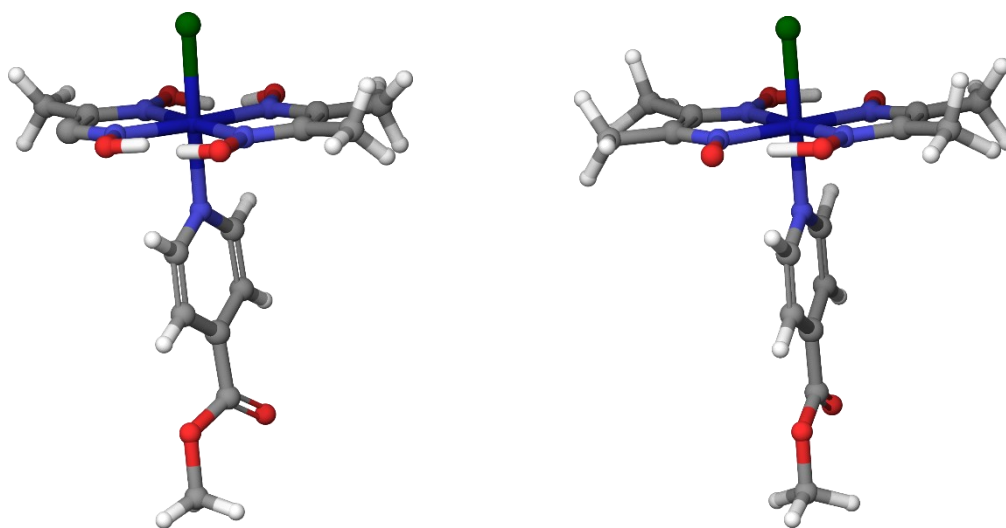


Figure 6-24: Geometry of **Co-1-pyCOOMe** compound. a) Crystal structure; b) optimized on PBE0-D3/def2-SVP level of theory.

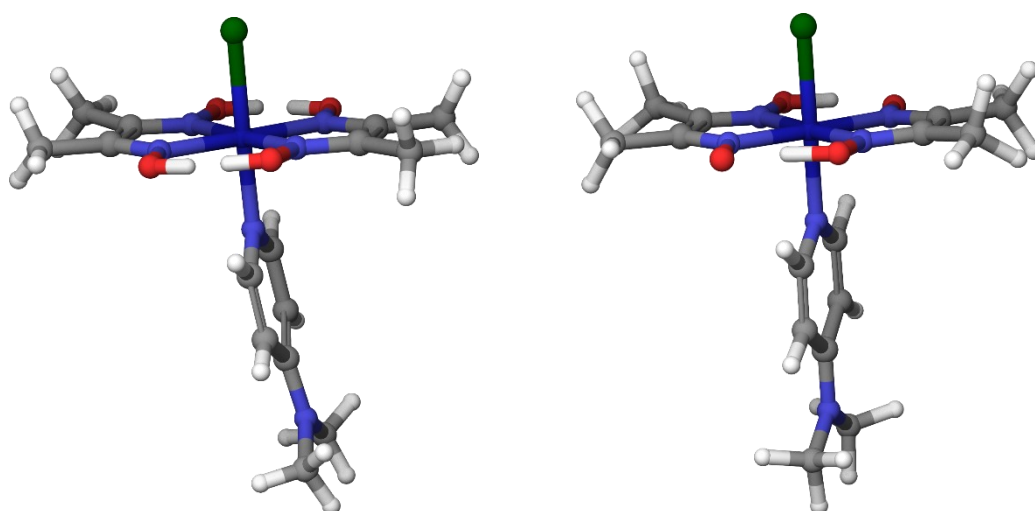


Figure 6-25: Geometry of **Co-1-pyNMe₂** compound. a) Crystal structure; b) optimized on PBE0-D3/def2-SVP level of theory.

Table 6-7: Comparison of experimental (crystal structure data) and calculated (PBE0-D3/def2-SVP) cobalt-axial nitrogen bond distances of reported reference compounds.

Compound	Co-N Distance [Å]		
	Exp. (Crystal Structure)	Calc. (PBE0-D3/def2-SVP)	Error [%]
Co-1-pyNMe ₂	1.946	1.959	0.67
Co-1-pyCOOMe	1.959	1.964	0.26

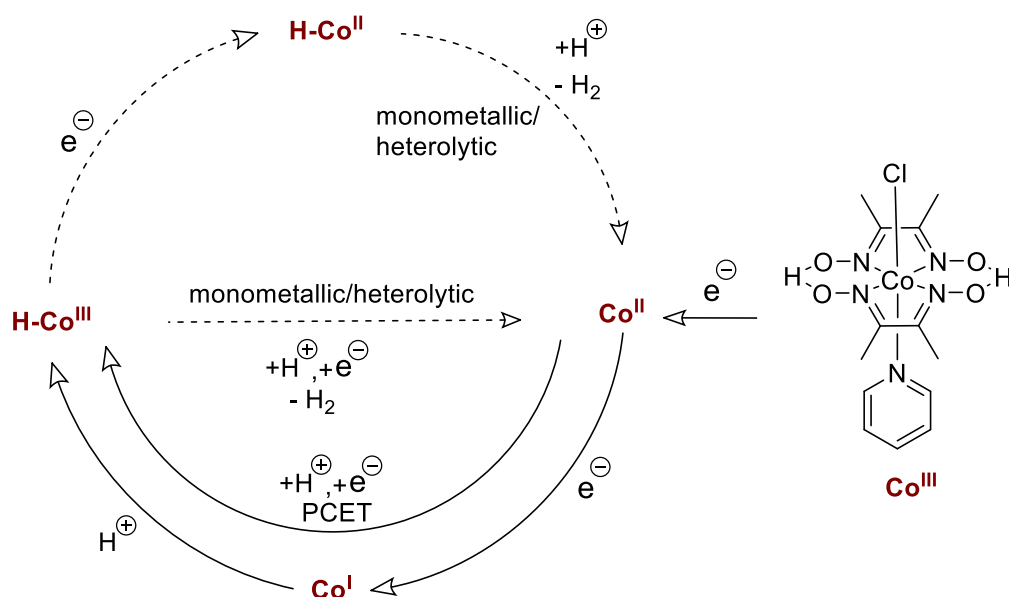


Figure 6-26: Mechanism of H₂ evolution with N₂-COF photosensitizer and **Co-1** co-catalyst.

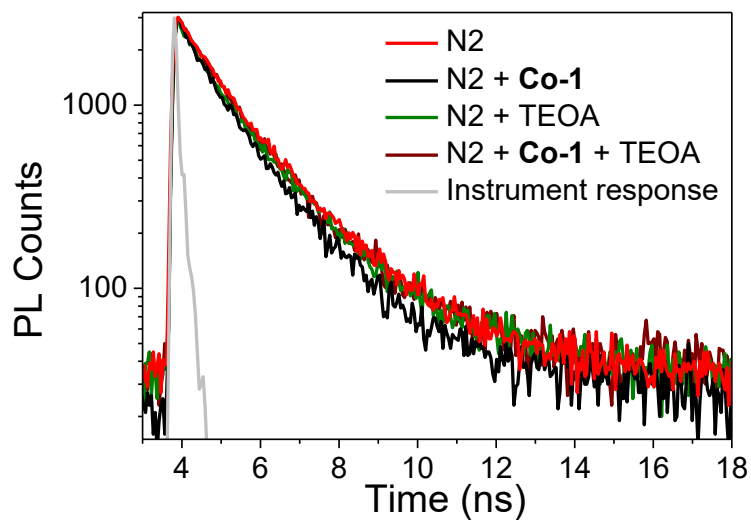


Figure 6-27: TCSPC decay traces of N₂-COF with added **Co-1**, TEOA and both in 4:1 ACN/water solvent monitored at 630 nm.

Table 6-8: Biexponential fits of the TCSPC decay traces of N₂-COF with added **Co-1**, TEOA and both in 4:1 ACN/water solvent at 630 nm.

τ at 630 nm	
N ₂	0.33 ns (14%) and 1.62 ns (86%)
N ₂ + Co-1	0.18 ns (13%) and 1.39 ns (8%)
N ₂ + TEOA	0.21 ns (13.4%) and 1.6 ns (86.6%)
N ₂ + Co-1 + TEOA	0.12 ns (9.4%) and 1.43 ns (90.6%)

6.1.2 Materials and methods for Chapter 3.4

PXRD

PXRD patterns were recorded at room temperature on a Bruker D8 Discovery with Ni-filtered $\text{CuK}\alpha$ -radiation (1.5406 Å) and a position-sensitive detector (Lynxeye).

FT-IR

Fourier-transform infrared spectra were measured on a Jasco FT/IR-4100 or a Perkin Elmer Spectrum NX FT-IR System.

UV/Vis

UV/VIS samples were recorded in solid state on a Varian Cary 50.

Structural models

Structural models were obtained with Materials Studio v6.0.0 Copyright © 2011 Accelrys Software using the Forcite Geometry optimization with Ewald electrostatic and van der Waals summation methods.

Sorption

Sorption measurements were performed on a Quantachrome Instruments Autosorb iQ MP with Argon at 87 K or with CO_2 at 273, 288 or 298 K. Weight percentage was calculated by referencing to sorbent weight.

Solid-state NMR measurements

ssNMR was recorded on a Bruker Avance III-500 (500 MHz, 11.74 T) spectrometer. For ssNMR spectroscopy, the sample was filled in a 4 mm ZrO_2 rotor, which was mounted in a standard double resonance MAS probe (Bruker). NMR chemical shifts were referenced relative to TMS. The spinning rate was 12 kHz. A standard cross polarization sequence with a 2.5 ms ramped contact pulse was used.

Fast MAS solid-state NMR measurements

Solid-state NMR experiments of [1a]- COF_{10} and [Co-1a]- COF_{10} were performed on a narrow-bore Bruker Neo spectrometer operating at 700 MHz Larmor frequency equipped with a 1.3 mm triple-resonance HCN MAS probe. In all experiments, unless otherwise stated, the spinning frequency was set to 55 555 Hz and the temperature was regulated so that the inner temperature was estimated to be 20 °C. In all experiments the $\pi/2$ pulse length was 1.55 μs for (161 kHz), 2.8 μs for (89 kHz). During direct or indirect evolution, an XiX decoupling was applied on the channel with a nutation frequency of 13.88 kHz. and chemical shifts were indirectly referenced to 4,4-dimethyl-4-silapentane-1-sulfonic acid (DSS). All spectra



were acquired and processed using Bruker Topspin version 4.0, and later analyzed with Sparky.

1D experiments

For the spinning-frequency-dependent 1D experiments 128 scans were recorded over a spectral width of 100 kHz using a single pulse direct polarization experiment with a recycle delay of 1 s at spinning frequencies of 10, 20, 30, 40, 50, 55.55, and 58 kHz, as a reference, a static spectrum was also recorded with the same conditions. An inversion-recovery experiment was applied to determine the longitudinal relaxation time (T_1) of protons. A direct polarization experiment was used for quantitative and qualitative signal intensity analysis. A total of 4096 (16384) scans were collected with a recycle delay of 25 s (1 s) for identifying the rigid (mobile) sites.

For the 1D -detected CP MAS experiments, a total of 1024 scans were collected over a spectral width of 71 kHz with a recycle delay of 1 s. During the CP the rf nutation frequency was tangentially ramped between 45 and 85 kHz, whereas the nutation frequency was kept constant at 10 kHz. The carrier was set to 130 ppm. A 13.88 kHz XiX decoupling was applied during the acquisition.

2D experiments

^1H -detected 2D ^1H - ^{13}C correlation spectra were acquired using the double-quantum CP technique. The same CP steps were employed as for the 1D CP MAS experiment with a CP contact time of either 500 μs (short CP experiments) or 2250 μs (long CP experiments). The spectra were recorded with a spectral width of 20.8 kHz and 55.55 kHz in the t_2 and t_1 dimensions, respectively using 356 indirect time points, 128 scans and 0.5 s recycle delay time for [1a]-COF₁₀ and 240 indirect time points, 704 scans and 0.7 s recycle delay time for [Co-1a]-COF₁₀. The carrier for t_2 and t_1 was centered at 6 and 130 ppm, respectively.

2D - homonuclear through-space double quantum - single quantum correlation spectra were measured with $R14_4^{-2}$ symmetry sequence, with a $R = 180_0$ symmetry element using the same number of elements both excitation and reconversion of the DQCs, and a t_1 dwell time of 36 μs corresponding to a rotor-synchronized F1 spectral width. 96 complex t_1 points were acquired with 64 scans for each indirect time points. A four step phase cycle was used to obtain the double-quantum coherence in the t_1 dimension. A States method was used for signal acquisition.

Quantum chemical calculations

Atom positions and lattices of all periodic structures were optimized on RI-PBE-D3/def2-TZVP^[1-4] level of theory using an acceleration scheme based on the resolution of the identity (RI) technique and the continuous fast multipole method (CFMM)^[5-7] implemented^[8-9] in

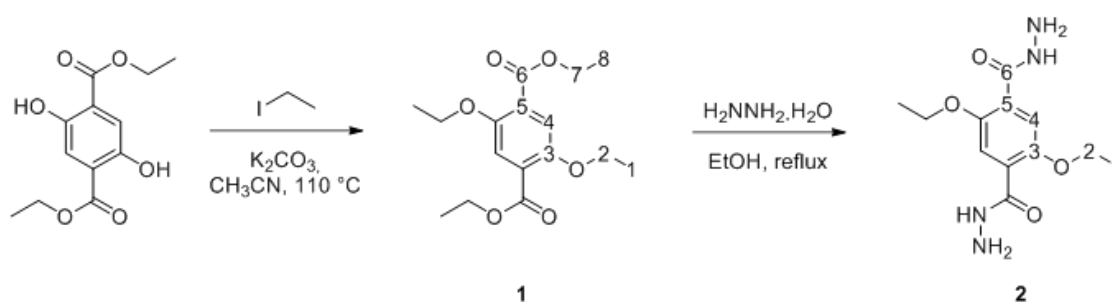
Turbomole version V7.1.^[10] The CFMM uses multipole moments of maximum order 20, together with a well-separateness value of 3 and a basis function extent threshold of 10E-9 a.u. Grid 7 was used for the numerical integration of the exchange-correlation term. The norm of the gradient was converged to 10E-4 a.u. and the total energy to 10E-8 Hartree within the structure optimization using the gamma point approximation.

Parameters for molecular dynamics simulations for COF pores were prepared using antechamber.^[11] Force field minimizations and dynamics were performed using the NAMD program package^[12-13] using GAFF parameters.^[14] Periodic boundary conditions and particle mesh Ewald summation (PME) with a cutoff value of 12 Å were employed. The modeled COF pore was minimized using the conjugate gradient algorithm in 1000 steps by constraining the coordinates for the COF backbone excluding all hydrogen atoms that were allowed to relax along with the functionalized linker of the 1a linker moiety. The system was then heated to 300 K in 30 ps and equilibrated subsequently for 15 ns with time steps of 2 fs employing the SETTLE algorithm.

NMR chemical shifts were obtained on B97-2/pcSseg-1^[15-16] level of theory using the FermiONs++^[17-18] program package performed on cut models of previously obtained structures.

Synthetic procedures

1,3,5-triformylbenzene and 3-(azidomethyl)pyridine were used as purchased. 2,5-diethoxyterephthalohydrazide was synthesized according to known procedures as follows. All reactions were performed under Ar atmosphere with dry solvents and magnetically stirred, unless otherwise noted.



Diethyl-2,5-diethoxyterephthalate (1)

Diethyl-2,5-dihydroxyterephthalate (4 mmol, 1.05 g, 1 eq) and potassium carbonate (13.2 mmol, 1.82 g, 3.3 eq) were suspended in acetonitrile (10 mL). Iodoethane (13.2 mmol, 1.07 mL, 3.3 eq) was added. After the reaction mixture was refluxed for 72 h, the solvent was removed. The brownish residue was added into water and extracted with ethyl acetate. The organic extract was dried over magnesium sulfate. The solvent was removed to give the product as a light yellow solid (1.20 g, 3.87 mmol, 97%).

$^1\text{H-NMR}$ (400 MHz, CDCl_3): $\delta = 7.34$ (s, 2H, H_{arom}), 4.37 (q, $J = 7.1$ Hz, 4H, Me-CH_2), 4.08 (q, $J = 7.0$ Hz, 4H, $\text{O-C-H}_2\text{-CH}_3$), 1.41 (dt, $J = 15.2, 7.0$ Hz, 12H, $\text{CO-CH}_2\text{-CH}_3/\text{COO-CH}_2\text{-CH}_3$) ppm.

$^{13}\text{C-NMR}$ (101 MHz, CDCl_3): $\delta = 166.1$ (C6), 151.8 (C3), 125.1 (C5), 117.1 (C4), 65.8 (C2), 61.41 (C7), 14.94 (C1), 14.39 (C8) ppm.

HR-ESI-MS: calc. for $\text{C}_{16}\text{H}_{22}\text{O}_6$: $[\text{M}]^+$: 310.1416; found: 310.1408.

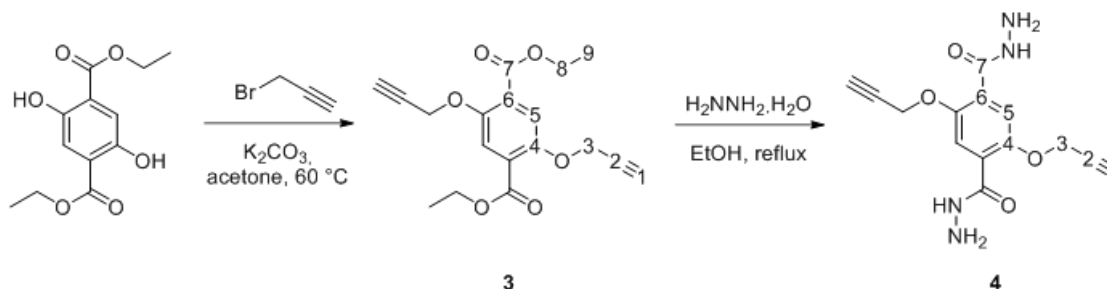
2,5-Diethoxyterephthalohydrazide (**2**)

Diethyl 2,5-diethoxyterephthalate (3.96 mmol, 1.2 g, 1 eq) was suspended in a solution of ethanol/toluene (20 mL, 1:1). Hydrazine hydrate (39.6 mmol, 1.94 mL, 10 eq) was added. The reaction mixture was heated to 110 °C for 8 h. The solvent was evaporated to yield an off-white solid (903 mg, 3.20 mmol, 81%).

$^1\text{H-NMR}$ (400 MHz, DMSO-d_6): $\delta = 9.24$ (s, 2H, N-H), 7.38 (s, 2H, H_{arom}), 4.58 (s, 4H, $\text{O-C-H}_2\text{-CH}_3$), 4.12 (q, $J = 6.9$ Hz, 4H, N-H₂), 1.35 (t, $J = 6.9$ Hz, 6H, $-\text{CH}_3$) ppm.

$^{13}\text{C-NMR}$ (101 MHz, DMSO-d_6): $\delta = 163.8$ (C6), 149.53 (C3), 125.0 (C5), 114.7 (C4), 64.81 (C2), 14.54 (C1) ppm.

HR-EI-MS: calc. for $[\text{M}]^+$: 282.1328; found: 282.1433.



Diethyl 2,5-bis(prop-2-yn-1-yloxy)terephthalate (**3**)

Diethyl 2,5-dihydroxyterephthalate (1.05 g, 4.00 mmol, 1.00 eq) and potassium carbonate (2.21 g, 16.0 mmol, 4.00 eq) were flushed with argon and dissolved in acetone (20 mL). The mixture was degassed (3x argon/3x vacuum) and propargyl bromide (2.38 g, 16.0 mmol, 4.00 eq) was added. The reaction mixture was stirred at 60 °C for 72 h. The reaction was monitored by TLC ($\text{CH}_2\text{Cl}_2:\text{MeOH}$ 9:1) and after complete conversion, the reaction mixture was added on ice. The solid was filtered, washed with water and dried *in vacuo* for 48 h, yielding the product (1.24 g, 3.75 mmol, 94%) as a light brown solid.

$^1\text{H-NMR}$ (400 MHz, CDCl_3): $\delta = 7.56$ (s, 2H- arom), 4.76 (d, $J = 2.4$ Hz, 4H, Me-CH_2), 4.39 (q, $J = 7.1$ Hz, 4H, $\text{O-CH}_2\text{-CH}_2$), 2.54 (t, $J = 2.4$ Hz, 2H, $-\text{CCH}$), 1.40 (t, $J = 7.1$ Hz, 6H, $-\text{CH}_3$) ppm.

$^{13}\text{C-NMR}$ (101 MHz, CDCl_3): $\delta = 165.2$ (C7), 151.4 (C4), 126.0 (C6), 119.0 (C5), 78.17 (C2), 76.36 (C1), 61.68 (C8), 58.38 (C3), 14.37 (C9) ppm.

HR-ESI-MS: calc. for $C_{18}H_{18}O_6$ $[M]^+$: 330.1103; found: 330.1096.

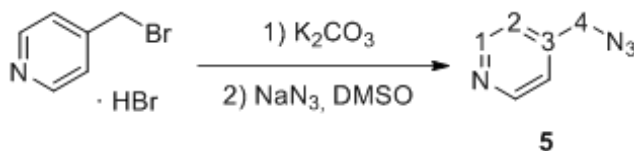
2,5-Bis(prop-2-yn-1-yloxy)terephthalohydrazide (**4**)

A suspension of diethyl 2,5-bis(prop-2-yn-1-yloxy)terephthalate (**3**) (0.90 g, 2.9 mmol, 1.0 eq) in EtOH/toluene (1:1, 15 mL) was degassed (3x argon/3x vacuum). Hydrazine hydrate (1.49 mL, 1.53 g, 30.3 mmol, 10.0 eq) was added and the solution was stirred at 80 °C over night. The resulting white precipitate was filtered and washed with EtOH and CH_2Cl_2 , yielding the product (0.70 mg, 2.3 mmol, 79%) as a white solid.

1H -NMR (400 MHz, $DMSO-d_6$): δ = 9.30 (s, 2H, N-H), 7.48 (s, 2H, H_{arom}), 4.89 (d, J = 2.4 Hz, 4H, O-C- H_2 - CH_3), 4.57 (s, 4H, N-H2) 3.62 (t, J = 2.4 Hz, 2H, -CCH) ppm.

^{13}C -NMR (101 MHz, $DMSO-d_6$): δ = 163.5 (C7), 148.8 (C4), 125.6 (C6), 115.4 (C5), 78.97 (C2), 78.85 (C1), 56.78 (C3) ppm.

HR-ESI-MS: calc. for $C_{14}H_4N_4O_4$ $[M]^+$: 302.1015; found: 302.1014.



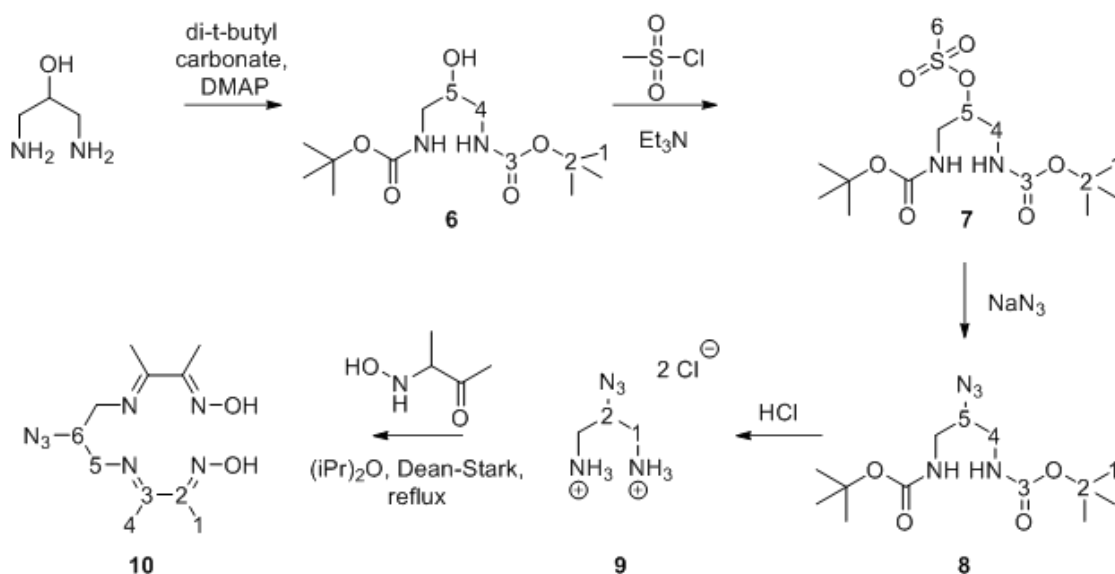
4-(azidomethyl)pyridine (**5**)

4-(Bromomethyl)pyridine hydrobromide (1.26 g, 5.00 mmol, 1.00 eq) was dissolved in DMF (15 mL). Potassium carbonate (0.96 g, 5.00 mmol, 1.00 eq) was added and the reaction mixture was stirred at room temperature for 15 min. Sodium azide (0.49 g, 7.50 mmol, 1.50 eq) was added and the reaction mixture was stirred at room temperature for 72 h. EtOAc (10 mL) and water (10 mL) were added, the organic layer was separated and the reaction mixture was extracted with EtOAc (3x 20 mL). The combined organic layers were washed with water (3x 25 mL), dried over and the solvent was removed *in vacuo* yielding **5** (0.33 g, 2.46 mmol, 49%) as a light-yellow oil.

1H -NMR (400 MHz, $CDCl_3$): δ = 8.63 (d, J = 6.1 Hz, 2H, 1-H), 7.27 (d, J = 6.0 Hz, 2H, 2-H), 4.43 (s, 2H, 4-H) ppm.

^{13}C -NMR (101 MHz, $CDCl_3$): δ = 150.24 (C1), 144.71 (C3), 122.53 (C2), 53.42 (C4) ppm.

HR-EI-MS: calc. for $[M]^+$: 134.0593 found: 134.0585.



Di-tert-butyl (2-hydroxypropane-1,3-diyl)dicarbamate (6)

1,3-Diamino-2-propanol (4.6 g, 51 mmol, 1.00 eq) was dissolved in water (50 mL). A solution of di-*tert*-butylpyrocarbonat (23 g, 105 mmol, 2.05 eq) in acetonitrile (50 mL) was added at 0 °C. DMAP (13 g, 107 mmol, 2.1 eq) was added at 0 °C. The reaction mixture was stirred at 0 °C for 2 h and for further 16 h at room temperature as the ice bath melted. The crude product was extracted with dichloromethane (200 mL) and 1M HCl. The combined organic layers were washed with saturated NaHCO₃ solution (3x 50 mL) and brine (2x 25 mL). The organic layer was dried over and the solvents were removed in vacuo, yielding 6 (19 g, 48 mmol, 95%) as a white solid.

¹H-NMR (400 MHz, CDCl₃): δ = 6.99 (s, 2H, NH), 5.05 (s, 1H, OH), 3.73 (q, J = 5.5, 5.1 Hz, 1H, 4-H), 3.34 – 3.09 (m, 4H, 3-H), 1.44 (s, 18H, 1-H) ppm.

¹³C-NMR (101 MHz, CDCl₃): δ = 162.54 (C3), 79.63 (C2), 70.49 (C5), 40.92 (C4), 28.30 (C1) ppm. LR-El-MS: calc. for [M+H]⁺: 291.18 found: 291.24.

2-[[tert-Butoxycarbonyl]amino]-1-[[tert-butoxycarbonyl]amino]ethyl methane-sulfonate (7)

Di-*tert*-butyl (2-hydroxypropane-1,3-diyl)dicarbamate (6) (8.0 g, 20 mmol, 1.0 eq) and triethylamine (4.8 mL, 3.5 g, 34 mmol, 1.7 eq) were dissolved in dry CH₂Cl₂. Methanesulfonyl chloride (3.1 mL, 4.6 g, 40 mmol, 2.0 eq) was added dropwise at 0 °C while stirring under argon. The reaction mixture was allowed to warm to room temperature and was stirred for 18 h. Water was slowly added to quench the reaction. The organic layer was separated, washed with water and dried over MgSO₄. The solvents were removed in vacuo and the crude product was recrystallized with hexanes, yielding 7 (7.3 g, 20 mmol, 98%) as a white solid.

$^1\text{H-NMR}$ (400 MHz, CDCl_3): $\delta = 5.14$ (s, 2H, NH), 4.70 – 4.62 (m, 1H, 5-H), 3.55 – 3.24 (m, 4H, 4-H), 3.09 (s, 3H, 6-H), 1.44 (s, 18H, 1-H) ppm.

$^{13}\text{C-NMR}$ (101 MHz, CDCl_3): $\delta = 157.46$ (C3), 80.02 (C2), 71.50 (C5), 43.79 (C4), 41.83 (C6), 28.51 (C1) ppm.

HR-EI-MS: calc. for $[\text{M}+\text{H}]^+$: 369.1617 found: 369.1692.

Di-tert-butyl (2-azidopropane-1,3-diyl)dicarbamate (8)

2-[(*tert*-Butoxycarbonyl)amino]-1-[[(*tert*-butoxycarbonyl)amino]methyl]ethyl methane-sulfonate (7) (0.50 mg, 1.4 mmol, 1.0 eq) was dissolved in dry DMF (5 mL). A suspension of sodium azide (0.35 mmol, 5.4 mmol, 4.0 eq) in dry DMF (2.5 mL) was added and the reaction mixture was stirred at 80 °C for 18 h. Water (25 mL) and CH_2Cl_2 (25 mL) were added, the organic layer was separated, washed with water (3x 25 mL) and dried over MgSO_4 . The solvents were removed in vacuo, yielding 8 (0.33 g, 1.0 mmol, 71%) as a light yellow solid.

$^1\text{H-NMR}$ (400 MHz, CDCl_3): $\delta = 5.17$ (s, 2H, NH), 3.73 – 3.49 (m, 1H, 5-H), 3.36 – 3.05 (m, 4H, 4-H), 1.41 (s, 18H, 1-H) ppm.

$^{13}\text{C-NMR}$ (101 MHz, CDCl_3): $\delta = 162.58$ (C3), 79.75 (C2), 60.99 (C5), 40.94 (C4), 28.37 (C1) ppm.

HR-EI-MS: calc. for $[\text{M}+\text{H}]^+$: 316.19065 found: 316.1960.

2-Azidopropane-1,3-diamine dihydrochloride (9)

Di-*tert*-butyl (2-azidopropane-1,3-diyl)dicarbamate (8) (0.90 g, 2.8 mmol, 1.0 eq) was dissolved in EtOAc (3 mL). Hydrochloric acid (6 M, 1.5 mL, 8.9 mmol, 8.0 eq.) was added. The reaction mixture was stirred for 8 h and relaxed over night at 5 °C. The obtained crystals were filtered and washed with EtOAc, yielding 9 (0.32 g, 1.7 mmol, 60%) as white crystals.

$^1\text{H-NMR}$ (400 MHz, DMSO-d_6): $\delta = 8.51$ (s, 6H, NH_3^+), 4.28 (t, $J = 8.5, 4.1$ Hz, 1H, 2-H), 3.16 (dd, $J = 13.4, 4.1$ Hz, 2H, 1-H), 2.91 (dd, $J = 13.4, 8.8$ Hz, 2H, 1-H) ppm.

$^{13}\text{C-NMR}$ (101 MHz, DMSO-d_6): $\delta = 57.03$ (C2), 40.19 (C1) ppm.

2-Butanone, 3,3'-[(2-azido-1,3-propanediyl)dinitrilo]bis-2,2'-dioxime (10)

A solution of 2-azidopropane-1,3-diamine dihydrochloride (9) (0.20 g, 1.1 mmol, 1.0 eq), 2,3-butanedione monoxime (0.21 g, 2.1 mmol, 2.0 eq) and sodium hydrogen carbonate (0.18 g, 2.1 mmol, 2.0 eq) in a two-phase mixture of water and $i\text{Pr}_2\text{O}$ (1:4, 25 mL) was refluxed for 18 h using a Dean-Stark apparatus. The reaction mixture was hot filtered, washed with and the solvent removed in vacuo. The residue was recrystallized in heptane and the solvent was evaporated, yielding 10 (0.25 g, 0.87 mmol, 82%) as a white solid.

$^1\text{H-NMR}$ (400 MHz, DMSO-d_6): $\delta = 11.43$ (s, 2H, OH), 3.67 – 3.57 (m, 1H, 6-H), 3.41 – 3.19 (m, 4H, 5-H), 1.99 (s, 6H, 1-H/4-H), 1.92 (s, 6H, 1-H/4-H) ppm.



^{13}C -NMR (101 MHz, DMSO- d_6): δ = 153.01 (C3), 149.94 (C2), 59.73 (C6), 52.08 (C5), 20.74 (C4), 9.31 (C1) ppm.

HR-EI-MS: calc. for $[\text{M}+\text{H}]^+$: 282.16002 found: 282.16726.

COF synthesis

All products were obtained as fluffy solids. To remove residual starting materials, powders were washed intensely with DMF, THF and dichloromethane and subsequently dried in a vacuum desiccator overnight.

COF-42

To a Biotage© 2 mL microwave vial, 1,3,5 triformylbenzene (0.066 mmol, 10.7 mg, 2 eq) and 2,5-diethoxyterephthalohydrazide (0.099 mmol, 27.9 mg, 3 eq) were added. Dioxan (0.25 mL), mesitylene (0.75 mL) and acetic acid (6M, 150 μL) were added. The vial was sealed and heated under microwave irradiation at 160 °C for 30 min. Subsequently, the vial was heated in a muffle furnace at 120 °C for 72 h. After cooling to room temperature, the solid was filtered and washed with DMF (3 x 2 mL), THF (3 x 2 mL) and DCM (3 x 2 mL) to yield a light-yellow powder.

pCOF₁₀

For the copolymerized systems, corresponding amounts of 2,5-diethoxyterephthalohydrazide were replaced by 2,5-bis(2-(dimethylamino)ethoxy)terephthalohydrazide while the procedure was retained as described before. Solvents were used according to Table S1. The products yielded as yellow to orange powders.

Postmodification

Route (I)

1st step:

1 eq **1a/1b/2**, 0.5 eq $\text{CoCl}_2 \cdot 6 \text{H}_2\text{O}$ and 1.1 eq dimethylglyoxime (in the case of **1a** and **1b**) was dissolved in hot ethanol. Upon oxidation with air for 1 h, the dispersion turns brown and yields [**Co-1a**]/[**Co-1b**]/[**Co-2**] after filtration and washing with water, ethanol, ethyl acetate and acetone.

2nd step:

1 eq pCOF₁₀, 2 eq [**Co-1a**]/[**Co-1b**]/[**Co-2**], 0.25 eq $\text{CuSO}_4 \cdot 5 \text{H}_2\text{O}$ and 0.5 eq sodium ascorbate were dispersed in a 1:1 mixture of degassed toluene and *tert*-butyl alcohol under argon. Stirring for 72 h at room temperature yields [**Co-1a**]/[**Co-1b**]/[**Co-2**]-COF₁₀ after filtration and washing with water, ethanol, ethyl acetate and acetone.

For controlling the cobaloxime content of the resulting samples, experimental conditions were altered as follows: Temperature: rt, 40 , 60 . Reaction time: 72 h, 120 h, 7 days, 14 days Concentration: 1 eq = 0.0111 mmol in 8 mL solvent, 1 eq = 0.0111 mmol in 4 mL solvent, 1 eq = 0.0222 mmol in 8 mL solvent

Route (II)

1st step:

1 eq pCOF₁₀, 2 eq **1a/1b/2**, 0.25 eq CuSO₄ 5 and 0.5 eq sodium ascorbate were dispersed in a 1:1 mixture of degassed toluene and *tert*-butyl alcohol under argon. Stirring at room temperature yields [**1a**]/[**1b**]/[**2**]-COF₁₀ after filtration and washing with water, ethanol, ethyl acetate and acetone.

For controlling the cobaloxime content of the resulting samples, experimental conditions were altered as follows: Temperature: rt, 40 , 60 . Reaction time: 72 h, 120 h, 7 days, 14 days Concentration: 1 eq = 0.0111 mmol in 8 mL solvent, 1 eq = 0.0111 mmol in 4 mL solvent, 1 eq = 0.0222 mmol in 8 mL solvent.

2nd step:

1 eq [**1a**]/[**1b**]/[**2**]-COF₁₀, 0.5 eq CoCl₂ 6 H₂O and 1.1 eq dimethylglyoxime (in the case of **1a** and **1b**) were dispersed in ethanol. Upon oxidation with air for 1 h, the dispersion turns brown and yields [**Co-1a**]/[**Co-1b**]/[**Co-2**]-COF₁₀ after filtration and washing with water, ethanol, ethyl acetate and acetone.

Photocatalysis measurements

In a typical photocatalysis experiment, 5 mg of COF hybrid were suspended in 10 mL of acetonitrile and water in a ratio of 4:1 at pH 8 containing 100 μ L triethanolamine (TEOA) as sacrificial donor. Irradiation with 100 mW cm⁻¹ AM1.5 radiation resulted in hydrogen evolution.

Spectral distribution of our solar simulator was nominally AM 1.5G by means of a housed Xe lamp and a AM 1.5G filter, which is presented below, though the beam integrated power intensity had a recorded value of 45 mW cm⁻². During experiments, intensity was adjusted to 100 mW cm⁻² but at a more uncertain spectral distribution which was not recorded in this document. For some experiments measured few months later, the Xe lamp of our solar simulator was replaced achieving a more stable spectral distribution with an integrated beam power of 100 mW cm⁻², which is also shown in Figure 6-28. As different lamps were used for different measurements, photocatalytic activity of the samples were compared in photonic efficiencies in the main text.

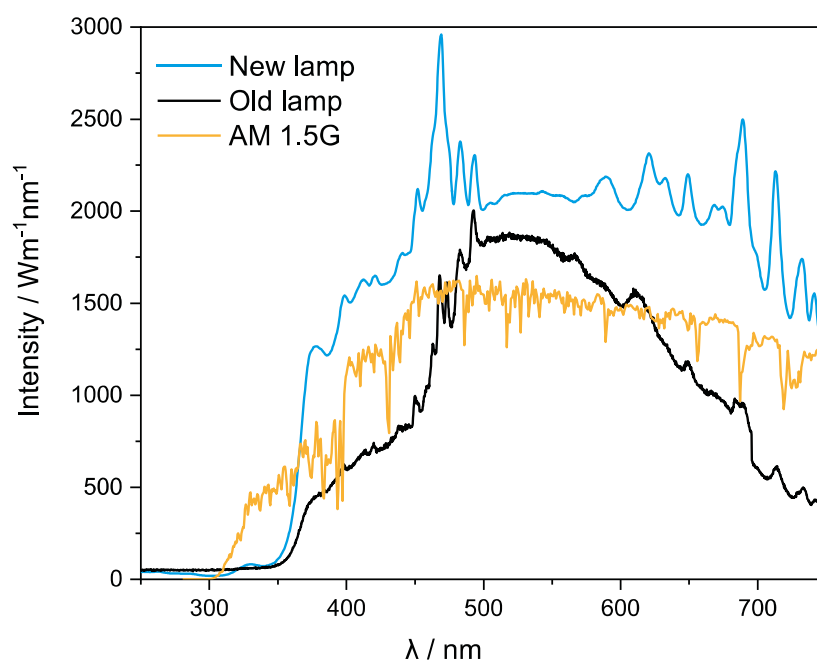


Figure 6-28: Light intensities of the solar simulator that was used earlier for the measurements in the main manuscript (old lamp, black), the lamp that was used for the experiments in EDI where stated (new lamp, blue), compared to AM 1.5G (yellow).

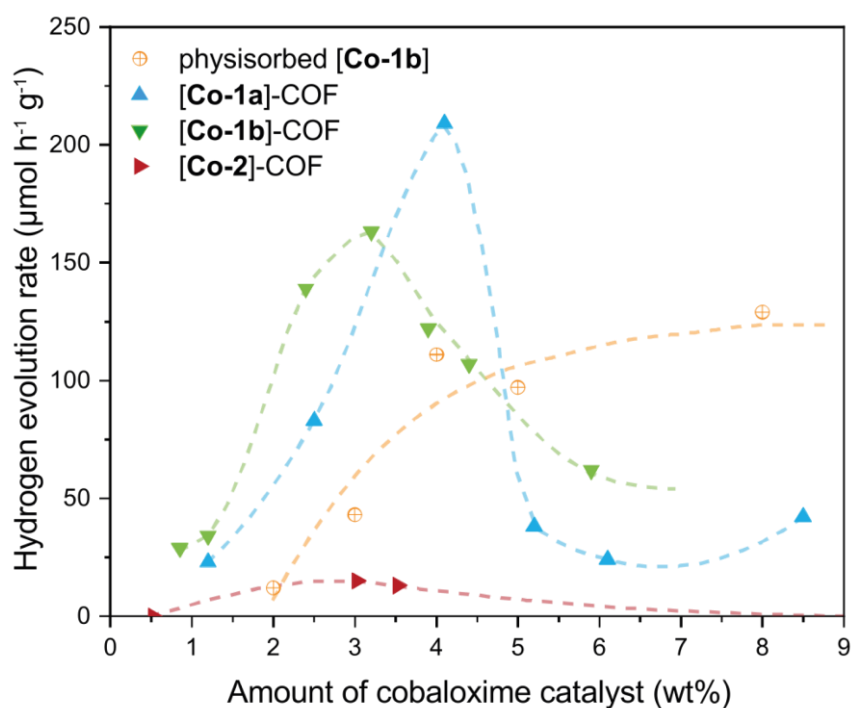


Figure 6-29: Comparison of hydrogen evolution rates for hybrid samples and COF-42 with physisorbed [Co-1b] measured with the old lamp.

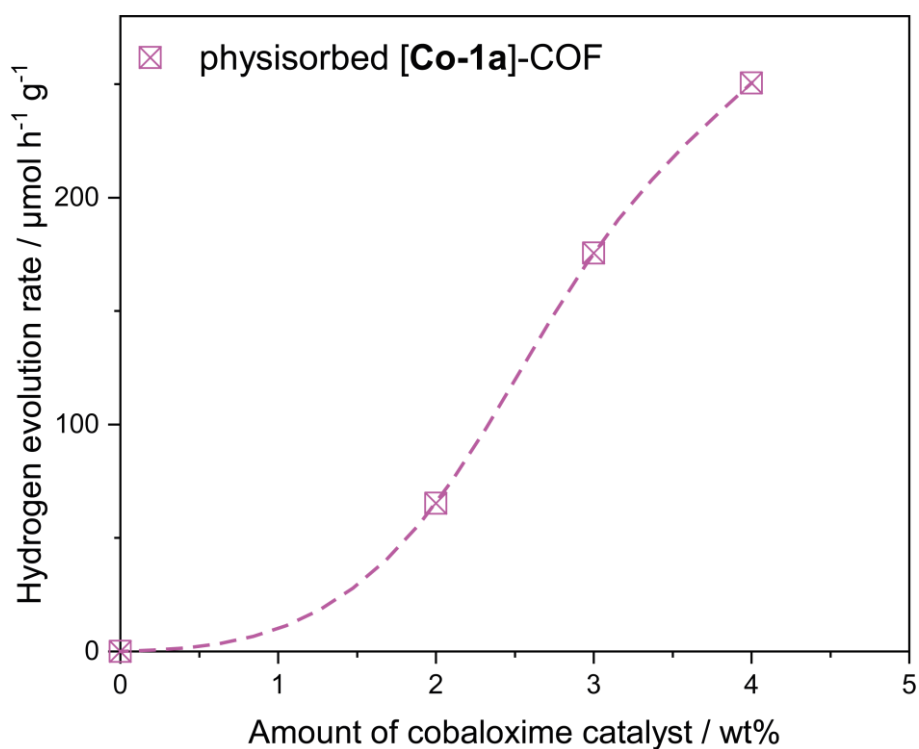


Figure 6-30: Hydrogen evolution rate for [Co-1a]-COF measured with the new lamp.

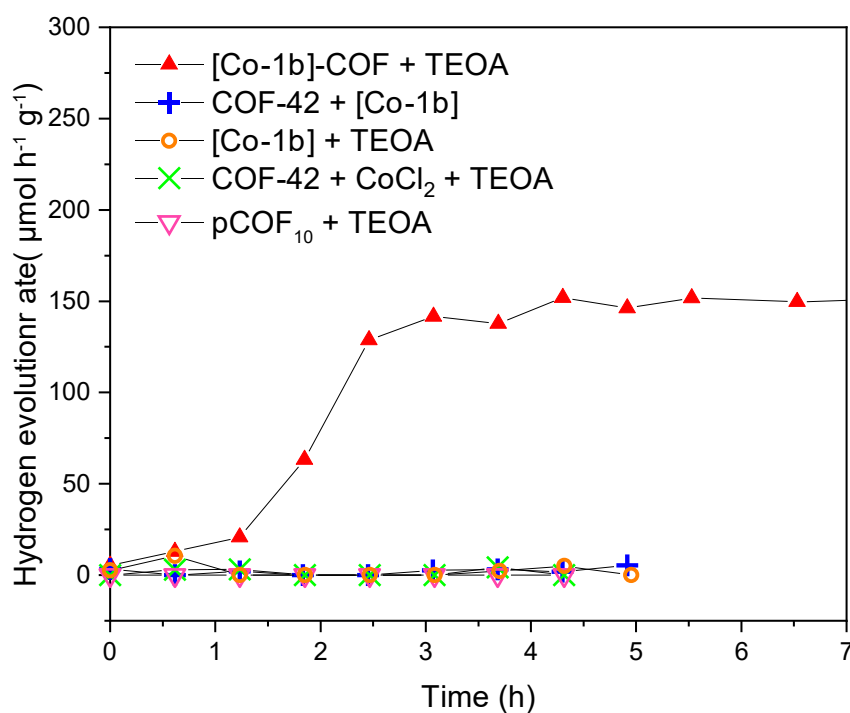


Figure 6-31: Photocatalytic hydrogen evolution experiments in acetonitrile and water in a ratio of 4:1 at pH 8. Red triangles: [Co-1b]-COF with TEOA as sacrificial donor. Blue pluses: COF-42 with [Co-1b], no sacrificial donor added. Orange circles: [Co-1b] with TEOA as sacrificial donor, no COF added. Green crosses: COF-42 with TEOA as sacrificial donor and CoCl₂.

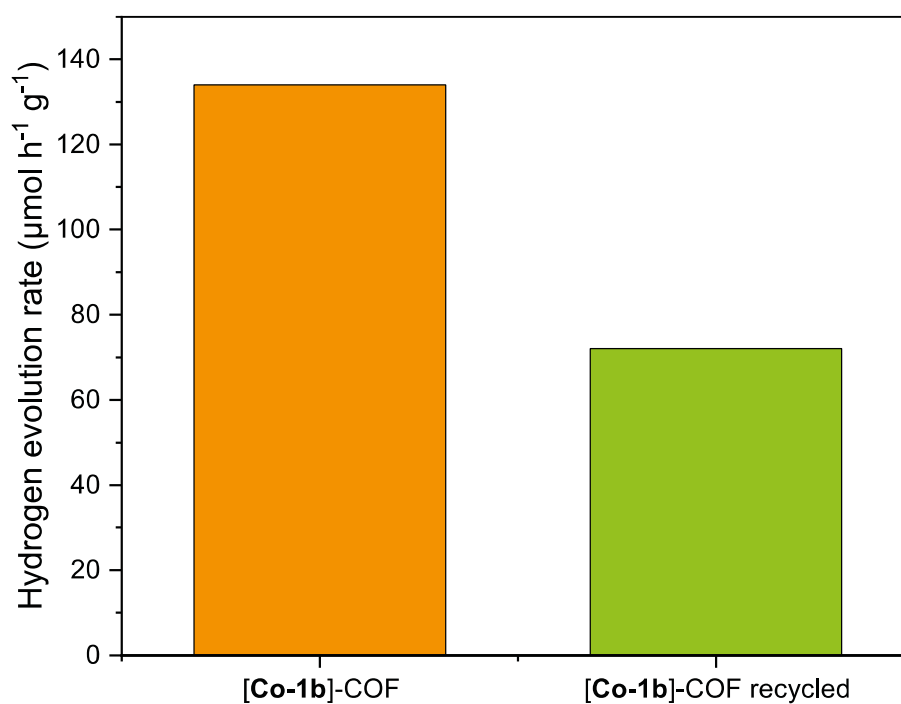


Figure 6-32: Photocatalytic activity of [Co-1b]-COF with 4.2 wt% cobaloxime content. Orange: first measurement, green: measurement after recycling.

Sorption analysis

Table 6-g: BET surface areas based on argon sorption measurements of the presented COFs.

Sample name	BET surface area ($\text{m}^2 \text{g}^{-1}$)
pCOF ₁₀	1839
[1a]-COF	1306
[1b]-COF	1117
[2]-COF	1031
[Co-1a]-COF	900
[Co-1b]-COF	1330
[Co-2]-COF	1101

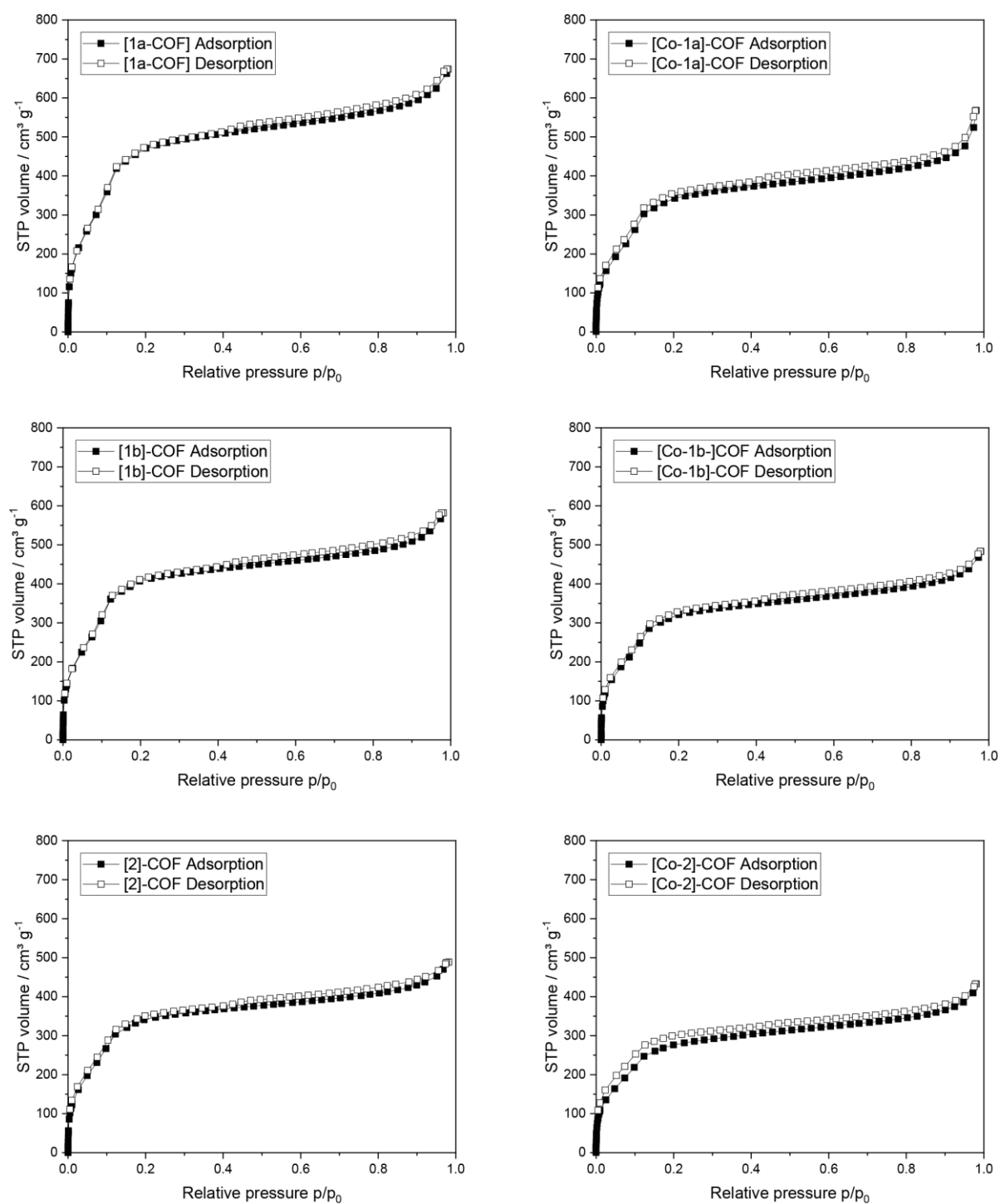


Figure 6-33: Argon isotherms of [1a]-COF, [1a]-COF, [2]-COF, [Co-1a]-COF, [Co-1a]-COF, and [Co-2]-COF.

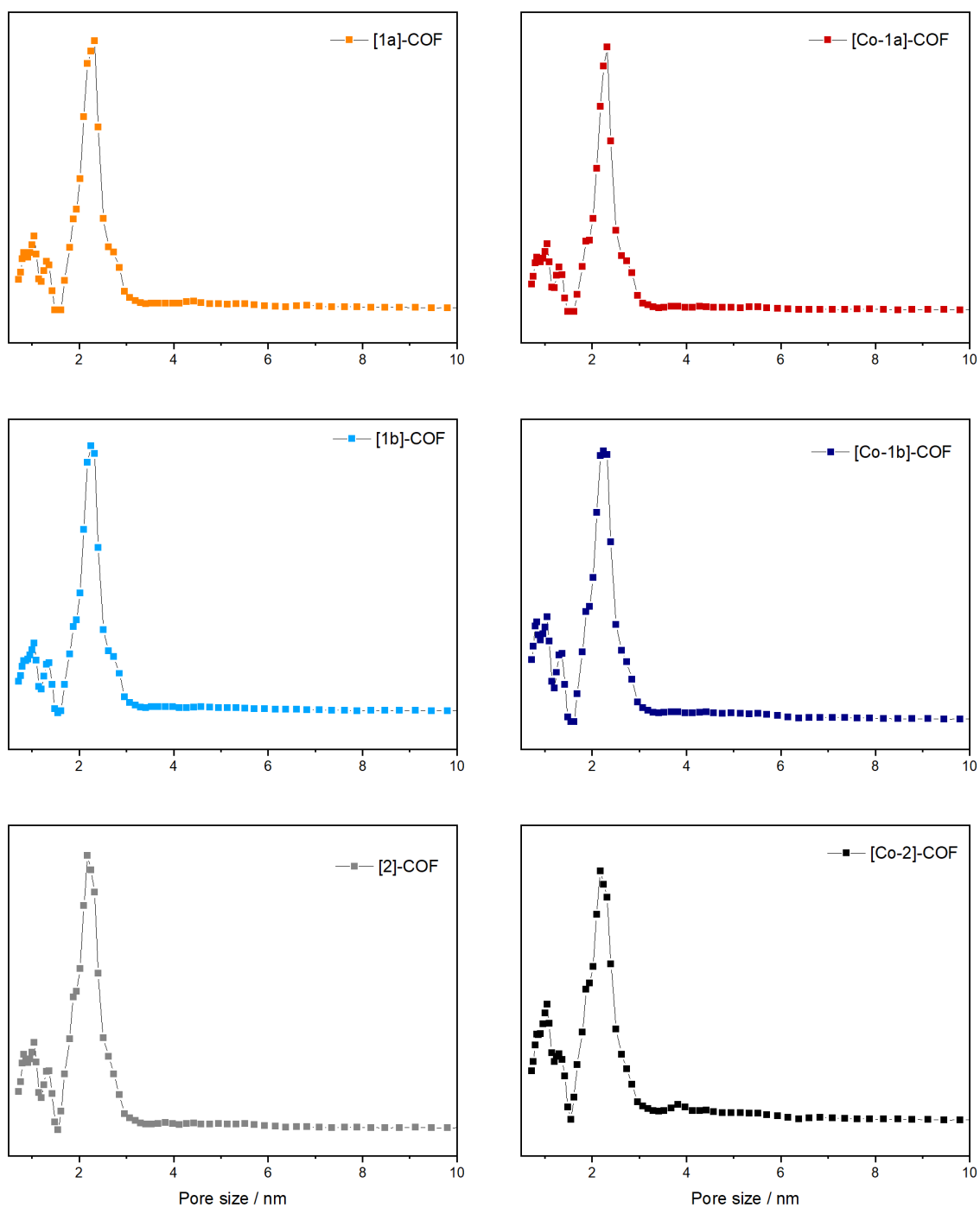


Figure 6-34: Pore size distributions of [1a]-COF, [1a]-COF, [2]-COF, [Co-1a]-COF, [Co-1a]-COF, and [Co-2]-COF.

Powder X-ray diffraction

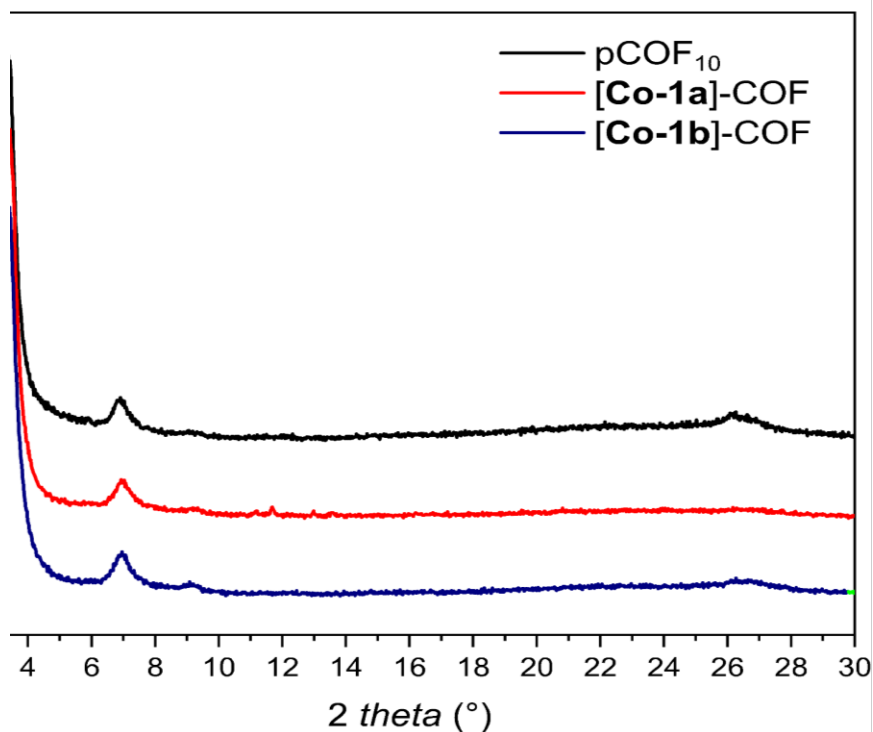
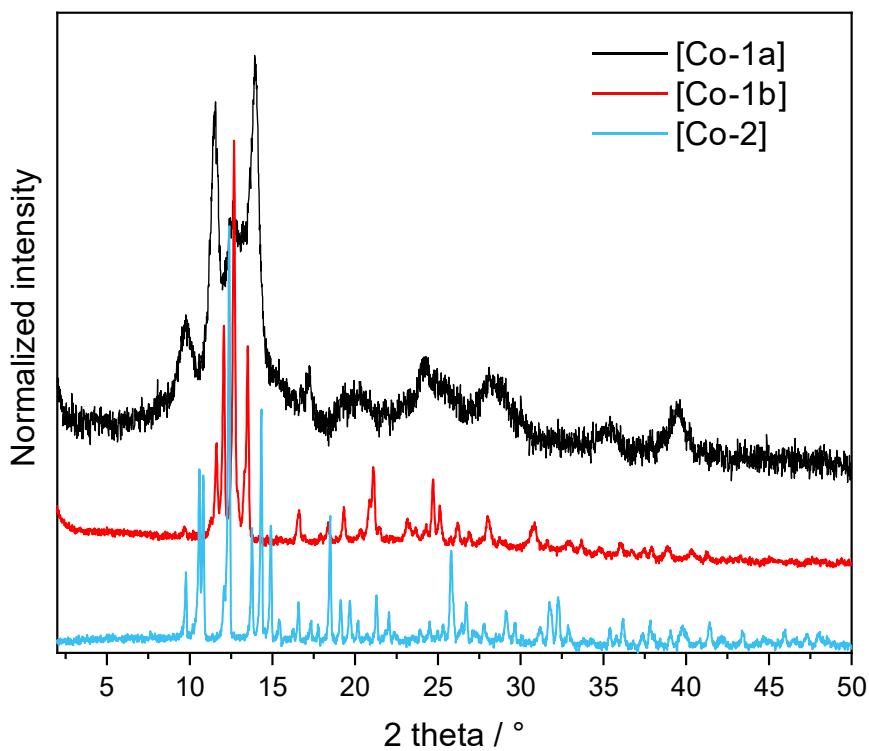
Figure 6-35: Powder X-ray diffractograms of pCOF₁₀, [Co-1a]-COF and [Co-1b]-COF.

Figure 6-36: Powder X-ray diffractograms of [Co-1a], [Co-1b], and [Co-2].



Scanning electron microscopy

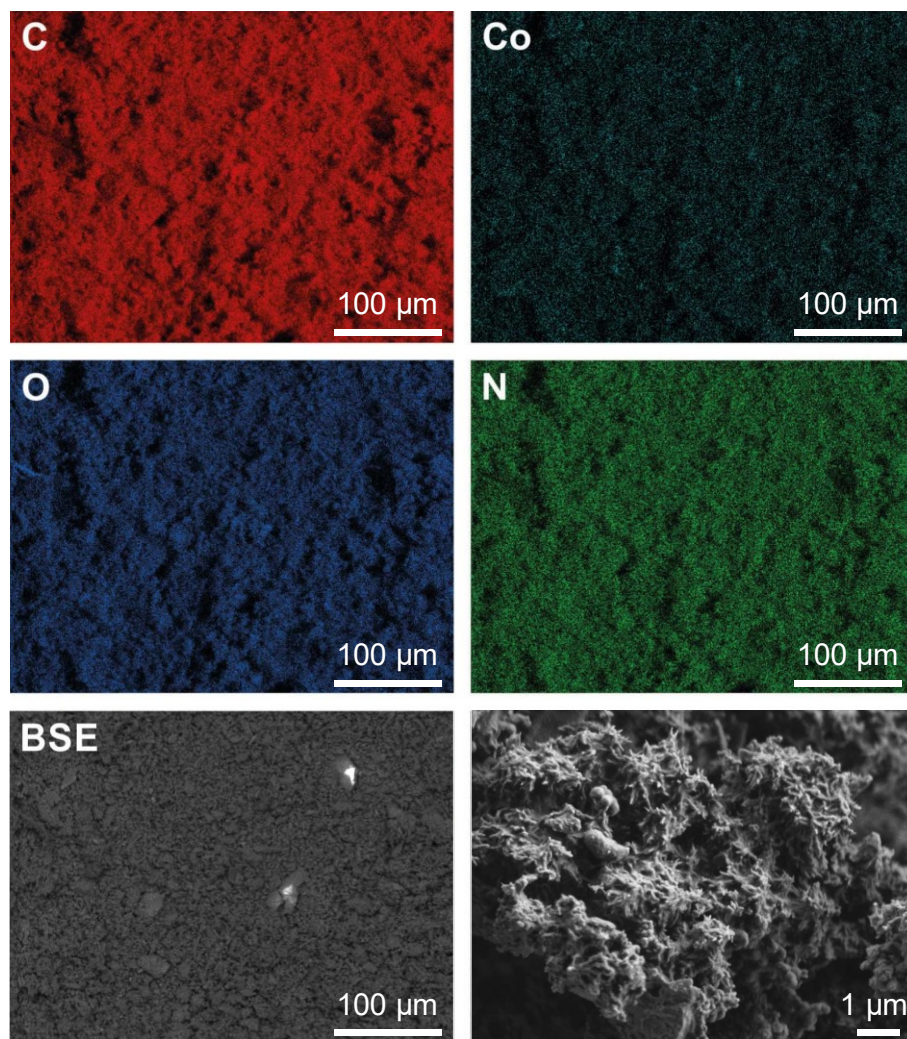


Figure 6-37: Scanning electron microscopy image of [Co-1a]-COF.

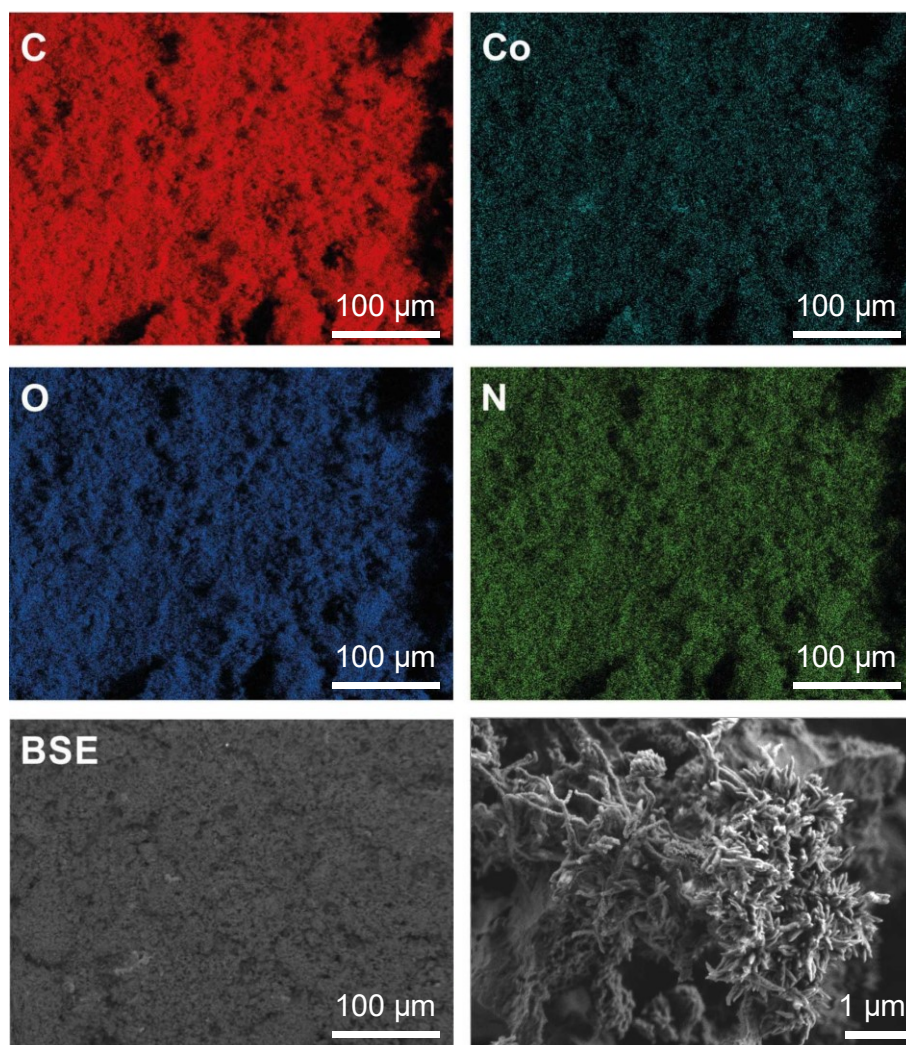


Figure 6-38: Scanning electron microscopy image of [Co-1b]-COF.

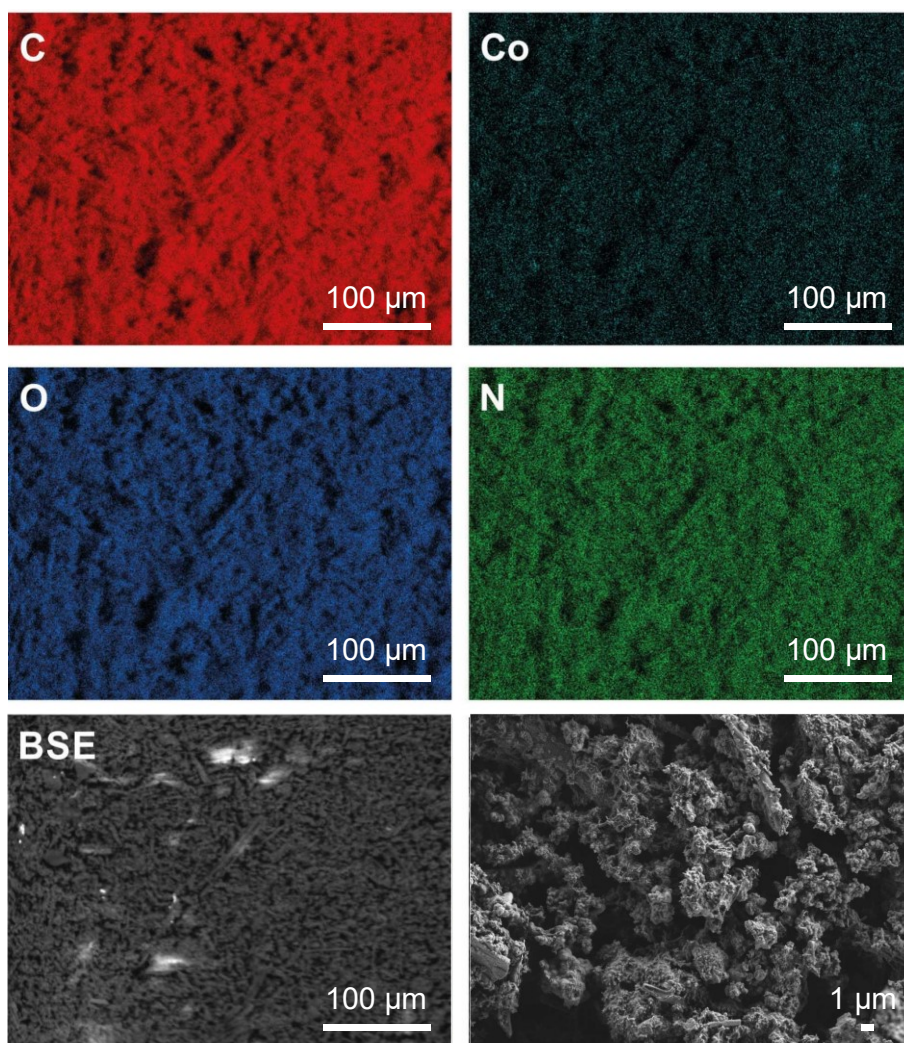


Figure 6-39: Scanning electron microscopy image of [Co-2]-COF.

Photoluminescence spectroscopy

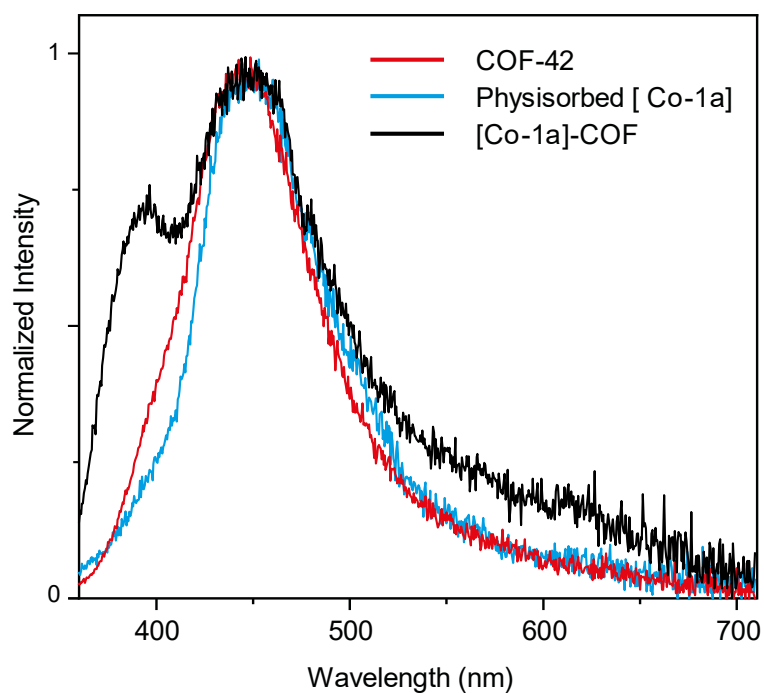


Figure 6-40: Emission spectra of COF-42, physisorbed [Co-1a], and [Co-1a]-COF. All samples were suspended in acetonitrile. All samples were excited at 300 nm.

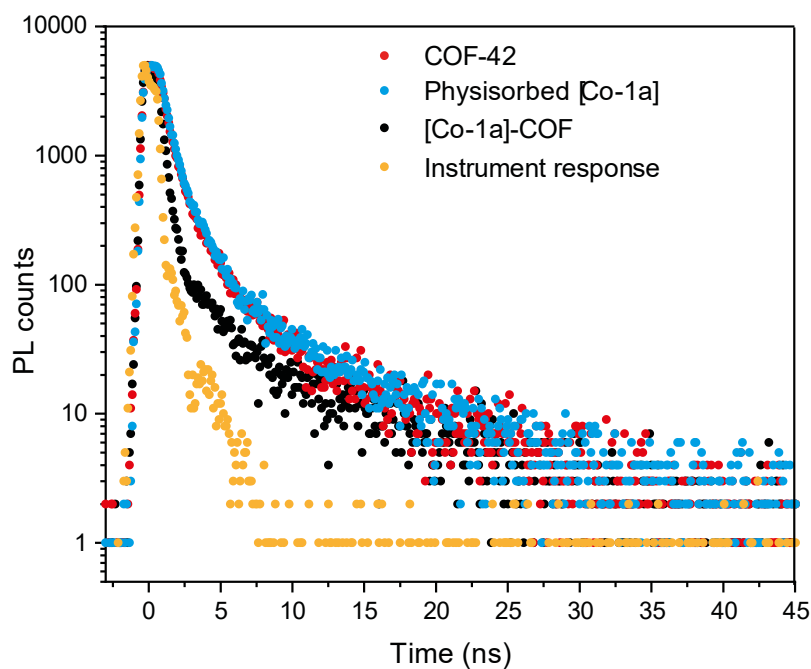


Figure 6-41: Fluorescence lifetime measurements of COF-42, physisorbed [Co-1a], and [Co-1a]-COF. All samples were suspended in acetonitrile. Samples were excited at 375 nm and the decay of the emission was monitored at 456 nm.



Emission spectra were recorded following excitation of [Co-1a]-COF, physisorbed [Co-1a] and only COF-42 samples at 300 nm. The poor dispersibility as well as the poorly emissive character of the samples prevented accurate measurement of absolute quantum yields (<1%) and relative emission intensities correctly and thus we present the normalized emission spectra of these three samples. We observe that while the emission spectra of physisorbed [Co-1a] and COF-42 only samples are identical, the spectrum for [Co-1a]-COF has two new emission features at 390 nm and around 550 – 600 nm. While we are presently uncertain about the origin of the former emission feature, we believe the latter emission feature could correspond to charge transfer interaction between the COF backbone and the co-catalyst. We further attempted to evaluate the quenching of the photoexcited COF by cobaloxime using time-correlated single photon counting (TCSPC) technique. The samples were excited using a 372 nm LASER source and the time decay of the emission was monitored at 456 nm. In comparison to physisorbed [Co-1a] sample, the emission decay for the covalently tethered [Co-1a]-COF is observed to be faster. This faster decay could correspond to relaxation of the locally excited state to the charge transfer state in [Co-1a]-COF and hence better charge transfer due to close contact and confinement of the cobaloxime co-catalyst. The 310 ps component in the decay of [Co-1a]-COF possibly hints to the fast charge separation in the covalently linked sample and could be a possible contributing factor towards its improved photocatalytic activity. Unfortunately, attempts to monitor the lifetime of the emission at ca. 600 nm were hindered due to the extremely low emission counts at that wavelength thus preventing an analysis of the population of this possible charge transfer state and subsequent recombination kinetics.

Table 6-10: Emission lifetimes of COF-42, physisorbed [Co-1a], and [Co-1a]-COF.

Sample	Lifetime (weight factor)
COF-42	$\tau_1 = 0.48$ ns (65.26%) $\tau_2 = 1.48$ ns (26.76%) $\tau_3 = 7.63$ ns (7.98%)
Physisorbed Co-1a	$\tau_1 = 0.48$ ns (63.56%) $\tau_2 = 1.48$ ns (28.12%) $\tau_3 = 7.63$ ns (8.32%)
[Co-1a]-COF	$\tau_1 = 0.31$ ns (93.19%) $\tau_2 = 6.46$ ns (6.81%)

ICP analysis

Table 6-11 Calculated catalyst content in weight percent according to ICP measurements. Functionalization of total amount of propargyl units in the pCOF₁₀ sample.

Sample name	Catalyst content (wt%)	Functionalization degree (%)
[Co-1a]-COF Route I	4.1	16
[Co-1a]-COF Route II	1.2	4.9
[Co-1b]-COF Route I	1.2	4.9
[Co-1b]-COF Route I	3.2	13
[Co-1b]-COF Route I	3.8	15
[Co-1b]-COF Route II	2.4	9.5
[Co-2]-COF Route I	3.5	15
[Co-2]-COF Route II	0.47	2.0

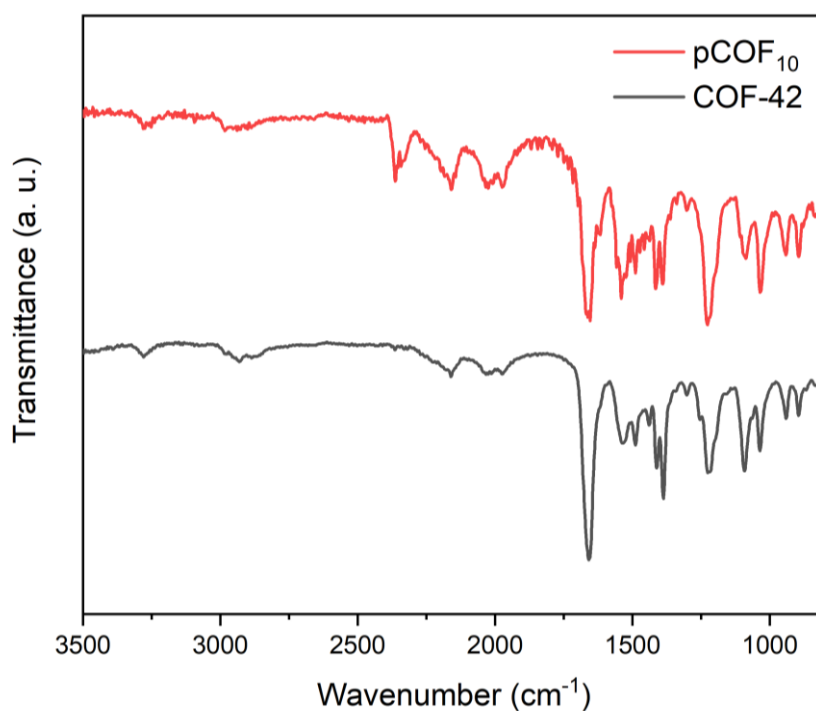
FTIR spectra

Figure 6-42: FTIR spectra of COF-42 and pCOF₁₀.

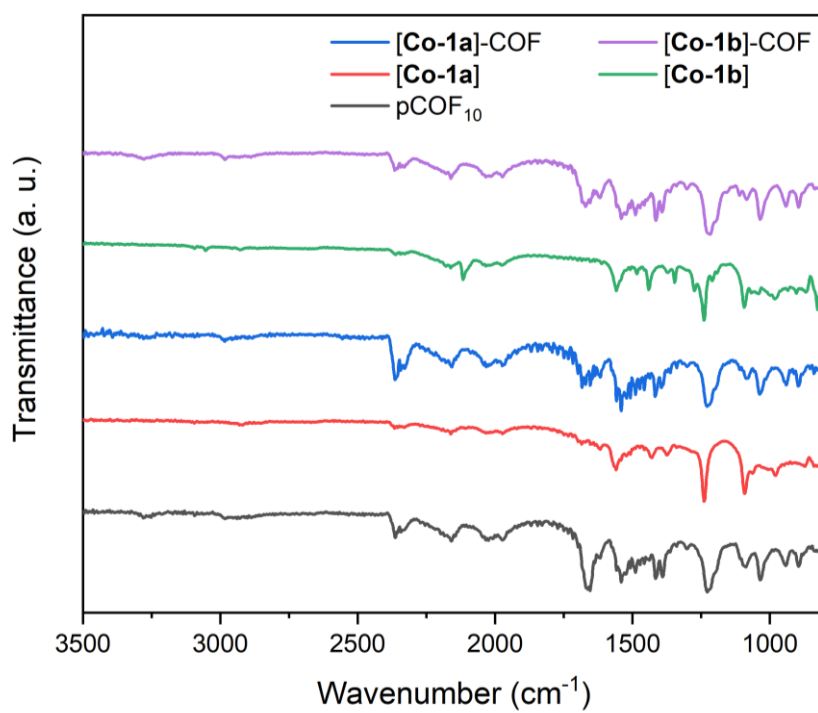


Figure 6-43: FTIR spectra of pCOF₁₀, [Co-1a], [Co-1a]-COF, [Co-1b], and [Co-1b]-COF.

UV/Vis absorption spectra

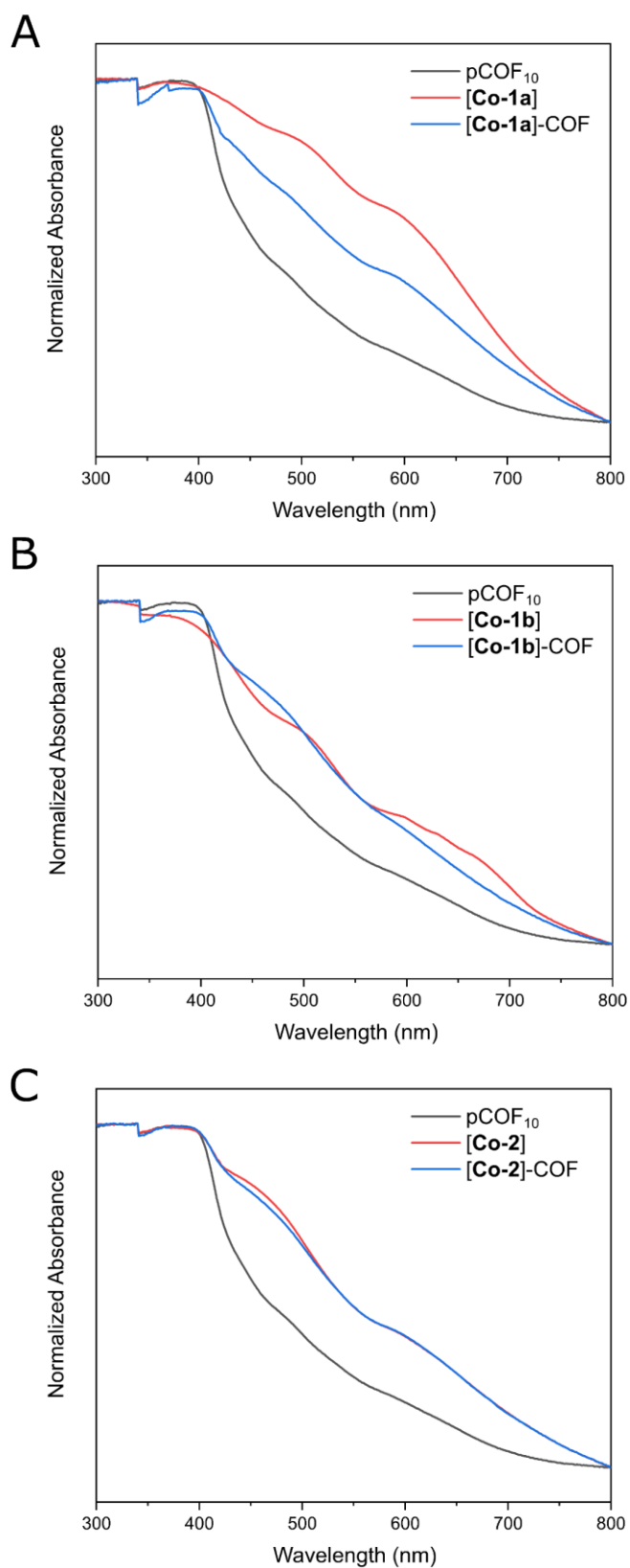


Figure 6-44: UV/Vis absorption spectra of (A) pCOF₁₀, [Co-1a] and [Co-1a]-COF; (B) pCOF₁₀, [Co-1b] and [Co-1b]-COF; (C) pCOF₁₀, [Co-2] and [Co-2]-COF.



Additional NMR measurements

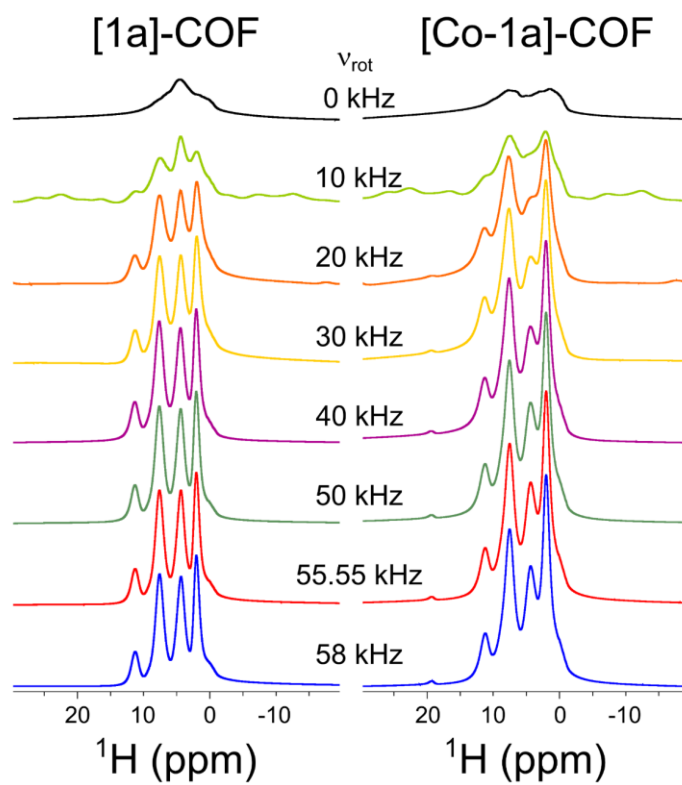


Figure 6-45: Dependence of the 1D spectrum quality of [1a]-COF and [Co-1a]-COF on the applied MAS frequency.

Quantum chemical calculations

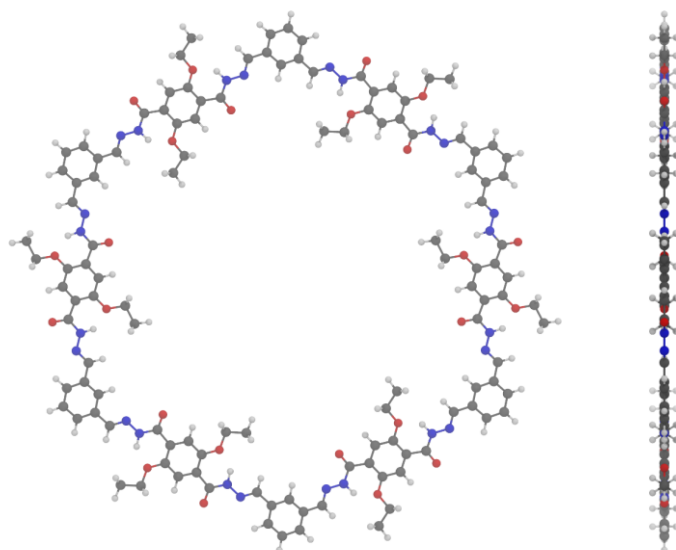


Figure 6-46: Optimized geometry for the COF-42 pore model, obtained on RI-PBE-D3/def2-TZVP level of theory. Top and side view.

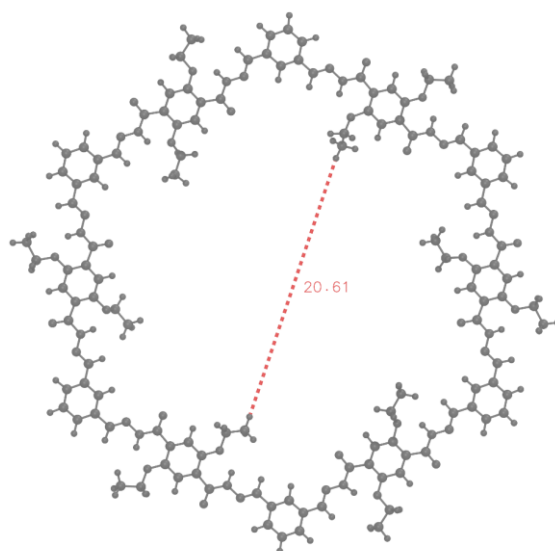


Figure 6-47: Visualization of the calculated pore diameter of 20.61 Å obtained from the optimized COF-42 pore model.

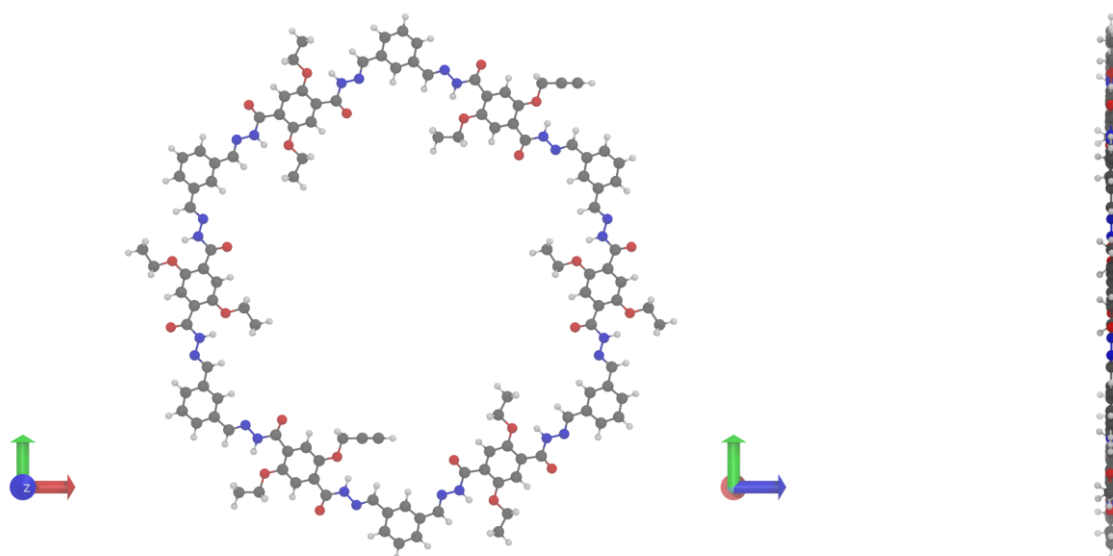


Figure 6-48: Optimized pCOF₁₀ pore model, obtained on RI-PBE-D₃/def2-TZVP level of theory. Top and side view.

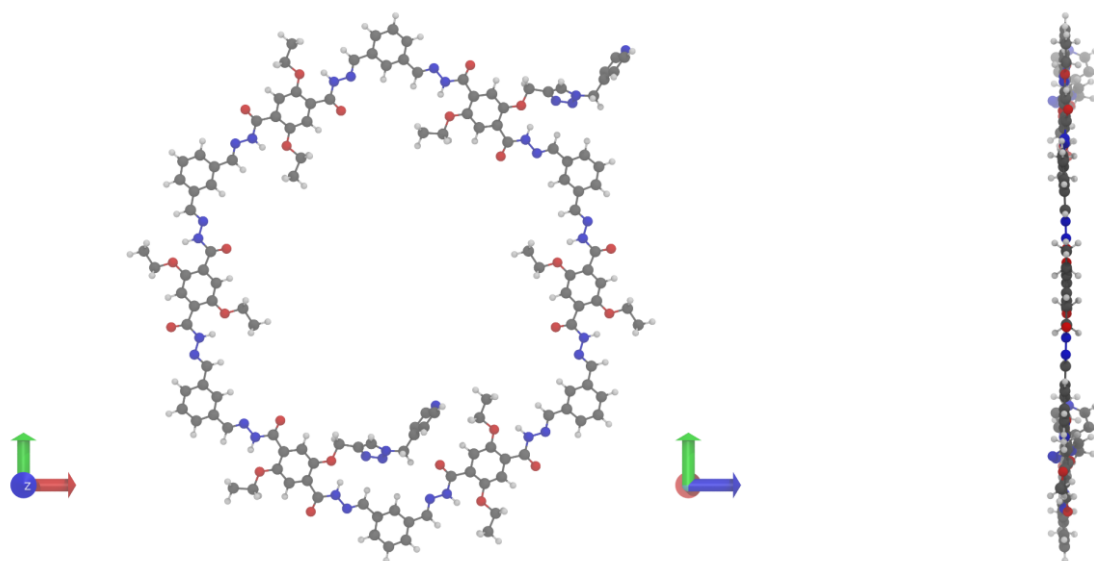


Figure 6-49: Optimized COF-42-pPy pore, obtained on RI-PBE-D₃/def2-TZVP level of theory. Top and side view.

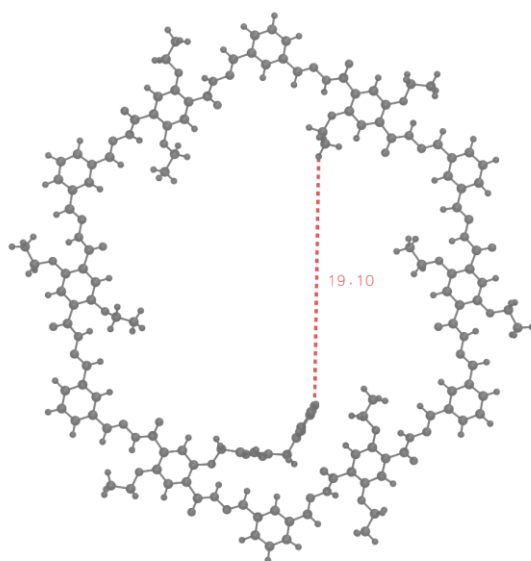


Figure 6-50: Visualization of the calculated pore diameter of 19.10 Å for the COF₄₂-pPy-COF pore model.

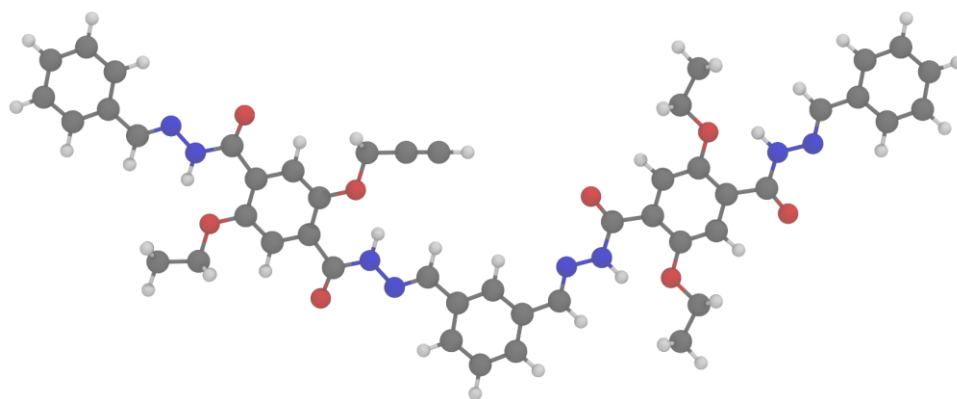
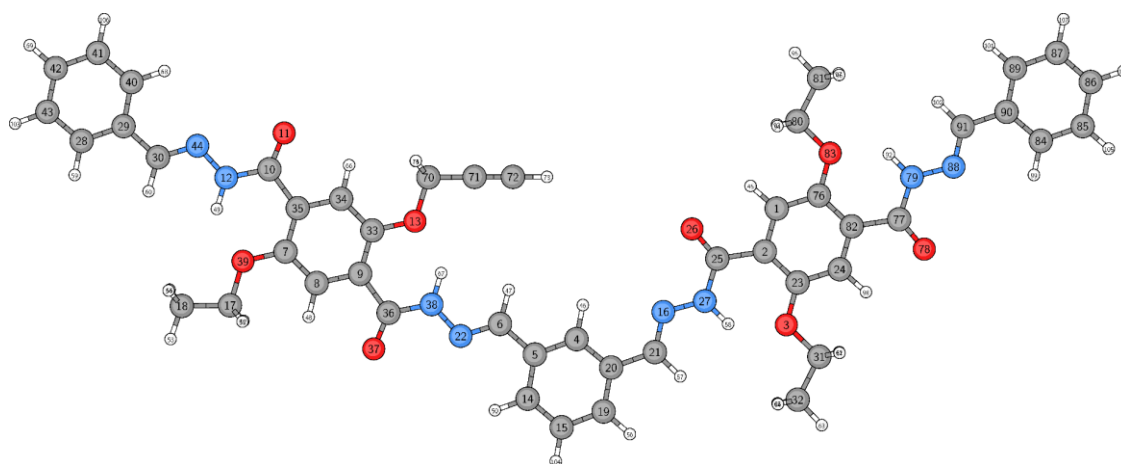
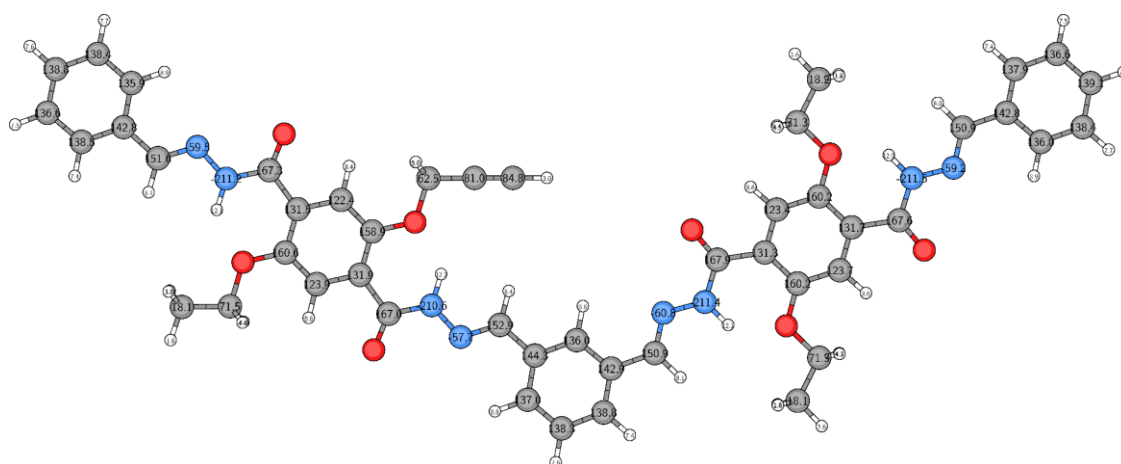


Figure 6-51: Geometry for the pCOF₁₀ cut model system, obtained by cutting the optimized pCOF₁₀ pore model.

Figure 6-52: Atom labels for the pCOF₁₀ cut model system.Figure 6-53: Calculated NMR Chemical Shifts for the pCOF₁₀ cut model system, obtained on level of theory.Table 6-12: Calculated NMR Chemical Shifts for the pCOF₁₀ model system, obtained on B97-2/pcS-2//RI-PBE-D₃/def2-TZVP level of theory.

Atom number	Element	NMR chemical shielding [ppm]	NMR chemical shift [ppm]
1	C	61.75	123.39
2	C	53.85	131.29
3	O	198.64	-
4	C	49.14	136.00
5	C	40.88	144.25
6	C	32.21	152.92
7	C	24.56	160.57
8	C	61.25	123.89

9	C	53.21	131.93
10	C	17.82	167.32
11	O	-76.77	-
12	N	50.70	-211.18
13	O	209.02	-
14	C	48.12	137.02
15	C	46.87	138.27
16	N	-99.68	-60.80
17	C	113.68	71.46
18	C	167.00	18.14
19	C	46.29	138.85
20	C	42.21	142.92
21	C	34.25	150.89
22	N	-102.74	-57.74
23	C	24.97	160.17
24	C	61.42	123.71
25	C	17.25	167.89
26	O	-73.41	-
27	N	50.91	-211.39
28	C	46.61	138.52
29	C	42.36	142.78
30	C	33.51	151.63
31	C	113.79	71.34
32	C	167.04	18.09
33	C	26.28	158.85
34	C	62.74	122.39
35	C	53.62	131.52
36	C	18.13	167.01



37	O	-75.58	-
38	N	50.09	-210.57
39	O	198.26	-
40	C	49.19	135.94
41	C	46.70	138.43
42	C	46.31	138.83
43	C	48.57	136.56
44	N	-100.95	-59.53
45	H	22.82	8.57
46	H	22.63	8.75
47	H	22.99	8.40
48	H	22.76	8.63
49	H	19.32	12.07
50	H	22.56	8.83
51	H	27.03	4.36
52	H	27.05	4.34
53	H	29.83	1.56
54	H	29.59	1.80
55	H	29.59	1.80
56	H	24.00	7.39
57	H	23.32	8.07
58	H	19.25	12.14
59	H	23.95	7.44
60	H	23.34	8.05
61	H	27.05	4.34
62	H	27.04	4.35
63	H	29.83	1.55
64	H	29.57	1.82

65	H	29.57	1.82
66	H	23.01	8.38
67	H	19.14	12.24
68	H	22.46	8.93
69	H	23.79	7.60
70	C	122.65	62.49
71	C	104.10	81.03
72	C	100.32	84.82
73	H	28.40	2.99
74	H	26.36	5.02
75	H	26.39	5.00
76	C	24.98	160.15
77	C	17.55	167.58
78	O	-79.09	-
79	N	51.03	-211.50
80	C	113.81	71.32
81	C	166.98	18.16
82	C	53.48	131.66
83	O	199.13	-
84	C	49.11	136.02
85	C	46.72	138.41
86	C	46.00	139.14
87	C	48.51	136.63
88	N	-101.30	-59.18
89	C	47.25	137.88
90	C	42.32	142.81
91	C	34.27	150.86
92	H	19.37	12.02



93	H	27.02	4.37
94	H	27.04	4.35
95	H	29.77	1.62
96	H	29.58	1.81
97	H	29.58	1.81
98	H	22.80	8.59
99	H	22.44	8.95
100	H	23.78	7.61
101	H	23.95	7.44
102	H	23.34	8.04
103	H	23.87	7.52
104	H	23.76	7.63
105	H	23.73	7.66
106	H	23.71	7.68
107	H	23.86	7.53

Molecular dynamics simulations

14970 equidistant frames were extracted from a 15 ns MD simulation of a single COF-42-pPy pore model. Frames, where the **1a** linker moves within more than ± 2 Å out of the COF pore plane were discarded, to avoid linker positions clashing with COF pores below and above the simulated pore, leaving 3730 frames. All missing Cobaloxime ligands were now attached to the **1a** linker unit and rotated conjointly in 10 degree steps around the Nitrogen-Cobalt-Chlorine axis, to sample possible orientations of the docked complex. Structures with overlapping atoms, close-contact clashes and multivalent bonds were rejected subsequently, leaving 60321 structures. 200 structures with the largest possible diversity, based on the largest component of the principal axes of inertia, were selected, cut to the size of the defined NMR model to then compute NMR chemical shifts and prepare simulated 2D SQDQ ^1H NMR spectra.

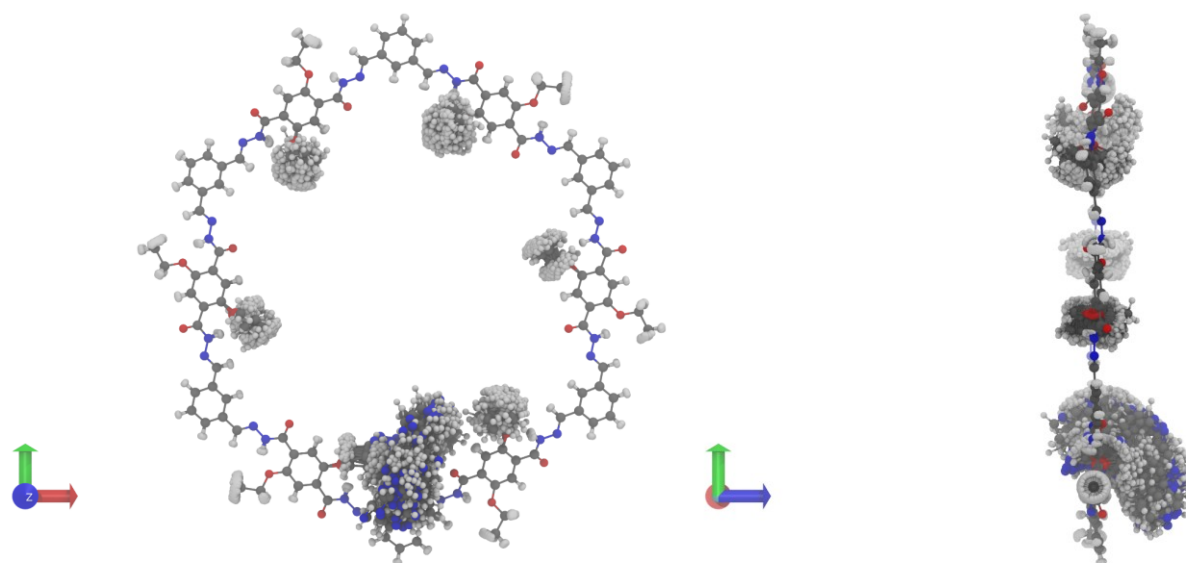


Figure 6-54: Overlay of every 100th frame from a 15 ns MD simulation visualizing the flexibility of the **1a**-ligand in comparison to the ethoxy-ligands. Top and side view.

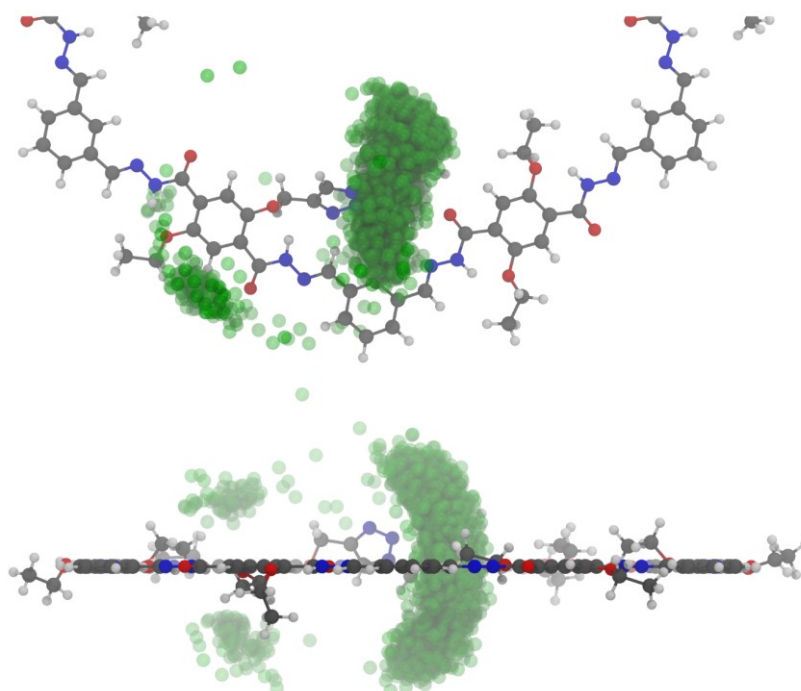


Figure 6-55: Overlay of every Nitrogen position of the **1a**-ligand showing positions from every 5th frame from a 15 ns MD simulation visualizing visited positions of the Pyridine subunit. Top and side view.



6.1.3 Materials and methods for chapter 4.2

SEM

SEM measurements were performed on a Zeiss Merlin or a VEGA TS 51300MM (TESCAN).

TEM

TEM was performed on a Philips cm30ST (300 kV, LaB₆ cathode) with a cmOSS camera F216 (TVIPS). Samples were suspended in butanol and drop-cast onto a lacey carbon film (Plano).

PXRD

PXRD patterns were recorded at room temperature on a Bruker D8 Discovery with Ni-filtered CuK α -radiation (1.5406 Å) and a position-sensitive detector (Lynxeye).

IR

Fourier-transform infrared spectra were measured on a Jasco FT/IR-4100 or a Perkin Elmer Spectrum NX FT-IR System.

Structural models

Structural models were obtained with Materials Studio v6.0.0 Copyright © 2011 Accelrys Software using the Forcite Geometry optimization with Ewald electrostatic and van der Waals summation methods.

Sorption

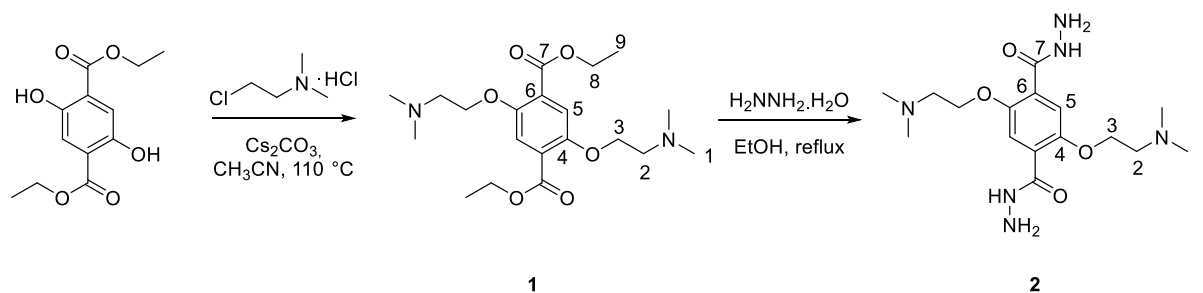
Sorption measurements were performed on a Quantachrome Instruments Autosorb iQ MP with Argon at 87 K or with CO₂ at 273, 288 or 298 K. Weight percentage was calculated by referencing to sorbent weight.

Quantum chemical Calculations

NMR chemical shifts were obtained on B97-2/pcS-2/PBE0-D3/def2-TZVP level of theory^[1-2, 15, 19-21] using the Turbomole^[10, 22] program package in version 7.0.2 for geometries and the FermiONs+ +^[17-18] program package for the calculation of NMR chemical shifts.

Synthetic procedures

1,3,5-triformylbenzene was used as purchased. 2,5-diethoxyterephthalohydrazide and 2,4,6-trihydroxybenzene-1,3,5-tricarbaldehyde were synthesized according to known procedures as follows. All reactions were performed under Ar atmosphere with dry solvents and magnetically stirred, unless otherwise noted.



Diethyl 2,5-bis(2(dimethylamino)ethoxy)terephthalate (**1**)

Diethyl 2,5-dihydroxyterephthalate (2 mmol, 524 mg, 1 eq) and cesium carbonate (8.4 mmol, 2.74 g, 4.2 eq) were suspended in acetonitrile (20 mL). 2-Dimethylaminoethyl chloride hydrochloride (4.4 mmol, 640 mg, 2.1 eq) was added. After the reaction mixture was refluxed for 2 h, the solvent was removed. The brownish residue was added into water and extracted with ethyl acetate. The organic extract was dried over magnesium sulfate. The substrate was acidified (HCl 3 M, 3 x 15 mL) and washed with diethyl ether (3 x 15 mL). The mixture was made alkaline with a saturated solution of potassium carbonate in water and extracted with ethyl acetate (3 x 5 mL) until all the organic product was precipitated from the water layer. The organic layer was dried over magnesium sulfate. The solvent was removed to give the product as a light yellow solid (502 mg, 1.27 mmol, 65%).

$^1\text{H NMR}$ (400 MHz, CDCl_3): δ = 7.38 (s, 2H, H_{arom}), 4.36 (q, 4H, Me- CH_2), 4.11 (t, 4H, O-C- H_2 - CH_2), 2.75 (t, 4H, N-C- H_2 - CH_2), 2.34 (s, 12H, N-C- H_3), 1.38 (t, 6H, O- CH_2 -C- H_3) ppm.

$^{13}\text{C NMR}$ (101 MHz, CDCl_3): δ = 165.8 (C-7), 152.0 (C-4), 125.2 (C-6), 117.3 (C-5), 68.8 (C-3), 61.5 (C-8), 58.3 (C-2), 46.3 (C-1), 14.4 (C-9) ppm.

$^{15}\text{N NMR}$ (400 MHz, CDCl_3): δ = -244.5 (- NH_2), -247.5 (-NH-), -360.3 (- NMe_2) ppm.

HRMS (DEI, positive): calc. for $\text{C}_{20}\text{H}_{33}\text{N}_2\text{O}_6$ (M) $^+$: 396.2260; found: 396.2256.

IR (FT, ATR): 3801 (br, w), 3076 (br, w, C- H_{arom}), 2939 (m, C- H_3), 2820 (w, C- H_3), 2660 (br, m), 2416 (m), 1871 (br, m, C=O), 1623 (s, C=C $_{\text{arom}}$), 1496 (w, C- $\text{H}_{2\text{deform}}$), 1392 (s), 1368 (s), 1300 (w), 1231 (m), 1205 (m), 1100 (m), 1006 (s), 976 (s), 829 (s, C- $\text{H}_{\text{aromdeform}}$), 792 (w), 701 (s), 665 (m) cm^{-1} .

2,5-bis(2-(dimethylamino)ethoxy)terephthalohydrazide (**2**)

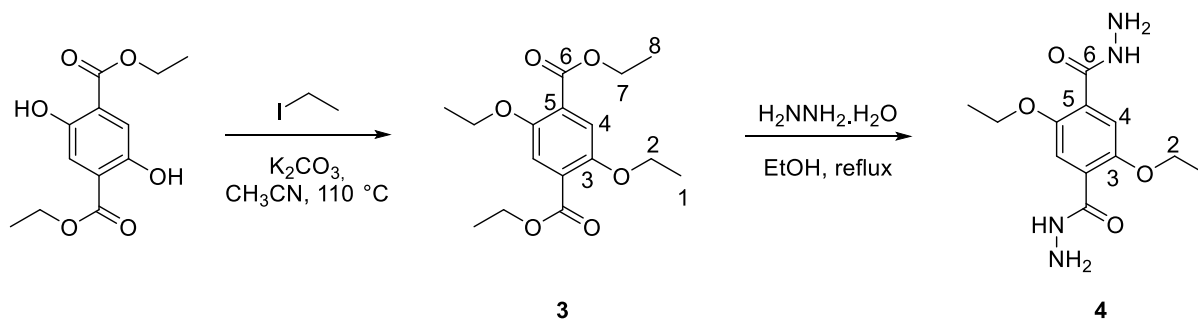
Diethyl 2,5-bis(2-(dimethylamino)ethoxy)terephthalate (0.175 mmol, 70 mg, 1 eq) was suspended in a solution of ethanol/toluene (5 mL, 1:1). Hydrazine hydrate (1.75 mmol, 54.4 μL , 10 eq) was added. The reaction mixture was heated to 110 $^\circ\text{C}$ for 8 h. The solvent was evaporated to yield an off-white solid (57 mg, 0.155 mmol, 88%).

^1H NMR (400 MHz, CDCl_3): δ = 10.52 (s, 2H, N-H), 7.76 (s, 2H, H_{arom}), 4.23 (t, 4H, O-C-H₂-CH₂), 4.17 (bs, 4H, N-H₂), 2.70 (t, 4H, N-C-H₂-CH₂), 2.33 (s, 12H, N-C-H₃) ppm.

^{13}C NMR (101 MHz, CDCl_3): δ = 164.8 (C-7), 151.2 (C-4), 125.0 (C-6), 117.4 (C-5), 67.3 (C-3), 57.8 (C-2), 45.1 (C-1) ppm.

HRMS (DEI, positive): calc. for $\text{C}_{16}\text{H}_{29}\text{N}_6\text{O}_4$ (M)⁺: 368.2172; found: 368.2169.

IR (FT, ATR): 3538 (br, m, N-H), 2944 (m, C-H₃), 2892 (s), 2820 (m, C-H₃), 2772 (m), 2269 (m), 2103 (m), 1647 (m, C=O), 1597 (m, C=C_{arom}), 1487 (m, C-H₂deform), 1470 (s), 1417 (w), 1402 (m), 1361 (m), 1302 (m), 1258 (m), 1209 (s), 1161 (m), 1120 (m), 1100 (m), 1063 (m), 1023 (s), 962 (s), 928 (m), 912 (w), 888 (m, C-H_{arom}deform), 856 (w), 793 (m), 774 (m), 720 (m), 656 (m) cm^{-1} .



Diethyl 2,5-diethoxyterephthalate (3)

Diethyl 2,5-dihydroxyterephthalate (4 mmol, 1.05 g, 1 eq) and potassium carbonate (13.2 mmol, 1.82 g, 3.3 eq) were suspended in acetonitrile (10 mL). Iodoethane (13.2 mmol, 1.07 mL, 3.3 eq) was added. After the reaction mixture was refluxed for 72 h, the solvent was removed. The brownish residue was added into water and extracted with ethyl acetate. The organic extract was dried over magnesium sulfate. The solvent was removed to give the product as a light yellow solid (1.20 g, 3.87 mmol, 97%).

^1H NMR (400 MHz, CDCl_3): δ = 7.35 (s, 2H, H_{arom}), 4.36 (q, 4H, Me-CH₂), 4.09 (t, 4H, O-C-H₂-CH₂), 1.43 (t, 6H, CO-CH₂-C-H₃), 1.38 (t, 6H, COO-CH₂-C-H₃) ppm.

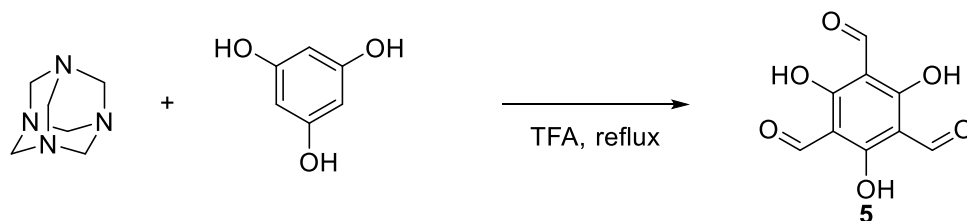
2,5-diethoxyterephthalohydrazide (4)

Diethyl 2,5-diethoxyterephthalate (3.96 mmol, 1.2 g, 1 eq) was suspended in a solution of ethanol/toluene (20 mL, 1:1). Hydrazine hydrate (39.6 mmol, 1.94 mL, 10 eq) was added. The reaction mixture was heated to 110°C for 8 h. The solvent was evaporated to yield an off-white solid (903 mg, 3.20 mmol, 81%).

^1H NMR (400 MHz, CDCl_3): δ = 9.20 (s, 2H, N-H), 7.78 (s, 2H, H_{arom}), 4.27 (q, 4H, O-C-H₂-CH₃), 4.18 (bs, 4H, N-H₂), 1.51 (s, 12H, -CH₃) ppm.

^{13}C NMR (101 MHz, CDCl_3): $\delta = 163.7$ (C-6), 149.5 (C-3), 125.0 (C-5), 114.7 (C-4), 64.8 (C-2), 14.5 (C-1) ppm.

HRMS (DEI, positive): calc. for $\text{C}_{16}\text{H}_{29}\text{N}_6\text{O}_4$ (M) $^+$: 282.1328; found: 282.1433.

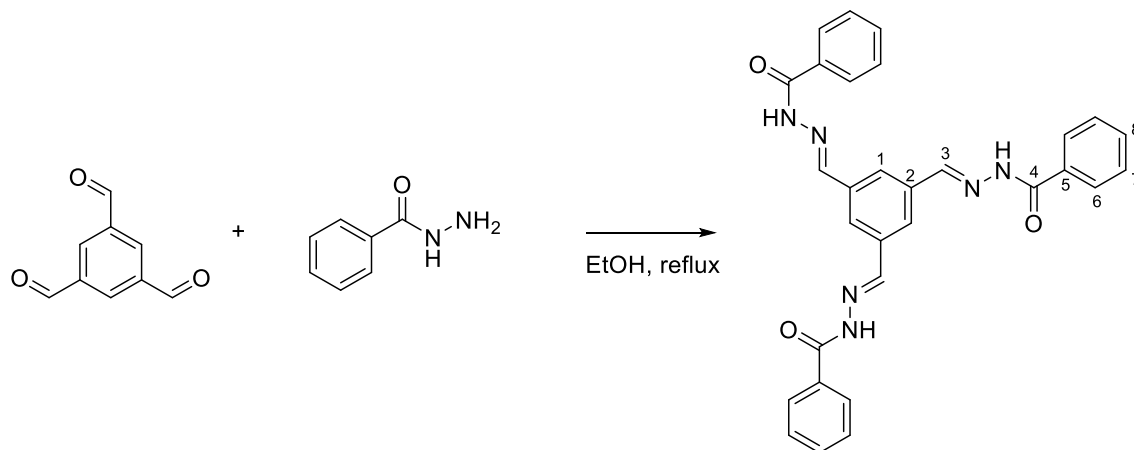


2,4,6-trihydroxybenzene-1,3,5-tricarbaldehyde (5)

A solution of hexamethylenetetramine (0.91 mol, 12.9 g, 2.2 eq) and phloroglucinol (0.42 mol, 5.3 g, 1 eq) in trifluoroacetic acid (75 ml) was heated at 100 °C for 2.5 h. 3M HCl (150 mL) was added slowly and heated for 1 h. After cooling to room temperature, the mixture was filtered through a bed of celite. The filtrate was extracted with dichloromethane (4 x 100 mL) and dried over magnesium sulfate. The solvent was evaporated, and the residue washed with cold CHCl_3 and hot ethanol to yield a light orange solid (2.60 g, 12.3 mmol, 30%).

^1H NMR (400 MHz, CDCl_3): $\delta = 14.11$ (s, 3H, O-H), 10.15 (s, 3H, -CH=O) ppm.

^{13}C NMR (101 MHz, CDCl_3): $\delta = 192.4$ (-CH=O), 174.0 (C-OH), 103.2 ($\text{C}_{\text{arom.}}$) ppm.



Model compound N',N''',N'''' -((1*E*,1'*E*,1''*E*)-benzene-1,3,5-triyltris(methanylylidene))-tri(benzohydrazide) (6)

A mixture of 1,3,5-triformylbenzene (0.27 mmol, 44 mg, 1 eq) and benzoic hydrazide (1.08 mmol, 150 mg, 4 eq) in absolute ethanol (10 ml) was heated at reflux under argon for 4 h. The pale yellow solid separated was collected by filtering the hot heterogeneous reaction mixture and repeatedly washed with ethanol and dried in vacuo (112 mg, 0.22 mmol, 80%).



^1H NMR (400 MHz, d_6 -DMSO): δ = 12.04 (s, 3H, N-H), 8.57 (s, 3H, N=C-H), 8.13 (s, 3H, $H_{\text{arom.,core}}$), 7.94 (d, 6H, $H_{\text{arom.}}$), 7.62 (t, 3H, $H_{\text{arom.}}$), 7.56 (t, 6H, $H_{\text{arom.}}$) ppm.

^{13}C NMR (101 MHz, d_6 -DMSO): δ = 163.8 (C-4), 147.0 (C-3), 136.1 (C-2), 133.8 (C-5), 132.4 (C-8), 129.0 (C-1), 128.2 (C-7), 127.1 (C-6) ppm.

HRMS (DEI, positive): calc. for $\text{C}_{30}\text{H}_{24}\text{N}_6\text{O}_3$ (M) $^+$: 516.1910; found: 516.1893.

COF synthesis

All products were obtained as fluffy solids. To remove residual starting materials, powders were washed intensely with DMF, THF and dichloromethane and subsequently dried in a vacuum desiccator overnight.

coCOF-H – COF-42

To a Biotage© 2 mL microwave vial, 1,3,5-triformylbenzene (0.066 mmol, 10.7 mg, 2 eq) and 2,5-diethoxyterephthalohydrazide (0.099 mmol, 27.9 mg, 3 eq) were added. Dioxan (0.25 mL), mesitylene (0.75 mL) and acetic acid (6M, 150 μL) were added. The vial was sealed and heated under microwave irradiation at 160 °C for 30 min. Subsequently, the vial was heated in a muffle furnace at 120 °C for 72 h. After cooling to room temperature, the solid was filtered and washed with DMF (3 x 2 mL), THF (3 x 2 mL) and DCM (3 x 2 mL) to yield a light-yellow powder.

For the copolymerized systems, corresponding amounts of 2,5-diethoxyterephthalohydrazide were replaced by 2,5-bis(2-(dimethylamino)ethoxy)terephthalohydrazide while the procedure was retained as described before. Solvents were used according to Table S1. The products yielded as yellow to orange powders.

coCOF-OH – HTFG-COF

To a Biotage© 5 mL microwave vial, 2,4,6-trihydroxybenzene-1,3,5-tricarbaldehyde (0.132 mmol, 28.6 mg, 2 eq) and 2,5-diethoxyterephthalohydrazide (0.198 mmol, 55.9 mg, 3 eq) were added. Dimethylacetamide (2.25 mL) and 1,2-dichlorobenzene (0.75 mL) and acetic acid (6M, 150 μL) were added. The vial was sealed and heated under microwave irradiation at 160 °C for 30 min. Subsequently the vial was heated in a muffle furnace at 120 °C for 72 h. After cooling to room temperature, the solid was filtered and washed with DMF (3 x 2 mL), THF (3 x 2 mL) and DCM (3 x 2 mL) to yield an orange powder. For the copolymerized systems, corresponding amounts of 2,5-diethoxyterephthalohydrazide were replaced by 2,5-bis(2-(dimethylamino)ethoxy)terephthalohydrazide while the procedure was retained as described before. Solvents were used according to Table S1. The products were obtained as orange to red powders.

Table 6-13: Solvent mixtures used in the synthesis of different coCOF-samples.

COF system	Amount of DtATH	Solvent
coCOF-H - COF-42	0%	1,4-dioxane/mesitylene 1:3
	25%	1,4-dioxane/mesitylene 1:1
	50%	o-dichlorobenzene/dimethylacetamide 1:3
	75%	1,4-dioxane/mesitylene 1:1
	100%	o-dichlorobenzene/dimethylacetamide 1:3
coCOF-OH - HTFG-COF	0%	o-dichlorobenzene/dimethylacetamide 1:3
	25%	o-dichlorobenzene/dimethylacetamide 1:3
	50%	o-dichlorobenzene/dimethylacetamide 1:3
	75%	o-dichlorobenzene/dimethylacetamide 1:3
	100%	o-dichlorobenzene/dimethylacetamide 1:3

FTIR spectra

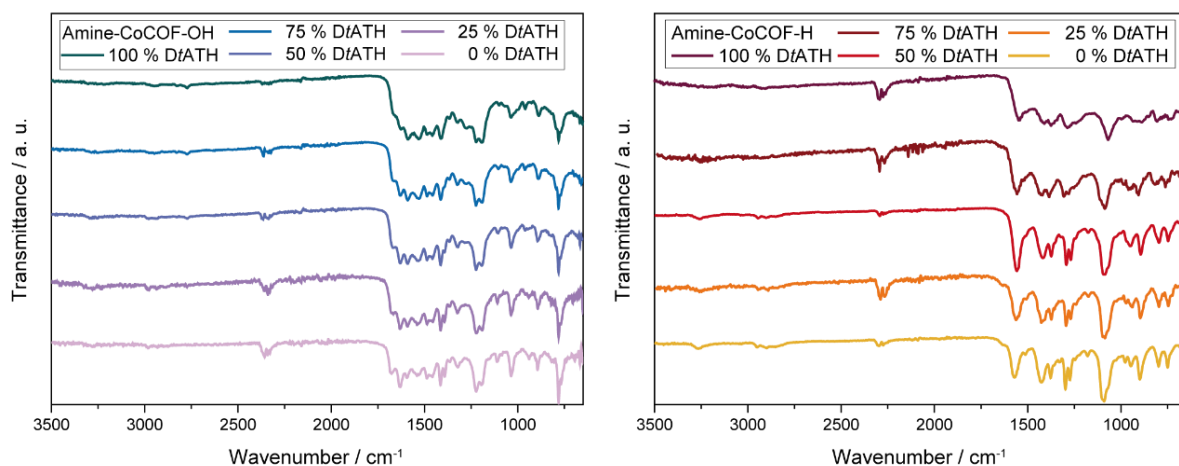


Figure 6-56: FTIR spectra of Amine-coCOF-OH (left, blue) and Amine-coCOF-H (right, red). Darker color indicates higher amount of DtATH.



XRD of amine containing samples

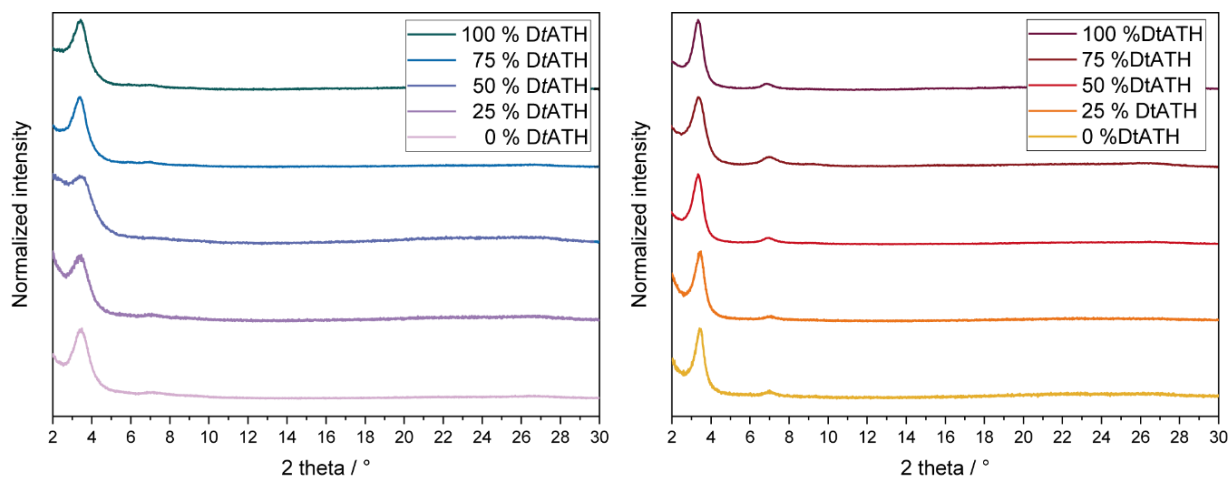


Figure 6-57: PXR D patterns of Amine-coCOF-OH (left, blue) and Amine-coCOF-H (right, red). Darker color indicates higher amount of DtATH.

UV/Vis absorption spectra

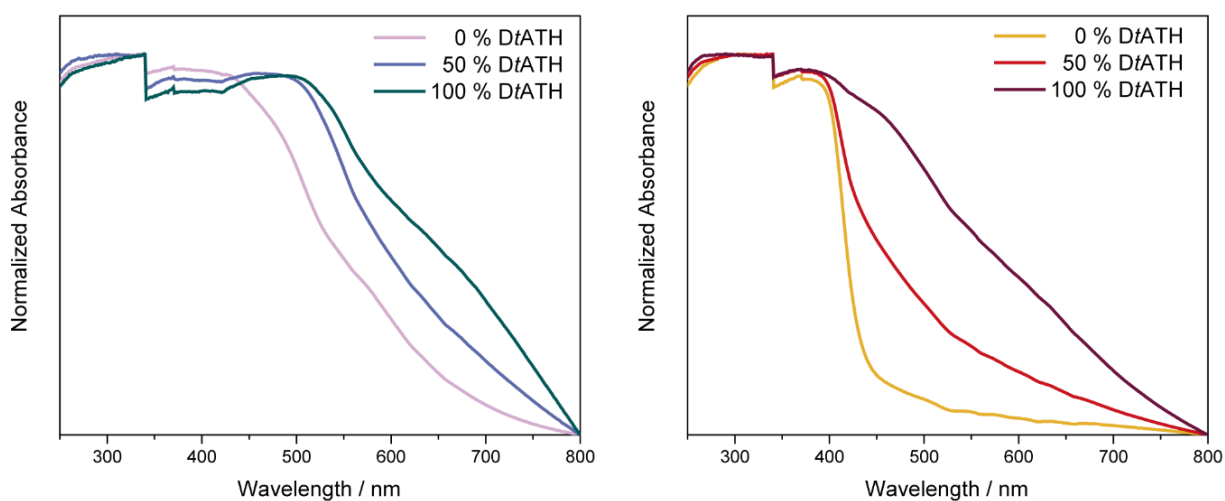


Figure 6-58: UV/Vis absorption spectra of Amine-coCOF-OH (left, blue) and Amine-coCOF-H (right, red). Darker color indicates higher amount of DtATH.

Additional sorption measurements

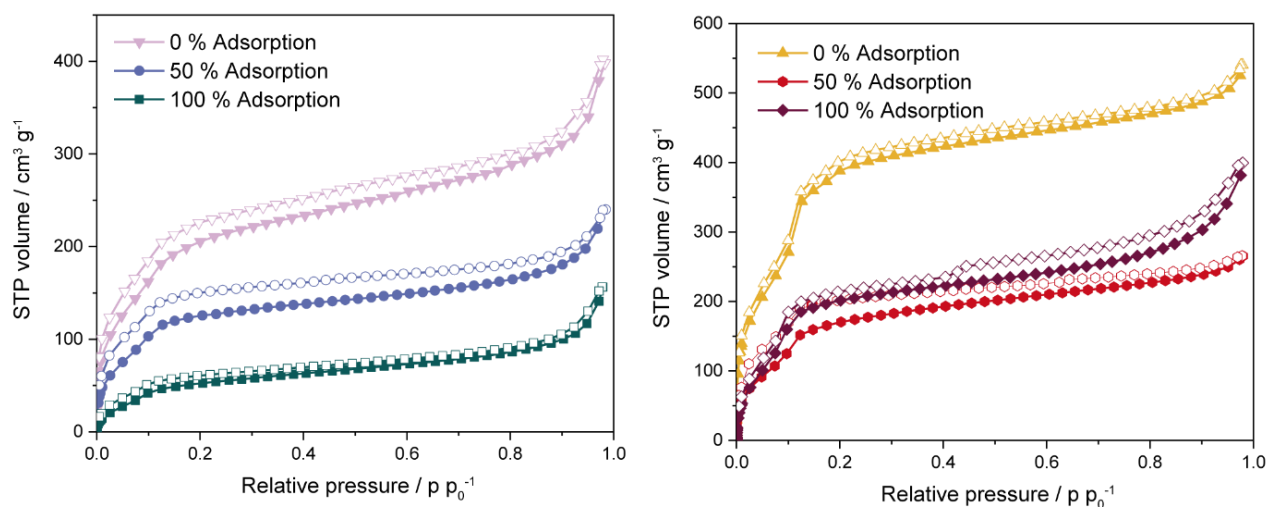


Figure 6-59: Argon sorption isotherms of Amine-coCOF-OH (left, blue) and Amine-coCOF-H (right, red). Darker color indicates higher amount of DtATH. Adsorption is represented by filled symbols, desorption by open symbols.

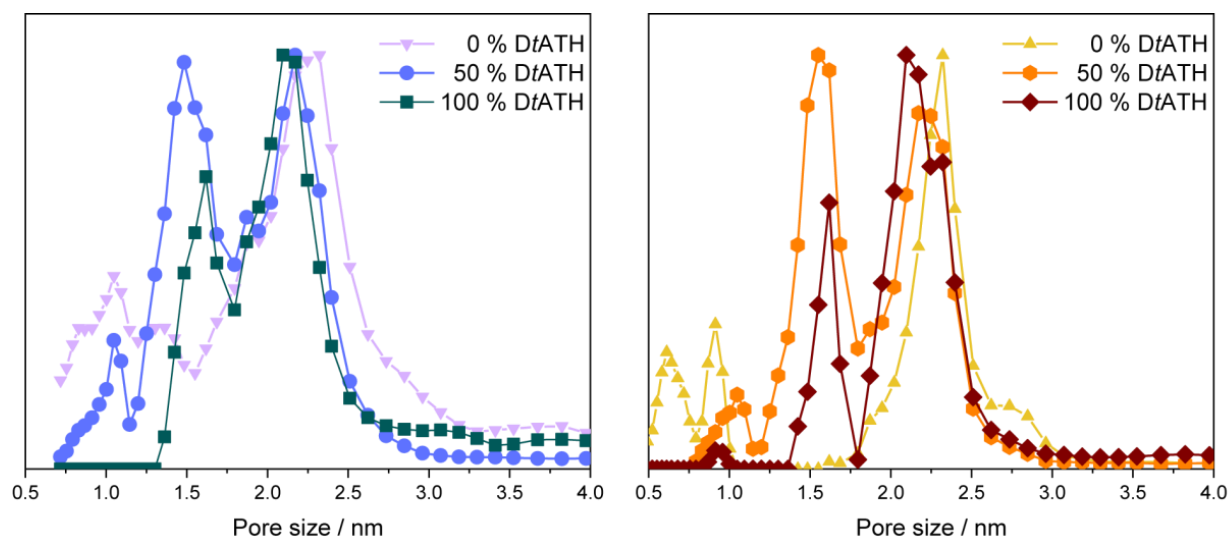


Figure 6-60: Pore size distribution derived from argon isotherms of Amine-coCOF-OH (left, blue) and Amine-coCOF-H (right, red). Darker color indicates higher amount of DtATH.

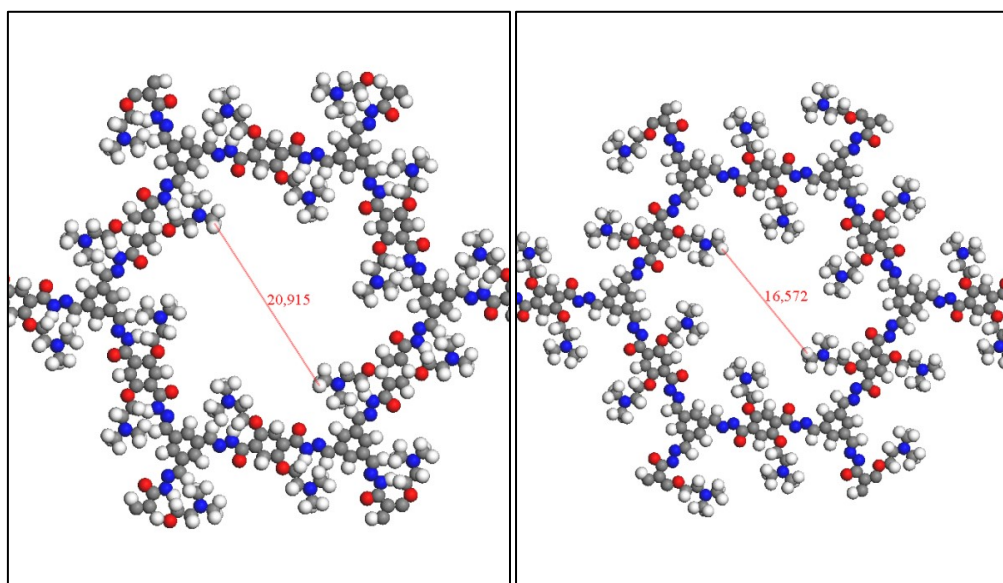


Figure 6-61: Model for one pore of 100% Amine-coCOF-H. Left: amine side chains at pore walls. Right: amine side chains protruding the pores. C, N, H, and O are represented in grey, blue, white, and red. Smallest pore diameter is marked by red line.

Table 6-14: Pore sizes, pore volume ($\text{cm}^3 \text{g}^{-1}$) and pore volume fractions (%) of the presented COFs.

COF system	Amount of DfATH	Pore size [nm]	Pore volume ($\text{cm}^3 \text{g}^{-1}$)	Pore volume fraction (%) ^a
Amine-coCOF-H	0%	2.4	0.28	65
		0.92	0.032	7.4
		0.61	0.036	8.3
	50%	2.24	0.090	36
		1.62	0.067	27
		1.05	0.0067	2.7
100%	2.09	0.13	59	
	1.62	0.04	17	
Amine-coCOF-OH	0%	2.3	0.086	55
		0.91	0.041	26
		0.61	0.025	16
	50%	2.17	0.070	39
		1.48	0.052	29
		1.04	0.0073	4.1
	100%	2.16	0.034	56
		1.62	0.0095	16

^a From 0.0 to 2.7 nm pore size.

Heats of adsorption

Heats of Adsorption were calculated from Henry's law. At low surface excess concentration, the dilute adsorbate phase is treated as a two-dimensional ideal gas. The relation is given by

$$n = k_H p$$

Where k_H is the Henry's law constant and n represents the specific surface excess amount. By modeling adsorption in the low-pressure region via a virial-type equation, Henry's law constants can be calculated.

$$\ln\left(\frac{n}{p}\right) = K_0 + K_1 n + K_2 n^2 + \dots$$

With $k_H = \lim_{n \rightarrow 0} \left(\frac{n}{p}\right)$, Henry's law constant is obtained from the zero-order virial coefficient $K_0 = \ln(K_H)$. With CO₂ adsorption measurements at 273, 287, and 295 K, Henry's law constants for each temperature were identified. The differential enthalpy of adsorption at zero coverage Δh_0 was then calculated from the Van't Hoff equation.

$$\Delta h_0 = R \left(\frac{\partial \ln[k_H]}{\partial \left(\frac{1}{T}\right)} \right)_n$$

By plotting $\ln[k_H]$ versus $\frac{1}{T}$ and linearly fitting, the zero coverage enthalpy is equal to the slope of the fit multiplied by the ideal gas constant R .

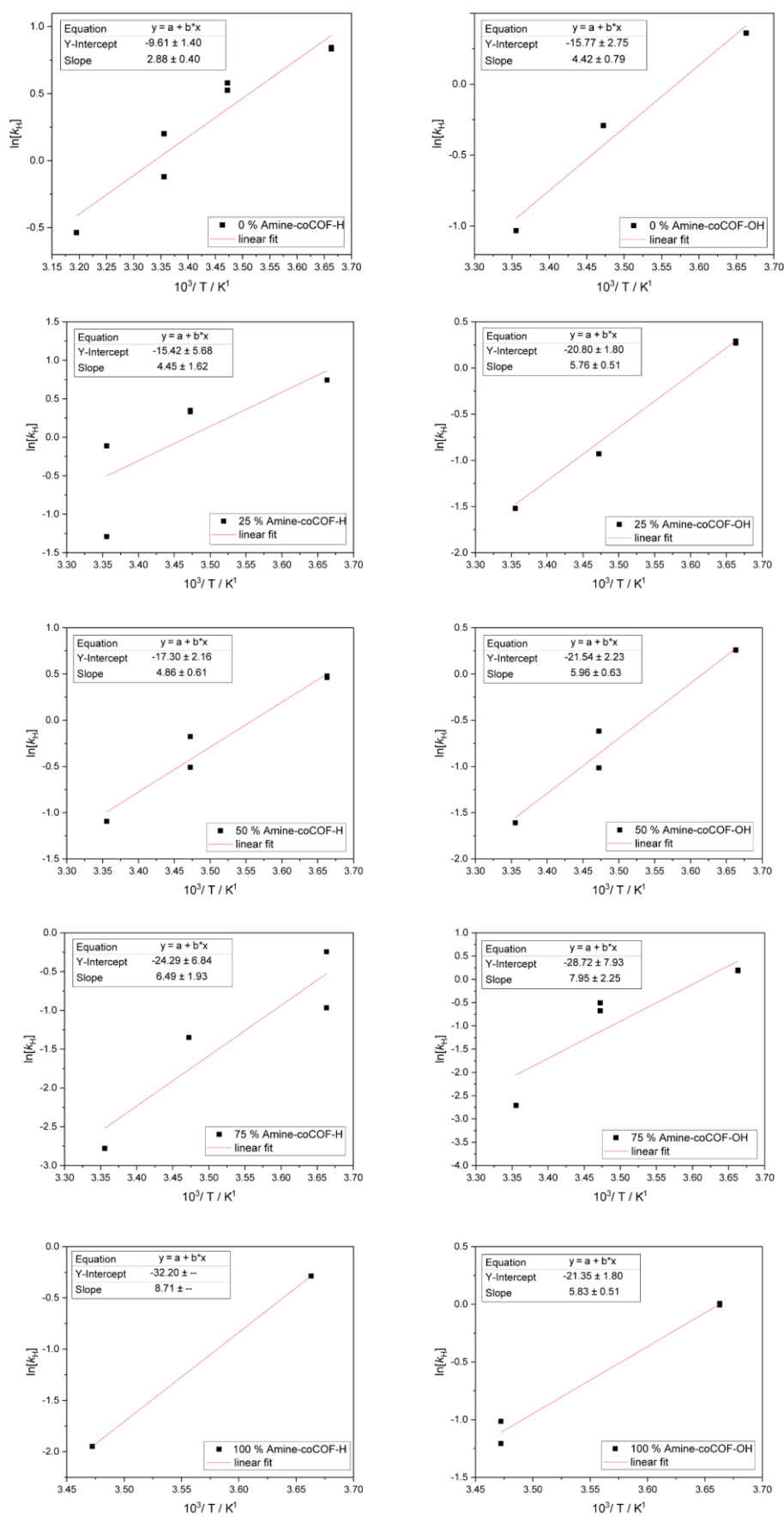


Figure 6-62: Linear fits of the van't Hoff equation for the different coCOF-systems and amine amounts.

Additional NMR measurements

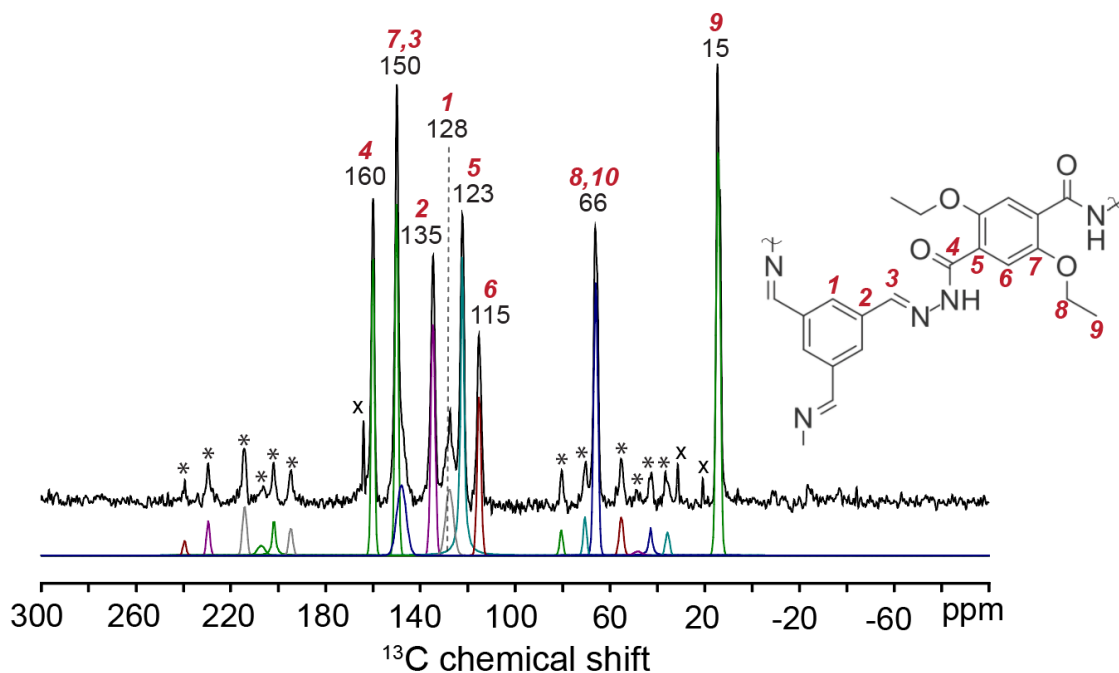


Figure 6-63: Spectral deconvolution of coCOF-H with spinning side-bands and solvent impurities indicated by asterisks and crosses respectively.

As shown by the 1D $^{13}\text{C}\{^1\text{H}\}$ DNP-CP MAS spectra in Fig. S9(a,b), the ^{13}C amide signal (orange band) has stronger intensity for the longest CP contact time of 5 ms. Although ^{13}C -depleted glycerol was used in the DNP solvent formulation, there is a small intensity shoulder ranging from 65 to 80 ppm from dilute amounts of ^{13}C -containing glycerol. By comparison, the 1D $^{13}\text{C}\{^1\text{H}\}$ LTMAS-CP MAS spectra in Fig. S9(c,d) were acquired on vacuum-dried 100%-amine-coCOF-H upon exposure to dry 100% ^{13}C -enriched CO_2 , before and after a subsequent degassing step. As discussed in the materials section, these materials were characterized without DNP to minimally influence adsorbed CO_2 . Under otherwise identical conditions, there is significantly more ^{13}C signal at 160 ppm for the material exposed to ^{13}C -enriched CO_2 . In the 1D spectra the adsorbed bicarbonate (red band) and amide have overlapping signal intensity at 160 ppm, however for short contact times (500 μs) signal contributions from the amide are partially reduced.

Similarly, the 2D $^{13}\text{C}\{^1\text{H}\}$ DNP-HETCOR presented in Fig. S10a shows only weak correlated intensity from correlations between the ^{13}C amide signal (ca. 159 ppm) and ^1H aromatic signals (7.0 – 8.0 ppm). DNP-NMR can improve signal sensitivity by up to $\gamma_e/\gamma_{^1\text{H}} = 658$ or $\gamma_e/\gamma_{^{15}\text{N}} = 6,500$ for ^1H and ^{15}N nuclei respectively. Compared to Figure 6b in the main text, the 2D $^{13}\text{C}\{^1\text{H}\}$ DNP-HETCOR spectra depicted in Figure S10a has significantly improved signal-to-noise and resolves two additional ^{13}C signals at 21 and 32 ppm from residual ethoxy linker moieties. The ^{13}C signal at 159 ppm from framework amide moieties in both Figure S10a and Figure 6b exhibits weak $^{13}\text{C}\{^1\text{H}\}$ -correlated intensities due to the short CP contact time (500 μs). Similarly, in Figure 6a in the main text, the absence of correlated 2D intensity associated with bicarbonate ^1H species and ^{13}C moieties (1.1% natural abundance) in the 100%-amine-coCOF-H framework is explained by the low absolute

quantity of these dipolar-coupled spin pairs in comparison to the quantity of spin pairs arising from ^{13}C moieties in $^{13}\text{C}\text{-CO}_2$ and ^1H species in the COF framework. Importantly, as depicted in Figure S10b, DNP-NMR enables the acquisition of 1D and 2D $^{15}\text{N}\{^1\text{H}\}$ natural abundance spectra in low- ^1H containing COF materials which would otherwise be infeasible. In Figure S10b, the tertiary amine linker moieties with ^{15}N signals at 24 and 36 ppm and the framework amide ^{15}N signal at 181 ppm are strongly correlated to ^1H signals at ca. 4.0 ppm, which arise from H_2O adsorbed in the COF pore or introduced by the DNP solvent. All five ^{15}N signals have correlated intensity with aromatic or hydrazone ^1H moieties ranging from 7 – 8 ppm. Lastly, weakly correlated $^{15}\text{N}\{^1\text{H}\}$ intensity between the amide ^{15}N signal at 181 ppm and a ^1H signal at 11.7 ppm is consistent with the ^1H chemical shift measured for compound (6). Overall, the DNP-enhanced 2D $^{13}\text{C}\{^1\text{H}\}$ and $^{15}\text{N}\{^1\text{H}\}$ HETCOR spectra confirm that the local structure of the COF framework is retained on addition of the tertiary amine linker moieties, consistent with the analyses presented in the main text.

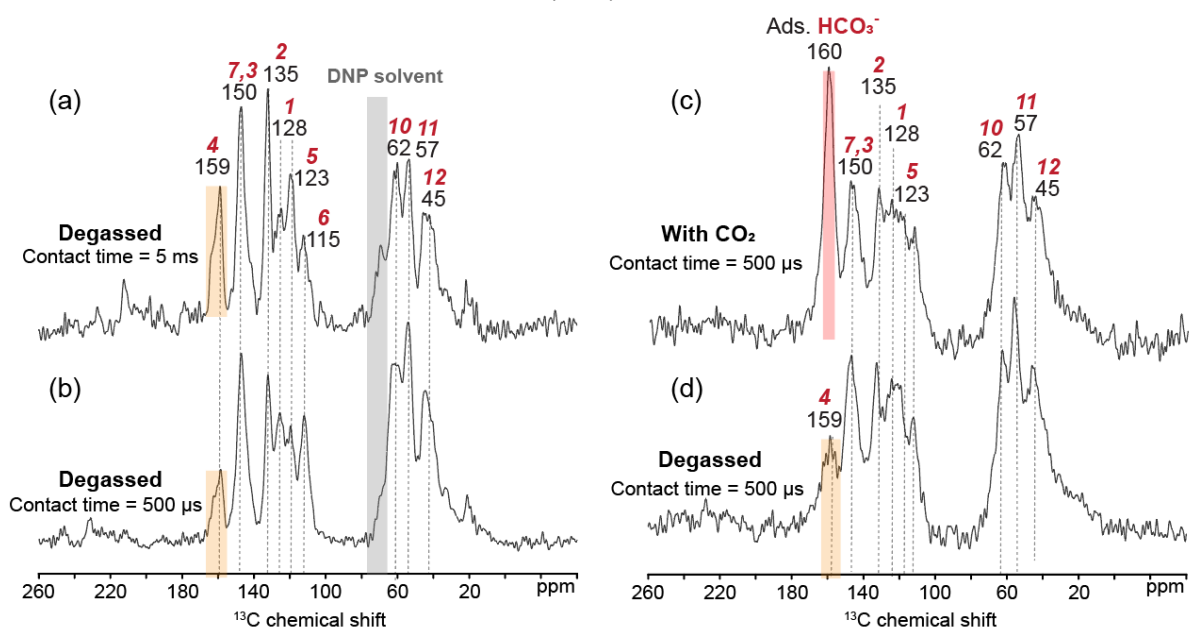


Figure 6-64: Vacuum dried 100%-amine-coCOF-H solid-state 1D $^{13}\text{C}\{^1\text{H}\}$ DNP-CP MAS spectra using a cross-polarization contact time of (a) 5 ms, and (b) 500 μs respectively. DNP-CP MAS spectra were acquired with 16 scans at 9.4 T, 8 kHz MAS, 95 K in the presence of 16 mM AMUPOL biradical in 60:30:10 $\text{d}_8\text{-glycerol}$ (^{13}C -depleted): $\text{D}_2\text{O}:\text{H}_2\text{O}$, under microwave irradiation at 263 GHz. Solid-state 1D $^{13}\text{C}\{^1\text{H}\}$ LTMAS-CP MAS spectra acquired with 256 scans and a cross-polarization contact time of 500 μs for 100%-Amine-coCOF-H (c) after exposure to 100% ^{13}C -enriched CO_2 for 12 h at 1 bar pressure and 298 K, and (d) after desorption of CO_2 for 48 h by vacuum heating at 0.1 bar and 363 K.

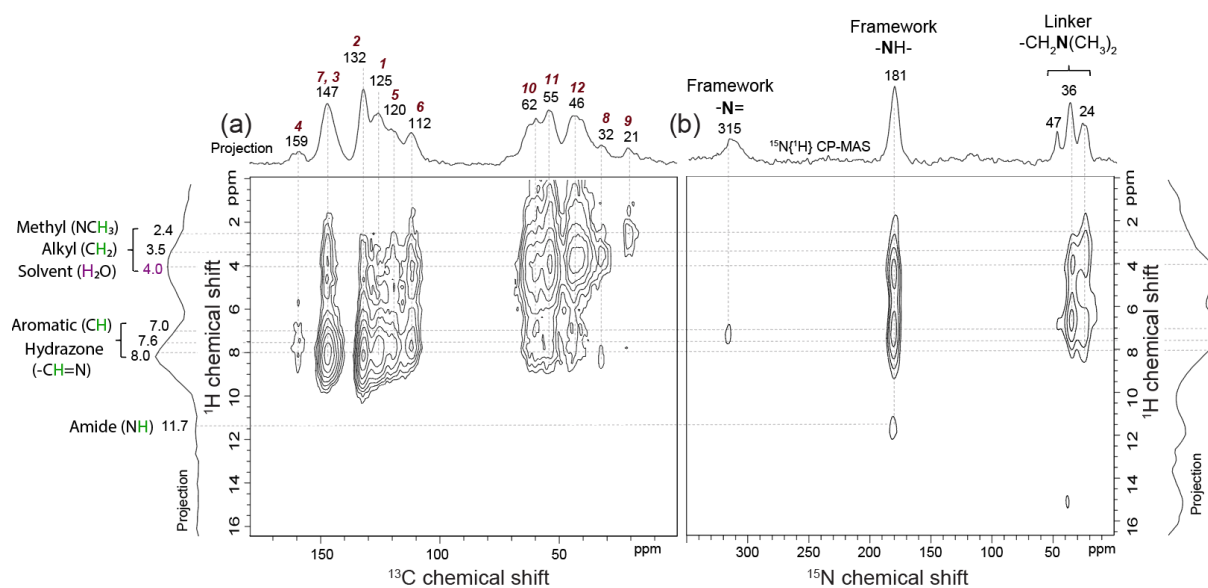


Figure 6-65: Vacuum-dried 100%-amine-coCOF-H (a) solid-state 2D $^{13}\text{C}\{^1\text{H}\}$ DNP-HETCOR spectra using cross-polarization contact time of 500 μs (b) and solid-state 2D $^{15}\text{N}\{^1\text{H}\}$ DNP-HETCOR spectra using cross-polarization contact time of 5 ms. The spectra were acquired at 9.4 T, 8 kHz MAS, 95 K in the presence of 16 mM AMUPOL biradical in 60:30:10 d_8 -glycerol (^{13}C -depleted): $\text{D}_2\text{O}:\text{H}_2\text{O}$, under microwave irradiation at 263 GHz. With DNP sensitivity enhancements weak $^{13}\text{C}\{^1\text{H}\}$ -correlated signal intensity is observed from residual pendant ethyl ether moieties in unmodified coCOF-H.

Quantum chemical calculations

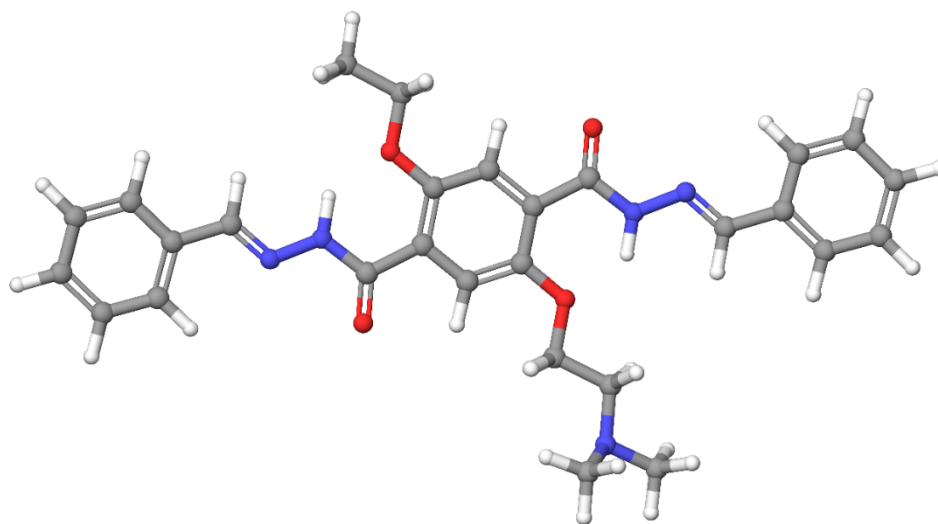


Figure 6-66: Optimized geometry for the DETH-M model system obtained on PBE0-D3/def2-TZVP level of theory.

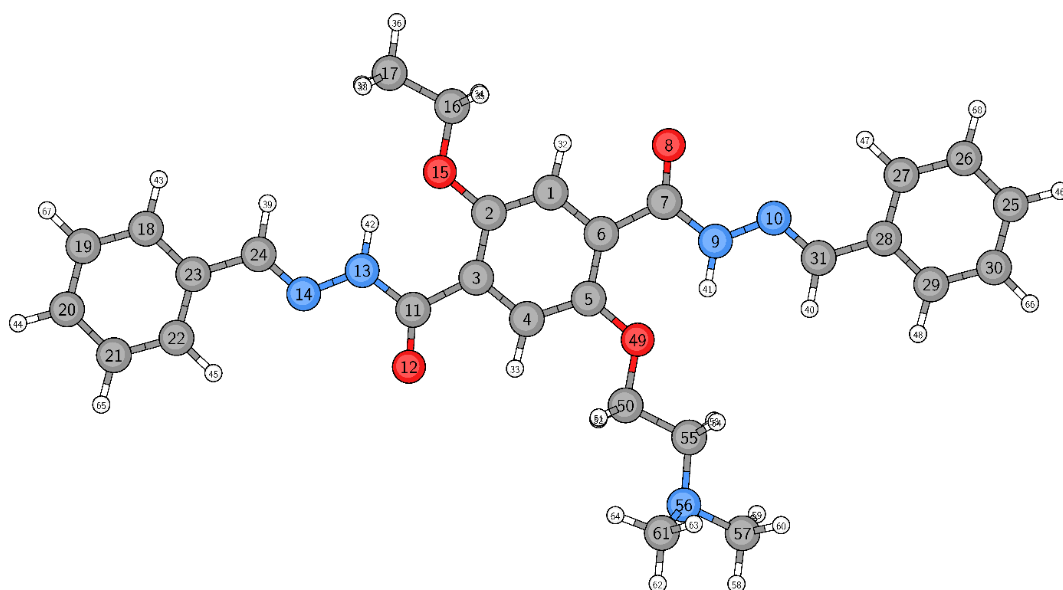


Figure 6-67: Atom labels for the DETH-M model system based on the optimized geometry, obtained on PBE0-D3/def2-TZVP level of theory.

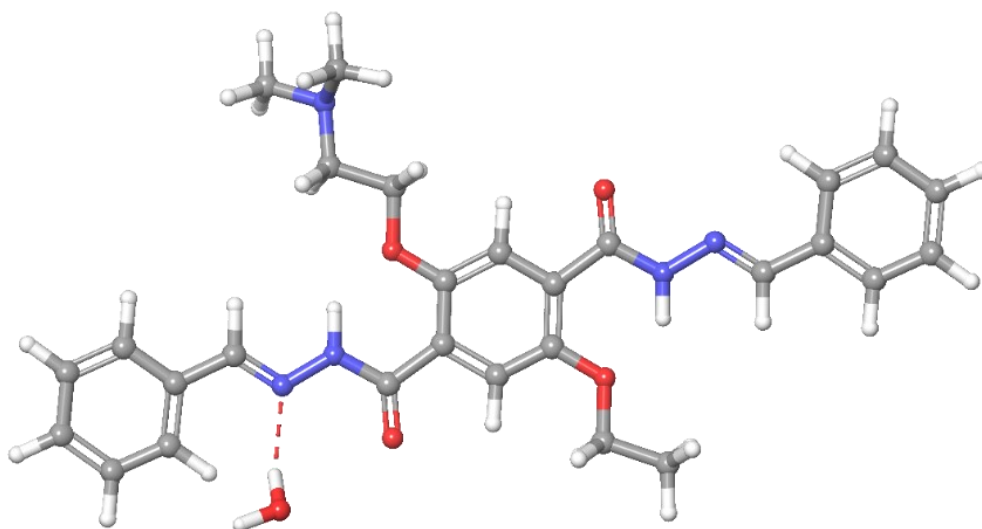


Figure 6-68: Optimized geometry for modeled DETH-M model system, including a single water molecule hydrogen bonded to carbonyl and imine bond, on obtained on PBE0-D3/def2-TZVP level of theory.

Table 6-15: Calculated ^{13}C NMR Chemical Shifts for the DETH-M model system, obtained on B97-2/pcS-2//PBE0-D3/def2-TZVP level of theory.

Atom number	Atom Type	NMR Chemical Shift [ppm]
18, 29	aromatic	137.0
23, 28	aromatic, bridge	143.5
24, 31	-CH=N-	149.3
11, 7	C=O	165.5
3, 6	central aromatic bridge	130.7
4, 1	aromatic C-H	122.9
5, 2	aromatic C-O	158.3
16	O-CH ₂ -	69.3
17	-CH ₃	18.3
50	-O-CH ₂ -	72.3
55	-CH ₂ -CH ₂ -N-	63.1
57, 61	-N-CH ₃	51.9

Table 6-16: Calculated ^{15}N NMR Chemical Shifts for the DETH-M model system, obtained on B97-2/pcS-2//PBE0-D3/def2-TZVP level of theory.

Atom number	Atom Type	NMR Chemical Shift [ppm]	
		IUPAC Nitromethane scale	liq. NH ₃ scale
9, 13	-NH-	-201.8	178.7
10, 14	-N=	-50.4	330.1
	-N= · H ₂ O	-62.0	318.5
56	-N(Me) ₂	-367.4	13.1

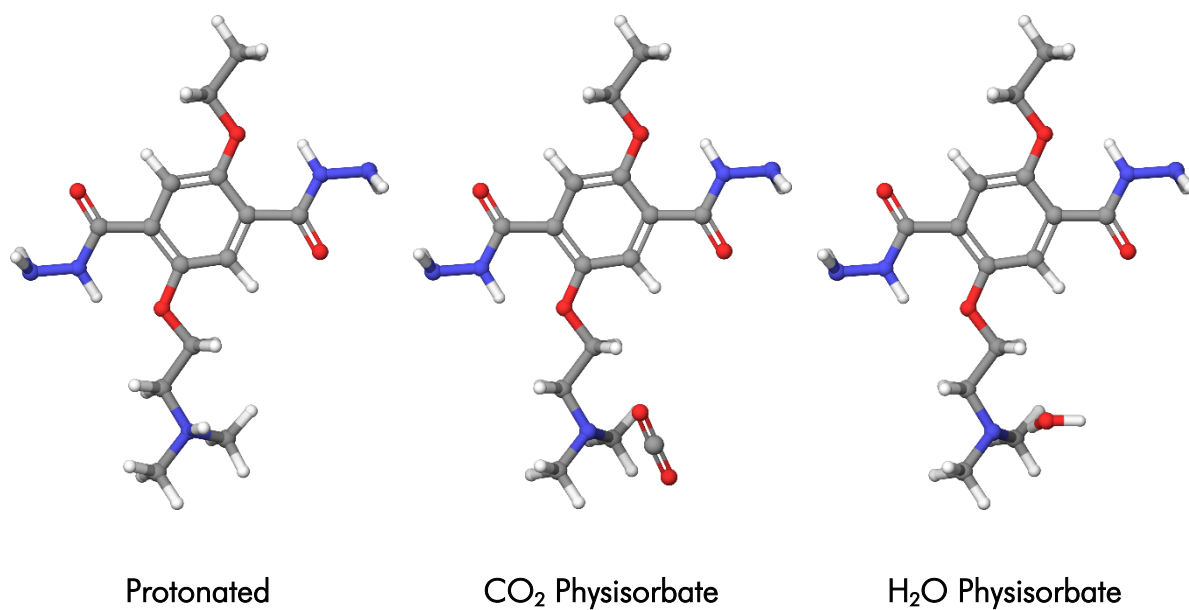


Figure 6-69: Optimized geometries for modeled DETH monomer modifications, obtained on PBE0-D3/def2-TZVP level of theory.

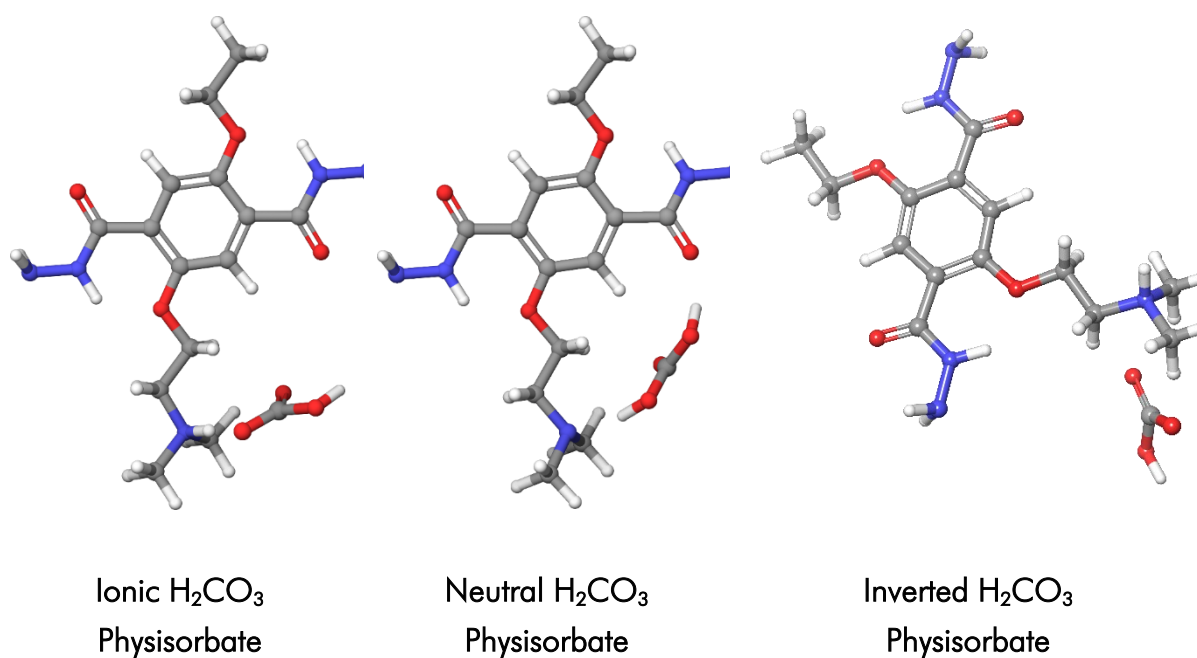


Figure 6-70: Optimized geometries for modeled physisorbates of carbonic acid to the DETH monomer, obtained on PBE0-D3/def2-TZVP level of theory.

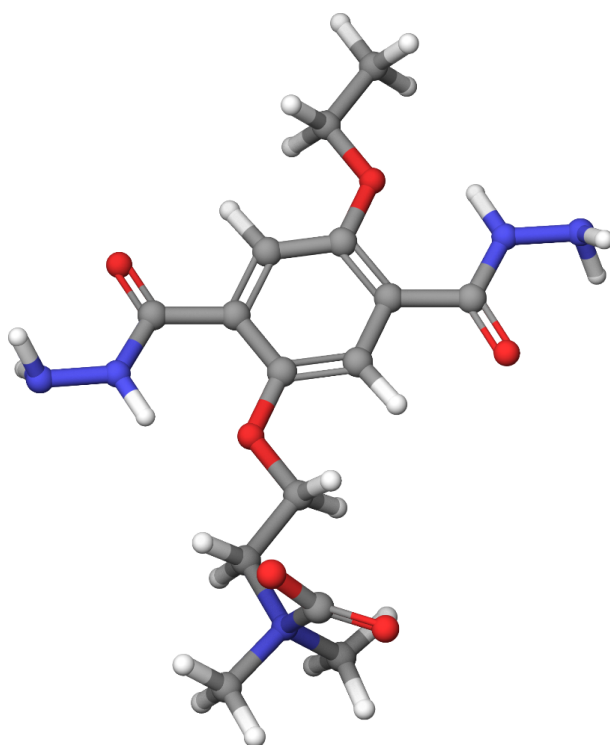


Figure 6-71: Optimized geometry for the modeled chemisorbate of CO₂ to the DETH monomer, obtained on PBE0-D3/def2-TZVP level of theory.

Table 6-17: Calculated ¹H NMR Chemical Shifts for the modeled DETH monomer modifications, obtained on B97-2/pcS-2//PBE0-D3/def2-TZVP level of theory.

Model	Atom Type	NMR Chemical Shift [ppm]
Ionic H ₂ CO ₃ physisorbate	HCO ₃ ⁻	5.0
	R-NH-(CH ₃) ₂	15.4
Neutral H ₂ CO ₃ physisorbate	R-N-(CH ₃) ₂ ...HCO ₃ H	11.1
	R-N-(CH ₃) ₂ ...HCO ₃ H	10.6

Table 6-18: Calculated ¹³C NMR Chemical Shifts for the modeled DETH monomer modifications, obtained on B97-2/pcS-2//PBE0-D3/def2-TZVP level of theory.

Model	Atom Type	NMR Chemical Shift [ppm]
Ionic H ₂ CO ₃ physisorbate	HCO ₃ ⁻	171.5
Neutral H ₂ CO ₃ physisorbate	H ₂ CO ₃	167.6



Table 6-19: Calculated ^{15}N NMR chemical shifts for the modeled DETH monomer modifications, obtained on B97-2/pcS-2//PBE0-D3/def2-TZVP level of theory.

	NMR Chemical Shift [ppm]		Δ Reference
	IUPAC		
	Nitromethane scale	Liq. NH_3 scale	
Unmodified Reference	-367.69	12.81	0.00
Protonated	-335.81	44.69	31.88
CO_2 physisorbate	-365.18	15.32	2.51
H_2O physisorbate	-363.21	17.29	4.48
Ionic H_2CO_3 physisorbate	-358.50	22.00	9.19
Neutral H_2CO_3 physisorbate	-362.52	17.98	5.16
Inverted H_2CO_3 physisorbate	-345.50	35.00	22.19
CO_2 Chemisorbate	-306.79	73.71	60.90

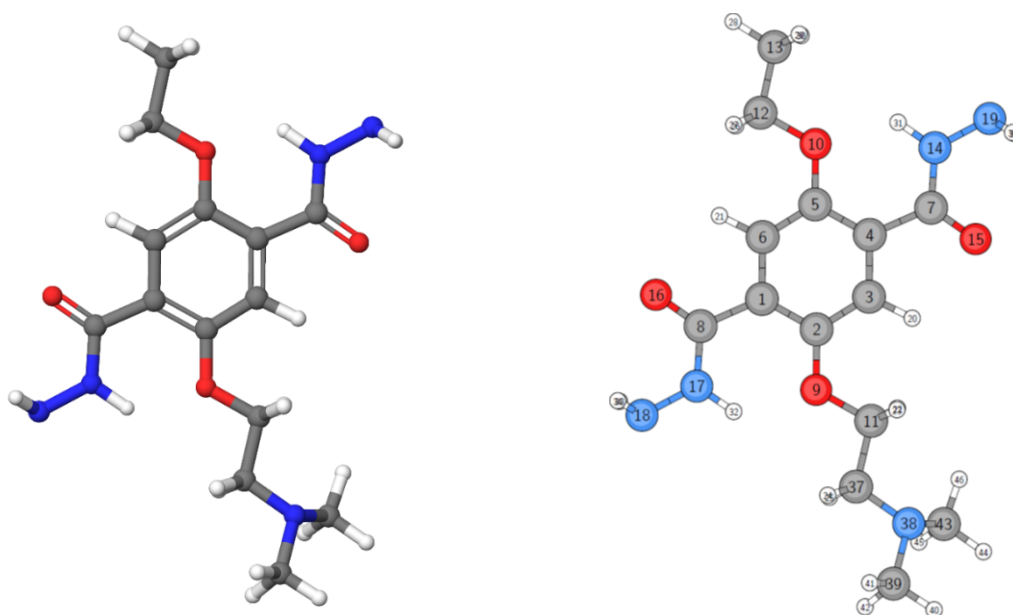


Figure 6-72: Optimized geometry for the DETH building block unit obtained on PBE0-D3/def2-TZVP level of theory. Corresponding atom labels are shown on the right.

Table 6-20: Calculated ^{15}N NMR Chemical Shifts for the DETH building block unit, obtained on B97-2/pcS-2//PBE0-D3/def2-TZVP level of theory.

Atom number	Atom Type	NMR Chemical Shift [ppm]	
		IUPAC Nitromethane scale	liq. NH_3 scale
14, 17	-NH-	-254.8	125.7
18, 19	-NH ₂	-342.4	38.1

38

-N(Me)₂

-367.7

12.8

6.1.4 Supporting References

- [1] J. P. Perdew, K. Burke, M. Ernzerhof, *Phys. Rev. Lett.* **1996**, *77*, 3865-3868.
- [2] S. Grimme, J. Antony, S. Ehrlich, H. Krieg, *The Journal of Chemical Physics* **2010**, *132*, 154104.
- [3] A. Schäfer, C. Huber, R. Ahlrichs, *The Journal of Chemical Physics* **1994**, *100*, 5829-5835.
- [4] K. Eichkorn, F. Weigend, O. Treutler, R. Ahlrichs, *Theoretical Chemistry Accounts: Theory, Computation, and Modeling (Theoretica Chimica Acta)* **1997**, *97*, 119-124.
- [5] A. M. Burow, M. Sierka, F. Mohamed, *The Journal of Chemical Physics* **2009**, *131*, 214101-214101.
- [6] L. Grajciar, *J. Comput. Chem.* **2015**, *36*, 1521-1535.
- [7] A. M. Burow, M. Sierka, *Journal of Chemical Theory and Computation* **2011**, *7*, 3097-3104.
- [8] R. Łazarski, A. M. Burow, M. Sierka, *Journal of Chemical Theory and Computation* **2015**, *11*, 3029-3041.
- [9] R. Łazarski, A. M. Burow, L. Grajciar, M. Sierka, *J. Comput. Chem.* **2016**, *37*, 2518-2526.
- [10] TURBOMOLE, developer version based on version V7.1 2017, a development of University of Karlsruhe and Forschungszentrum Karlsruhe GmbH, 1989-2007, TURBOMOLE GmbH, since 2007; available from <http://www.turbomole.com>.
- [11] J. Wang, W. Wang, P. A. Kollman, D. A. Case, *J. Mol. Graphics Modell.* **2006**, *25*, 247-260.
- [12] J. C. Phillips, R. Braun, W. Wang, J. Gumbart, E. Tajkhorshid, E. Villa, C. Chipot, R. D. Skeel, L. Kalé, K. Schulten, *J. Comput. Chem.* **2005**, *26*, 1781-1802.
- [13] in D.A. Case, R.M. Betz, D.S. Cerutti, T.E. Cheatham, III, T.A. Darden, R.E. Duke, T.J. Giese, H. Gohlke, A.W. Goetz, N. Homeyer, S. Izadi, P. Janowski, J. Kaus, A. Kovalenko, T.S. Lee, S. LeGrand, P. Li, C. Lin, T. Luchko, R. Luo, B. Madej, D. Mermelstein, K.M. Merz, G. Monard, H. Nguyen, H.T. Nguyen, I. Omelyan, A. Onufriev, D.R. Roe, A. Roitberg, C. Sagui, C.L. Simmerling, W.M. Botello-Smith, J. Swails, R.C. Walker, J. Wang, R.M. Wolf, X. Wu, L. Xiao and P.A. Kollman (2016), AMBER 2016, University of California, San Francisco.
- [14] J. Wang, R. M. Wolf, J. W. Caldwell, P. A. Kollman, D. A. Case, *J. Comput. Chem.* **2004**, *25*, 1157-1174.
- [15] P. J. Wilson, T. J. Bradley, D. J. Tozer, *The Journal of Chemical Physics* **2001**, *115*, 9233-9242.
- [16] F. Jensen, *Journal of Chemical Theory and Computation* **2014**, *11*, 132-138.
- [17] J. Kussmann, C. Ochsenfeld, *Journal of Chemical Theory and Computation* **2015**, *11*, 918-922.
- [18] J. Kussmann, C. Ochsenfeld, *The Journal of Chemical Physics* **2013**, *138*, 134114.
- [19] F. Jensen, *Journal of Chemical Theory and Computation* **2006**, *2*, 1360-1369.
- [20] F. Weigend, M. Häser, H. Patzelt, R. Ahlrichs, *Chem. Phys. Lett.* **1998**, *294*, 143-152.
- [21] F. Weigend, *PCCP* **2006**, *8*, 1057-1065.



- [22] R. Ahlrichs, M. Bär, M. Häser, H. Horn, C. Kölmel, *Chem. Phys. Lett.* **1989**, *162*, 165-169.

6.2 List of figures

- Figure 1-1: Solar energy is transformed into thermal, electrical, or chemical energy by different techniques. Further, these types of energy can be converted into each other. 2
- Figure 1-2: Schematic representation of three different approaches for carbon dioxide separation – post-combustion, pre-combustion and oxy-fuel combustion. 4
- Figure 1-3: Possible pore structures and shapes in porous materials. Accessibility: (a) closed pores, (c) – (f) open pores, (b) and (f) blind pores, (e) through pores; shape: (b) inkbottle shaped, (c) cylindrical open, (d) funnel shape, (f) cylindrical blind, (g) roughness.^[19] 6
- Figure 1-4: (a) Schematic structure of Zeolite A consisting of cubes (green), truncated octahedra (orange) and truncated cuboctahedra (yellow). Reprinted from ^[29]. (b) X-ray single crystal structure of ZIF-20. ZnN₄ tetrahedra are shown in blue. Both show LTA topology. Reprinted from ^[29] (c) X-ray single crystal structure of MOF-5 consisting of [OZn₄(CO₂)₆] clusters bridged by organic carboxylate linkers. ZnO₄ tetrahedra are shown in blue. Reprinted from ^[31]. 7
- Figure 1-5: Chronology of COF linkage units. 8
- Figure 1-6: Schematic examples of different building blocks used for COF synthesis. Framework morphologies resulting from different building block symmetries. 9
- Figure 1-7: Schematic representations of (a) boronic acid self-condensation, (b) boronic acid co-condensation, (c) borosilicate linking unit, and (d) spiroborate linking unit. 10
- Figure 1-8: Schematic representation of the condensation of an aromatic amine and aromatic aldehyde to form an imine bond. 11
- Figure 1-9: Condensation of aniline **A** with benzaldehyde **B** forms the molecular N-benzylidene-aniline **C**. Condensation of divergent **D** with ditopic **E** leads to the rod-like bis-imines **F** which will join together the tetrahedral building blocks to give the diamond structure of COF-300: **G** single framework (space filling, C gray and pink, N green, H white) and **H** representation of the dia-c5 topology. Reprinted from ^[61]. 12
- Figure 1-10 (a) Synthesis of azine-linked COFs by the acetic acid catalyzed condensation reaction between the pyrene-based aldehyde linkers and hydrazine. (b) Ball-and-stick model of the shifted AA' arrangement of A-TEBPY-COF. All COFs in this series adopt similar stackings. Reprinted from ^[52]. 13
- Figure 1-11: Cartoon representation for the synthesis of dual-pore and triple-pore COFs. Reprinted from ^[73]. 14



- Figure 1-12: Schematic representation of the keto-enol-tautomerism used in COF formation. The imine form (left) reacts to form the more stable ketoenamine form (right)..... 15
- Figure 1-13: (a) Chemical structure of COF-42. Chemical structures of (b) 2,5-diethoxyterephthalohydrazide and (c-g) a selection of its modifications. 17
- Figure 1-14: Acetic acid-catalyzed azine formation furnishes two microporous honeycomb frameworks. (a) Scheme shows the condensation of hydrazine and 1,3,5-triformylbenzene to AB-COF. (b) The condensation of the two monomers to AFG-COF results in two different tautomers: OH (left) and NH (right). (c) Structure representation of AB-COF with quasi-eclipsed layer stacking; (d) a mixture of both OH and NH tautomers within AFG-COF with quasi-eclipsed layer stacking, and structure of the OH and NH tautomers (red, oxygen; blue, nitrogen; black, carbon; white, hydrogen). Reprinted from ^[101]..... 18
- Figure 1-15: Synthesis and structures of the olefin-linked 2D conjugated polymer framework (2DPPV). (i) Argon, cesium carbonate, 1,2-dichlorobenzene, 150 °C, 3 days. Reprinted from ^[120] - Published by The Royal Society of Chemistry. 20
- Figure 1-16: Postsynthetic modification of COFs can be realized via metal complexation, covalent linker modification, linker exchange, or linkage conversion. 21
- Figure 1-17: Schematic representation of metal complexation strategies. (a) Metal complexation in the COF sheet, (b) confinement of metal nanoparticles in the COF pores, (c) complexation of metal between COF sheets, and (d) metal nanoparticles on the outer COF surface..... 22
- Figure 1-18: Possible linkage conversion strategies for imine-linked COFs. Formation of (a) amide linkage, (b) benzoxazole linkage, (c) thiazole linkage, and (d) an aza-Diels-Alder COF. 24
- Figure 1-19: Schematic representation of (a) copper-click reaction, (b) thiol-ene click reaction, and (c) aminolysis of acetic anhydride. 26
- Figure 1-20: (a) Basic principle of overall water splitting. After excitation, charge carriers migrate to the surface to react with surface bound co-catalysts and water. Hydrogen and oxygen are generated. (b) Simplified reaction conditions to evaluate the hydrogen evolution reaction. A sacrificial donor is introduced to trap generated holes by oxidation. NHE is standard hydrogen electrode..... 27
- Figure 1-21: Acetic acid catalyzed hydrazone formation furnishes a mesoporous 2D network with a honeycomb-type in-plane structure. (a) Scheme showing the condensation of the two monomers to form the TFPT-COF. (b) TFPT-COF with a cofacial orientation of the aromatic building blocks, constituting a close-to eclipsed primitive hexagonal lattice (grey: carbon, blue: nitrogen, red: oxygen). Reprinted from [14]..... 28

- Figure 2-1: Types of physisorption isotherms according to IUPAC recommendation. Reprinted from [2]. 40
- Figure 2-2: Schematic representation of the magic angle (54.7°). Rapid spinning of the sample about this axis averages the dipolar interactions..... 45
- Figure 2-3: Schematic representation of thin film synthesis methods used in this thesis. Solvothermal synthesis in autoclave reactors (left), in which the wafer (dark blue) is placed floating in the synthetic mixture. Interfacial synthesis (right), where material deposition is carried out by lifting the substrate through the interface..... 46
- Figure 3-1: Artificial Photosynthetic Water Splitting. SED, sacrificial electron donor; WOC, water oxidation catalyst; PA, photoabsorber; HEC, hydrogen evolution catalyst. 53
- Figure 3-2: Photocatalytic H_2 evolution with metallic Pt (left) and molecular co-catalysts (right). The sacrificial electron donor molecules have been omitted for clarity. 54
- Figure 3-3: Molecular structure (a) of the TFPT-COF hexagonal pore as seen by TEM at 300 kV (b). Visible light-mediated H_2 evolution (c) with TFPT-COF using sodium ascorbate donor and Pt co-catalyst. The inset shows H_2 evolution using TEOA as an electron donor. Photodeposited Pt nanoparticles (d) on TFPT-COF after photocatalysis for 84 h. Adapted with permission from ref 36. Copyright 2014 Royal Society of Chemistry. 55
- Figure 3-4: Molecular structure (a) of the hexagonal pore of N_x - and PTP-COF. For the N_x -COFs, the crystallinity increases gradually from N_0 - to N_3 -COF as seen in the PXRD pattern (b). The H_2 evolution rate with Pt co-catalyst and TEOA donor (c) analogously increases by 4 times for every additional N atom in the central aryl ring. The stability of the radical anion consonantly increases (d) as one goes from N_0 - to N_3 -COF. Four different conformations are possible around torsion angle A in PTP-CHO (e) as opposed to only two around torsion angle C in N_3 -CHO. Additional D–A type interactions (f) and H-bonding interactions (g) can be seen in single-crystal structure solutions of PTP-H. All of these possibly contribute to the lower crystallinity of PTP-COF. Panels a–d are adapted with permission from ^[41]. Copyright 2015 by Nature Publishing Group. Panels e–g are adapted with permission from ^[42]. Copyright 2017 Royal Society of Chemistry. 57
- Figure 3-5: Representative variables that need to be optimized for maximizing photocatalytic H_2 evolution efficiency of COF-based systems..... 62
- Figure 3-6: (a) Photocatalytic H_2 evolution with N_2 -COF and **Co-1**, (b) H_2 evolution rates with the N_x -COFs and with COF-42 photosensitizers using **Co-1** co-catalyst and TEOA donor, and (c) spectrophotometrically monitoring the reduced Co^{II} state and subsequent formation of the Co^I and/or $H-Co^{III}$ state using COF-42 and **Co-1** co-catalyst. (d) The paramagnetic Co^{II} state formed during photocatalysis can be



- observed in the X-band EPR spectrum. (e) The $\text{Co}^{\text{III}}\text{-H}$ and/or the $\text{Co}^{\text{II}}\text{-H}$ species are shown to produce H_2 by a heterolytic pathway involving a single cobalt center in the reaction involving $\text{N}_2\text{-COF}$ and **Co-1** co-catalyst. Reprinted from [60]. Copyright 2017 American Chemical Society..... 65
- Figure 3-7: Structures of $\text{N}_2\text{-COF}$ and the cobaloxime co-catalysts used in this study. Schematic representation of photocatalytic H_2 evolution with $\text{N}_2\text{-COF}$ and **Co-1** is shown on the left..... 71
- Figure 3-8: (a) H_2 evolution using $\text{N}_2\text{-COF}$ and **Co-1** (see text for details) as well as $\text{N}_2\text{-COF}$ and metallic platinum (5 μL of 8 wt% H_2PtCl_6 solution in water) in the presence of TEOA, when irradiated with 100 mW cm^{-2} AM 1.5 light. Control experiments in absence of either of the three components, with all other conditions being the same, show no H_2 evolution in 3 h. (b) H_2 evolution using optimized parameters, 5 mg of $\text{N}_2\text{-COF}$ dispersed in 10 mL of 4:1 ACN/ H_2O solvent together with 100 μL of TEOA, 400 μL of a 2.48 mM solution of **Co-1** in ACN, and 4.69 mM dmgH_2 at a final pH of 8. The reaction mixture is illuminated with 100 mW cm^{-2} AM 1.5 light. 72
- Figure 3-9: (a) H_2 evolution with $\text{N}_2\text{-COF}$ and different co-catalysts. The co-catalyst concentration is 0.1 mM in all measurements. All other conditions are the same including a pH of 10. (b) H_2 evolution with different COFs at pH 8. 5 mg COF sample has been used in all the measurements. All other conditions are the same. Rates are 233, 390, 163, and 100 $\mu\text{mol g}^{-1} \text{h}^{-1}$ for COF-42, N_2 , N_3 and N_1 COFs, respectively. TON for the reaction with $\text{N}_2\text{-COF}$ is 10.89 at 6.5 h..... 76
- Figure 3-10: (a) ^{13}C CPMAS NMR spectra of $\text{N}_2\text{-COF}$ under different conditions. No change in chemical shift in the COF signals is seen. Please see Figure S12 for peak assignments. (b) ATR-IR spectra of $\text{N}_2\text{-COF}$ under different conditions. Again, no shift in the frequencies of the bands is seen. 77
- Figure 3-11: Constrained optimized geometry of (a) pore-diazene, (b) pore-diazene-90°, (c) surface-diazene, and (d) surface-triazine cobaloxime-COF models, obtained on the PBE0-D3/def2-SVP level of theory using the Turbomole program package. The surface-diazene and triazine models are for possible interactions on the surface of the COF microstructure. Other details of the calculations can be found in the Supporting Information. The dashed pink lines show the shortest Co-N distance obtained and are 4.197, 4.082, 2.792, and 3.00 Å, respectively, in panels a-d. 78
- Figure 3-12: (a) Red trace: UV-vis spectra of the degassed photocatalytic reaction dispersion containing 2.5 mg of COF-42, 50 μL of TEOA and 200 μL of **Co-1** (2.48 mM in ACN) in 5 mL 4:1 ACN/ H_2O mixture at pH 8 illuminated with 100 mW cm^{-2} AM 1.5 light. The reaction mixture was allowed to stand for 1 h after illumination before a spectrum was recorded. Blue trace: similar reaction conditions as before except at

- pH 10 of the reaction mixture and 5 equiv of externally added P(n-Bu)₃. The noise in the spectra is from the still suspended COF particles. (b) X-band EPR spectrum at 4K of the photocatalytic reaction dispersion containing COF-42 before and after illumination. The microwave frequencies are 9.47614 GHz in both cases. The reaction conditions are identical to those in Figure 5a. (c) H₂ evolution at 3 h after illumination under different [Co-1]. In all measurements, 5 mg of N₂-COF and 100 μL of TEOA in 10 mL of 4:1 ACN/H₂O has been used. The reaction pH is 8. 80
- Figure 3-13: (A) Synthesis of pCOF₁₀ by solvothermal condensation of triformyl benzene (TFB) and a 9:1 mixture of 2,5-diethoxyterephthalohydrazide (DETH) and 2,5-bis(prop-2-yn-1-yloxy)terephthalohydrazide (DPTH). (B) Eclipsed stacking model for pCOF₁₀. C, N and O atoms are represented in grey, blue and red. H atoms are omitted, the second and third layer are represented in orange and yellow for clarity. (C) Solid state 1D ¹³C{¹H} CP-MAS NMR spectrum of pCOF₁₀ acquired at 11.7 T, 12 kHz MAS, 298 K, and using cross-polarization times of 5 ms. Spinning side bands are marked with asterisks. Calculated shifts are marked with yellow bars. The narrow signals labelled with crosses at 164 ppm, 37 ppm, and 32 ppm correspond to residual dimethylformamide. (D) Argon adsorption isotherm of pCOF₁₀. Inset: Pore size distribution from NLDFT calculations with cylindrical pores in equilibrium mode. Resulting main pore size is 2.3 nm. (E) PXRD pattern of pCOF₁₀ (open, green circles), Pawley refined profile (blue line) and calculated XRD pattern for the idealized AA stacking (black line). 89
- Figure 3-14: (A) Structure of the azide-functionalized ligands **1a**, **1b**, **2** and (B) the azide-functionalized complexes [Co-1a], [Co-1b], and [Co-2]. (C) Exemplary postsynthetic COF modification towards [Co-1b]-COF. Synthesis conditions can be found in Chapter 6.1.2. 90
- Figure 3-15: Solid-state NMR comparison of the ¹H spectra of [1a]-COF (yellow) and [Co-1a]-COF (blue) measured at 700 MHz ¹H Larmor frequency at $\nu_{rot} = 55.55$ kHz. (A) Schematic structure of the subsection of [Co-1a]-COF with proton labeling. (B) 1D ¹H spectra of [1a]-COF (yellow) and [Co-1a]-COF (blue). Distinct ¹H resonances are given in ppm and labelled with the corresponding atom labels as displayed in (A). (C) and (D) ¹H-¹H DQ-SQ correlation spectra of [1a]-COF (yellow) and [Co-1a]-COF (blue). Horizontal dashed lines indicate the ¹H-¹H connectivities, and vertical solid lines reflect the individual ¹H SQ resonances. Assignments are given next to the dashed lines. In (D) the assignment for only the two new connectivities are shown. The skyline projection of both dimensions are also shown. 92
- Figure 3-16: (A) Schematic structure of the subsection of [Co-1a]-COF with carbon labeling. (B), (C) and (D) Comparison of the natural abundance ¹³C one-dimensional solid-state



NMR spectra of [1a]-COF (blue shades) and [Co-1a]-COF (orange shades) measured at 700 MHz Larmor frequency at $\nu_{\text{rot}} = 55.55$ kHz. Direct polarization spectra recorded with $d1 = 1$ s (B) or with long $d1 = 25$ s (C) are compared with CP MAS spectra (D). For the CP MAS experiment, the carrier was centered at 130 ppm and the CP was optimized to transfer magnetization to the aromatic region. The CP contact time was $500 \mu\text{s}$. Signals with short longitudinal relaxation times are enhanced in the ^{13}C direct MAS spectrum measured with 1 s recycle delay. The assignment of the ^{13}C resonances was obtained from 2D ^1H - ^{13}C , and ^1H - ^1H correlation experiments, and from the quantum chemical calculations. The signals marked with crosses correspond to impurities, e.g. to residual solvent signals. (E) and (F) ^1H -detected 2D ^1H - ^{13}C correlation spectra of [1a]-COF (E) and [Co-1a]-COF (F) recorded with $500 \mu\text{s}$ (red and green), or with $2250 \mu\text{s}$ (orange and blue) CP contact times. The CP-based spectra are overlaid with INEPT-based HSQC spectra which display only one methyl cross-peak displayed with blue (E) and magenta (F) colors. For each cross peak the ^1H and ^{13}C assignments are displayed with red and green colors, respectively. Signals marked with an asterisk are measurement artefacts and they do not appear in 1D ^{13}C -detected $^1\text{H}\{^{13}\text{C}\}$ CP spectra. 95

Figure 3-17: Direct comparison of quantum-chemically obtained ^1H - ^{13}C (A, D, G, J) and ^1H - ^1H DQ-SQ (B, E, H, K) 2D ssNMR spectra with corresponding structural models of [Co-1a]-COF on the right (C, F, I, L). For a better comparison, the same NMR chemical shift region is displayed as in the experimentally obtained spectra (Fig. 3C, D and Fig. 4D, E). In the ^1H - ^{13}C 2D spectra blue and green colors represent ^1H - ^{13}C atom pairs that are within 6 and 2 Å, respectively. In the ^1H - ^1H DQ-SQ spectra, the orange color highlights the oxime proton cross-peaks. In C, F, I, and L the Co, Cl, O, N, and H atoms are displayed with pink, lime, red, blue, and white colors, respectively..... 96

Figure 3-18: Front and side views of the MD simulated structural model of [Co-1a]-COF showing a possible arrangement of the co-catalyst. The linker and the cobaloxime group are depicted by spheres and their carbon atoms are displayed with orange color. Co, Cl, O, N, and H atoms are displayed with pink, lime, red, blue, and white colors, C atoms of the backbone is light blue. 97

Figure 3-19: (A) Comparison of photonic efficiencies for hybrid samples and COF-42 with physisorbed [Co-1a] and [Co-1b]. (B) Comparison of the hydrogen evolution rate of [Co-1b]-COF containing 3.2 wt% [Co-1b] and COF-42 with 4.0 wt% physisorbed [Co-1b] and coarse-grained model fits of both systems. (C) Projection of the hydrogen evolution of [Co-1b]-COF containing 3.2 wt% [Co-1b] and COF-42 with 4.0 wt% physisorbed [Co-1b] based on the coarse-grained models. 99

- Figure 4-1: Synthesis of COF-42 (coCOF-H) from 2,5-diethoxyterephthalohydrazide (DETH) and 1,3,5-triformylbenzene (TFB, left) and HTFG-COF (coCOF-OH) from DETH and 2,4,6-trihydroxybenzene-1,3,5-tricarbaldehyde (TFG, right). Structure of 2,5-bis(2-(dimethylamino)ethoxy)terephthalohydrazide (DtATH), center. 112
- Figure 4-2: Schematic structural diagrams showing subsections of the (a) coCOF-H framework, (e) coCOF-OH framework, and the tertiary amine linker DtATH. Solid state 1D $^{13}\text{C}\{^1\text{H}\}$ CP-MAS NMR spectra of (b-d) coCOF-H and (f-h) coCOF-OH with (b, f) 0%, (c, g) 50%, and (d, h) 100% of DtATH substitution of the original DETH linker. The spectra in (b-d) and (f-h) were acquired at 11.7 T, 10 kHz MAS, 298 K, using cross-polarization contact times of 5 ms. The NMR spectrum (d) was acquired at 11.7 T, 12 kHz MAS, 298 K, and using cross-polarized contact times of 5 ms. Spinning sidebands are marked with asterisks. Distinct carbon atoms in the schematic structures in (a) and (e) are numbered and their associated ^{13}C NMR signals labeled accordingly in (b-d) and (f-h) respectively. The narrow signals labelled with crosses at 164 ppm, 37 ppm and 32 ppm correspond to residual dimethylformamide and at 25 ppm to residual tetrahydrofuran. 113
- Figure 4-3: (a) PXRD pattern of coCOF-OH (open green squares), Pawley refined profile (blue line), calculated XRD pattern for the idealized eclipsed (AA) stacking (black line). (b) PXRD pattern of coCOF-H (open orange circles), Pawley refined profile (red line), calculated XRD pattern for the idealized eclipsed (AA) stacking (black line). (c) and (d) Eclipsed stacking model for coCOF-OH and coCOF-H, respectively. C, N and O atoms are represented in grey, blue and red. H atoms are omitted. The second and third layers are represented in orange and yellow for clarity. 114
- Figure 4-4: (a) Argon adsorption isotherms of coCOF-H (red) and coCOF-OH (blue). Water sorption at 273 K of (b) amine-coCOF-H and (c) amine-coCOF-OH with 0%, 50%, 100% DtATH substitution of the original DETH linker. Adsorption is represented by filled symbols, desorption by open symbols. (d) Relative CO_2 adsorption capacities at 273 K and BET surface areas of amine-coCOF-OH (blue and purple) and amine-coCOF-H (red and orange). BET surface area is indicated by triangles. 116
- Figure 4-5: Solid-state 1D $^{15}\text{N}\{^1\text{H}\}$ DNP-CP-MAS spectra of 100%-amine-coCOF-H without CO_2 exposure. The spectrum was acquired at 9.4 T, 8 kHz MAS, 95 K, in the presence of 16 mM AMUPol biradical in 60:30:10 d_8 -glycerol: D_2O : H_2O , under microwave irradiation at 263 GHz, and using cross-polarization contact times of 5 ms. Blue markings correspond to values obtained by quantum chemical calculations (See Table 6-15, Table 6-16, and Table 6-18). 119
- Figure 4-6: Solid-state 2D $^{13}\text{C}\{^1\text{H}\}$ LTMAS-HETCOR spectra of vacuum-dried 100%-amine-coCOF-H (a) after exposure to 100% ^{13}C -enriched CO_2 for 12 h at 1 bar pressure



- and 298 K, and (b) after desorption of CO₂ for 48 h by vacuum heating at 0.1 bar and 363 K. The spectra were acquired at 9.4 T, 8 kHz MAS, 95 K using short cross-polarization contact times of 500 μs. 1D ¹³C projections are shown along the horizontal axes for comparison with the 2D spectra, and 1D ¹H projections are shown along the vertical axes. Strong correlated ¹³C signal intensity (ca. 160 ppm) with ¹H signal at 12 - 14 ppm establishes that CO₂ chemisorbs to form a bicarbonate (HCO₃⁻) species..... 121
- Figure 5-1: Chemical structures of different Ni-based hydrogen evolution co-catalysts. 127
- Figure 5-2: Chemical structures of different Ru- and Ir-based water oxidation co-catalysts. 128
- Figure 5-3: [FeFe] hydrogenase active site model complexes [FeFe](dcbdt)(CO)₆ (**1**) and [FeFe](bdt)(CO)₆ (**2**) and the BDC ligand. Reprinted from [10]. 128
- Figure 5-4: Synthesis of doped UiO-67. Reprinted from [12]. 129
- Figure 6-1: PXRD pattern of N2-COF before and after photocatalysis showing retention of crystallinity..... 134
- Figure 6-2: ¹H MAS spectra of N2-COF before and after photocatalysis showing no change in the chemical shift values. The peak at 3.7 ppm is due to water, probably in the pores. Also shown are the illuminated and dried COF samples with 8 and 35 wt% **Co-1** with the broad peak around 1.4 ppm due to large amounts of **Co-1**. 134
- Figure 6-3: SEM images of N2-COF before and after photocatalysis showing retention of the rod like morphology..... 135
- Figure 6-4: TEM images of N2-COF before and after photocatalysis in presence of **Co-1** co-catalyst. Fast Fourier Transform (FFT) images show the same 23 Å d-spacing corresponding to the (100) reflection before and after. 135
- Figure 6-5: Variation of H₂ evolution rates in different solvents. For all measurements 5 mg of N2-COF was dispersed in 10 ml of the solvent together with 100 μL of TEOA and 400 μL of a 2.48 mM solution of **Co-1** in acetonitrile. 100 mW/cm² AM 1.5 radiation was used for illumination. 136
- Figure 6-6: Variation of H₂ evolution rates with ratio of ACN/water in the photocatalytic reaction mixture. All conditions were the same as in Figure S5 caption. With increase in ACN content, the H₂ evolution rate increases from 27 μmolg⁻¹h⁻¹ to 130 μmolg⁻¹h⁻¹ and finally to 160 μmolg⁻¹h⁻¹ for 4:1 ACN/water. For 10:1 ACN/water the rate again drops to 130 μmolg⁻¹h⁻¹. 136
- Figure 6-7: Variation of H₂ evolution rates with the pH of the photocatalytic reaction mixture. pH was adjusted by addition of 0.1 M aqueous HCl or NaOH dropwise. All other conditions were the same as before with 4:1 ACN/water as the solvent. The H₂ evolution rates are 138 μmolg⁻¹h⁻¹ at pH 6.6, 390 μmolg⁻¹h⁻¹ at pH 8.05, 160 μmolg⁻¹h⁻¹

$^1\text{h}^{-1}$ at pH 10.05 and $26 \mu\text{molg}^{-1}\text{h}^{-1}$ at pH 12. The inset shows the amount of H_2 generated after 6h at different pH values.....	137
Figure 6-8: Variation of H_2 evolution rates with TEA and different concentrations of TEOA as the electron donor.	137
Figure 6-9: H_2 evolution is restored after addition of 8 equivalents of dmgH_2 to the reaction mixture. Initially, 5 mg of $\text{N}_2\text{-COF}$ was dispersed in 10 ml of 4:1 $\text{ACN}/\text{H}_2\text{O}$ solvent together with $100 \mu\text{L}$ of TEOA and $400 \mu\text{L}$ of a 2.48 mM solution of Co-1 in acetonitrile. The reaction mixture is irradiated with $100 \text{ mW}/\text{cm}^2$ AM 1.5 radiation.	138
Figure 6-10: H_2 evolution with 0.05 M dmgH_2 as the electron donor. 5 mg of $\text{N}_2\text{-COF}$ was dispersed in 10 ml of 4:1 $\text{ACN}/\text{H}_2\text{O}$ solvent together with $400 \mu\text{L}$ of a 2.48 mM solution of Co-1 in acetonitrile. The reaction mixture is irradiated with $100 \text{ mW}/\text{cm}^2$ AM 1.5 radiation. No TEOA was added to the reaction mixture.....	138
Figure 6-11: TEM micrographs of post photocatalysis sample of $\text{N}_2\text{-COF}$ showing (a) even distribution of $\sim 2 \text{ nm}$ Pt nanoparticles on one section of the COF sample. (b) no appreciable Pt deposition can be seen on another section of the same sample. Photocatalysis was carried out in 4:1 ACN/water solvent with metallic platinum co-catalyst.	139
Figure 6-12: Structure of COF-42.	140
Figure 6-13: Structure of $\text{N}_x\text{-COFs}$	141
Figure 6-14: ^{13}C CPMAS NMR spectra of $\text{N}_2\text{-COF}$ and the peak assignments.	142
Figure 6-15: TEM energy dispersive X-ray (EDX) spectroscopic analysis of $\text{N}_2\text{-COF}$ before photocatalysis. Three positions were sampled.	143
Figure 6-16: TEM energy dispersive X-ray (EDX) spectroscopic analysis of $\text{N}_2\text{-COF}$ after photocatalysis showing no cobalt present. Three positions were sampled.....	144
Figure 6-17: TEM energy dispersive X-ray (EDX) spectroscopic analysis of an illuminated and dried $\text{N}_2 \text{ COF} + 8 \text{ wt}\% \text{ Co-1}$ sample showing characteristic peaks of cobalt. Three positions were sampled.....	145
Figure 6-18: Geometry of Co-1 optimized on PBE0 D3/def2-SVP level of theory.....	146
Figure 6-19: Geometry of Co-1-acn model compound, optimized on PBE0 D3/def2-SVP level of theory.....	146
Figure 6-20: Geometry of Co-1-h2o model compound, optimized on PBE0 D3/def2-SVP level of theory.....	147
Figure 6-21: Diphenyl diazene model used for modelling the interaction of the co-catalyst with the COF in the pore walls.	147
Figure 6-22: Constrained optimized geometry of the pore-diazene cobaloxime-COF model obtained on PBE0-D3/def2-SVP level of theory.	147



Figure 6-23: Constrained optimized geometry of the pore-diazene-90° cobaloxime-COF model obtained on PBE0-D3/def2-SVP level of theory.	148
Figure 6-24: Geometry of Co-1-pyCOOMe compound. a) Crystal structure; b) optimized on PBE0-D3/def2-SVP level of theory.	149
Figure 6-25: Geometry of Co-1-pyNMe2 compound. a) Crystal structure; b) optimized on PBE0-D3/def2-SVP level of theory.	150
Figure 6-26: Mechanism of H ₂ evolution with N ₂ -COF photosensitizer and Co-1 co-catalyst.	150
Figure 6-27: TCSPC decay traces of N ₂ -COF with added Co-1 , TEOA and both in 4:1 ACN/water solvent monitored at 630 nm.	151
Figure 6-28: Light intensities of the solar simulator that was used earlier for the measurements in the main manuscript (old lamp, black), the lamp that was used for the experiments in EDI where stated (new lamp, blue), compared to AM 1.5G (yellow).	161
Figure 6-29: Comparison of hydrogen evolution rates for hybrid samples and COF-42 with physisorbed [Co-1b] measured with the old lamp.	161
Figure 6-30: Hydrogen evolution rate for [Co-1a]-COF measured with the new lamp.	162
Figure 6-31: Photocatalytic hydrogen evolution experiments in acetonitrile and water in a ratio of 4:1 at pH 8. Red triangles: [Co-1b]-COF with TEOA as sacrificial donor. Blue pluses: COF-42 with [Co-1b], no sacrificial donor added. Orange circles: [Co-1b] with TEOA as sacrificial donor, no COF added. Green crosses: COF-42 with TEOA as sacrificial donor and CoCl ₂	162
Figure 6-32: Photocatalytic activity of [Co-1b]-COF with 4.2 wt% cobaloxime content. Orange: first measurement, green: measurement after recycling.	163
Figure 6-33: Argon isotherms of [1a]-COF, [1a]-COF, [2]-COF, [Co-1a]-COF, [Co-1a]-COF, and [Co-2]-COF.	164
Figure 6-34: Pore size distributions of [1a]-COF, [1a]-COF, [2]-COF, [Co-1a]-COF, [Co-1a]-COF, and [Co-2]-COF.	165
Figure 6-35: Powder X-ray diffractograms of pCOF ₁₀ , [Co-1a]-COF and [Co-1b]-COF.	166
Figure 6-36: Powder X-ray diffractograms of [Co-1a]-, [Co-1b]-, and [Co-2].	166
Figure 6-37: Scanning electron microscopy image of [Co-1a]-COF.	167
Figure 6-38: Scanning electron microscopy image of [Co-1b]-COF.	168
Figure 6-39: Scanning electron microscopy image of [Co-2]-COF.	169
Figure 6-40: Emission spectra of COF-42, physisorbed [Co-1a], and [Co-1a]-COF. All samples were suspended in acetonitrile. All samples were excited at 300 nm.	170

Figure 6-41: Fluorescence lifetime measurements of COF-42, physisorbed [Co-1a], and [Co-1a]-COF. All samples were suspended in acetonitrile. Samples were excited at 375 nm and the decay of the emission was monitored at 456 nm.	170
Figure 6-43: FTIR spectra of COF-42 and pCOF ₁₀	172
Figure 6-44: FTIR spectra of pCOF ₁₀ , [Co-1a], [Co-1a]-COF, [Co-1b], and [Co-1b]-COF.	173
Figure 6-45: UV/Vis absorption spectra of (A) pCOF ₁₀ , [Co-1a] and [Co-1a]-COF; (B) pCOF ₁₀ , [Co-1b] and [Co-1b]-COF; (C) pCOF ₁₀ , [Co-2] and [Co-2]-COF....	174
Figure 6-46: Dependence of the 1D spectrum quality of [1a]-COF and [Co-1a]-COF on the applied MAS frequency.	175
Figure 6-47: Optimized geometry for the COF-42 pore model, obtained on RI-PBE-D3/def2-TZVP level of theory. Top and side view.	176
Figure 6-48: Visualization of the calculated pore diameter of 20.61 Å obtained from the optimized COF-42 pore model.	176
Figure 6-49: Optimized pCOF ₁₀ pore model, obtained on RI-PBE-D3/def2-TZVP level of theory. Top and side view.	177
Figure 6-50: Optimized COF-42-pPy pore, obtained on RI-PBE-D3/def2-TZVP level of theory. Top and side view.	177
Figure 6-51: Visualization of the calculated pore diameter of 19.10 Å for the COF42-pPy-COF pore model.	178
Figure 6-52: Geometry for the pCOF ₁₀ cut model system, obtained by cutting the optimized pCOF ₁₀ pore model.	178
Figure 6-53: Atom labels for the pCOF ₁₀ cut model system.	179
Figure 6-54: Calculated NMR Chemical Shifts for the pCOF ₁₀ cut model system, obtained on level of theory.	179
Figure 6-55: Overlay of every 100th frame from a 15 ns MD simulation visualizing the flexibility of the 1a -ligand in comparison to the ethoxy-ligands. Top and side view.	184
Figure 6-56: Overlay of every Nitrogen position of the 1a -ligand showing positions from every 5th frame from a 15 ns MD simulation visualizing visited positions of the Pyridine subunit. Top and side view.	184
Figure 6-57: FTIR spectra of Amine-coCOF-OH (left, blue) and Amine-coCOF-H (right, red). Darker color indicates higher amount of DtATH.....	190
Figure 6-58: PXRD patterns of Amine-coCOF-OH (left, blue) and Amine-coCOF-H (right, red). Darker color indicates higher amount of DtATH.....	191
Figure 6-59: UV/Vis absorption spectra of Amine-coCOF-OH (left, blue) and Amine-coCOF-H (right, red). Darker color indicates higher amount of DtATH.....	191



- Figure 6-60: Argon sorption isotherms of Amine-coCOF-OH (left, blue) and Amine-coCOF-H (right, red). Darker color indicates higher amount of DtATH. Adsorption is represented by filled symbols, desorption by open symbols. 192
- Figure 6-61: Pore size distribution derived from argon isotherms of Amine-coCOF-OH (left, blue) and Amine-coCOF-H (right, red). Darker color indicates higher amount of DtATH. 192
- Figure 6-62: Model for one pore of 100% Amine-coCOF-H. Left: amine side chains at pore walls. Right: amine side chains protruding the pores. C, N, h, and O are represented in grey, blue, white, and red. Smallest pore diameter is marked by red line. 193
- Figure 6-63: Linear fits of the van't Hoff equation for the different coCOF-systems and amine amounts. 195
- Figure 6-64: Spectral deconvolution of coCOF-H with spinning side-bands and solvent impurities indicated by asterisks and crosses respectively. 196
- Figure 6-65: Vacuum dried 100%-amine-coCOF-H solid-state 1D $^{13}\text{C}\{^1\text{H}\}$ DNP-CP MAS spectra using a cross-polarization contact time of (a) 5 ms, and (b) 500 μs respectively. DNP-CP MAS spectra were acquired with 16 scans at 9.4 T, 8 kHz MAS, 95 K in the presence of 16 mM AMUPOL biradical in 60:30:10 d_8 -glycerol (^{13}C -depleted): $\text{D}_2\text{O}:\text{H}_2\text{O}$, under microwave irradiation at 263 GHz. Solid-state 1D $^{13}\text{C}\{^1\text{H}\}$ LTMAS-CP MAS spectra acquired with 256 scans and a cross-polarization contact time of 500 μs for 100%-Amine-coCOF-H (c) after exposure to 100% ^{13}C -enriched CO_2 for 12 h at 1 bar pressure and 298 K, and (d) after desorption of CO_2 for 48 h by vacuum heating at 0.1 bar and 363 K. 197
- Figure 6-66: Vacuum-dried 100%-amine-coCOF-H (a) solid-state 2D $^{13}\text{C}\{^1\text{H}\}$ DNP-HETCOR spectra using cross-polarization contact time of 500 μs (b) and solid-state 2D $^{15}\text{N}\{^1\text{H}\}$ DNP-HETCOR spectra using cross-polarization contact time of 5 ms. The spectra were acquired at 9.4 T, 8 kHz MAS, 95 K in the presence of 16 mM AMUPOL biradical in 60:30:10 d_8 -glycerol (^{13}C -depleted): $\text{D}_2\text{O}:\text{H}_2\text{O}$, under microwave irradiation at 263 GHz. With DNP sensitivity enhancements weak $^{13}\text{C}\{^1\text{H}\}$ - correlated signal intensity is observed from residual pendant ethyl ether moieties in unmodified coCOF-H. 198
- Figure 6-67: Optimized geometry for the DETH-M model system obtained on PBE0-D3/def2-TZVP level of theory. 198
- Figure 6-68: Atom labels for the DETH-M model system based on the optimized geometry, obtained on PBE0-D3/def2-TZVP level of theory. 199
- Figure 6-69: Optimized geometry for modeled DETH-M model system, including a single water molecule hydrogen bonded to carbonyl and imine bond, on obtained on PBE0-D3/def2-TZVP level of theory. 199

Figure 6-70: Optimized geometries for modeled DETH monomer modifications, obtained on PBE0-D3/def2-TZVP level of theory.	201
Figure 6-71: Optimized geometries for modeled physisorbates of carbonic acid to the DETH monomer, obtained on PBE0-D3/def2-TZVP level of theory.	201
Figure 6-72: Optimized geometry for the modeled chemisorbate of CO ₂ to the DETH monomer, obtained on PBE0-D3/def2-TZVP level of theory.	202
Figure 6-73: Optimized geometry for the DETH building block unit obtained on PBE0-D3/def2-TZVP level of theory. Corresponding atom labels are shown on the right.....	203



6.3 List of tables

Table 3-1: Summary of H ₂ Evolution Activity of COF-Based Photocatalytic Systems.....	59
Table 3-2: Gibbs Free Energy of formation of Co ^{II} and Co ^I by Oxidative and Reductive Electron Transfer Pathways. The N ₂ -COF energy levels are the calculated values for a model hexagon with hydrazone termination. ^[9] E(Co ^{III} /Co ^{II}) and E(Co ^{II} /Co ^I) potential values have been obtained from ref 25.	72
Table 4-1: BET surface areas, CO ₂ uptake at 273 K, relative CO ₂ adsorption at 273 K and heats of CO ₂ adsorption of the presented COFs.	117
Table 6-1: Gibbs free energy of formation of Co ^{II} and Co ^I in the reaction of N ₂ with Co-2 and Co-3 by oxidative and reductive electron transfer pathways. The N ₂ energy levels are for a model hexagon with hydrazone termination. The Co(III)/Co(II) and Co(II)/Co(I) reduction potential values have been obtained from literature. ^{2,3}	139
Table 6-2: Gibbs free energy of formation of Co ^{II} and Co ^I in the reaction of N ₁ , N ₃ and COF 42 with Co-1 by oxidative and reductive electron transfer pathways. The COF 42 energy levels are for a model with methyl terminations, unlike model hexagons with hydrazone termination for the N _x COFs. ⁴	141
Table 6-3: H ₂ evolution rate (μmolg ⁻¹ h ⁻¹) for N ₂ and N ₃ COFs with platinum and Co-1 co-catalysts under different conditions.....	142
Table 6-4: Calculated cobalt-axial nitrogen bond distances for cobaloxime model systems, obtained on PBE0-D3/def2-SVP level of theory.	148
Table 6-5: Calculated cobalt-nitrogen bond distances for cobaloxime-COF model systems, obtained on PBE0-D3/def2-SVP level of theory. For the pore-diazene and the pore-diazene-90° models, the distances to the four nearest N atoms are shown.....	148
Table 6-6: Comparison of calculated interaction energies, obtained on PBE0-D3/def2-TZVP level of theory. Interaction Energies (IAE) and Counterpoise Corrected Interaction Energies (CPC-IAE) are listed, as well as differences between Counterpoise Corrected Interaction Energies (ΔCPC-IAE) with respect to the Co-1 model.....	149
Table 6-7: Comparison of experimental (crystal structure data) and calculated (PBE0-D3/def2-SVP) cobalt- axial nitrogen bond distances of reported reference compounds.	150
Table 6-8: Biexponential fits of the TCSPC decay traces of N ₂ -COF with added Co-1 , TEOA and both in 4:1 ACN/water solvent at 630 nm.	151
Table 6-9: BET surface areas based on argon sorption measurements of the presented COFs.	163
Table 6-10: Emission lifetimes of COF-42, physisorbed [Co-1a], and [Co-1a]-COF. ..	171
Table 6-11 Calculated catalyst content in weight percent according to ICP measurements. Functionalization of total amount of propargyl units in the pCOF ₁₀ sample.	172

Table 6-12: Calculated NMR Chemical Shifts for the pCOF10 model system, obtained on B97-2/pcS-2//RI-PBE-D3/def2-TZVP level of theory.	179
Table 6-13: Solvent mixtures used in the synthesis of different coCOF-samples.	190
Table 6-14: Pore sizes, pore volume ($\text{cm}^3 \text{g}^{-1}$) and pore volume fractions (%) of the presented COFs.	193
Table 6-15: Calculated ^{13}C NMR Chemical Shifts for the DETH-M model system, obtained on B97-2/pcS-2//PBE0-D3/def2-TZVP level of theory.	200
Table 6-16: Calculated ^{15}N NMR Chemical Shifts for the DETH-M model system, obtained on B97-2/pcS-2//PBE0-D3/def2-TZVP level of theory.	200
Table 6-17: Calculated ^1H NMR Chemical Shifts for the modeled DETH monomer modifications, obtained on B97-2/pcS-2//PBE0-D3/def2-TZVP level of theory....	202
Table 6-18: Calculated ^{13}C NMR Chemical Shifts for the modeled DETH monomer modifications, obtained on B97-2/pcS-2//PBE0-D3/def2-TZVP level of theory....	202
Table 6-19: Calculated ^{15}N NMR chemical shifts for the modeled DETH monomer modifications, obtained on B97-2/pcS-2//PBE0-D3/def2-TZVP level of theory....	203
Table 6-20: Calculated ^{15}N NMR Chemical Shifts for the DETH building block unit, obtained on B97-2/pcS-2//PBE0-D3/def2-TZVP level of theory.	203



6.4 List of abbreviations

2D	<i>Two-dimensional</i>
AFM	<i>Atomic force microscopy</i>
BDBA	<i>1,4-Benzenediboronic acid</i>
BET	<i>Brunauer-Emmet-Teller</i>
BETH	<i>2,5-Bis(2-(ethylthio)ethoxy)terephthalohydrazide</i>
BJH	<i>Barret-Joyner-Halenda</i>
Bth	<i>Benzene-1,3,5-tricarbohydrazide</i>
CCS	<i>Carbon capture and storage, Carbon capture and storage</i>
CCU	<i>Carbon capture and utilization</i>
COF	<i>Covalent organic framework</i>
CP	<i>Cross-polarization</i>
CuTAPP	<i>5,10,15,20-Tetra(p-amino-phenyl)porphyrinatocopper(II)</i>
DAA _n	<i>2,6-diaminoanthracene</i>
DABD	<i>2,5-Diamino-1,4-benzenediol dihydrochloride</i>
DCC	<i>Dynamic covalent chemistry</i>
DDQ	<i>2,3-Dichloro-5,6-dicyano-1,4-benzoquinone</i>
DETH	<i>2,5-Diethoxyterephthalohydrazide, 2,5-Diethoxyterephthalohydrazide</i>
DFT	<i>Density functional theory</i>
Dha	<i>2,5-Dihydroxyterephthalaldehyde</i>
DHTH	<i>Dihydroxyterephthalohydrazide</i>
Dma	<i>2,5-Dimethoxyterephthalaldehyde</i>
DNP	<i>Dynamic nuclear polarization</i>
DP	<i>Direct polarization</i>
DQ-SQ	<i>Double quantum-single quantum</i>
DtATH	<i>2,5-Bis(2-(dimethylamino)ethoxy)terephthalohydrazide</i>
ETTA	<i>(4,4',4'',4''')-(Ethene-1,1,2,2-tetrayl)tetraaniline</i>
FT-IR	<i>Fourier transform infrared</i>
FTO	<i>Fluorinated tin oxide</i>
HATN-6CHO	...	<i>2,3,8,9,14,15-Hexa(4-formylphenyl)diquinoxalino[2,3-a:2',3'-c]phenazine</i>
HER	<i>Hydrogen evolution rate</i>
HETCOR	<i>Heteronuclear correlation</i>
ITO	<i>Indium tin oxide</i>

IUPAC.....	<i>International Union of Pure and Applied Chemistry</i>
LTMAS	<i>Low-temperature magic angle spinning</i>
MC.....	<i>Monte Carlo</i>
MOF.....	<i>Metal organic framework</i>
MTh.....	<i>2,5-Bis[(2S)-2-methylbutoxy]terephthalohydrazide</i>
NLDFT	<i>Non-local density functional theory</i>
ODH	<i>Oxalaldihydrazide</i>
PDA.....	<i>1,4-Phenylenediamine</i>
PDAN	<i>1,4-Phenylenediacetonitrile</i>
POP.....	<i>Porous organic polymer</i>
PPF	<i>Porous polymer framework</i>
p-Por-CHO	<i>5,10,15,20-Tetrakis(4-benzaldehyde)porphyrin</i>
PXRD.....	<i>Powder X-ray diffraction</i>
QSDFT.....	<i>Quenched solid density functional theory</i>
Q _{st}	<i>Isosteric heat of adsorption</i>
TAPP.....	<i>5,10,15,20-Tetra(p-amino-phenyl)porphyrin</i>
TEA.....	<i>Triethylamine</i>
TEOA.....	<i>Triethanolamine</i>
TFB.....	<i>1,3,5-Triformylbenzene, Triformylbenzene</i>
TFBE	<i>1,1,2,2-Tetrakis(4-formyl-(1,1'-biphenyl))ethane</i>
TFG	<i>Triformyl phloroglucinol, Triformylphloroglucinol</i>
TFPPy.....	<i>1,3,6,8-Tetrakis(4-formylphenyl)pyrene</i>
TON.....	<i>Turnover number</i>
WOC.....	<i>Water oxidation catalyst</i>
XRD	<i>X-ray diffraction</i>
ZIF.....	<i>Zeolitic imidazolate framework</i>



6.5 List of publications

Published as part of this thesis

1. Single site photocatalytic H₂ evolution from Covalent Organic Frameworks with molecular cobaloxime co-catalysts

T. Banerjee, F. Haase, G. Savasci, K. Gottschling, C. Ochsenfeld, B. V. Lotsch
J. Am. Chem. Soc. **2017**, *139*, 16228–16234.

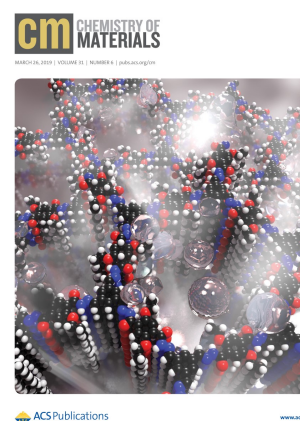
2. H₂ evolution with covalent organic framework photocatalysts

T. Banerjee, K. Gottschling, G. Savasci, C. Ochsenfeld, B. V. Lotsch
ACS Energy Lett. **2018**, *3*, 400–409.

3. Molecular insights into carbon dioxide sorption in hydrazone-based covalent organic frameworks with tertiary amine moieties

K. Gottschling, L. Stegbauer, G. Savasci, N. A. Prisco, Z. J. Berkson, C. Ochsenfeld, B. F. Chmelka, B. V. Lotsch
Chem. Mater **2019**, *31* (6), 1946–1955.

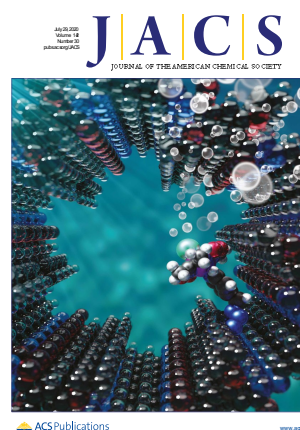
This project was highlighted as a supplementary cover image of the journal Chemistry of Materials, the cover image was designed by Kerstin Gottschling.



4. Rational design of covalent cobaloxime-COF hybrids for enhanced photocatalytic hydrogen evolution

K. Gottschling, G. Savasci, H. Vignolo-González, S. Schmidt, P. Mauker, T. Banerjee, P. Rovó, C. Ochsenfeld, B. V. Lotsch
J. Am. Chem. Soc. **2020**, *142* (28), 12146–12156

This project was highlighted as a supplementary cover image of the Journal of the American Chemical Society, the cover image was designed by Kerstin Gottschling.



Not part of this thesis

1. Borane-Catalyzed Room-Temperature Hydrosilylation of Alkenes/Alkynes on Silicon Nanocrystal Surfaces

T. K. Purkait, M. Iqbal, M. h. Wahl, K. Gottschling, C. M. Gonzalez, M. A. Islam, J. G. C. Veinot
J. Am. Chem. Soc. **2014**, *136*, 17914 – 17917.

2. Tuning the stacking behaviour of a 2D covalent organic framework through non-covalent interactions

F. Haase, K. Gottschling, L. Stegbauer, L.S. Germann, R. Gutzler, V. Duppel, V. S. Vyas, K. Kern, R.E. Dinnebier, B.V. Lotsch

Mater. Chem. Front. **2017**, *1*, 1354–1361.

3. Functional organo-nano particles by RAFT copolymerisation

H. Langhals, D. Zgela, A. Haffner, C. Koschnick, K. Gottschling, C. Paulik

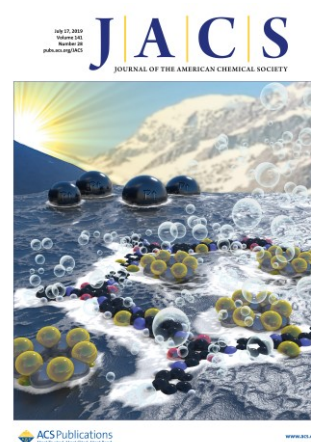
Green and Sustainable Chem. **2018**, *8*, 247–274.

4. Sustained Solar H₂ Evolution from a Thiazolo[5,4-d]thiazole-Bridged Covalent Organic Framework and Nickel-Thiolate Cluster in Water

B. P. Biswal, H Vignolo-González, T. Banerjee, L. Grunenberg, G. Savasci, K. Gottschling, J. Nuss, C. Ochsenfeld, B. V. Lotsch

J. Am. Chem. Soc. **2019**, *141*, 11082–11092 .

This project was highlighted as a supplementary cover image of the Journal of the American Chemical Society, the cover image was designed by Kerstin Gottschling.





6.6 Contributions to conferences

Oral presentations

1. Photocatalytic hydrogen evolution by covalent organic frameworks modified with molecular co-catalysts – highly commended talk

12/2018, MOF2018, Auckland (NZ)

2. Fuel from sunlight – Covalent organic frameworks as platforms for photocatalytic water splitting”

09/2018, NIM Summer Retreat 2018, Herrsching/Ammersee:

3. Covalent organic what!? Organic framework compounds for photocatalysis

07/2016, NIM Summer Retreat 2016, Herrsching/Ammersee

Poster presentations

09/2018, GDCh 26. Lecture Conference on Photochemistry, Garching

10/2017, EuroMOF 2017, Delft (NLD)

07/2017, NIM Summer Retreat 2017, Schloss Hirschberg/Beilngries

09/2016, MOF2016, Long Beach (US)

03/2016, DPG Spring Meeting 2016, Regensburg

07/2015, NIM Summer retreat 2015, Lenggries